Modelling and Analysis of Seawater Scrubbers for Reducing SOx Emissions from Marine Engines

Simonsen, Anders Schou

DOI (link to publication from Publisher):
10.54337/aau300042422

Publication date:
2018

Document Version
Publisher's PDF, also known as Version of record

Citation for published version (APA):
Simonsen, A. S. (2018). *Modelling and Analysis of Seawater Scrubbers for Reducing SOx Emissions from Marine Engines*. Aalborg Universitetsforlag. https://doi.org/10.54337/aau300042422

MODELLING AND ANALYSIS OF SEAWATER SCRUBBERS FOR REDUCING SOx EMISSIONS FROM MARINE ENGINES

BY
ANDERS SCHOU SIMONSEN

DISSERTATION SUBMITTED 2018

AALBORG UNIVERSITY
DENMARK

Modelling and Analysis of Seawater Scrubbers for Reducing SOx Emissions from Marine Engines

Ph.D. Dissertation

Anders Schou Simonsen

Dissertation submitted November 2018

Dissertation submitted: November 19, 2018

PhD supervisors: Associate Professor Kim Sørensen
Aalborg University

Søren Mølgaard
Alfa Laval Aalborg

Assistant PhD supervisors: Associate Professor Thomas J. Condra
Aalborg University

Professor Lasse A. Rosendahl
Aalborg University

Ruddi K. Mortensen
Alfa Laval Aalborg

PhD committee: Associate professor Samuel Simon Araya (Chairman)
Aalborg University

Professor Dr.-Ing. Milovan Perić
Founder and general manager of CoMeT Continuum Mechanics Technologies

Professor Dr. Hans Kuerten
Eindhoven University

PhD Series: Faculty of Engineering and Science, Aalborg University

Department: Department of Energy Technology

ISSN (online): 2446-1636
ISBN (online): 978-87-7210-357-0

Published by:
Aalborg University Press
Langagervej 2
DK – 9220 Aalborg Ø
Phone: +45 99407140
aauf@forlag.aau.dk
forlag.aau.dk

Printed in Denmark by Rosendahls, 2018

ABSTRACT

Air pollution has increased in recent years and is one of the largest environmental risks to human health, where one-in-nine deaths can be linked to air pollution. One of these pollutants is $\mathrm{SO_x}$, which include $\mathrm{SO_2}$ and $\mathrm{SO_3}$ emissions, where the marine sector accounts for 13 % of the global $\mathrm{SO_x}$ emissions. The *International Maritime Organization*, IMO, adopted the *International Convention for the Prevention of Pollution from Ships*, MARPOL, in 1973, as a means to reduce pollution from ships. MARPOL consists of six annexes, where *Annex VI: Prevention of Air Pollution from Ships* was adopted in 2005 and concerns nitrogen oxide, particulate matter, and sulfur oxide emissions. The $\mathrm{SO_x}$ regulations have changed over time, where further restrictions will be adopted in 2020, where the equivalent sulfur content in the flue gas must be 0.5 % and 0.1 % by mass outside and inside *Emissions Control Areas*, ECAs, respectively, which are typically areas near coastal lines.

The sulfur equivalent limit regulations can be complied with by installing a scrubber, which allow ships to use fuel oil with a greater sulfur content than the allowable limits, and this reduces operational costs. A scrubber removes sulfur by injecting seawater (or freshwater with added chemicals) over the exhaust gas stream, which washes the sulfur out by chemical processes. This process requires large volume flows of seawater and thus significant pumping power. Therefore, by optimizing the scrubber design, water consumption and back pressure can be reduced, which decreases the energy requirements. This will imply a reduced fuel consumption and thereby lower $\mathrm{CO_2}$ and particulate matter emissions.

In order to efficiently optimize a scrubber for a specific application, an accurate computational model is required, which takes all aspect of seawater scrubbing into account. This study proposes a model, where both the continuous phase, the liquid phase, and the liquid wall films flowing down the scrubber shell, are taken into account. The chemistry governing $\mathrm{SO_x}$ absorption in seawater is modelled as well, where 17 species are taken into account in the liquid phase. This multi-disciplinary model combines numerous submodels, where several model parameters are unknown. Therefore, the model was tuned to match results from experimental tests, which were carried out at the Alfa Laval Test & Training Centre.

The tuned scrubber model was capable of predicting the outlet temperature, sulfur concentration, and overall pressure loss with an average accuracy of $-1.8\,\mathrm{K}$, $-10.1\,\mathrm{ppm}\ (\mathrm{v/v})$, and $-57.5\,\mathrm{Pa}$ respectively. The accuracies fluctuated for each test carried out, where the RMS-errors were $3.1\,\mathrm{K}$, $20.4\,\mathrm{ppm}\ (\mathrm{v/v})$, and

$77.3\,\mathrm{Pa}$, which corresponds to relative deviations compared to the experimental tests of 11.5, 11.1, and $11.5\,\%$ respectively. The model was found to be most accurate for high water flows, and the errors quoted are from these. At low water flows, which is an atypical operating scenario, the errors increase.

This Ph.D. project has contributed to a better understanding of seawater scrubbers and the modelling of these, which allows for developing more efficient scrubbers, which will reduce particulate matter and $\mathrm{CO_2}$ emissions.

Anders Schou Simonsen
Aalborg University, 2018

RESUMÉ

Luftforurening er steget over den seneste årrække og er en af de største miljømæssige risici for menneskers sundhed, hvor et ud af ni dødsfald skyldes luftforurening. Et af disse forurenende stoffer er SO_x, som inkluderer SO_2 og SO_3 emissioner, hvor marinesektoren står for 13 % af den globale SO_x udledning. *International Maritime Organization*, IMO, vedtog i 1973 *International Convention for the Prevention of Pollution from Ships*, MARPOL, for at reducere forureningen fra skibe. MARPOL består af seks annekser, hvoraf *Annex VI: Prevention of Air Pollution from Ships* blev vedtaget i 2005 og vedrører kvælstofoxid-, partikel- og svovloxidemissioner. SO_x regulativerne er ændret over tid, og yderligere restriktioner vil blive vedtaget i 2020, hvor svovlindholdet i røggassen ikke må overskride grænseværdier på 0,5 % og 0,1 % (massefraktioner) udenfor og indenfor *Emissions Control Areas*, ECA'er, henholdsvis, som typisk er områder nær kystlinier.

Grænseværdierne for SO_x udledning kan overholdes ved at installere en scrubber, som tillader skibe at anvende brændstof med et højere svovlindhold end de tilladte værdier, hvilket reducerer driftsomkostningerne. En scrubber fjerner SO_x ved at skylle havvand (eller ferskvand tilsat kemikalier) udover udstødningsgassen, som vasker svovlet ud ved kemiske processer. Denne proces kræver imidlertid store mængder havvand, hvor energiforbruget er signifikant. Vandforbruget og modtrykket kan reduceres ved at optimere scrubberdesignet, hvilket reducerer energibehovet og dermed brændstofforbruget, som medfører mindre CO_2 og partikelemissioner.

For effektivt at kunne optimere en scrubber kræves en præcis beregningsmodel, som tager alle fysiske aspekter med i betragtning. En sådan model er resultatet af dette Ph.d. projekt, hvor både gasfasen, væskefasen og vægfilmen, som løber langs væggene, modelleres. Kemien vedrørende SO_x absorption i havvand modelleres også, hvor der tages højde for 17 forskellige stoffer i væskefasen. Den tværfaglige scrubbermodel kombinerer adskillige undermodeller, hvor flere modelparametre er ukendte. Disse parametre blev justeret, så resultaterne fra modellen kom til at passe med lignende eksperimentelle forsøg, som blev udført i testcenteret hos Alfa Laval i Aalborg.

Efter at have justeret modelparametrene var scrubbermodellen i stand til at forudsige temperaturen og svovlkoncentrationen i udstødningsgassen samt det samlede tryktab med en gennemsnitlig nøjagtighed på henholdsvis $-1{,}8$K, $-10{,}1$ ppm (v/v) og $-57{,}5$ Pa. Nøjagtighederne flukturerede for de forskellige experimenter, hvor de gennemsnitlige RMS-fejl var på henholdsvis 3,1 K, 20,4 ppm (v/v) og 77,3 Pa, som svarer til relative afvigelser sammenlignet med

de eksperimentelle forsøg på henholdsvis 11,5, 11,1 og 11,5 %. Modellen viste sig at være mest præcis ved høje vandbelastninger, hvor de viste fejl er fra. Ved lav vandbelastning, som er et atypisk driftsscenarie, steg fejlene.

Dette Ph.d.-projekt har bidraget til en bedre forståelse af havvandscrubbere og modellering af disse, hvilket gør det muligt at udvikle mere effektive scrubbere, som vil reducere partikel- og CO_2 emissioner.

Anders Schou Simonsen
Aalborg Universitet, 2018

PREFACE

This thesis is submitted at the Faculty of Engineering and Science, Aalborg University, Denmark, for the degree of Doctor of Philosophy, Ph.D. This industrial Ph.D. dissertation covers research work conducted from October 2015 to October 2018 and was carried out in corporation with Alfa Laval Aalborg A/S. The project was supervised by Associate Professor Kim Sørensen from Aalborg University and Søren Mølgaard from Alfa Laval, and was funded by Innovationsfonden (Grant No. 5016-00061) and Alfa Laval Aalborg A/S.

This study is presented as a monograph, where the main findings and contributions are shown along with a general description of the work carried out. As this study is an industrial Ph.D., the aim has been a precise working scrubber model, which can be used industrially. Scientific contributions were made during the project period, but this monograph also serves as a complete documentation of the scrubber model, where practical details are included, which might not have been included in a more conventional Ph.D. monograph. Furthermore, this study tries to give an intuitive understanding of the numerous sub-models used, where in-depth analyses were carried out for most of these.

Two papers were written during the project period, where one has been submitted to *Computers & Fluids* and is currently under review, whereas the other is presented at the *20th International Conference on Computational Fluid Dynamics, ICCDF 2018*, in October 2018. Another paper was co-authored during the project period [Singh et al. (119)]. References are cited by [*Main author* et al. (*Reference number*)] such as [Millero et al. (96)], where the references are ordered by the last name in the reference list.

I would like to express my sincere gratitude to my supervisors at Aalborg University, where Kim Sørensen and Tom Condra have been supporting and helping me throughout my studies. Furthermore, I would like to thank my forgiving colleagues from the university, where Anna L. Jensen, Marie C. Pedersen, and Jakob Hærvig have been listening to a noisy hard-working computer for quite some time. From Alfa Laval I would like to thank all my colleagues - including former employee and main supervisor Jens Peter Hansen. I would also like to thank Niels Deen from Eindhoven University of Technology, with whom I wrote a paper in corporation with during my five weeks stay at TU-Eindhoven. Additionally, I would like to thank my hard-working girlfriend Sissel for supporting me and keeping me in balance, when mass and energy wasn't. Finally, I would like to thank my family for motivating me to do whatever I found interesting in life:

> *"At gøre, hvad man holder af, er forudsætningen*
> *for at opleve overskud i tilværelsen"* - Unknown

NOMENCLATURE

Symbols

	Unit	Representation		Unit	Representation
a	$\mathrm{m/s^2}$	Acceleration	A	$\mathrm{m^2}$	Area
A_T	$\mathrm{mol/m^3}$	Alkalinity	c	$\mathrm{mol/m^3}$	Molar concentration
$\mathbf{C}_\mathrm{g}$	–	Gas component matrix	$\mathbf{C}_\mathrm{l}$	–	Liquid component matrix
C_IP	–	Instability constant	D	m	Diameter
E	J	Thermal energy	f	Pa	Fugacity
F	N	Force	g	$\mathrm{m/s^2}$	Gravitational acceleration
h	$\frac{\mathrm{W}}{\mathrm{m^2\,K}}$	Heat transfer coefficient	H	m	Height
I	mol/L	Ionic strength	k	Mixed	Rate constant
k_l	m/s	Liquid mass transfer coefficient	k_g	m/s	Gas mass transfer coefficient
$\bar{k}$	m/s	Overall mass transfer coefficient	k_t	$\mathrm{m^2/s^2}$	Turbulence kinetic energy
K_a	Mixed	Equilibrium/acid dissociation constant	L	m	Length
m	kg	Mass	M	mol/L	Molar mass
n	Mixed	Mole (mol) or integer (–)	N	–	Droplet count in a parcel
p	$\mathrm{N \cdot s}$	Momentum	P	Pa	Pressure
Q	–	Quantile function	$\dot{Q}$	W	Heat flux
r	m	Radius	R	J/mol K	Ideal gas constant
S	–	Salinity	S_Eq	–	Sulfur equivalent
t	s	Time	T	K	Temperature
v	m/s	Velocity	V	$\mathrm{m^3}$	Volume
w	–	Mass fraction or weight coefficient	x	Mixed	Position (m) or mole fraction (mol/mol)
y	–	Probability density function	y_g	mol/mol	Gas mole fraction
Y	–	Cumulative density function	z	–	Charge

Greek symbols

	Unit	Representation		Unit	Representation
α	Mixed	Species ratio $(-)$ or thermal diffusivity $(\mathrm{m}^2/\mathrm{s})$	$\mathscr{D}_{\mathrm{AB}}$	m^2/s	Mass diffusivity
γ	$-$	Activity coefficient or deformation parameter	ϵ_{t}	$1/\mathrm{s}$	Turbulence dissipation rate
κ	$\mathrm{W}/\mathrm{m\,K}$	Thermal conductivity	λ	$-$	Wave number or excess air ratio
μ	$\mathrm{Pa}\cdot\mathrm{s}$	Dynamic viscosity	ν	m^2/s	Kinematic viscosity
ω	$1/\mathrm{s}$	Angular frequency	ω_{t}	$1/\mathrm{s}$	Specific rate of turbulence dissipation
ϕ	Mixed	Scalar $(-)$ or angle (rad)	φ	Mixed	Source term
ψ	Mixed	Sphericity $(-)$ or stream function $(\mathrm{m}^2/\mathrm{s})$	Ψ	$1/\mathrm{s}$	Trace component
ρ	kg/m^3	Density	σ	$-$	Standard deviation
σ_{l}	N/m	Surface tension	τ	Mixed	Time constant (s) or shear stress (Pa)
ζ	$-$	Random number between 0 and 1			

Sub- and superscripts

	Representation		Representation
$(...)_{\mathrm{CP}}$	Current Point	$(...)_{\mathrm{d}}$	Droplet
$(...)_{\mathrm{F}}$	Film	$(...)_{\mathrm{g}}$	Gas
$(...)_{\mathrm{l}}$	Liquid	$(...)_{\mathrm{LP}}$	Low Pass (filter)
$(...)_{\mathrm{Rel}}$	Relative	$(...)^{\mathrm{s}}$	Surface
$(...)_{\mathrm{ST}}$	Stochastic Tracking	$(...)_{\mathrm{t}}$	Turbulence property

Dimensionless groups

Definition	Name	Definition	Name
$Bi_{\mathrm{m}} = \frac{k \cdot D}{\mathscr{D}_{\mathrm{AB}}}$	Mass transfer Biot number	$Bi_{\mathrm{T}} = \frac{h \cdot D}{\kappa}$	Heat transfer Biot number
$c_{\mathrm{D}} = \frac{2 \cdot F}{\rho \cdot v^2 \cdot A}$	Coefficient of drag	$Fo = \frac{\mathscr{D}_{\mathrm{AB}} \cdot t}{r^2}$	Fourier number
$La = \frac{\sigma \cdot \rho \cdot L}{\mu^2}$	Laplace number	$\mu^* = \frac{\mu_{\mathrm{l}}}{\mu_{\mathrm{g}}}$	Viscosity ratio
$Nu = \frac{h \cdot L}{k}$	Nusselt number	$Pe = \frac{D \cdot v}{\mathscr{D}_{\mathrm{AB}}}$	Peclet number
$Pr = \frac{c_{\mathrm{P}} \cdot \mu}{k}$	Prandtl number	$Ra = Gr \cdot Pr$	Rayleigh number
$Re = \frac{L \cdot v \cdot \rho}{\mu}$	Reynolds number	$Sc = \frac{\mu}{\rho \cdot \mathscr{D}_{\mathrm{AB}}}$	Schmidt number
$Sh = \frac{k \cdot D}{\mathscr{D}_{\mathrm{AB}}}$	Sherwood number	$We = \frac{\rho \cdot L \cdot v^2}{\sigma}$	Weber number

Abbreviations

	Representation		Representation
BC	Black Carbon	CFD	Computational Fluid Dynamics
CL	Closed-Loop	CV	Control Volume
ECA	Emission Control Area	EGCSA	Exhaust Gas Cleaning Systems Association
FVM	Finite Volume Method	HFO	Heavy Fuel Oil
IMO	International Maritime Organization	LSA	Least Squares Adjustment
MDO	Marine Diesel Oil	MGO	Marine Gas Oil
OL	Open-Loop	PM	Particulate Matter
RMS	Root Mean Square	SCR	Selective Catalytic Reduction
TAB	Taylor Analogy Breakup	WHO	World Health Organization

Species

	Group	Species	Name	Molar mass [g/mol]	Charge [−]
Gas phase	–	CO_2	Carbon dioxide	44.010	0
		O_2	Dioxygen	31.999	0
		H_2O	Water	18.015	0
		SO_2	Sulfur dioxide	64.064	0
		SO_3	Sulfur trioxide	80.063	0
		N_2	Dinitrogen	28.013	0
Liquid phase	–	O_2	Dioxygen	31.999	0
		H^+	Proton	1.008	+1
	OH^*	H_2O	Water	18.015	0
		OH^-	Hydroxide	17.007	−1
	DIC	CO_2	Carbon dioxide	44.010	0
	DIC and CO_3^*	H_2CO_3	Carbonic acid	62.025	0
		HCO_3^-	Bicarbonate	61.017	−1
		CO_3^{2-}	Carbonate	60.009	−2
	$S(IV)$	H_2SO_3	Sulfurous acid	82.079	0
		HSO_3^-	Bisulfite	81.071	−1
		SO_3^{2-}	Sulfite	80.063	−2
	$S(VI)$	H_2SO_4	Sulfuric acid	98.078	0
		HSO_4^-	Bisulfate	97.071	−1
		SO_4^{2-}	Sulfate	96.063	−2
	B^*	$B(OH)_3$	Boric acid	61.833	0
		$B(OH)_4^-$	Tetrahydroxyborate	78.840	−1

CONTENTS

1 INTRODUCTION

Air pollution has increased throughout the industrial age, and is possibly the largest environmental risk to human health, where one in nine deaths are caused by air pollution. An estimated 3 million deaths could be attributed to outdoor air pollution in 2012 [WHO (142)], where the causes comprise chronic obstructive pulmonary disease, acute lower respiratory, heart disease, strokes, and lung cancer. Only 10 % of the global population lives in cities, which actually comply with the *World Health Organization Air quality guidelines* [WHO (141)] [WHO (142)], where the main indicator for air pollution is particulate matter.

Particulate matter consists of solid and liquid particles suspended in air, which comprises organic and inorganic substances such as ammonia, nitrates, sodium chloride, sulphates, black carbon, mineral dust, and water. Particulate matter is measured using two metrics, $\mathrm{PM}_{2.5}$ and PM_{10}, which are particles with diameters less than 2.5 and 10 $\mu\mathrm{m}$ respectively, where the smaller particles pose the biggest threat to health, as these can penetrate deep inside the lungs [WHO (142)]. On average, the world population is exposed to $\mathrm{PM}_{2.5} = 43$ $\mu\mathrm{g/m}^3$, where the guideline limit is 10 $\mu\mathrm{g/m}^3$ [WHO (142)]. Particulate matter emissions include *Black Carbon*, BC, where approximately 10 to 20% is deposited on the Arctic [Gogoi et al. (60)]. This decreases the reflectance of the snow/ice regions, which can affect the global climate. Simulations carried out by [Flanner et al. (52)] estimated an increased global warming of 0.10 to 0.15 K, and [Shindell and Faluvegi (116)] estimated an Arctic temperature increase between 0.5 and 1.4 K due to BC deposition on the snow.

Greenhouse gas emissions also pose an immediate threat to the environment, where CO_2 emissions is one of the main contributors. One way to reduce greenhouse gas emissions is to optimize equipment to operate more efficiently, which will reduce energy requirements and thus emit less CO_2. Pollution and greenhouse gas emissions arise from numerous sources, where shipping is one of these. Emissions from the international shipping traffic account for an estimated 49500 and 53200 premature deaths in Europe for the years 2000 and 2020 respectively, and is estimated to cost 64 billion €/year in 2020, which corresponds to 12 % of the total health costs [Brandt et al. (18)]. Greenhouse gas emissions from shipping was 938 million tonnes of CO_2 for the year 2012, which account for 2.6 % of the global CO_2 emissions, which was 35.64 billion tonnes. This number should be seen in contrast to the global world trade, where shipping carries as much as 90 % of the total world trade by volume, which makes shipping the most efficient mean of transportation with respect to CO_2 emissions [IMO (70)] [MAN Diesel & Turbo (91)].

Most vessels use *Heavy Fuel Oil*, HFO, as fuel, which is a residual refinery product. HFO contains large amounts of sulfur compared to *Marine Gas Oil*, MGO, or *Marine Diesel Oil*, MDO, which are alternatives to HFO. The global marine fuel consumption in 2012 was 300 million tonnes, where 76 % was HFO, 21.3 % was MDO, and 2.66 % was LNG [CONCAWE (26)].

The average annual emission of SO_x from shipping between 2007 and 2012 totals 11.3 million tonnes, which corresponds to 13 % of the global SO_x emissions from anthropogenic sources [IMO (70)]. SO_x is a combination of SO_2 and SO_3, where the latter constitute to between 2 and 4 % of the flue gas mass flow [CIMAC (24)]. SO_2 can cause acid rain, which contributes to deforestation, and is thus affecting the global climate. Furthermore, SO_2 can cause respiratory failure, and is estimated to be one of the major health risks [EGCSA (42)]. Reference [Saiyasitpanich et al. (114)] found that particulate matter emissions almost correlate linearly with the sulfur content in the fuel, so decreasing the sulfur content also reduces particulate matter emissions. The historic emissions of BC and SO_2 are shown in Figure 1.1 along with predictions until year 2100 [Smith and Bond (121)].

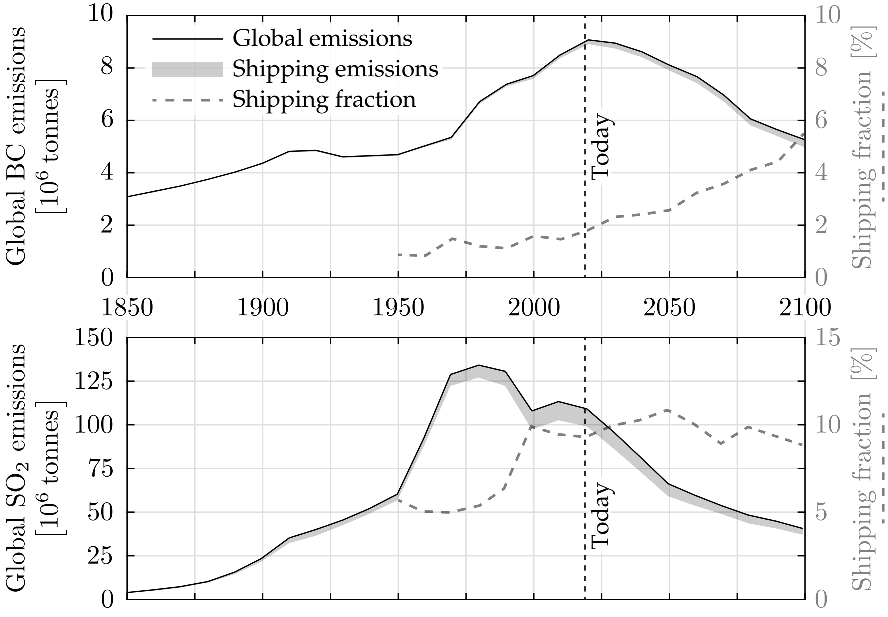

Figure 1.1: Historic and predicted emissions of black carbon, BC, and SO_2 between 1850 and 2100 [Smith and Bond (121)]. The dashed lines are the *Shipping fractions*, which are shown on the right y-axes.

As seen in Figure 1.1, the BC emissions are peaking today, but these are expected to decrease in the future. The shipping fraction accounts for approximately 2 % of the global BC emissions, although this fraction is expected to increase towards year 2100. The global SO_2 emissions have been increasing until 1980, after which these have decreased. Both the global and shipping emissions of SO_2 are expected to decrease in the future, where the main reduction can be attributed to alternative fuels for energy production [Smith and Bond (121)].

1.1 Regulations

The *International Convention for the Prevention of Pollution from Ships*, MARPOL, are the regulations defined by IMO to reduce pollution from ships. A new annex was added in 1997, MARPOL Annex VI, which seeks to reduce the emissions of SO_x and NO_x among others. These regulations have changed over time, and the emission of SO_x is defined in terms of the sulfur equivalent, S_{Eq}, at the outlet of the exhaust gas funnel, which is shown in (1.1) [IMO (72)].

$$S_{\mathrm{Eq}} = \frac{y_{\mathrm{SO_2}}}{y_{\mathrm{CO_2}}} \cdot \frac{100}{43.3} \tag{1.1}$$

Where $y_{\mathrm{SO_2}}$ and $y_{\mathrm{CO_2}}$ are the mole fractions at the outlet of the funnel of SO_2 and CO_2 respectively. The S_{Eq} limits have changed over time, which are shown in Figure 1.2 [IMO (72)].

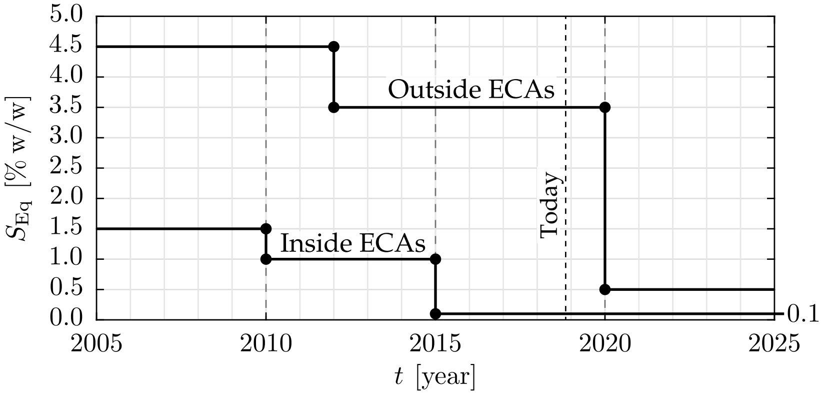

Figure 1.2: The fuel sulfur equivalent limits, S_{Eq}, over time [IMO (72)]. The limits are different inside and outside the *Emission Control Areas*, ECAs.

As seen in Figure 1.2, the S_{Eq} limits have been decreasing over time, where the new regulations to be enforced in 2020 allow 0.5 % and 0.1 % outside and inside the *Emission Control Areas*, ECAs, respectively. ECAs are regions near coastal lines, which are shown in Figure 1.3 [IMO (71)].

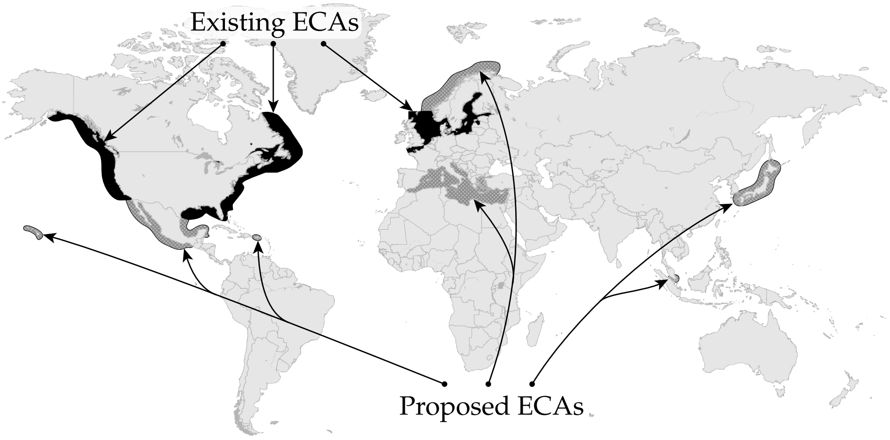

Figure 1.3: The exiting and proposed SO_x *Emission Control Areas* [IMO (71)].

Reference [Sofiev et al. (122)] made an assessment of the health benefits of implementing the new regulations in 2020, where cleaner fuel will reduce shipping related premature mortality and morbidity rates by 34 and 54 % respectively, which is a result of lower sulfur and particulate matter emissions. This study focusses on scrubbers, which is one way to remove SO_x from the exhaust gas.

1.2 SO_x removal

By 2020 the entire world fleet must comply with the new sulfur emission limits shown in Figure 1.2. One way to comply with the new regulations is to switch to another fuel type, where *Liquefied Natural Gas*, LNG, contain minor amounts of sulfur. Another way to comply is to switch to low sulfur fuel, which only contains 0.5 or 0.1 % sulfur by mass, which can be used directly on-board the ship without a scrubber. However, low sulfur fuel is approximately 50 % more expensive compared to HFO, which costs $760\,\$/\mathrm{tonnes}$ and $501\,\$/\mathrm{tonnes}$ respectively as of September 2018 [Ship & Bunker (117)]. Seen from an environmental perspective, low sulfur fuel oil will reduce SO_x and particulate matter emissions, but a consequence is that more energy is required at the refineries for the desulfurization process [Trans Oleum (131)].

A third way to comply with the sulfur emission regulations is to remove the sulfur from the exhaust gas, while continuing to use HFO. This can be done using a scrubber, which washes out the sulfur by chemical processes. A dry scrubber uses a packed bed of granulated material, where calcium hydroxide can be used. A dry scrubber operates between 240 and $450°\mathrm{C}$, and is typically installed after the turbocharger [EGCSA (42)]. A more widespread solution is to use a wet scrubber, which removes sulfur by washing with water. A drawback with using a scrubber is the initial and operating costs and the loss of profit due to the reduces cargo capacity [Panasiuk and Turkina (104)].

Up to 70000 ships may be affected by the SO_x regulations in 2020. By switching to LNG, the payback time would be 6 to 10 years, whereas by using HFO as fuel in combination with a scrubber, the payback time is expected to be from 2.5 to 6 years, although these numbers are sensitive to fuel prices [DNV-GL (39)]. Many factors affect, whether a scrubber is a good investment, where [Jiang et al. (77)] estimated that installing a scrubber on vessels with less than 4 years of remaining lifetime is not feasible [Jiang et al. (77)].

1.2.1 Working principles of wet scrubbers

A scrubber removes SO_x and particulate matter from the exhaust gas by scrubbing with water. The working principles for the two scrubber designs within the Alfa Laval portfolio [Alfa Laval (2)] are illustrated in Figure 1.4 on the next page.

Various scrubber designs exist, where the most common is a packed bed scrubber, where SO_x is removed in an absorption column, as shown to the left in Figure 1.4. The gas enters the scrubber in the jet section, where the gas is quenched and some of the sulfur is removed. The gas continues to the absorber section, where water is injected from a set of sprayer nozzles located above the filling column, which distributes evenly over the entire absorption column. The gas will also distribute evenly, as the back pressure is fairly high over the packed bed. This creates a counter flow, where a large surface area is present due to the filling material.

An alternative to the U-shaped scrubber is the I-shaped/Inline design, which does not use any filling material. Instead, water is injected from a set of sprayer nozzles, which creates a mist of small droplets. SO_x is transferred to the liquid phase on the surfaces of the droplets, and to the liquid wall films flowing along the surfaces within the scrubber. The inline design has some challenges associated with it, as a mist of very fine droplets will tend to be carried upwards by the exhaust gas. On the contrary, a mist of large droplets will have a reduced surface area per unit volume of water, so more water is required to be sulfur compliant according to the regulations. One of the advantages of an inline design is the more compact footprint, which is especially advantageous for retrofit projects. A typical inline scrubber designed for a $10\ \mathrm{MW}$ engine will have a diameter of approximately $2.7\ \mathrm{m}$, whereas a U-shaped scrubber will have an absorber diameter of $3.2\ \mathrm{m}$ plus the jet section, which is installed next to the absorber as seen in Figure 1.4.

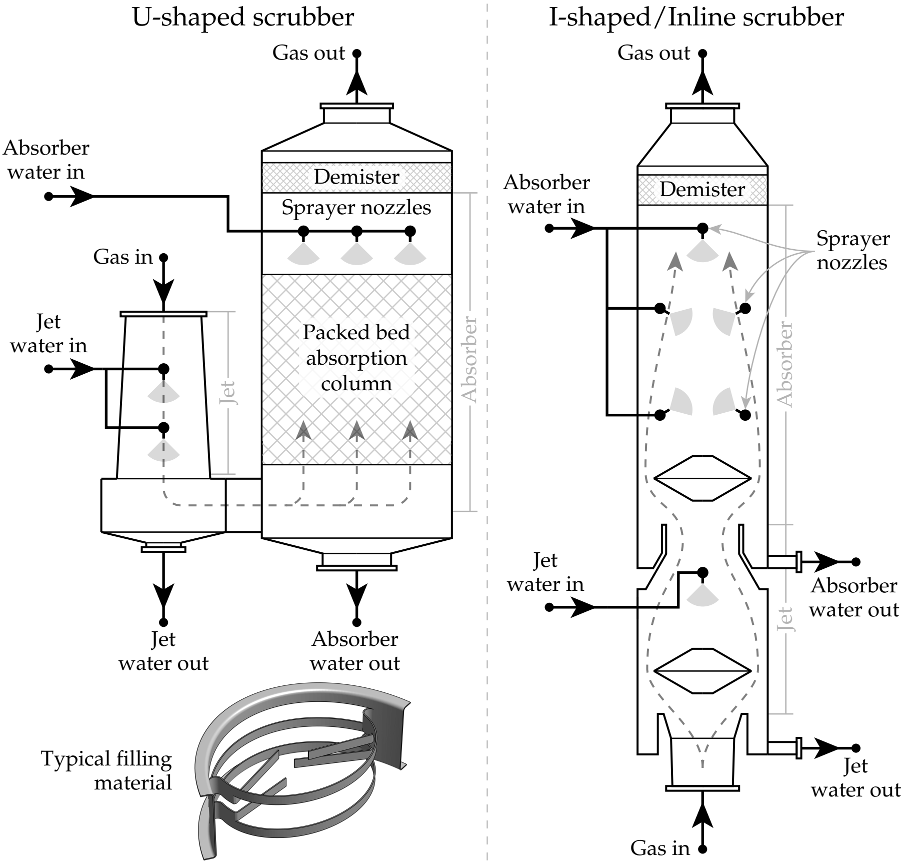

Figure 1.4: An overview of the two scrubber products within the Alfa Laval portfolio [Alfa Laval (2)]. Notice that neither of the scrubbers are to scale and are not reflecting the actual designs.

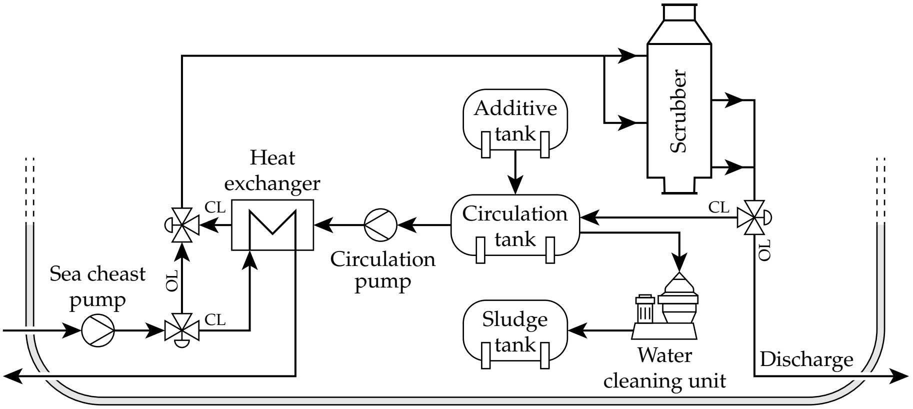

Figure 1.5: A system diagram of a hybrid scrubber installation [Alfa Laval (3)]. The valves are indicating the flow direction depending on the operating mode.

A scrubber can operate in two different modes, which are closed- and open-loop mode, CL and OL respectively. The differences are shown in Figure 1.5 on the previous page, where the valves indicate the flow direction in either of the modes.

In closed-loop mode, freshwater is pumped from the circulation tank and injected into the scrubber, after which the water flows back to the circulation tank again. Alkaline additives are added to the water so that $\mathrm{SO_x}$ can be removed; NaOH is commonly used. A plate heat exchanger cools the freshwater, as it heats up when passing through the scrubber. Particulate matter accumulates over time in the circulation tank, so a water cleaning unit is installed to remove this. The bi-product of the cleaning process is collected in a sludge tank, which is emptied in port. Closed-loop mode is used within some ECAs, where no discharge is allowed.

In open-loop mode, seawater is drawn from the sea chest and injected directly into the scrubber, where $\mathrm{SO_x}$ is absorbed. After passing through the scrubber, the water is discharged to the sea again. The discharged water contains the absorbed $\mathrm{SO_x}$ along with some oil and heavy metals, where the latter two are considered hazardous substances. Reference [Danish Ministry of the Environment (30)] investigated the possible impacts of discharged scrubber water on the marine environment, and found that the acidic water has a negligible impact due to the natural buffer capacity of seawater. The impact of discharging the small quantities of oil and heavy metals would result in concentrations, which are orders of magnitude below the *Environmental Quality Standards* issued by EU for marine environments [Danish Ministry of the Environment (30)] [EUR-Lex: European Union law (46)]. The discharged water is regulated according to *MARPOL Annex VI*, where both pH, *Polycyclic Aromatic Hydrocarbons*, PAH, turbidity, and nitrate are regulated, such that the marine environment is not damaged.

The two operation modes can be combined to a hybrid system, where closed-loop mode can be activated upon entering ECAs, which was illustrated in Figure 1.5.

1.3 Objectives

The U-shaped scrubber is a proven product, and more than 100 Alfa Laval U-shaped scrubbers have been delivered and commissioned. The inline scrubber is a newer product, which is more complex to model compared to the U-shaped, as packed bed absorption is more thoroughly documented in the literature. A computational model of an inline scrubber requires modelling the droplets and all the associated phenomena governing these. Therefore, the aim of this study is to model and analyse an inline scrubber operating in open-loop mode. Such a model can be used to optimize the scrubber to be more energy efficient, which will reduce fuel consumption and thus decrease greenhouse gas and particulate matter emissions.

As numerous phenomena govern a wet scrubber, a combined model, which encompasses the complete process, is of interest. The model is tuned and verified with experimental data gathered from the Alfa Laval Test & Training Centre, where the engine and water loads are varied.

1.4 State of the art

Previous studies have analysed scrubbers using computational models. Reference [Jia et al. (76)] modelled a sprayer based scrubber by assuming counterflow of the gas and the liquid. This is similar to modelling a U-shaped scrubber, where the gas and liquid distribute evenly in the radial direction. However, the results from the study deviate by $\pm 32.5~\%$ from experimental tests, which indicate that this approach is not suitable for sprayer based modelling, where the droplets are moving freely inside the scrubber.

Reference [Bandyopadhyay and Biswas (14)] modelled a spray tower using a simplified model in order to describe the removal process of SO_2. Similar to the previous study, this study assumed a uniform reaction front, so the radial variation of the gas concentration was assumed as zero. The effects of various parameters were investigated, where the SO_x removal efficiency was found to be a strong function of spray hydrodynamics, flow rates, and dimensions of the spray tower. Therefore, the geometry of a wet scrubber is likely to be a determining parameter for the efficiency of the scrubber. This is in agreement with [Li et al. (88)], where an *umbrella plate scrubber* was simulated. This study used *Computational Fluid Dynamics*, CFD, in combination with a *Discrete Phase Model*, DPM, to simulate the removal of fly-ash for the atypical *umbrella plate scrubber* geometry. The results showed that by altering the geometry, an increased retention time for the particles could be obtained, which, in turn, increased the scrubbing efficiency. Although this study did not simulate liquid effects, the results indicate the importance of the scrubber geometry with respect to particulate matter removal, as fly-ash consists of small particles as well.

Reference [Brown et al. (20)] used CFD to model a sprayer based scrubber, where different nozzle designs were computationally tested. The results from this study showed that by increasing the injection velocity of the liquid, an increase in SO_2 absorption could be achieved, although this led to concerns related to undesirable wall interactions. However, a liquid wall film was not modelled, which might improve the results. The results from the study also indicated that smaller droplet sizes increases the SO_2 removal efficiency, which is in agreement with [Hadlocon et al. (64)], where ammonia absorption in an acid spray scrubber was investigated. From the latter study it was concluded that the mean droplet diameter had the greatest effect on the scrubbing efficiency, after which liquid flow rate and retention time were affecting the efficiency most.

A similar tendency was found by [Mi and Yu (95)], where a venturi scrubber for dust and sulfur removal was investigated. It was found that the desulfurization efficiency increased linearly with the liquid-to-gas ratio, which was supported by [Johnstone et al. (79)]. The latter study found that $\mathrm{SO_2}$ removal by alkaline solutions was proportional to the droplet specific surface area in a venturi scrubber, and that the mass transfer coefficient in the gas phase increased significantly with the liquid-to-gas ratio. However, a venturi scrubber operates at high gas velocities, so similar tendencies might not apply to the type of scrubber investigated in this study, where the bulk velocity at design load is approximately $4\text{-}5\ \mathrm{m/s}$.

The removal of sulfur using seawater was investigated by [Flagiello et al. (51)] using a laboratory-sized packed bed scrubber. It was shown that seawater alone had an absorption efficiency of $98\ \%$ for low sulfur concentrations in the gas. However, for high sulfur concentrations, seawater alone could not achieve the same efficiency, but by adding NaOH to the seawater, a significant increase in removal efficiency was found. This is in agreement with [Pourmohammadbagher et al. (108)], where a *swirl wet scrubber* was investigated for $\mathrm{SO_2}$, NO, $\mathrm{NO_2}$, and $\mathrm{CO_2}$ removal. It was found that the removal efficiencies for the different species increased with NaOH addition, which indicates the importance of the acid buffer capacity in the liquid medium used, whether this is seawater or freshwater with added alkali.

This study describes a complete scrubber model, where numerous phenomena are taken into account. These include droplet, wall film, and continuous phase modelling, which are all taken into account in an attempt to accurately predict the performance of a sprayer based scrubber. Several of these phenomena are modelled according to previous studies, where independent models were developed based on controlled experiments and theoretical derivations. All sub-models are combined to the scrubber model presented in this study, where the state of the art for each phenomena is described in the report for each of the sub-model.

1.5 Report overview

This report is divided into three parts:

Part I: Modelling describes the different parts of the model, which are the chemistry model, the disperse liquid phase, the liquid wall film phase, and the continuous phase. The coupling between these phases is described as well, and an extensive independence study is carried out, where five different model parameters are investigated.

Part II: Verification concerns the experimental tests carried out at the Alfa Laval Test & Training Centre, where the results are processed according to an underlying physical model using a *Least Squares Adjustment* approach. These results are used to tune several model parameters in order to match the model results to the experimentally obtained results.

Part III: Results describes the model results for a given operating scenario. Numerous sub-models are combined in the scrubber model, where details from these are shown. A parametric study is carried out, where certain parameters are varied to reveal general tendencies for the efficiency of the scrubber. Furthermore, a discussion about uncertainties and further work is described, which is follows by the conclusion to the study.

PART I

MODELLING

2 MODELLING APPROACH

In order to model the phenomena governing a wet scrubber, both the liquid and the gas phases must be resolved and coupled. This can be done in numerous ways, and different computational models exist for carrying out this task. This study aims to model the scrubber sufficiently well for accurate results in a practical manner, where aspects of scrubber operation can be investigated, and improvements can be made based on the model results. The model should include methods and procedures to resolve the dynamics of the scrubber, where both the liquid and continuous phases, the liquid wall films, and the shell heat transfer all affect the overall performance of the scrubber. The approach is to include existing models when applicable, and to develop models based on first principles, where no existing model is found applicable. The combination of these sub-models form the basis of the scrubber model, which is then tuned to match experimental results obtained from the Alfa Laval Test & Training Centre. This chapter will give an overview of the modelling approaches, which are described in more detail in the subsequent chapters.

2.1 Continuous phase

The continuous gas phase is governed by the Navier-Stokes equations, which are solved using the finite volume method in this study. This method requires the continuous domain to be meshed, on which the coupled partial differential equations are solved, and this allows the flow properties, such as temperature, velocity, and pressure, to be modelled. The liquid phase interacts with the continuous gas phase, so these phases must be coupled. This is done by calculating source terms for each computational cell, such that species, thermal energy, and momentum sources can be imposed on the gas phase to mimic the phenomena inside the scrubber.

The scrubber domain is meshing using ANSYS Fluent Meshing, and the continuous phase is modelled using OpenFOAM, which is an open-source software package capable of solving partial differential equations using the finite volume method. The meshing process and the continuous phase is described in more detail in *Chapter 6: Continuous phase*.

2.2 Liquid phase

The liquid phase inside a scrubber is present as both suspended droplets and as the liquid wall films flowing along the surfaces within the scrubber. The chemistry governing SO_2 absorption in seawater must be resolved as well, where these three aspects are briefly described in the following subsections.

2.2.1 Suspended droplets

The suspended liquid droplets inside a scrubber can be modelled using either an Eulerian or a Lagrangian approach, where each method have both advantages and disadvantages.

Eulerian approach

The liquid phase can be represented using an Eulerian approach, where the properties of the liquid phase are defined on the computational mesh. This method is well suited for two-phase problems, where the liquid fraction is high and the liquid can be interpreted as continuous. However, as the liquid phase within a wet scrubber occupies only a few percent of the total volume, the Eulerian approach is ill-suited. The same approach can also be used for droplet modelling, where the liquid is disperse and each droplet size is represented by a scalar field. This method is illustrated in Figure 2.1.

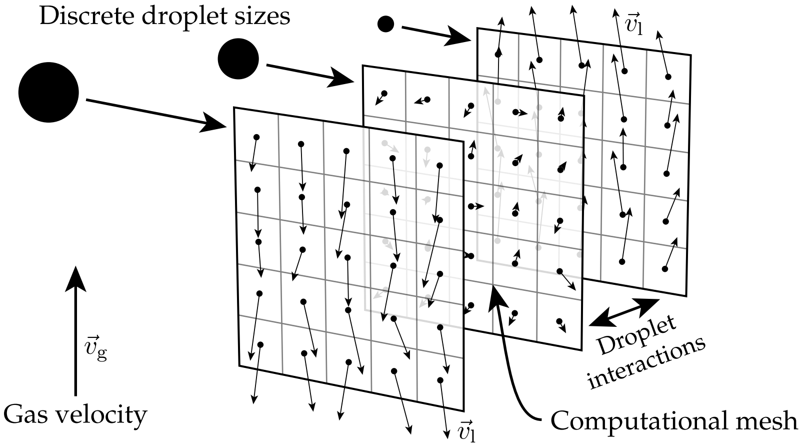

Figure 2.1: An Eulerian approach to a liquid dispersed phase requires multiple scalars for each discrete droplet size.

Figure 2.1 illustrates an Eulerian approach to a dispersed liquid phase. Each droplet size requires multiple scalars on the computational mesh, where the velocity, temperature etc., can be modelled. Three different sized droplets are shown in Figure 2.1, where the larger droplets are falling downwards due to gravity, whereas the smaller droplets are carried upwards by the gas phase. In order to resolve the complex multiphase phenomena of a wet scrubber, a large number of droplet sizes need to be modelled, which makes the Eulerian approach impractical. Furthermore, an additional problem arises with this approach, as two droplets with similar size cannot cross each other in a single cell, as the velocity of the liquid phase in each cell for each discrete droplet size is constant. The advantage of the Eulerian approach is that source terms are easily calculated and associated with each cell, as the droplet phases are resolved directly on the computational mesh. The interaction between the droplets, such as collision, can be modelled using statistical methods.

Lagrangian approach

The liquid phase can also be modelled using a Lagrangian approach, where the droplets are represented by discrete points, which are tracked through the domain. This method is well suited for multiphase flows, where the volume fraction is low, as it is in a wet scrubber. Furthermore, the Lagrangian approach allows for complex droplet models to be incorporated, such as breakup and collision, which are required for modelling a wet scrubber accurately. A disadvantage of the Lagrangian approach is the calculation of the source terms for each cell, as the discrete points/droplets are not associated with any particular cell. Therefore, the influence of each discrete droplet must be spread out to the neighbouring cells, where smoothing is typically used to maintain solver stability. By doing so, the influence of the discrete phase on the continuous phase will be represented by source terms in the Navier-Stokes equations.

The Lagrangian approach is used in this study, as this allows for complex droplet models. The discrete droplet phase is described in detail in *Chapter 4: Discrete phase*, and the method of distributing the source terms to the neighbouring cells is described in detail in *Chapter 7: Phase coupling*.

2.2.2 Wall films

When the discrete droplets impinge the inner surfaces of the scrubber, a fraction will be deposited, and a liquid wall film will form. A total of 15 wall films are modelled inside the scrubber in this study using an Eulerian approach, where each wall film is discretized into a finite number of wall film elements. By solving the transport equation, the advection of the film can be resolved, where sub-models are used to model separation, atomization etc., which are covered in detail in *Chapter 5: Eulerian wall films*. The wall film interacts with the continuous phase as well, where this coupling is described in detail in *Chapter 7: Phase coupling*.

2.2.3 Chemistry

In order to resolve a wet scrubber for SO_x removal, a chemistry model is required, which models the absorption of the continuous gas phase species. This model takes 17 liquid species into account, where both equilibria and internal kinetics govern the species concentrations over time. An efficient method of satisfying equilibrium for a given mixture is proposed, where simplifications are introduced to decrease computational requirements. This is done by only satisfying two of the eight equilibria considered in this study, where the resulting associated errors were found to be negligible. The chemistry model is covered in detail in *Chapter 3: Chemistry*.

2.3 Shell

The wall films flow along the inner surfaces and structures of the scrubber, which were seen in Figure 1.4. All internal surfaces have a thickness and the metal will conduct heat, which is resolved in this study as well. Furthermore, the shells will exchange thermal energy with the wall films due to forced convection, and the outer shell will also exchange thermal energy with the ambient air due to natural convection. These phenomena are included in the scrubber model, and are covered in detail in *Chapter 5: Eulerian wall films*.

2.4 Phase coupling

The continuous phase is modelled using OpenFOAM, whereas the discrete phase and the liquid wall films are modelled using MATLAB. These phases need to be coupled, which requires sharing information between the two software packages. This is done using link-files, which send data from OpenFOAM to MATLAB and source terms the other way, and this is described in detail in *Chapter 7: Phase coupling*. The coupled scalars for each computational cell are energy, momentum, and mass transfer of CO_2, O_2, H_2O, and SO_2. The two software programs will repeatedly switch and iterate towards a steady-state solution, so only a single software package is active at any given time.

As the liquid droplets are interacting with the continuous phase and vice versa, a two-way coupling exist between these phases. However, in order to fully capture the dynamics of a wet scrubber, the collisions between the droplets need to be modelled as well. Therefore, a four-way coupling is used in this study, where the droplets interact with each other and with the continuous phase.

2.5 Overview

An overview of the modelling part of this study is illustrated in Figure 2.2 on the next page, which are covered in the subsequent chapters.

The outcome of *Part I: Modelling* is a model capable of simulating a wet scrubber. This model is subsequently tuned and verified according to the experimental tests, which is described in *Part II: Verification*.

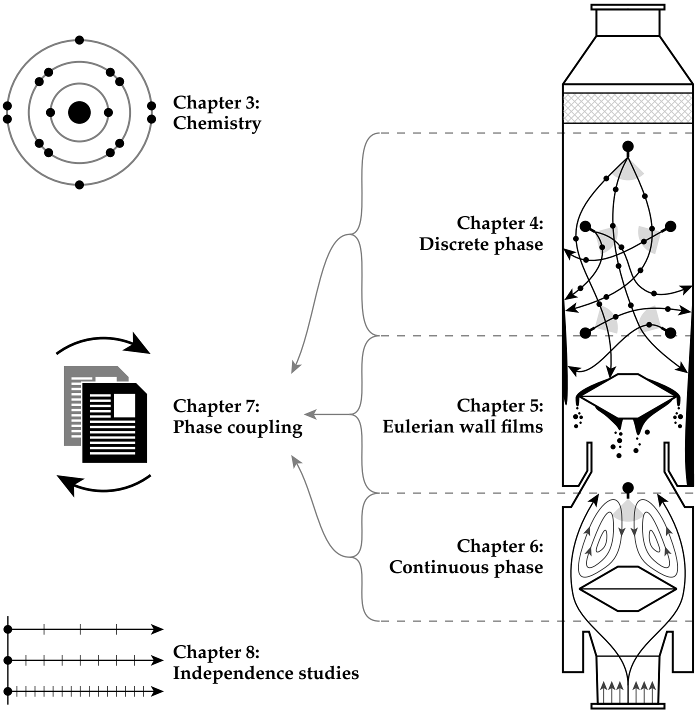

Figure 2.2: An overview of the chapters in the modelling part of this report.

3 | CHEMISTRY

The process of $\mathrm{SO_x}$ removal from exhaust gases is governed by chemical processes, which need to be resolved in order to accurately model a wet scrubber. Multiple species from the gas phase are absorbed in the liquid phase, which takes place on the surfaces of the droplets and the interfaces of the liquid wall films. The absorbed gas phase species will instantly affect the concentrations of most liquid species, as the pH decreases with $\mathrm{SO_x}$ absorption. Furthermore, internal reactions take place in the liquid phase, which are relatively slow compared to the instant equilibria.

This chapter describes the different reactions and mechanisms required to resolve the chemistry, which is divided into several sections. These are outlined in Figure 3.1.

Section 3.1: **Seawater**	Composition and properties: $\rho_\mathrm{l} \quad I \quad A_\mathrm{T} \quad z$
Section 3.2: **Surface reactions**	$\dot{n} = A \cdot k \cdot \left(c_{\mathrm{g,i}} - c^{s}_{\mathrm{g,i}}\right)$
Section 3.3: **Equilibria**	$\mathrm{HA} \rightleftharpoons \mathrm{A^-} + \mathrm{H^+} \qquad K_\mathrm{a} = \frac{[\mathrm{A^-}] \cdot [\mathrm{H^+}]}{[\mathrm{HA}]}$
Section 3.4: **Kinetics of $\mathrm{CO_2}$**	$\mathrm{CO_2} + \mathrm{H_2O} \longleftrightarrow \mathrm{H_2CO_3} \rightleftharpoons \mathrm{H^+} + \mathrm{HCO_3^-} \rightleftharpoons 2\,\mathrm{H^+} + \mathrm{CO_3^{2-}}$ $\mathrm{CO_2} + \mathrm{OH^-} \longleftrightarrow \mathrm{HCO_3^-}$
Section 3.5: **Oxidation**	$\mathrm{S}(IV) + \frac{1}{2}\,\mathrm{O_2} \rightarrow \mathrm{S}(VI)$
Section 3.6: **Initialization**	$c_\mathrm{i}(t = 0)$
Section 3.7: **Examples and analyses**	$c_\mathrm{i}(t)$
Section 3.8: **Simplifications**	8 equilibria reduced to 2 equilibria

Figure 3.1: An overview of the sections in this chapter.

In order to distinguish between the different reaction types used in this study, the definitions in (3.1) apply.

$$\begin{aligned}
&\text{Reactants} \xrightleftharpoons{K_\mathrm{a}} \text{Products} \quad \text{(Equilibrium)} \\
&\text{Reactants} \longleftrightarrow \text{Products} \quad \text{(Bi-directional reaction)} \\
&\text{Reactants} \longrightarrow \text{Products} \quad \text{(Uni-directional reaction)}
\end{aligned} \tag{3.1}$$

The first equation is an instantaneous equilibrium, where the ratio between the reactants and products is defined by an equilibrium constant, K_a. This type of reaction is modelled as an algebraic constraint when solving the concentrations of the reactants and the products. The two latter equations are slow reaction, which are bi- and uni-directional respectively. These are both governed by rate equations, which are implemented as differential equations when solving for the concentrations of the involved species.

The concentration of a given species with respect to volume is represented using square brackets or the symbol c, such as $[\mathrm{CO_2}] = c_{\mathrm{CO_2}}$. All species in this chapter are aqueous unless otherwise specified, such as $\mathrm{CO_2(g)}$. The molar mass of a given species is denoted using the operator $M(...)$, such as $M(\mathrm{CO_2}) = 44.01\,\mathrm{g/mol}$. The gas and liquid phases are shown with a subscript, $c_{\mathrm{g,i}}$ and $c_{\mathrm{l,i}}$ respectively, where i indicates the i^{th} species.

3.1 Seawater

Seawater is composed of numerous species, where the concentration of these vary with both geography and depth. Seawater contains approximately $3.5\,\%$ salt by mass, which affect the properties of seawater significantly compared to freshwater. Some of these properties are described in this section, which are related to the chemistry model used in this study.

3.1.1 Species

Seawater contains numerous species, where [Millero et al. (96)] made an extensive summary of previous studies and combined the findings into a reference seawater. The mass fractions and concentrations of these species are shown in Table 3.1 on the next page.

As seen in the table, the salts in seawater are primarily composed of $\mathrm{Na^+}$ and $\mathrm{Cl^-}$. Numerous other species are shown in Table 3.1, where their effects vanish due to the low concentrations. The different salts and their respective concentrations and charges are used to calculate the alkalinity and the ironic strength, which are used to satisfy equilibrium, which is explained in detail later.

Table 3.1: The major species in seawater [Millero et al. (96)], where the mass fraction of $H_2O = 96.5$ %, which indicates 3.5 % salt.

Species	**Name**	**Mass fraction** [%]
H_2O	Water	96.5
Cl^-	Chloride	1.94
Na^+	Sodium	1.08
SO_4^{2-}	Sulfate	0.271
Mg^{2+}	Magnesium	0.128
Ca^{2+}	Calcium	0.0412
K^+	Potassium	0.0399
HCO_3^-	Bicarbonate	0.0105
Br^-	Bromide	0.00673
$B(OH)_3$	Boric acid	0.00194
CO_3^{2-}	Carbonate	0.00143
$B(OH)_4^-$	Tetrahydroxyborate	0.000795
Sr^{2+}	Strontium	0.000795
F^-	Fluoride	0.000130
CO_2	Carbon dioxide	0.000042
OH^-	Hydroxide	0.000014

3.1.2 Density

The density of seawater is a function of salinity, S, temperature, T, and pressure. Several studies have investigated the correlations between these properties, where TEOS-10, *Thermodynamic Equation Of Seawater - 2010*, have provided an accurate software package, which calculates various seawater properties including density [TEOS-10 (129)], which is seen in Figure 3.2.

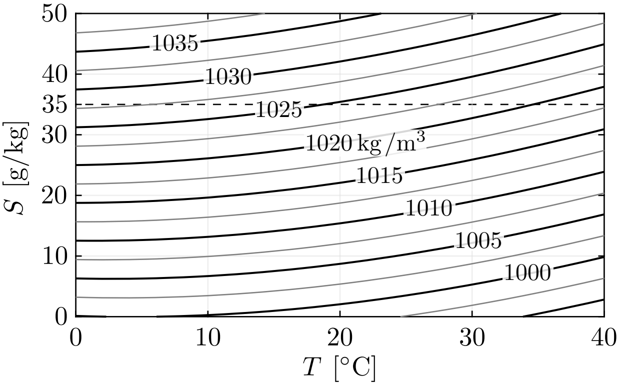

Figure 3.2: The density of seawater as a function of salinity and temperature at a pressure of 1 atm. The numbers on the contour lines have units of $\mathrm{kg/m^3}$.

The density is calculated using a 75-term polynomial expression [Roquet et al. (112)], and can be seen to vary significantly with salinity in Figure 3.2. The salinity of seawater is approximately $35\,\mathrm{g/kg}$, so the density will vary between 1028 and $1018\ \mathrm{kg/m^3}$ at 0 and $40°\mathrm{C}$ respectively, which is indicated by the dashed line in the figure.

3.1.3 Electroneutrality

A mixture of species will have a net charge of zero, which is known as *Pauling's principle of electroneutrality* [Pauling (105)]. The net charge is calculated by summing the product between each species concentration, c_i, and the charge, z_i, which is stated in (3.2).

$$0 = \sum z_\mathrm{i} \cdot c_\mathrm{i} \tag{3.2}$$

The condition of electroneutrality must be satisfied at all times, and will be used to calculate the equilibrium concentration of $\left[\mathrm{H^+}\right]$, which is described in detail in *Section 3.3: Equilibria*.

3.1.4 Alkalinity

Alkalinity, A_T, is a mathematically derived property of seawater, which defines the acid absorption capacity. When an acid is added to seawater, some species will exchange protons, and some will not in any significant amount. The species that do exchange protons will neutralize the acid, and the total concentration of these species in seawater is defined as the alkalinity. This is demonstrated in Table 3.2.

Table 3.2: An overview of the cations and anions in seawater, which are positive and negative charged species respectively. The table is from [Emerson and Hedges (45)] and has been slightly altered. Only species with concentrations greater than 10 µmol/kg are included.

Cations			Anions					
			Insignificant proton exchange			Significant proton exchange		
Species	c	$c \cdot z$	Species	c	$-c \cdot z$	Species	c	$-c \cdot z$
	$\left[\frac{\mathrm{mmol}}{\mathrm{kg}}\right]$	$\left[\frac{\mathrm{mmol}}{\mathrm{kg}}\right]$		$\left[\frac{\mathrm{mmol}}{\mathrm{kg}}\right]$	$\left[\frac{\mathrm{mmol}}{\mathrm{kg}}\right]$		$\left[\frac{\mathrm{mmol}}{\mathrm{kg}}\right]$	$\left[\frac{\mathrm{mmol}}{\mathrm{kg}}\right]$
$\mathrm{Na^+}$	469.06	469.06	$\mathrm{Cl^-}$	545.86	545.86	$\mathrm{HCO_3^-}$	1.80	1.80
$\mathrm{Mg^{2+}}$	52.82	105.64	$\mathrm{SO_4^{2-}}$	28.24	56.48	$\mathrm{CO_3^{2-}}$	0.25	0.51
$\mathrm{Ca^{2+}}$	10.28	20.56	$\mathrm{Br^-}$	0.84	0.84	$\mathrm{B(OH)_4^-}$	0.11	0.11
$\mathrm{K^+}$	10.21	10.21	$\mathrm{F^-}$	0.07	0.07			
$\mathrm{Sr^{2+}}$	0.09	0.18						
$\mathrm{Li^+}$	0.02	0.02						
$\sum$ Cations $=$		605.67	$\sum$ Anions $=$		603.25	$A_\mathrm{T} =$		2.42

The species concentrations in a seawater sample are shown in Table 3.2, where all charged species contribute to either the cation or anion concentrations, which are shown in the bottom row. Only a small fraction of the anions is present for the significant proton exchanging species, which are defining the alkalinity. Notice that the overall charge is zero, as $605.67-(603.25+2.42)=0$, which was stated in (3.2). The species that do significantly exchange protons in seawater are $\mathrm{HCO_3^-}$, $\mathrm{CO_3^{2-}}$, $\mathrm{B(OH)_4^-}$, and $\mathrm{OH^-}$, which implies that the alkalinity can be calculated using (3.3) [Dickson (35)].

$$A_\mathrm{T} = \left[\mathrm{HCO_3^-}\right] + 2\cdot\left[\mathrm{CO_3^{2-}}\right] + \left[\mathrm{B(OH)_4^-}\right] + \left[\mathrm{OH^-}\right] - \left[\mathrm{H^+}\right] - \left[\mathrm{HSO_4^-}\right] \tag{3.3}$$

Notice that $\mathrm{HSO_4^-}$ is included in the definition of A_T in (3.3), whereas $\mathrm{SO_4^{2-}}$ is not. The reason is that (3.3) was defined using the definition of alkalinity in [Dickson (35)], where species with dissociation constants greater than $K_\mathrm{a} > 10^{-4.5}\ \mathrm{mol/L}$ were considered proton donors, whereas all other species were considered proton acceptors.

3.1.5 Ionic strength

Another parameter used for classifying seawater is the ionic strength, I. This value is a measure of the concentration of ions in the solution, and is calculated using (3.4) [Lewis and Randall (86)].

$$I = \frac{1}{2}\sum z_\mathrm{i}^2 \cdot c_\mathrm{i} \tag{3.4}$$

The ionic strength is used to correct the equilibrium constants, K_a, as the activity of each species is a function of the ionic strength of the solution, which is described in detail in *Section 3.3: Equilibria*. The ionic strength is also used to calculate the oxidation rate of $\mathrm{S}(IV)$ to $\mathrm{S}(VI)$, which is described in *Section 3.5: Oxidation*.

When evaluating (3.4) with the values in Table 3.2, the ionic strength equals $I = 0.6972\ \mathrm{mol/L}$. However, this study will use a correlation, which does not require the concentrations of all species in Table 3.2 to be specified. This correlation is a function of the salinity, and is shown in (3.5) [Dickson and Goyet (37)].

$$I(S) = \left(\frac{\mathrm{mol}}{\mathrm{L}}\right)\frac{19.924\cdot\frac{S}{\mathrm{g/kg}}}{1000-1.005\cdot\frac{S}{\mathrm{g/kg}}} \tag{3.5}$$

3.2 Surface reactions

The exhaust gas from a combustion engine consists of five major species: CO_2, H_2O, O_2, SO_2, and N_2. All species except N_2 interact with the liquid phase, and are transferred between the gas and liquid phases at the liquid surfaces. These reactions are shown in (3.6) [Danish Ministry of the Environment (30)].

$$\begin{aligned} H_2O(g) &\xleftrightarrow{\dot{n}_{H_2O}} H_2O(l) \\ O_2(g) &\xleftrightarrow{\dot{n}_{O_2}} O_2(l) \\ CO_2(g) &\xleftrightarrow{\dot{n}_{CO_2}} CO_2(l) \\ SO_2(g) + H_2O(l) &\xleftrightarrow{\dot{n}_{SO_2}} H_2SO_3(l) \\ SO_3(g) + H_2O(l) &\xleftrightarrow{\dot{n}_{SO_3}} H_2SO_4(l) \end{aligned} \tag{3.6}$$

The first reaction in (3.6) is the evaporation and condensation of H_2O. The subsequent two reactions concern $O_2(g)$ and $CO_2(g)$, which dissolve in water to yield $O_2(l)$ and $CO_2(l)$. The last two reactions show $SO_2(g)$ and $SO_3(g)$, which also dissolve, but hydrate immediately to yield $H_2SO_3(l)$ and $H_2SO_4(l)$ respectively. SO_3 forms during combustion, and the concentration is a function of combustion temperature and pressure, where [Cordtz et al. (27)] estimated that between 0.5 to 2.4 % of the sulfur in the fuel oil will react to SO_3, whereas [CIMAC (24)] reported between 2 and 4 %. Due to these low concentrations, $SO_3(g)$ is not considered in this project, and all sulfur in the fuel oil is assumed to react to SO_2 upon combustion.

The absorption rates, $\dot{n}$, are calculated using the *two resistance model* [ANSYS Inc. (6)], which is shown in (3.7), where $c_{l,i}$ and $c_{g,i}$ are the bulk concentrations of the i^{th} species in the liquid and gas phase respectively. The superscripts $(...)^s$ indicate surface concentrations.

$$\begin{aligned} \dot{n}_i &= A \cdot k_{l,i} \cdot \left(c^s_{l,i} - c_{l,i}\right) \\ \dot{n}_i &= A \cdot k_{g,i} \cdot \left(c_{g,i} - c^s_{g,i}\right) \end{aligned} \tag{3.7}$$

Where $k_{l,i}$ and $k_{g,i}$ are the mass transfer coefficients in the two phases. The surface concentrations are related via the *Henry's Law coefficient*, $K_{H,i}$, according to (3.8).

$$\begin{aligned} f_i &= \frac{c^s_{l,i}}{K_{H,i}} \\ c^s_{g,i} &= \frac{f_i}{R \cdot T_l} = \frac{c^s_{l,i}}{K_{H,i} \cdot R \cdot T_l} \end{aligned} \tag{3.8}$$

The values of K_H for the different species shown in (3.6) are listed in *Chapter A: Constants and correlations*. f_i is the fugacity [Ott and Boerio-Goates (103)], which is the partial pressure of the i^th species in the gas phase at the droplet surface. This value can be converted to a molar concentration by dividing with $(R \cdot T_\mathrm{l})$. The species concentrations during unsteady mass transfer are illustrated in Figure 3.3.

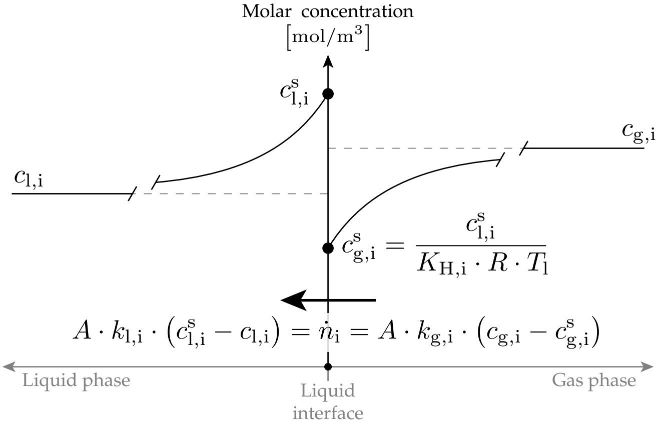

Figure 3.3: An illustration of the molar concentrations near a liquid surface. Notice that the figure is constructed and does not reflect actual values.

As seen in Figure 3.3, the species concentrations vary close to the liquid interface, where the absorption rate, $\dot{n}_\mathrm{i}$, is calculated using an overall rate constant, $\bar{k}_\mathrm{i}$. This value is derived by combining (3.7) and (3.8), which is shown in (3.9).

$$\begin{aligned}\dot{n}_\mathrm{i} &= A \cdot \bar{k}_\mathrm{i} \cdot \left(c_\mathrm{g,i} - \frac{c_\mathrm{l,i}}{K_\mathrm{H,i} \cdot R \cdot T_\mathrm{l}}\right) \\ \bar{k}_\mathrm{i} &= \frac{k_\mathrm{g,i} \cdot k_\mathrm{l,i}}{k_\mathrm{l,i} + \dfrac{k_\mathrm{g,i}}{K_\mathrm{H,i} \cdot R \cdot T_\mathrm{l}}}\end{aligned} \tag{3.9}$$

$k_\mathrm{l,i}$ and $k_\mathrm{g,i}$ are described in *Section 4.9: Mass transfer coefficient* and *Section 5.7: Chemistry and mass transfer* for the dispersed droplet phase and the wall film phase respectively.

3.3 Equilibria

Multiple equilibria govern the chemistry of the liquid phase. Some species related to seawater scrubbing dissociate according to an acid-base reaction, which is defined symbolically in (3.10) [Chicone (23)], where HA is a generic acid, and A$^-$ is its conjugate base.

$$\mathrm{HA} + \mathrm{H_2O} \rightleftharpoons \mathrm{A^-} + \mathrm{H_3O^+} \tag{3.10}$$

The acid in (3.10) reacts with water to form its conjugate base and a free proton, $\mathrm{H^+}$, which reacts with water to form $\mathrm{H_3O^+}$. The concentration of the solvent, which is water, is dominant and can thus be ignored, so (3.10) reduces to (3.11).

$$\mathrm{HA} \overset{k_\mathrm{f}}{\underset{k_\mathrm{r}}{\rightleftharpoons}} \mathrm{A^-} + \mathrm{H^+} \tag{3.11}$$

The ratio between the left- and right-hand sides is equal to the ratio between the forward and backward reaction rates at equilibrium, k_f and k_r respectively, which is shown in (3.12).

$$\begin{aligned} K_\mathrm{a} &= \frac{\left[\mathrm{A^-}\right] \cdot \left[\mathrm{H^+}\right]}{\left[\mathrm{HA}\right]} = \frac{k_\mathrm{f}}{k_\mathrm{r}} \\ \mathrm{p}K_\mathrm{a} &= -\log_{10}(K_\mathrm{a}) \end{aligned} \tag{3.12}$$

Where K_a is an acid dissociation constant, and $\mathrm{p}K_\mathrm{a}$ is the negative logarithmic value of K_a, which is convenient to use in many purposes, as it is related directly to the pH of the solution. This is illustrated in Figure 3.4, where the concentration of either HA or $\mathrm{A^-}$ dominates as a function of the relative value between $\mathrm{p}K_\mathrm{a}$ and pH. The ratio between these species is defined as α according to (3.13), where the definition of pH is shown as well.

$$\begin{gathered} \alpha_\mathrm{HA} = \frac{\left[\mathrm{HA}\right]}{\left[\mathrm{HA}\right] + \left[\mathrm{A^-}\right]} \qquad \alpha_\mathrm{A^-} = \frac{\left[\mathrm{A^-}\right]}{\left[\mathrm{HA}\right] + \left[\mathrm{A^-}\right]} \\ \mathrm{pH} = -\log_{10}\left(\frac{\left[\mathrm{H^+}\right]}{\mathrm{mol}/\mathrm{L}}\right) \end{gathered} \tag{3.13}$$

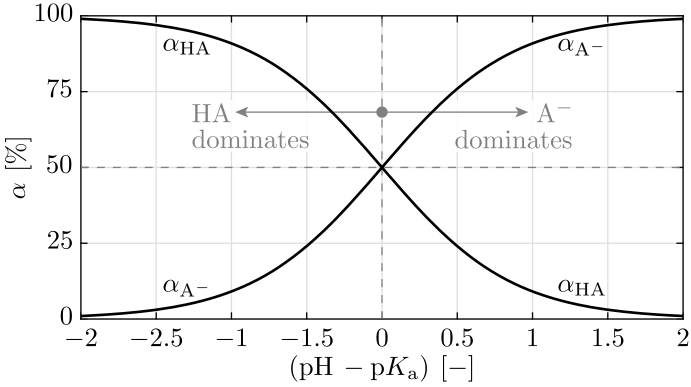

Figure 3.4: α_HA and $\alpha_\mathrm{A^-}$ as a function of $(\mathrm{pH} - \mathrm{p}K_\mathrm{a})$. When $\mathrm{pH} = \mathrm{p}K_\mathrm{a}$, the concentrations of $[\mathrm{HA}] = \left[\mathrm{A^-}\right]$, where $\alpha_\mathrm{HA} = \alpha_\mathrm{A^-} = 50\,\%$.

As seen in Figure 3.4, either HA or A^- dominates as a function of $(\mathrm{pH} - \mathrm{p}K_\mathrm{a})$. When $(\mathrm{pH} - \mathrm{p}K_\mathrm{a}) > 2$, the value of $\alpha_{\mathrm{A}^-} > 0.99$, which indicates that nearly all HA has dissociated to A^- and H^+ according to (3.11).

3.3.1 Seawater scrubbing equilibria

The major acid dissociation reactions for SO_x absorption in seawater are shown in (3.14) [Danish Ministry of the Environment (30)] [Emerson and Hedges (45)], where the K_a values are shown above each of the equilibria.

$$\begin{aligned}
\mathrm{H_2CO_3} &\xrightleftharpoons{K_{\mathrm{CO_3},1}} \mathrm{H^+ + HCO_3^-} \xrightleftharpoons{K_{\mathrm{CO_3},2}} \mathrm{2\,H^+ + CO_3^{2-}} \\
\mathrm{H_2SO_3} &\xrightleftharpoons{K_{\mathrm{SO_3},1}} \mathrm{H^+ + HSO_3^-} \xrightleftharpoons{K_{\mathrm{SO_3},2}} \mathrm{2\,H^+ + SO_3^{2-}} \\
\mathrm{H_2SO_4} &\xrightleftharpoons{K_{\mathrm{SO_4},1}} \mathrm{H^+ + HSO_4^-} \xrightleftharpoons{K_{\mathrm{SO_4},2}} \mathrm{2\,H^+ + SO_4^{2-}} \qquad (3.14) \\
\mathrm{B(OH)_3 + H_2O} &\xrightleftharpoons{K_\mathrm{B}} \mathrm{H^+ + B(OH)_4^-} \\
\mathrm{H_2O} &\xrightleftharpoons{K_\mathrm{W}} \mathrm{H^+ + OH^-}
\end{aligned}$$

The eight equilibria in (3.14) are all very fast reactions and can thus be assumed to settle instantaneously. Notice that H_2CO_3 is a product of a reaction taking place between $CO_2(l)$ and $H_2O(l)$, which is defined later in *Section 3.4: Kinetics of* CO_2. The species in (3.14) are grouped according to (3.15), which will be used later in this chapter.

$$\begin{aligned}
\left[\mathrm{CO_3^*}\right] &= \left[\mathrm{H_2CO_3}\right] + \left[\mathrm{HCO_3^-}\right] + \left[\mathrm{CO_3^{2-}}\right] \\
\left[\mathrm{DIC}\right] &= \left[\mathrm{H_2CO_3}\right] + \left[\mathrm{HCO_3^-}\right] + \left[\mathrm{CO_3^{2-}}\right] + \left[\mathrm{CO_2}\right] = \left[\mathrm{CO_3^*}\right] + \left[\mathrm{CO_2}\right] \\
\left[\mathrm{S}(IV)\right] &= \left[\mathrm{H_2SO_3}\right] + \left[\mathrm{HSO_3^-}\right] + \left[\mathrm{SO_3^{2-}}\right] \\
\left[\mathrm{S}(VI)\right] &= \left[\mathrm{H_2SO_4}\right] + \left[\mathrm{HSO_4^-}\right] + \left[\mathrm{SO_4^{2-}}\right] \qquad (3.15) \\
\left[\mathrm{B^*}\right] &= \left[\mathrm{B(OH)_3}\right] + \left[\mathrm{B(OH)_4^-}\right] \\
\left[\mathrm{OH^*}\right] &= \left[\mathrm{H_2O}\right] + \left[\mathrm{OH^-}\right]
\end{aligned}$$

The groups shown in (3.15) are useful when modelling the chemistry, as the species within each group are in equilibrium with each other, and are thus algebraically bound to each other. Therefore, the ratios between the species are only functions of pH and thus $\left[\mathrm{H^+}\right]$.

The group DIC is *Dissolved Inorganic Carbon*, and is commonly used within the field of oceanography [Emerson and Hedges (45)]. It should be noted that this group includes CO_2, which is not in equilibrium with the other species. Instead, CO_2 reacts with the species in the CO_3^* group, which is described in detail in *Section 3.4: Kinetics of* CO_2.

The equilibrium constants in (3.14) are all functions of both temperature and ionic strength, where the latter is a function of salinity. The correlations used to calculate all K_a values are listed in *Chapter A: Constants and correlations*.

3.3.2 Ionic activity

The general algebraic equilibrium constraint shown in (3.12) on page 26 applies for pure solutions, where the concentrations of the species are diluted towards infinity. However, in electrolytic solutions, where the ionic strength is significant such as in seawater, (3.12) is not valid. Instead, the activity of each species must be corrected using an *activity coefficient*, γ [Emerson and Hedges (45)], where various correlations exist for calculating these, which have originated from the *Debye–Hückel theory* [Debye and Hückel (33)]. The original correlation did not apply for high ionic strengths, which is the case for seawater, so the *Davies correlation* is used in this study, as it is valid between $0 \leq I < 0.5\,\mathrm{mol/L}$, and is shown in (3.16). The temperature dependency of A_γ is from [Rysselberghe (113)].

$$\begin{aligned} A_\gamma &= \frac{0.5091}{(T/298.16\,\mathrm{K})^{3/2}} \\ \log_{10}(\gamma_\mathrm{i}) &= -A_\gamma \cdot z_\mathrm{i}^2 \cdot \left(\frac{\sqrt{\frac{I}{\mathrm{mol/L}}}}{1+\sqrt{\frac{I}{\mathrm{mol/L}}}} \right) - 0.2 \cdot \frac{I}{\mathrm{mol/L}} \end{aligned} \tag{3.16}$$

The ionic strength of seawater is typically $0.7\,\mathrm{mol/L}$, as previously stated, which is greater than the valid limit for the *Davies correlation*, but for the simulation of seawater scrubbers the correlations is assumed to suffice. The values of γ are shown in Figure 3.5 for varying ionic strength, I, and charge, z.

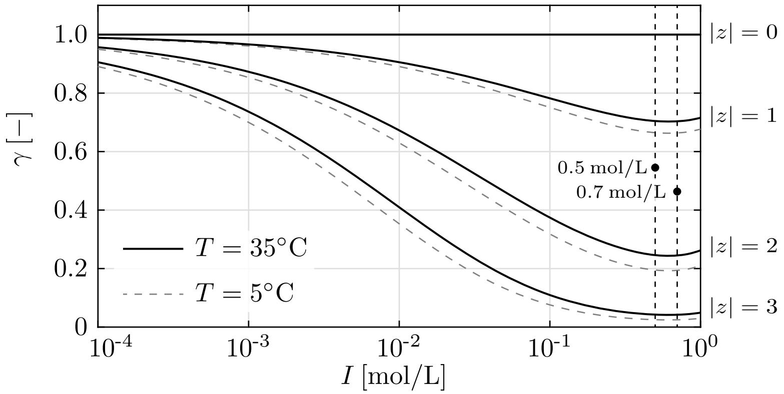

Figure 3.5: The activity coefficient, γ, as a function of ionic strength, I, charge, z, and temperature, T. The vertical dashed lines indicate the limit for the *Davies correlation*, $I = 0.5\,\mathrm{mol/L}$, and the approximate ionic strength for seawater, $I = 0.7\,\mathrm{mol/L}$.

As seen in Figure 3.5, the ionic activity increases with temperature. Having calculated the activity coefficients for all species, the modified algebraic equilibrium constraint can be defined, which takes the activity of each species into account. This is shown in (3.17) [Emerson and Hedges (45)].

$$\begin{aligned} K_\mathrm{a} &= \frac{\left(\gamma_{\mathrm{A}^-}\left[\mathrm{A}^-\right]\right)\cdot\left(\gamma_{\mathrm{H}^+}\left[\mathrm{H}^+\right]\right)}{\left(\gamma_{\mathrm{HA}}\left[\mathrm{HA}\right]\right)} \\ &\Downarrow \\ K_\mathrm{a}^\gamma &= \frac{\left[\mathrm{A}^-\right]\cdot\left[\mathrm{H}^+\right]}{\left[\mathrm{HA}\right]} \\ K_\mathrm{a}^\gamma &= K_\mathrm{a}\cdot\left(\frac{\gamma_{\mathrm{HA}}}{\gamma_{\mathrm{A}^-}\cdot\gamma_{\mathrm{H}^+}}\right) \end{aligned} \tag{3.17}$$

Where the superscript $(\ldots)^\gamma$ indicates that the value of K_a is adjusted to take the ionic activity into account. The carbon cycle has been thoroughly studied throughout the literature, where empirical correlations for the equilibrium constants have been derived as functions of both temperature and salinity, where the ionic strength is already taken into account. These correlations are assumed more valid compared to the correction applied in (3.17), so the values of K_a^γ for the carbon species are calculated using these correlations directly, which are shown in *Chapter A: Constants and correlations*. The species in the $\mathrm{S}(IV)$ and $\mathrm{S}(VI)$ groups do not have any direct correlations available, so the K_a values are adjusted according to (3.17). Table 3.3 shows the $\mathrm{p}K_\mathrm{a}$ values for the equilibria shown in (3.14) for different values of T and S.

Table 3.3: Examples of $\mathrm{p}K_\mathrm{a}^\gamma$ values for the different equilibria shown in (3.14) for different values of temperature and salinity. The values marked with an asterisk are using the activity correction in (3.17), whereas the others are using the direct correlations shown in *Chapter A: Constants and correlations*.

	$T = 5°\mathrm{C}$		$T = 35°\mathrm{C}$	
	$S = 0$ g/kg	$S = 35$ g/kg	$S = 0$ g/kg	$S = 35$ g/kg
$\mathrm{p}K_{\mathrm{CO_3},1}^\gamma$	6.315	6.052	6.034	5.771
$\mathrm{p}K_{\mathrm{CO_3},2}^\gamma$	9.786	9.300	9.296	8.810
$*\mathrm{p}K_{\mathrm{SO_3},1}^\gamma$	1.552	1.231	1.877	1.557
$*\mathrm{p}K_{\mathrm{SO_3},2}^\gamma$	7.140	6.499	7.207	6.566
$*\mathrm{p}K_{\mathrm{SO_4},1}^\gamma$	-2.724	-3.044	-3.125	-3.445
$*\mathrm{p}K_{\mathrm{SO_4},2}^\gamma$	1.645	1.004	2.045	1.405
$\mathrm{p}K_\mathrm{B}^\gamma$	9.439	8.844	9.163	8.483
$\mathrm{p}K_\mathrm{W}^\gamma$	14.739	14.068	13.686	12.846

As seen in Table 3.3, the $\mathrm{p}K_\mathrm{a}^\gamma$ values vary between -3.445 and 14.739, so the dominant species are very different at low and high pH values.

3.3.3 Species ratios

The species ratios, α, according to (3.13), for all equilibria in (3.14) are shown in Figure 3.6 as functions of pH. The dominant species are highlighted in the figure.

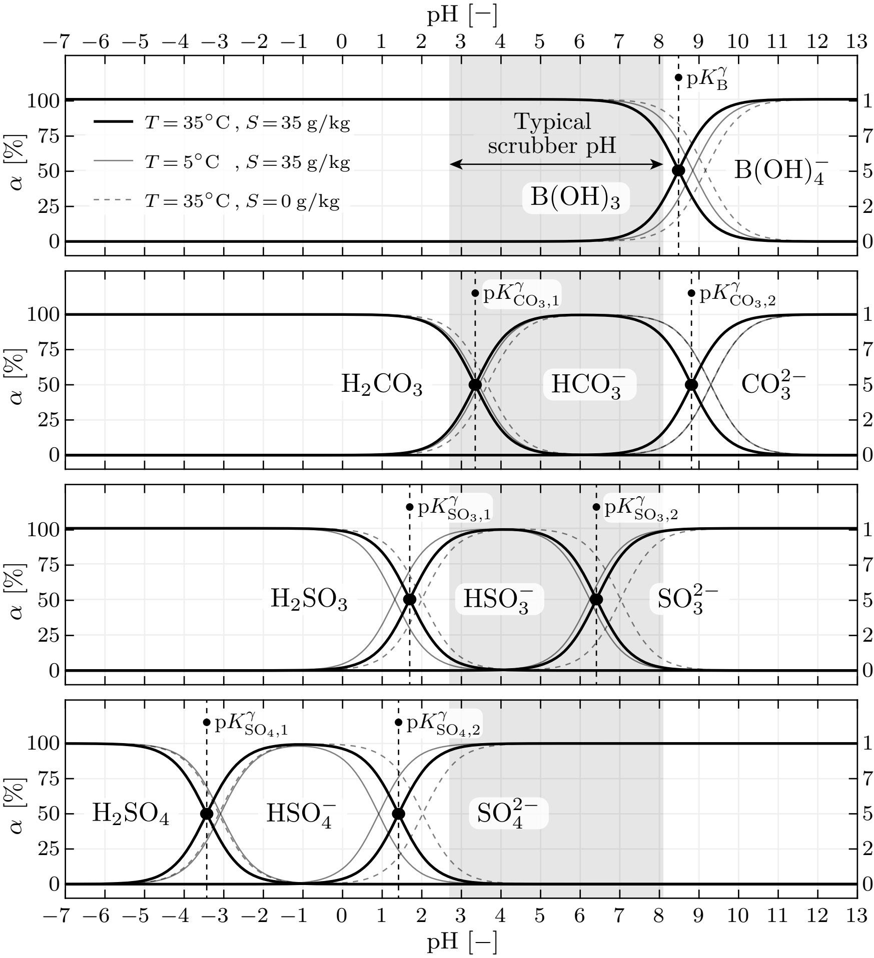

Figure 3.6: The species ratios, α, as functions of pH. The shaded area is the typical range, where seawater scrubbers operate. The tendency when changing salinity, S, or temperature, T, is shown with the thin lines according to the legend in the upper left corner.

As seen in Figure 3.6, several species only exist in very small quantities between $2.7 < \mathrm{pH} < 8.1$, where seawater scrubbers typically operate. This fact will be used to reduce the computational requirements to obtain equilibrium for any given mixture, which is described in the next subsection. Notice that H_2SO_3, which is the driving force for SO_2 absorption, only exist in small quantities within the typical pH range. The value of $\mathrm{p}K_{SO_3,1}$ can be seen to increase with increasing temperature, so a scrubber is more efficient using cold water compared to hot water, as the driving force between $SO_2(g)$ and $H_2SO_3(l)$ will be greater.

3.3.4 Solution procedure

The procedure of solving all equilibria in (3.14) simultaneously is done using the electroneutrality condition shown in (3.2) on page 22. This condition is used to calculate the concentration of free protons, $\left[H^+\right]$, by expressing all charged species as functions of this value. The electroneutrality conditions is applied in (3.18) to all charged species considered in this project.

$$
\begin{aligned}
0 &= \sum z_i \cdot c_i \qquad \text{(Equation (3.2) on page 22)} \\
&\Downarrow \\
0 &= (z_{Salt}) \cdot \left[Salt\right] + (-1) \cdot \left[B(OH)_4^-\right] + \\
&\quad (+1) \cdot \left[H^+\right] + (-1) \cdot \left[OH^-\right] + \\
&\quad (-1) \cdot \left[HCO_3^-\right] + (-2) \cdot \left[CO_3^{2-}\right] + \\
&\quad (-1) \cdot \left[HSO_3^-\right] + (-2) \cdot \left[SO_3^{2-}\right] + \\
&\quad (-1) \cdot \left[HSO_4^-\right] + (-2) \cdot \left[SO_4^{2-}\right]
\end{aligned}
\tag{3.18}
$$

z_{Salt} and $\left[Salt\right]$ are described in detail later. The concentrations of the different species in (3.18) are not shown as functions of $\left[H^+\right]$. However, this can be obtained by calculating the group concentrations shown in (3.15) on page 27 along with the equilibrium constraints. An example is shown in (3.19) for the species in the $S(IV)$ group, which contains H_2SO_3, HSO_3^-, and SO_3^{2-}.

$$
\begin{aligned}
K^{\gamma}_{SO_3,1} &= \frac{\left[H^+\right] \cdot \left[HSO_3^-\right]}{\left[H_2SO_3\right]} \\
K^{\gamma}_{SO_3,2} &= \frac{\left[H^+\right] \cdot \left[SO_3^{2-}\right]}{\left[HSO_3^-\right]} \\
\left[S(IV)\right] &= \left[H_2SO_3\right] + \left[HSO_3^-\right] + \left[SO_3^{2-}\right]
\end{aligned}
\tag{3.19}
$$

Equation (3.19) shows three equations with three unknown species concentrations: $\left[H_2SO_3\right]$, $\left[HSO_3^-\right]$, and $\left[SO_3^{2-}\right]$. The group concentration, $\left[S(IV)\right]$, and the equilibrium constants, $K^{\gamma}_{SO_3,1}$ and $K^{\gamma}_{SO_3,2}$, are known prior to satisfying equilibrium. The unknown concentrations in (3.19) are solved analytically, which is shown in (3.20). Notice that $\left[S(IV)\right]$ does not change before and after equilibrium is satisfied, but the three species concentrations do.

$$
\begin{aligned}
\Delta &= \left[\mathrm{H}^+\right]^2 + K^{\gamma}_{\mathrm{SO_3},1} \cdot \left[\mathrm{H}^+\right] + K^{\gamma}_{\mathrm{SO_3},1} \cdot K^{\gamma}_{\mathrm{SO_3},2} \\
f^{\mathrm{s}}_{[\mathrm{H_2SO_3}]}\left(\left[\mathrm{H}^+\right], \left[\mathrm{S}(IV)\right]\right) &= \left[\mathrm{H_2SO_3}\right] = \left[\mathrm{S}(IV)\right] \cdot \left(\frac{\left[\mathrm{H}^+\right]^2}{\Delta}\right) \\
f^{\mathrm{s}}_{[\mathrm{HSO_3^-}]}\left(\left[\mathrm{H}^+\right], \left[\mathrm{S}(IV)\right]\right) &= \left[\mathrm{HSO_3^-}\right] \;= \left[\mathrm{S}(IV)\right] \cdot \left(\frac{K^{\gamma}_{\mathrm{SO_3},1} \cdot \left[\mathrm{H}^+\right]}{\Delta}\right) \\
f^{\mathrm{s}}_{[\mathrm{SO_3^{2-}}]}\left(\left[\mathrm{H}^+\right], \left[\mathrm{S}(IV)\right]\right) &= \left[\mathrm{SO_3^{2-}}\right] \;= \left[\mathrm{S}(IV)\right] \cdot \left(\frac{K^{\gamma}_{\mathrm{SO_3},1} \cdot K^{\gamma}_{\mathrm{SO_3},2}}{\Delta}\right)
\end{aligned}
\tag{3.20}
$$

f^{s} are *species functions*, which express the concentrations of different species as functions of $\left[\mathrm{H}^+\right]$ and the group concentrations. The same procedure applies for all species in the other groups: $\mathrm{S}(VI)$, $\mathrm{CO_3^*}$, B^*, and OH^*, where species functions can be defined as well.

Having defined all species functions, f^{s}, for the charged species, the resulting expressions are substituted into (3.18) along with the equilibrium constants. The resulting expression is shown in (3.21).

$$
\begin{aligned}
0 = \; &(z_{\mathrm{Salt}}) \cdot \left[\mathrm{Salt}\right] && + (-1) \cdot f^{\mathrm{s}}_{[\mathrm{B(OH)_4^-}]}\left(\left[\mathrm{H}^+\right], \left[\mathrm{B}^*\right]\right) \; + \\
&(+1) \cdot \left[\mathrm{H}^+\right] && + (-1) \cdot f^{\mathrm{s}}_{[\mathrm{OH}^-]}\left(\left[\mathrm{H}^+\right], \left[\mathrm{OH}^*\right]\right) \; + \\
&(-1) \cdot f^{\mathrm{s}}_{[\mathrm{HCO_3^-}]}\left(\left[\mathrm{H}^+\right], \left[\mathrm{CO_3^*}\right]\right) && + (-2) \cdot f^{\mathrm{s}}_{[\mathrm{CO_3^{2-}}]}\left(\left[\mathrm{H}^+\right], \left[\mathrm{CO_3^*}\right]\right) \; + \\
&(-1) \cdot f^{\mathrm{s}}_{[\mathrm{HSO_3^-}]}\left(\left[\mathrm{H}^+\right], \left[\mathrm{S}(IV)\right]\right) && + (-2) \cdot f^{\mathrm{s}}_{[\mathrm{SO_3^{2-}}]}\left(\left[\mathrm{H}^+\right], \left[\mathrm{S}(IV)\right]\right) + \\
&(-1) \cdot f^{\mathrm{s}}_{[\mathrm{HSO_4^-}]}\left(\left[\mathrm{H}^+\right], \left[\mathrm{S}(VI)\right]\right) && + (-2) \cdot f^{\mathrm{s}}_{[\mathrm{SO_4^{2-}}]}\left(\left[\mathrm{H}^+\right], \left[\mathrm{S}(VI)\right]\right)
\end{aligned}
\tag{3.21}
$$

As seen in (3.21), all species concentrations from (3.18) are expressed as function of $\left[\mathrm{H}^+\right]$ along with the group concentrations, which are calculated prior to satisfying equilibrium. The concentration of salt, $\left[\mathrm{Salt}\right]$, is known as well, which is determined from the conserved salt in the mixture. The charge of this species, z_{Salt}, is determined upon initialization, as it must balance out the initial charge imbalance caused the non-zero alkalinity, A_{T}. This will be explained in detail in *Section 3.6: Initialization*.

Having defined the electroneutrality conditions in (3.21) in terms of the group concentrations and the equilibrium constants, the only unknown is $\left[\mathrm{H}^+\right]$. This concentration is calculated by solving (3.21), which can be reduced to a large polynomial, where the degree is equal to the number of included equilibria plus one. Therefore, when all eight equilibria in (3.14) are taken into account, the resulting polynomial is of order nine, which implies nine roots. One of these roots is real, which is the concentration of $\left[\mathrm{H}^+\right]$ at equilibrium. When $\left[\mathrm{H}^+\right]$ is known, all other species concentrations can be calculated using the species functions, f^{s}, which were used in (3.21).

An analytical solution to a ninth-order polynomial is inefficient to solve. Instead, the roots can be found by calculating the eigenvalues of the companion matrix of the polynomial, $p(x)$ [Edelman and Murakami (40)], which is stated in (3.22).

$$p(x) = a_0 + a_1 \cdot x + ... + a_{\mathrm{n}-1} \cdot x^{n-1} + \underbrace{(1)}_{a_\mathrm{n}} \cdot x^n$$

$$\left[\mathrm{H}^+\right] = \mathrm{eig}\left(\begin{bmatrix} 0 & 0 & \cdots & 0 & 0 & -a_0 \\ 1 & 0 & \cdots & 0 & 0 & -a_1 \\ 0 & 1 & \cdots & 0 & 0 & -a_2 \\ \vdots & \vdots & \ddots & \vdots & \vdots & \vdots \\ 0 & 0 & \cdots & 1 & 0 & -a_{\mathrm{n}-2} \\ 0 & 0 & \cdots & 0 & 1 & -a_{\mathrm{n}-1} \end{bmatrix}\right) \tag{3.22}$$

Where $p(x)$ is the polynomial, where the coefficient for x^n equals unity, $a_\mathrm{n} = 1$. Equation (3.22) is computationally expensive to solve, so by excluding insignificant equilibrium from (3.21), the degree of the polynomial can be reduced.

Numerical studies were carried out, where it was found that by only included two equilibria, namely between the species in the CO_3^* group: $\mathrm{H_2CO_3}$, $\mathrm{HCO_3^-}$ and $\mathrm{CO_3^{2-}}$, the absorption rates could still be accurately calculated compared to the solution, where all eight equilibria were included. The reduced polynomial is of order three, as the number of included equilibria is two, and is shown in (3.23).

$$\begin{aligned} 0 &= \left[\mathrm{H}^+\right]^3 + \left[\mathrm{H}^+\right]^2 \cdot a_2 + \left[\mathrm{H}^+\right] \cdot a_1 + a_0 \\ \Delta_\mathrm{a} &= z_\mathrm{Salt} \cdot \left[\mathrm{Salt}\right] - \left[\mathrm{S}(IV)\right] - 2 \cdot \left[\mathrm{S}(VI)\right] \\ a_2 &= K^\gamma_{\mathrm{CO_3},1} + \Delta_\mathrm{a} \\ a_1 &= -K^\gamma_{\mathrm{CO_3},1} \cdot \left(\left[\mathrm{CO}_3^*\right] - K^\gamma_{\mathrm{CO_3},2} - \Delta_\mathrm{a}\right) \\ a_0 &= -K^\gamma_{\mathrm{CO_3},1} \cdot K^\gamma_{\mathrm{CO_3},2} \cdot \left(2 \cdot \left[\mathrm{CO}_3^*\right] - \Delta_\mathrm{a}\right) \end{aligned} \tag{3.23}$$

The cubic polynomial shown in (3.23) can be solved analytically, where the solution is shown in (3.24).

$$\begin{aligned} \Delta_0 &= \frac{a_2^3}{27} - \frac{a_1 \cdot a_2}{6} + \frac{a_0}{2} \\ \Delta_1 &= \frac{a_1}{3} - \frac{a_2^2}{9} \\ \Delta_2 &= \sqrt[3]{\sqrt{\Delta_1^3 + \Delta_0^2} - \Delta_0} \\ \left[\mathrm{H}^+\right] &= \Delta_2 - \frac{\Delta_1}{\Delta_2} - \frac{a_2}{3} \end{aligned} \tag{3.24}$$

It should be noted that three solutions exist for $\left[\mathrm{H}^+\right]$, but the real and positive root is the one shown in (3.24). When the concentration of $\left[\mathrm{H}^+\right]$ at equilibrium is calculated using (3.24), only two equilibria in (3.14) are taken into account. Therefore, not all equilibria are satisfied exactly, which causes a mismatch after all species concentrations are recovered using the species functions, f^{s}. It can be shown that the error induced by using the simplified chemistry model in (3.24) only affects the mole balance of H^+, which will cause mass to either increase or decrease.

In order to cancel out this error, a new species is introduced, $\mathrm{H}^+_{\mathrm{E}}$, which is the excess mole number of H^+. This is stored alongside all other species, which means that no mass will be lost or gained during simulation. It should be noted that $\mathrm{H}^+_{\mathrm{E}}$ is very small but non-zero. After equilibrium is satisfied, the concentration of $\mathrm{H}^+_{\mathrm{E}}$ is calculated using (3.25), where $\vec{c}_{\mathrm{Pre}}$ is the concentration of all species in vector format prior to calculating equilibrium, and $\vec{c}_{\mathrm{Equil}}$ is the vector after equilibrium is obtained.

$$\vec{C}_{\mathrm{H}} \cdot \vec{c}_{\mathrm{Pre}} = \vec{C}_{\mathrm{H}} \cdot \vec{c}_{\mathrm{Equil}}$$
$$\Downarrow$$
$$\overbrace{\begin{bmatrix} 2 \\ 1 \\ 1 \\ 0 \\ 0 \\ 2 \\ 1 \\ 0 \\ 2 \\ 1 \\ 0 \\ 2 \\ 1 \\ 0 \\ 3 \\ 4 \\ 0 \\ 1 \end{bmatrix}}^{\vec{C}_{\mathrm{H}}}{}^{\mathrm{T}} \cdot \overbrace{\begin{bmatrix} [\mathrm{H_2O}] \\ [\mathrm{H^+}] \\ [\mathrm{OH^-}] \\ [\mathrm{O_2}] \\ [\mathrm{CO_2}] \\ [\mathrm{H_2CO_3}] \\ [\mathrm{HCO_3^-}] \\ [\mathrm{CO_3^{2-}}] \\ [\mathrm{H_2SO_3}] \\ [\mathrm{HSO_3^-}] \\ [\mathrm{SO_3^{2-}}] \\ [\mathrm{H_2SO_4}] \\ [\mathrm{HSO_4^-}] \\ [\mathrm{SO_4^{2-}}] \\ [\mathrm{B(OH)_3}] \\ [\mathrm{B(OH)_4^-}] \\ [\mathrm{Salt}] \\ [\mathrm{H_E^+}] \end{bmatrix}}^{\vec{c}_{\mathrm{Pre}}} = \vec{C}_{\mathrm{H}} \cdot \overbrace{\begin{bmatrix} [\mathrm{H_2O}] \\ [\mathrm{H^+}] \\ [\mathrm{OH^-}] \\ [\mathrm{O_2}] \\ [\mathrm{CO_2}] \\ [\mathrm{H_2CO_3}] \\ [\mathrm{HCO_3^-}] \\ [\mathrm{CO_3^{2-}}] \\ [\mathrm{H_2SO_3}] \\ [\mathrm{HSO_3^-}] \\ [\mathrm{SO_3^{2-}}] \\ [\mathrm{H_2SO_4}] \\ [\mathrm{HSO_4^-}] \\ [\mathrm{SO_4^{2-}}] \\ [\mathrm{B(OH)_3}] \\ [\mathrm{B(OH)_4^-}] \\ [\mathrm{Salt}] \\ [\mathrm{H_E^+}] \end{bmatrix}}^{\vec{c}_{\mathrm{Equil}}} \tag{3.25}$$

The vector $\vec{C}_{\mathrm{H}}$ is composed of the mole number of H for each species. $\left[\mathrm{H}^+_{\mathrm{E}}\right]_{\mathrm{Equil}}$, which is the value is the lower right corner of the equation, is calculated using (3.25), as all other values will be known, when the equation is used. Vectors similar to $\vec{C}_{\mathrm{H}}$ can be defined for each of the other elementary components, such as C, O, and S, which are combined in (3.26). The matrix $\mathbf{C}_{\mathrm{l}}$ is useful for evaluating mole balance for the elementary components, which will be used in *Section 7.3: Mass, energy, and mole balances*.

$$\mathbf{C}_\mathrm{l} = \begin{bmatrix} \vec{C}_\mathrm{C} \\ \vec{C}_\mathrm{H} \\ \vec{C}_\mathrm{O} \\ \vec{C}_\mathrm{S} \\ \vec{C}_\mathrm{N} \\ \vec{C}_\mathrm{B} \\ \vec{C}_\mathrm{Na} \\ \vec{C}_\mathrm{Cl} \end{bmatrix} = \left[\begin{array}{cccccccccccccccccc} \mathrm{H_2O} & \mathrm{H^+} & \mathrm{OH^-} & \mathrm{O_2} & \mathrm{CO_2} & \mathrm{H_2CO_3} & \mathrm{HCO_3^-} & \mathrm{CO_3^{2-}} & \mathrm{H_2SO_3} & \mathrm{HSO_3^-} & \mathrm{SO_3^{2-}} & \mathrm{H_2SO_4} & \mathrm{HSO_4^-} & \mathrm{SO_4^{2-}} & \mathrm{B(OH)_3} & \mathrm{B(OH)_4^-} & \mathrm{Salt} & \mathrm{H_E^+} \\ 0 & 0 & 0 & 0 & 1 & 1 & 1 & 1 & 0 & 0 & 0 & 0 & 0 & 0 & 0 & 0 & 0 & 0 \\ 2 & 1 & 1 & 0 & 0 & 2 & 1 & 0 & 2 & 1 & 0 & 2 & 1 & 0 & 3 & 4 & 0 & 1 \\ 1 & 0 & 1 & 2 & 2 & 3 & 3 & 3 & 3 & 3 & 3 & 4 & 4 & 4 & 3 & 4 & 0 & 0 \\ 0 & 0 & 0 & 0 & 0 & 0 & 0 & 0 & 1 & 1 & 1 & 1 & 1 & 1 & 0 & 0 & 0 & 0 \\ 0 & 0 & 0 & 0 & 0 & 0 & 0 & 0 & 0 & 0 & 0 & 0 & 0 & 0 & 0 & 0 & 0 & 0 \\ 0 & 0 & 0 & 0 & 0 & 0 & 0 & 0 & 0 & 0 & 0 & 0 & 0 & 0 & 1 & 1 & 0 & 0 \\ 0 & 0 & 0 & 0 & 0 & 0 & 0 & 0 & 0 & 0 & 0 & 0 & 0 & 0 & 0 & 0 & 1 & 0 \\ 0 & 0 & 0 & 0 & 0 & 0 & 0 & 0 & 0 & 0 & 0 & 0 & 0 & 0 & 0 & 0 & 1 & 0 \end{array}\right] \tag{3.26}$$

3.4 Kinetics of CO$_2$

When CO$_2$(g) is dissolved in water to CO$_2$(l), the liquid species will hydrate, which is a chemical reaction with water. Three different mechanisms occur, which are shown in (3.27) [Johnson (78)].

$$\begin{tikzcd}
 & \mathrm{HCO_3^-} + \mathrm{H^+} \arrow[r, shift left, "K^{\gamma}_{\mathrm{CO_3},2}"] \arrow[dd, shift left, "K^{\gamma}_{\mathrm{CO_3},1}"] & \mathrm{CO_3^{2-}} + 2\,\mathrm{H^+} \arrow[l, shift left] \\
\mathrm{CO_2} + \mathrm{H_2O} \arrow[ur, shift left, "k_{1,\mathrm{f}}"] \arrow[dr, shift right, "k_{2,\mathrm{f}}"'] & & \\
 & \mathrm{H_2CO_3} \arrow[uu, shift left] \arrow[ul, shift right, "k_{2,\mathrm{r}}"'] &
\end{tikzcd}$$

$$\mathrm{HCO_3^-} + \mathrm{H^+} \xrightarrow{k_{1,\mathrm{r}}} \mathrm{CO_2} + \mathrm{H_2O}$$

$$\mathrm{CO_2} + \mathrm{OH^-} \underset{k_{\mathrm{HCO_3^-}}}{\overset{k_{\mathrm{OH^-}}}{\rightleftharpoons}} \mathrm{HCO_3^-} \tag{3.27}$$

The reaction between CO$_2$ and H$_2$O forms H$_2$CO$_3$ and HCO$_3^-$, where the forward rate constants are $k_{1,\mathrm{f}}$ and $k_{2,\mathrm{f}}$ respectively, and the reverse are $k_{1,\mathrm{r}}$ and $k_{2,\mathrm{r}}$. The two products are in equilibrium according to (3.14), where the equilibrium constant is $K^{\gamma}_{\mathrm{CO_3},1}$.

The reaction between CO$_2$ and OH$^-$ will form HCO$_3^-$, where the forward and reverse rate constants are $k_{\mathrm{OH^-}}$ and $k_{\mathrm{HCO_3^-}}$ respectively. The temporal gradient of $[\mathrm{CO_2}]$ is shown in (3.28).

$$\begin{aligned} \frac{\partial[\mathrm{CO_2}]}{\partial t} =& \overbrace{[\mathrm{HCO_3^-}] \cdot [\mathrm{H^+}] \cdot k_{1,\mathrm{r}} - [\mathrm{CO_2}] \cdot k_{1,\mathrm{f}}}^{\text{From: } \mathrm{CO_2+H_2O} \longleftrightarrow \mathrm{HCO_3^-+H^+}} + \\ & \overbrace{[\mathrm{H_2CO_3}] \cdot k_{2,\mathrm{r}} - [\mathrm{CO_2}] \cdot k_{2,\mathrm{f}}}^{\text{From: } \mathrm{CO_2+H_2O} \longleftrightarrow \mathrm{H_2CO_3}} + \\ & \overbrace{[\mathrm{HCO_3^-}] \cdot k_{\mathrm{HCO_3^-}} - [\mathrm{CO_2}] \cdot [\mathrm{OH^-}] \cdot k_{\mathrm{OH^-}}}^{\text{From: } \mathrm{CO_2+OH^-} \longleftrightarrow \mathrm{HCO_3^-}} \end{aligned} \tag{3.28}$$

The equilibrium between H_2CO_3 and $HCO_3^- + H^+$ is very fast, so the use of $\left[H_2CO_3\right]$ and $\left[HCO_3^-\right]$ in (3.28) can be rewritten into the more general definition, where the concentrations are expressed using the species functions, $f^{\mathrm{s}}_{[H_2CO_3]}\left(\left[CO_3^*\right], \left[H^+\right]\right)$ and $f^{\mathrm{s}}_{[HCO_3^-]}\left(\left[CO_3^*\right], \left[H^+\right]\right)$. These are shown in (3.29), where the definition of $\left[CO_3^*\right]$ was shown in (3.15) on page 27.

$$\begin{aligned} \Delta &= \left[H^+\right]^2 + K^{\gamma}_{CO_3,1} \cdot \left[H^+\right] + K^{\gamma}_{CO_3,1} \cdot K^{\gamma}_{CO_3,2} \\ f^{\mathrm{s}}_{[H_2CO_3]}\left(\left[CO_3^*\right], \left[H^+\right]\right) &= \left[H_2CO_3\right] = \left[CO_3^*\right] \cdot \left(\frac{\left[H^+\right]^2}{\Delta}\right) \\ f^{\mathrm{s}}_{[HCO_3^-]}\left(\left[CO_3^*\right], \left[H^+\right]\right) &= \left[HCO_3^-\right] \ = \left[CO_3^*\right] \cdot \left(\frac{K^{\gamma}_{CO_3,1} \cdot \left[H^+\right]}{\Delta}\right) \end{aligned} \tag{3.29}$$

$\left[OH^-\right]$ in (3.28) can be expressed in terms of $\left[H^+\right]$ and K^{γ}_{W}. Furthermore, as $\left[H_2CO_3\right]$ and $\left[HCO_3^-\right]$ are in equilibrium and thus algebraically bound to each other, the two forward rate constants, $k_{1,\mathrm{f}}$ and $k_{1,\mathrm{r}}$, are indistinguishable from each other experimentally. Therefore, these are combined, and the same applies for the two reverse rate constants, $k_{1,\mathrm{r}}$ and $k_{2,\mathrm{r}}$. This is shown in (3.30).

$$\begin{aligned} \left[OH^-\right] &= \frac{K^{\gamma}_{\mathrm{W}}}{\left[H^+\right]} \\ k_{\mathrm{CO2,f}} &= k_{1,\mathrm{f}} + k_{2,\mathrm{f}} \\ k_{\mathrm{CO2,r}} &= k_{1,\mathrm{r}} + \frac{k_{2,\mathrm{r}}}{K^{\gamma}_{CO_3,1}} \end{aligned} \tag{3.30}$$

3.4.1 Reaction rates

Four rate constants are required to determined the temporal gradient of $\left[CO_2\right]$, which have been determined experimentally by [Johnson (78)]. These are calculated using the expression shown in (3.31), where the coefficients in Table 3.4 apply.

$$k = \beta_0 \cdot \exp\left(\beta_1 + \beta_2 \cdot \sqrt{\frac{S}{\mathrm{g/kg}}} + \frac{\beta_3}{T/\mathrm{K}} + \beta_4 \cdot \log_{\mathrm{e}}(T/\mathrm{K})\right) \tag{3.31}$$

Table 3.4: The coefficients for calculating the rate constants according to (3.31) [Johnson (78)].

Rate constant	β_0	β_1	β_2	β_3	β_4
$k_{CO_2,\mathrm{f}}$	1/s	1246.98	0	$-6.19 \cdot 10^4$	−183.0
$k_{CO_2,\mathrm{r}}$	L/(mol · s)	1346.24	−0.126	$-6.44 \cdot 10^4$	−196.4
$k_{OH^-} \cdot K^{\gamma}_{\mathrm{W}}$	mol/(L · s)	−930.13	0.110	$3.10 \cdot 10^4$	140.9
$k_{HCO_3^-}$	1/s	−2225.22	−0.049	$8.91 \cdot 10^4$	336.6

The definition of any equilibrium constant is the ratio of the forward and the reverse rate constants at equilibrium, which is shown in (3.32).

$$\begin{aligned} \mathrm{CO_2} + \mathrm{H_2O} &\xrightleftharpoons{K^\gamma_{\mathrm{CO_2}}} \mathrm{H_2CO_3} \\ K^\gamma_{\mathrm{CO_2}} &\equiv \frac{k_{\mathrm{CO_2,f}}}{k_{\mathrm{CO_2,r}}} \end{aligned} \tag{3.32}$$

The equilibrium constant introduced, $K^\gamma_{\mathrm{CO_2}}$, is the ratio of the reaction rates at equilibrium by definition. $k_{\mathrm{CO_2,f}}$ and $k_{\mathrm{CO_2,r}}$ are calculated using (3.31) and Table 3.4, and $K^\gamma_{\mathrm{CO_2}}$ is calculated using the correlation in Appendix A. However, when all three values are provided, the last equation in (3.32) is overdetermined. The rate constants, $k_{\mathrm{CO_2,f}}$ and $k_{\mathrm{CO_2,r}}$, are not adjusted to take the ionic activity into account, so these values are modified to satisfy the definition of the equilibrium constant. This is shown in (3.33).

$$\begin{aligned} k^\gamma_{\mathrm{CO_2,f}} &= k_{\mathrm{CO_2,f}} \cdot (1+\phi) \\ k^\gamma_{\mathrm{CO_2,r}} &= k_{\mathrm{CO_2,r}} \cdot (1-\phi) \\ K^\gamma_{\mathrm{CO_2}} &= \frac{k^\gamma_{\mathrm{CO_2,f}}}{k^\gamma_{\mathrm{CO_2,r}}} = \frac{k_{\mathrm{CO_2,f}} \cdot (1+\phi)}{k_{\mathrm{CO_2,r}} \cdot (1-\phi)} \\ &\Downarrow \\ \phi &= \frac{K^\gamma_{\mathrm{CO_2}} \cdot k_{\mathrm{CO_2,r}} - k_{\mathrm{CO_2,f}}}{k_{\mathrm{CO_2,f}} + K^\gamma_{\mathrm{CO_2}} \cdot k_{\mathrm{CO_2,r}}} \end{aligned} \tag{3.33}$$

Where ϕ is an adjustment coefficient. By applying (3.33), the definition of the equilibrium constant in (3.32) is satisfied.

3.4.2 Temporal gradient

By combining (3.28), (3.29), and (3.30) and substituting $k_{\mathrm{CO_2,f}}$ and $k_{\mathrm{CO_2,r}}$ with $k^\gamma_{\mathrm{CO_2,f}}$, and $k^\gamma_{\mathrm{CO_2,f}}$ respectively, an expression for the gradient of $[\mathrm{CO_2}]$ as a function of $[\mathrm{CO_2}]$, $[\mathrm{CO_3^*}]$, and $[\mathrm{H^+}]$ can be defined, which is shown in (3.34).

$$\begin{aligned} \frac{\partial[\mathrm{CO_2}]}{\partial t} = & -[\mathrm{CO_2}](t) \cdot \overbrace{\left(\frac{k_{\mathrm{OH^-}} \cdot K^\gamma_{\mathrm{W}}}{[\mathrm{H^+}]} + k^\gamma_{\mathrm{CO2},f} \right)}^{k_{\mathrm{CO_2}}} \\ & + [\mathrm{CO_3^*}](t) \cdot \underbrace{\left(\frac{K^\gamma_{\mathrm{CO3,1}} \cdot [\mathrm{H^+}] \cdot \left(k_{\mathrm{HCO3}} + [\mathrm{H^+}] \cdot k_{\mathrm{CO2},r}\right)}{[\mathrm{H^+}]^2 + K^\gamma_{\mathrm{CO3,1}} \cdot [\mathrm{H^+}] + K^\gamma_{\mathrm{CO3,1}} \cdot K^\gamma_{\mathrm{CO3,2}}} \right)}_{k_{\mathrm{CO_3^*}}} \end{aligned} \tag{3.34}$$

As seen in (3.34), two overall rate constants, $k_{\mathrm{CO_2}}$ and $k_{\mathrm{CO_3^*}}$, are governing the dynamics of $\left[\mathrm{CO_2}\right](t)$. These overall rate constants are functions of $\left[\mathrm{H^+}\right]$ and thus pH, where the tendencies of these are shown in Figure 3.7.

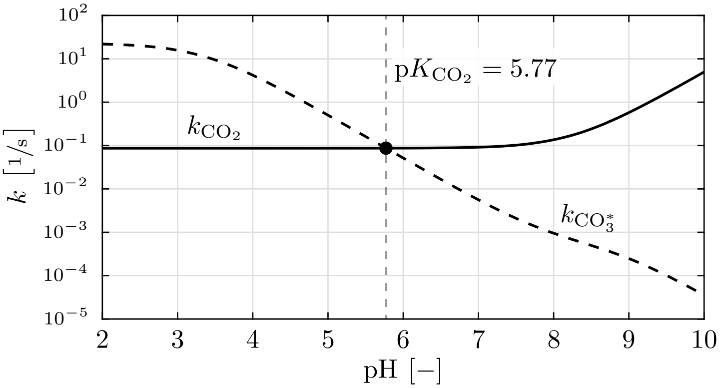

Figure 3.7: The overall rate constants in (3.34) as functions of pH.

As seen in Figure 3.7, the rate constants are dependent on pH, where the intersection of the two curves defines the equilibrium. In order to determine $\left[\mathrm{CO_2}\right]$ as a function of time, (3.34) must be temporally integrated. However, during integration both $\left[\mathrm{CO_2}\right]$, $\left[\mathrm{CO_3^*}\right]$, and $\left[\mathrm{H^+}\right]$ will change, so the substitution in (3.35) is made.

$$\left[\mathrm{CO_3^*}\right] = \left[\mathrm{CO_3^*}\right](0) - \left(\left[\mathrm{CO_2}\right](0) - \left[\mathrm{CO_2}\right](t)\right)$$

$$\Downarrow \text{ Substitute into (3.34) and assume constant } \left[\mathrm{H^+}\right]$$

$$\frac{\partial\left[\mathrm{CO_2}\right]}{\partial t} = \left[\mathrm{CO_2}\right](t)\cdot\overbrace{\left(k_{\mathrm{CO_3^*}} - k_{\mathrm{CO_2}}\right)}^{a} + \overbrace{k_{\mathrm{CO_3^*}}\cdot\left(\left[\mathrm{CO_3^*}\right](0) - \left[\mathrm{CO_2}\right](0)\right)}^{b} \tag{3.35}$$

$$\left[\mathrm{CO_2}\right](t) = \exp\left(a\cdot t\right)\cdot\left(\frac{b}{a} + \left[\mathrm{CO_2}\right](0)\right) - \frac{b}{a}$$

The concentration of $\left[\mathrm{H^+}\right]$ will change as well, which will change the values of $k_{\mathrm{CO_2}}$ and $k_{\mathrm{CO_3^*}}$ during integration, but due to the complex interaction with the other equilibria, no analytic solution exists for the differential equation when varying $\left[\mathrm{H^+}\right]$ during integration. Therefore, the analytical solution in (3.35) assumes that the reaction happens at constant pH and thus constant $\left[\mathrm{H^+}\right]$, and the constants a and b on the right-hand side are thus evaluated prior to the calculation of $\left[\mathrm{CO_2}\right](t)$. Having integrated the concentration of $\left[\mathrm{CO_2}\right]$ over a specified time-step, Δt, the concentrations of the other involved species are altered according to (3.36), where three different methods can be applied.

$$
\begin{aligned}
\Delta &= \big[\mathrm{CO_2}\big](t) - \big[\mathrm{CO_2}\big](0) \\
\big[\mathrm{H_2O}\big](t) &= \big[\mathrm{H_2O}\big](0) + \Delta
\end{aligned}
$$

$$
\begin{gathered}
\text{Method 1:} \\
\mathrm{CO_2 + H_2O \longleftrightarrow H_2CO_3} \Big\{ \big[\mathrm{H_2CO_3}\big](t) = \big[\mathrm{H_2CO_3}\big](0) \; -\Delta \\
\text{Method 2:} \\
\mathrm{CO_2 + H_2O \longleftrightarrow H^+ + HCO_3^-} \begin{cases} \big[\mathrm{HCO_3^-}\big](t) = \big[\mathrm{HCO_3^-}\big](0) \; -\Delta \\ \big[\mathrm{H^+}\big](t) = \big[\mathrm{H^+}\big](0) \qquad -\Delta \end{cases} \\
\text{Method 3:} \\
\mathrm{CO_2 + H_2O \longleftrightarrow 2\,H^+ + CO_3^{2-}} \begin{cases} \big[\mathrm{CO_3^{2-}}\big](t) = \big[\mathrm{CO_3^{2-}}\big](0) \; -\Delta \\ \big[\mathrm{H^+}\big](t) = \big[\mathrm{H^+}\big](0) \qquad -2 \cdot \Delta \end{cases}
\end{gathered}
\tag{3.36}
$$

As seen in (3.36), the change in $\big[\mathrm{CO_2}\big]$ over a given time-step, Δt, is defined as Δ. In order to ensure mole balance of C, H, and O, the concentration of $\big[\mathrm{H_2O}\big]$ must be altered with $+\Delta$. Three different methods of changing the species in the $\mathrm{CO_3^*}$ group are shown in (3.36), which are equally valid to use in the model. After having changed the concentrations using any of the three methods, equilibrium is satisfied using the previous mentioned method. It should be noted that the species concentrations *after* equilibrium is satisfied are identical for all three methods in (3.36), as the species functions, f^{s}, are functions of the group concentration, $\big[\mathrm{CO_3^*}\big]$.

3.5 Oxidation

The species in the $\mathrm{S}(IV)$ group will oxidise to the species in the $\mathrm{S}(VI)$ group in the presence of $\mathrm{O_2}$, which is shown in (3.37).

$$
\begin{gathered}
\mathrm{S}(IV) + \frac{1}{2}\mathrm{O_2} \rightarrow \mathrm{S}(VI) \\
\Downarrow \\
\mathrm{H_2SO_3} + \frac{1}{2}\mathrm{O_2} \rightarrow \mathrm{H_2SO_4} \\
\mathrm{HSO_3^-} + \frac{1}{2}\mathrm{O_2} \rightarrow \mathrm{HSO_4^-} \\
\mathrm{SO_3^{2-}} + \frac{1}{2}\mathrm{O_2} \rightarrow \mathrm{SO_4^{2-}}
\end{gathered}
\tag{3.37}
$$

The rate of oxidation is defined in (3.38) [Zhang and Millero (144)], where I is the ionic strength as defined in (3.4) on page 23.

$$\begin{aligned} \frac{\partial\big[\mathrm{S}(IV)\big]}{\partial t} &= -\,k_{\mathrm{Oxi}} \cdot \big[\mathrm{S}(IV)\big]^2 \cdot \big[\mathrm{O_2}\big]^{0.5} \\ \log_{10}\left(k_{\mathrm{Oxi}} \cdot 60 \cdot \left(\frac{\mathrm{s}\cdot\mathrm{mol}^{1.5}}{\mathrm{L}^{1.5}}\right)\right) &= 19.54 - \frac{5069.47 + 2877 \cdot \sqrt{\frac{I}{\mathrm{mol}/\mathrm{L}}}}{T/\mathrm{K}} + \\ & \quad 14.74 \cdot \sqrt{\frac{I}{\mathrm{mol}/\mathrm{L}}} - 2.93 \cdot \frac{I}{\mathrm{mol}/\mathrm{L}} \end{aligned} \tag{3.38}$$

When temporally integrating the differential equation in (3.38), both $\big[\mathrm{S}(IV)\big]$ and $\big[\mathrm{O_2}\big]$ will change over time. The change in $\big[\mathrm{O_2}\big]$ as a function of time is shown in (3.39) along with $\partial\big[\mathrm{S}(IV)\big]/\partial t$ from (3.38) in a rewritten form.

$$\begin{aligned} \Delta &= \big[\mathrm{S}(IV)\big](t) - \big[\mathrm{S}(IV)\big](0) \\ \big[\mathrm{O_2}\big](t) &= \big[\mathrm{O_2}\big](0) + \frac{1}{2} \cdot \Delta \\ \frac{\partial\big[\mathrm{S}(IV)\big]}{\partial t} &= -k_{\mathrm{Oxi}} \cdot \big(\big[\mathrm{S}(IV)\big](t)\big)^2 \cdot \left(\big[\mathrm{O_2}\big](0) + \frac{\big[\mathrm{S}(IV)\big](t) - \big[\mathrm{S}(IV)\big](0)}{2}\right)^{0.5} \end{aligned} \tag{3.39}$$

The differential equation in (3.39) does not have an analytical solution. Therefore, the rate of change of $\big[\mathrm{O_2}\big]$ is linearised at $t = 0$, which allows for an analytical solution. This is shown in (3.40).

$$\begin{aligned} \Delta &= \big[\mathrm{S}(IV)\big](t) - \big[\mathrm{S}(IV)\big](0) \\ \frac{\partial\big[\mathrm{S}(IV)\big]}{\partial t} &= -k_{\mathrm{Oxi}} \cdot \big(\big[\mathrm{S}(IV)\big](t)\big)^2 \cdot \left(\big[\mathrm{O_2}\big](0) + \frac{t}{2} \cdot \frac{\partial\big[\mathrm{S}(IV)\big]}{\partial t}\bigg|_{\mathrm{t=0}}\right)^{0.5} \end{aligned} \tag{3.40}$$

The differential equation in (3.40) does have an analytical solution, where the solution to $\big[\mathrm{S}(IV)\big](t)$ is shown in (3.41).

$$\begin{aligned} \big[\mathrm{S}(IV)\big](t) = \Bigg(\Bigg(&\sqrt{2} \cdot \left(2 \cdot \big[\mathrm{O_2}\big](0) + t \cdot \frac{\partial\big[\mathrm{S}(IV)\big]}{\partial t}\bigg|_{\mathrm{t=0}}\right)^{3/2} - \\ & 4 \cdot \big(\big[\mathrm{O_2}\big](0)\big)^{3/2}\Bigg) \cdot \frac{k_{\mathrm{Oxi}}}{3 \cdot \frac{\partial\big[\mathrm{S}(IV)\big]}{\partial t}\Big|_{\mathrm{t=0}}} + \frac{1}{\big[\mathrm{S}(IV)\big](0)}\Bigg)^{-1} \end{aligned} \tag{3.41}$$

When the concentration of $\big[\mathrm{S}(IV)\big]$ has been integrated over a given time-step, Δt, the concentrations of the other species are recovered in a similar manner to the kinetics of $\mathrm{CO_2}$, which is shown in (3.42).

$$\begin{aligned}
\Delta &= \left[\mathrm{S}(IV)\right](t) - \left[\mathrm{S}(IV)\right](0) \\
\left[\mathrm{O_2}\right](t) &= \left[\mathrm{O_2}\right](0) + \frac{1}{2}\cdot\Delta
\end{aligned}$$

$$\begin{gathered}
\text{Method 1:} \\
\mathrm{H_2SO_3} + \frac{1}{2}\mathrm{O_2} \longrightarrow \mathrm{H_2SO_4} \begin{cases} \left[\mathrm{H_2SO_3}\right](t) = \left[\mathrm{H_2SO_3}\right](0) + \Delta \\ \left[\mathrm{H_2SO_4}\right](t) = \left[\mathrm{H_2SO_4}\right](0) - \Delta \end{cases} \\
\text{Method 2:} \\
\mathrm{HSO_3^-} + \frac{1}{2}\mathrm{O_2} \longrightarrow \mathrm{HSO_4^-} \begin{cases} \left[\mathrm{HSO_3^-}\right](t) = \left[\mathrm{HSO_3^-}\right](0) + \Delta \\ \left[\mathrm{HSO_4^-}\right](t) = \left[\mathrm{HSO_4^-}\right](0) - \Delta \end{cases} \\
\text{Method 3:} \\
\mathrm{SO_3^{2-}} + \frac{1}{2}\mathrm{O_2} \longrightarrow \mathrm{SO_4^{2-}} \begin{cases} \left[\mathrm{SO_3^{2-}}\right](t) = \left[\mathrm{SO_3^{2-}}\right](0) + \Delta \\ \left[\mathrm{SO_4^{2-}}\right](t) = \left[\mathrm{SO_4^{2-}}\right](0) - \Delta \end{cases}
\end{gathered} \tag{3.42}$$

As seen in (3.42), the change in $\left[\mathrm{S}(IV)\right]$ over a given time-step, Δt, is defined as Δ. Similar to (3.36), either of the three subsequent methods in (3.42) can be applied, which all will results in the same concentrations *after* equilibrium is satisfied.

3.6 Initialization

The concentrations of the different species are initialized by solving the 19 equations in (3.43) on the next page simultaneously. $K^{\gamma}_{\mathrm{W,H_2O}}$ is a modified equilibrium constant, which takes the concentration of water into account, which is almost constant during calculation, and is done to ensure mole balance during calculations. M_{i} is the molar mass of the i^{th} species. The 19 equations can be solved for the 18 species concentrations (17 species and $\mathrm{H_E^+}$) and the charge of the mixed salts, z_{Salt}. The salts are assumed having a molar mass equal to that of NaCl, $M(\mathrm{NaCl}) = 58.44$ g/mol, as this is the main component of the salts. All values on the left-hand side of the equations in (3.43) are known prior to calculating any of the concentrations. The reason for subtracting $\left[\mathrm{S}(VI)\right]$ in the third to last equation is that the definition of salinity includes $\left[\mathrm{HSO_4^-}\right]$, which was apparent in Table 3.2 on page 22. It should be noted that $\mathrm{CO_2(l)}$ is not in equilibrium with $\mathrm{CO_2(g)}$ in (3.43), but rather with $\mathrm{H_2CO_3(l)}$. This is used to initialize the concentrations of all species, but after initialization, the equilibrium with $\mathrm{CO_2(g)}$ is enforced. This method does not change the alkalinity, but it does change the concentrations of the species in the CO_3^* group, which are the main components of A_T. A_T does not change as it is being bound to the total charge balance as stated in (3.18) on page 31 [R. E. Zeebe (109)], which does not change with CO_2 uptake.

$$\xleftarrow{\text{All values known \textit{a priori}}} \qquad \xrightarrow{\substack{\text{All concentrations unknown} \\ \text{+ charge of mixed salts, } z_{\text{Salt}}}}$$

$$\begin{aligned}
10^{-\mathrm{pH}}\,\mathrm{mol/L} &= \left[\mathrm{H^+}\right] \\
K^{\gamma}_{\mathrm{W,H_2O}} &= \left[\mathrm{OH^-}\right] \cdot \left[\mathrm{H^+}\right] / \left[\mathrm{H_2O}\right] \\
A_{\mathrm{T}} &= \left[\mathrm{HCO_3^-}\right] + 2 \cdot \left[\mathrm{CO_3^{2-}}\right] + \left[\mathrm{B(OH)_4^-}\right] + \\
&\quad \left[\mathrm{OH^-}\right] - \left[\mathrm{H^+}\right] - \left[\mathrm{HSO_4^-}\right] \\
K^{\gamma}_{\mathrm{CO_2}} / K^{\gamma}_{\mathrm{CO_3,1}} &= \left[\mathrm{H_2CO_3}\right] / \left[\mathrm{CO_2}\right] \\
K^{\gamma}_{\mathrm{CO_3,1}} &= \left[\mathrm{H^+}\right] \cdot \left[\mathrm{HCO_3^-}\right] / \left[\mathrm{H_2CO_3}\right] \\
K^{\gamma}_{\mathrm{CO_3,2}} &= \left[\mathrm{H^+}\right] \cdot \left[\mathrm{CO_3^{2-}}\right] / \left[\mathrm{HCO_3^-}\right] \\
K^{\gamma}_{\mathrm{SO_4,1}} &= \left[\mathrm{H^+}\right] \cdot \left[\mathrm{HSO_4^-}\right] / \left[\mathrm{H_2SO_4}\right] \\
K^{\gamma}_{\mathrm{SO_4,2}} &= \left[\mathrm{H^+}\right] \cdot \left[\mathrm{SO_4^{2-}}\right] / \left[\mathrm{HSO_4^-}\right] \\
K^{\gamma}_{\mathrm{B}} &= \left[\mathrm{H^+}\right] \cdot \left[\mathrm{B(OH)_4^-}\right] / \left[\mathrm{B(OH)_3}\right] \\
\phi_{\mathrm{B}} \cdot A_{\mathrm{T}} &= \left[\mathrm{B(OH)_4^-}\right] \\
\left[\mathrm{S}(VI)\right] &= \left[\mathrm{H_2SO_4}\right] + \left[\mathrm{HSO_4^-}\right] + \left[\mathrm{SO_4^{2-}}\right] \\
0 &= \left[\mathrm{H_2SO_3}\right] \\
0 &= \left[\mathrm{HSO_3^-}\right] \\
0 &= \left[\mathrm{SO_3^{2-}}\right] \\
0 &= \left[\mathrm{H_E^+}\right] \\
K_{\mathrm{H,O_2}} \cdot y_{\mathrm{g,O_2}} \cdot P &= \left[\mathrm{O_2}\right] \\
\frac{\rho_{\mathrm{l}}\left(T_{\mathrm{l}}, S\right) \cdot S}{M(\mathrm{NaCl})} - \left[\mathrm{S}(VI)\right] &= \left[\mathrm{Salt}\right] \\
\rho_{\mathrm{l}}\left(T_{\mathrm{l}}, S\right) &= \sum c_{\mathrm{i}} \cdot M_{\mathrm{i}} \\
0 &= \sum c_{\mathrm{i}} \cdot z_{\mathrm{i}}
\end{aligned} \tag{3.43}$$

Many of the knowns in (3.43) are constants or correlations of temperature and salinity. The required inputs variables to initialize the concentrations are listed in Table 3.5, where some typical values are shown for each variable.

Table 3.5: The required variables in (3.43) to initialization the concentrations of all species. ϕ_B and $\left[S(VI)\right]$ are from [Emerson and Hedges (45)].

Variable	Typical value
pH	8.1
A_T	2.1 mmol/L
ϕ_B	4 %
$\left[S(VI)\right]$	28.2 mmol/L
y_{O2}	20.95 %
S	35 g/kg
T	30°C

When using the values in Table 3.5 and solving the system of equations in (3.43), the concentrations in Table 3.6 are obtained.

Table 3.6: The concentration of all 18 species and the charge of the mixed salts, z_{Salt}, when solving the system of equations in (3.43) using the values in Table 3.5. The density at $T = 30°\text{C}$ is shown as well.

Species	Concentration	Species	Concentration
$[H_2O]$	54.68 mol/L	$[H_2CO_3]$	27.75 nmol/L
$[H^+]$	7.94 nmol/L	$[HCO_3^-]$	1.51 mmol/L
$[OH^-]$	11.63 µmol/L	$[CO_3^{2-}]$	246.68 µmol/L
$[H_E^+]$	0	$[H_2SO_3]$	0
$[O_2]$	253.98 µmol/L	$[HSO_3^-]$	0
$[CO_2]$	7.70 µmol/L	$[SO_3^{2-}]$	0
[Salt]	583.85 mmol/L	$[H_2SO_4]$	$1.63 \cdot 10^{-20}$ mol/L
$[B(OH)_3]$	231.37 µmol/L	$[HSO_4^-]$	4.88 nmol/L
$[B(OH)_4^-]$	84.00 µmol/L	$[SO_4^{2-}]$	28.20 mmol/L
ρ_l	1021.7 kg/m^3	z_{Salt}	0.100197

The charge of the mixed salts in Table 3.6, z_{Salt}, may seem rather high, as the mixed salts should have a very small charge. The reason for this high value is that $S(VI)$ is not treated as a salt in the chemistry model used in this study, as the definition of alkalinity does not include SO_4^{2-}, which has a charge of -2. If $\left[S(VI)\right] = 0$ and the system of equations in (3.43) is solved, the charge will be $z_{\text{Salt}} = 0.003431$, which is an expected value, as the charge of the salts should neutralize the negative charge of the alkalinity species.

3.7 Examples and analyses

This section investigates the described chemistry model in detail, where titration curves are shown along with a temporal example for a droplet placed in a typical exhaust gas stream.

3.7.1 Titration curves

Alkalinity is, in practice, determined for a given seawater sample by titrating with a strong acid and logging the pH as a function of the added acid. Typically, H_2SO_4 is used for titration, as the $\mathrm{p}K_\mathrm{a}$ value between H_2SO_4 and HSO_4^- is $\mathrm{p}K^{\gamma}_{\mathrm{SO_4},1} \approx -3.0$. After each added drop of acid, the pH is allowed to settle, as the kinetics of CO_2 acts to obtain equilibrium with the species in the CO_3^* group. Instead of generating the titration curves by temporally integrating the kinetics of CO_2, the equilibrium between CO_2, H_2O, and H_2CO_3 is enforced instead, which was shown in (3.32) on page 37. This results in nine equilibria, where the solution procedure in (3.22) is used, where the concentration of $\left[\mathrm{H}^+\right]$ was calculated by finding the eigenvalues of the companion matrix of the polynomial. It should be noted that this is only used in this section, as it is computationally expensive to evaluate.

In order to visualize the effects of the oxidation of $\mathrm{S}(IV)$ to $\mathrm{S}(VI)$, the titration curves are generated by adding both H_2SO_3 and H_2SO_4, where the ratio between these are indicating the oxidized fraction, which is shown in (3.44).

$$\begin{aligned} n_{\mathrm{H_2SO_3}} &= n_{\mathrm{Acid}} \cdot (1 - \phi_{\mathrm{Oxi}}) \\ n_{\mathrm{H_2SO_4}} &= n_{\mathrm{Acid}} \cdot \phi_{\mathrm{Oxi}} \end{aligned} \tag{3.44}$$

n_{Acid} is the total number of moles added to the seawater sample, and ϕ_{Oxi} is the fraction of H_2SO_3, which has oxidized to H_2SO_4. This is naturally a temporal problem, but the titration curve can simply be computationally generated by adding each species separately. The titration curves are generated with five different values for ϕ_{Oxi}, where approximately $10\,\%$ oxidation typically occurs for water entering and leaving a wet scrubber, which was found during tests at the Alfa Laval Test & Training Centre. The titration curves are shown in Figure 3.8 on the next page, where the typical values shown in Table 3.5 on page 43 are used.

As seen in Figure 3.8, H_2SO_4 is a stronger acid compared to H_2SO_3, as the pH decreases more rapidly when $\phi_{\mathrm{Oxi}} = 100\ \%$, which is indicated by the thick dashed line. A_T is determined when the pH value is approximately 4.4, which is shown in the figure. In the computational model, the remaining alkalinity can be evaluated as a function of the added acid according to the definition shown in (3.3) on page 23, where the results are shown in Figure 3.9 on the next page.

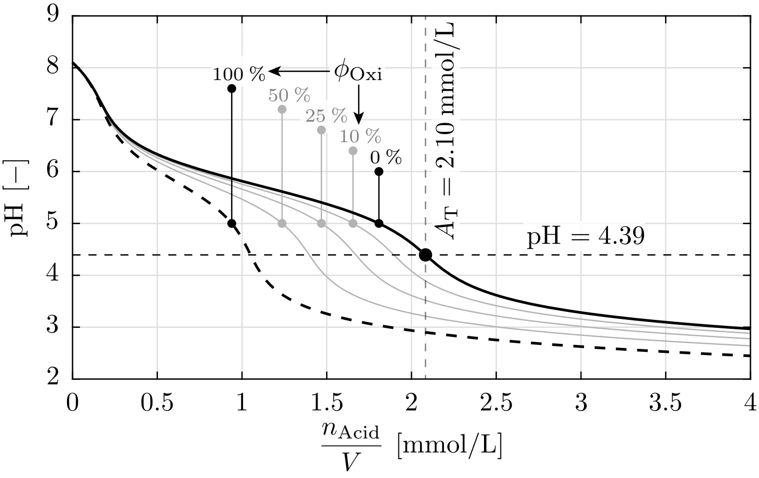

Figure 3.8: Titration curves for five different values for ϕ_{Oxi}.

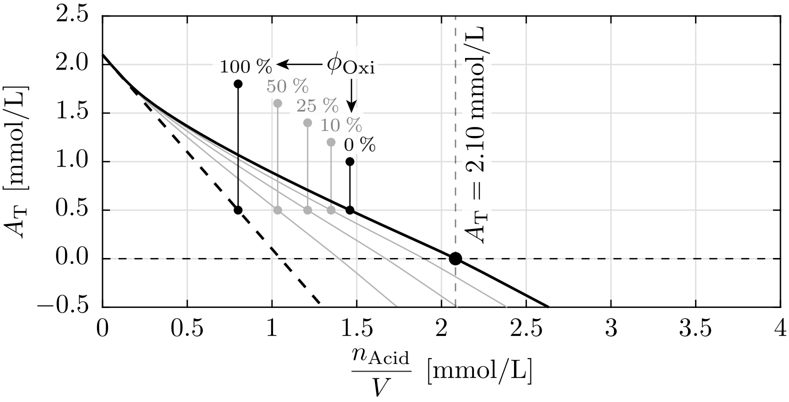

Figure 3.9: The remaining alkalinity according to (3.3) for different values of ϕ_{Oxi}.

The alkalinity for all values for ϕ_{Oxi} are equal when titration starts. It can be seen that the alkalinity decreases linearly, when titration is carried out with H_2SO_4, where $\phi_{\text{Oxi}} = 100\ \%$, whereas the alkalinity curve for $\phi_{\text{Oxi}} = 0\ \%$ is non-linear.

A comparison between the computational chemistry model and two seawater samples from *Limfjorden* in Aalborg, Denmark, is seen in Figure 3.10 on the next page, where titration was carried out with H_2SO_4. As seen in the figure, the model predicts pH accurately compared to the two seawater samples. It can be seen that the pH is slightly higher for $n_{H_2SO_4}/V < 1.0$, whereas the model accurately predicts pH beyond this point. Therefore, the chemistry model defined in this chapter is assumed valid for wet scrubber modelling.

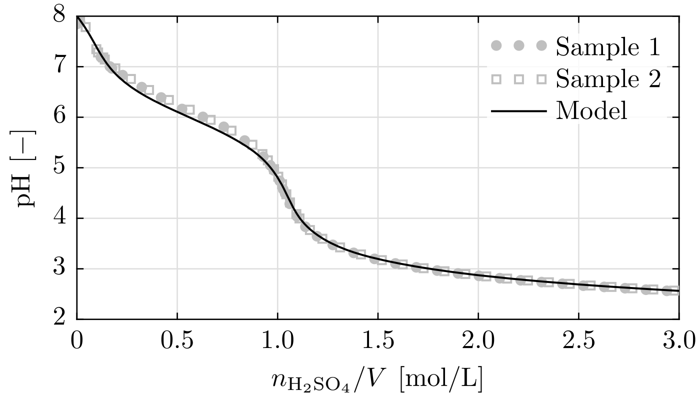

Figure 3.10: A comparison between the computational chemistry model and two seawater samples.

3.7.2 Droplet in exhaust gas

When seawater is injected into a wet scrubber, the water will absorb species from the exhaust gas as described in *Section 3.2: Surface reactions*. The absorption of SO_2(g) will form H_2SO_3(l), which dissociates into HSO_3^-(l), and SO_3^{2-}(l) dependent on pH. The species in the S(IV) group will oxidise into the species in the S(VI) group, which was illustrated in Figure 3.8 for different oxidation fractions. Meanwhile, CO_2(g), O_2(g), and H_2O(g) are absorbed through the liquid interface, where CO_2(l) will hydrate to the species in the CO_3^* group, which are slow reactions. This all happens while the eight equilibria in (3.14) are satisfied. This section serves to visualize the internal chemistry for a typical droplet placed in an exhaust gas stream.

An example case is simulated, where a droplet with a diameter of 2500 µm is placed in a typical exhaust gas stream for 10 s. The seawater values shown in Table 3.5 are used, where the initial concentration of all species were shown in Table 3.6. The gas properties are those listed in Table 3.7.

Table 3.7: The gas properties used for the example case, where a droplet is placed in a typical exhaust gas stream.

Variable	Value
T_g	100°C
v_g	5 m/s
y_{g,CO_2}	5.24 %
y_{g,H_2O}	4.71 %
y_{g,O_2}	13.17 %
y_{g,SO_2}	0.0519 %
y_{g,N_2}	76.83 %

The example case is carried out isothermally, and the gas phase is assumed having an infinite capacity, so the gas mole fractions, $y_{\mathrm{g,i}}$, remain constant. The mass transfer coefficient correlations have not been described yet, but are defined according to *Section 4.9: Mass transfer coefficient*. The figures on the following three pages show the concentrations for most species inside the droplet along with the group concentrations. The exchange rates with the gas phase are shown as well, along with the temporal cumulative exchanged species. Sub-figures are labelled A, B, and C for Figure 3.11, 3.12, and 3.13 respectively, where each sub-plot has an associated number, (A - 1), (A - 2) etc.

The pH decreases rapidly as seen in (A - 1), which is quite different compared to the titration curves in Figure 3.8. The reason for this tendency is caused by the kinetics of $\mathrm{CO_2(l)}$, which was simulated as an equilibrium for the titration curves. In the example case, the slow kinetics of $\mathrm{CO_2(l)}$ causes an accumulation of $\left[\mathrm{CO_3^*}\right]$, which is apparent from the ratio seen in (A - 5), where a value greater than unity indicates that $\left[\mathrm{CO_3^*}\right]$ is greater compared to the equilibrium concentration with $\mathrm{CO_2(l)}$. The positive ratio causes $\partial\left[\mathrm{CO_2}\right]_{\mathrm{Kin}}/\partial t$ to be positive, which is seen in (A - 6).

The alkalinity is depleted as $\mathrm{SO_2}$ is absorbed, which is shown in (A - 2), which primarily correlates with $\left[\mathrm{CO_3^*}\right]$, which decreases rapidly as seen in (A - 4). The time where $A_{\mathrm{T}}(t) = 0$ is indicated by the vertical dashed lines at $t \approx 2.3\,\mathrm{s}$. $\left[\mathrm{CO_3^*}\right]$ is almost constant for $t < 0.5\,\mathrm{s}$, which is caused by $\left[\mathrm{B(OH)_4^-}\right]$, which decreases before the species in the $\left[\mathrm{CO_3^*}\right]$ group, as $\mathrm{p}K_{\mathrm{B}}^{\gamma} > \mathrm{p}K_{\mathrm{CO_3,2}}^{\gamma}$. $\left[\mathrm{B(OH)_3}\right]$ is shown in (B - 8) along with $\left[\mathrm{B^*}\right]$ in (B - 7), where the group concentration remains constant, as no transfer of B with the gas phase exists.

As $\mathrm{SO_2(g)}$ is absorbed and reacts with $\mathrm{H_2O(l)}$ to form $\mathrm{S}(IV)$, oxidation occurs, where the oxidation rate is shown in (A - 7). It can be seen that $\left[\mathrm{O_2}\right]$ decreases accordingly in (A - 8), as the oxidation rate exceeds the absorption rate of $\mathrm{O_2(g)}$, which is shown in (C - 3). As oxidation occurs, the concentration of $\mathrm{S}(VI)$ increases as seen in (B - 5), which causes a further decrease in pH as the species in the $\mathrm{S}(VI)$ group are stronger acids compared to the species in the $\mathrm{S}(IV)$ group.

The most important aspect of seawater scrubbing is the absorption rate of $\mathrm{SO_2(g)}$, which is shown in (C - 5) along with the temporal cumulative mole transfer in (C - 6). When $A_{\mathrm{T}} > 0$, the rate of $\mathrm{SO_2(g)}$ absorption, $\dot{n}_{\mathrm{SO_2}}$, is almost constant, whereas it decreases when $A_{\mathrm{T}} \leq 0$, which is indicated by the vertical dashed lines. The driving force for $\mathrm{SO_2(g)}$ absorption is the concentration of $\mathrm{H_2SO_3(l)}$, so as oxidation occurs, the concentration of $\mathrm{H_2SO_3(l)}$ decreases, as it reacts with $\mathrm{O_2(l)}$ to form $\mathrm{H_2SO_4(l)}$. Therefore, a higher oxidation rate increases $\mathrm{SO_2(g)}$ absorption, which is shown in Figure 3.14 on page 50.

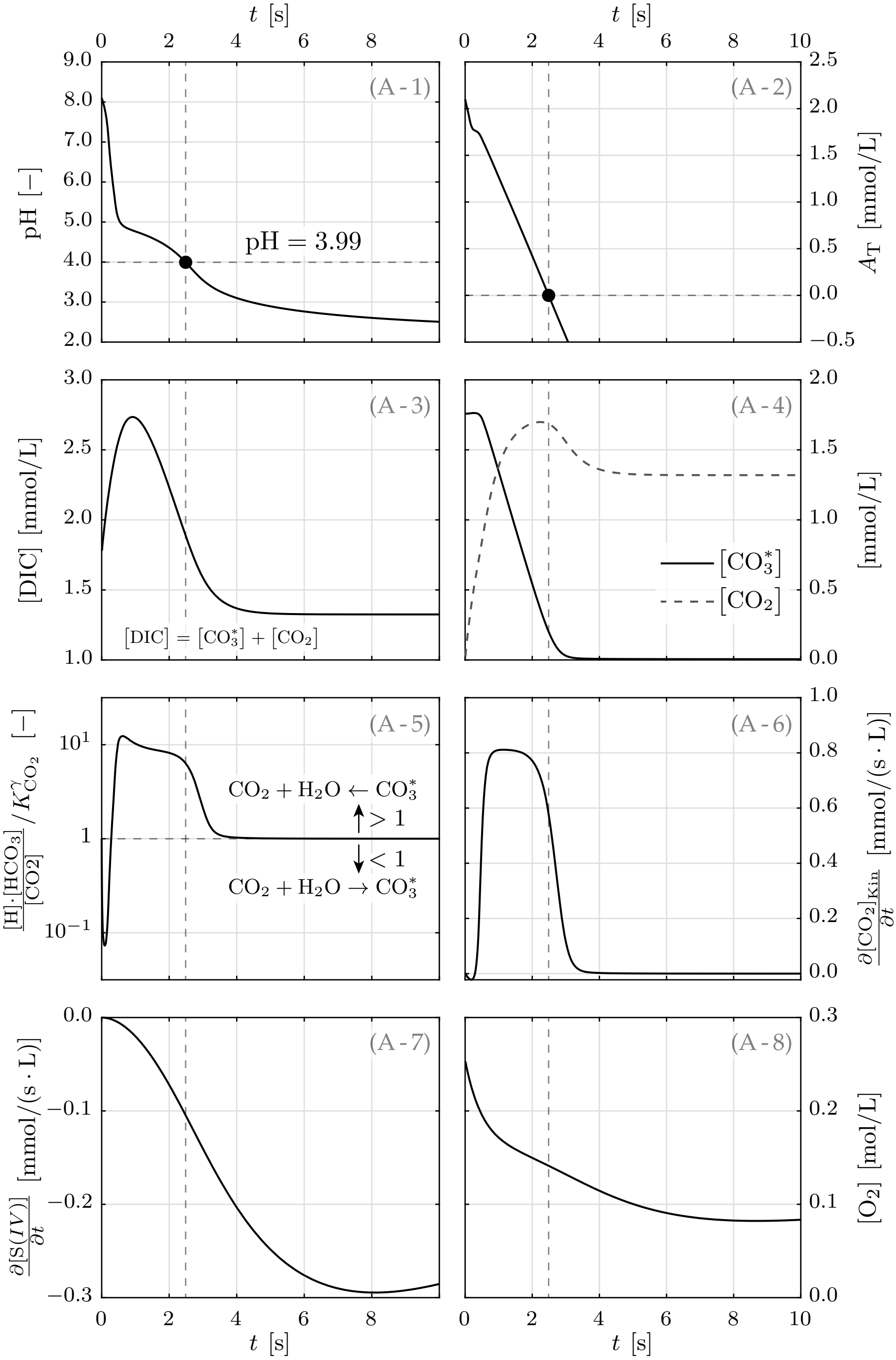

Figure 3.11: Various concentrations, rates, and values for the droplet in a typical exhaust gas. The vertical dashed lines are indicating $A_\mathrm{T} = 0$.

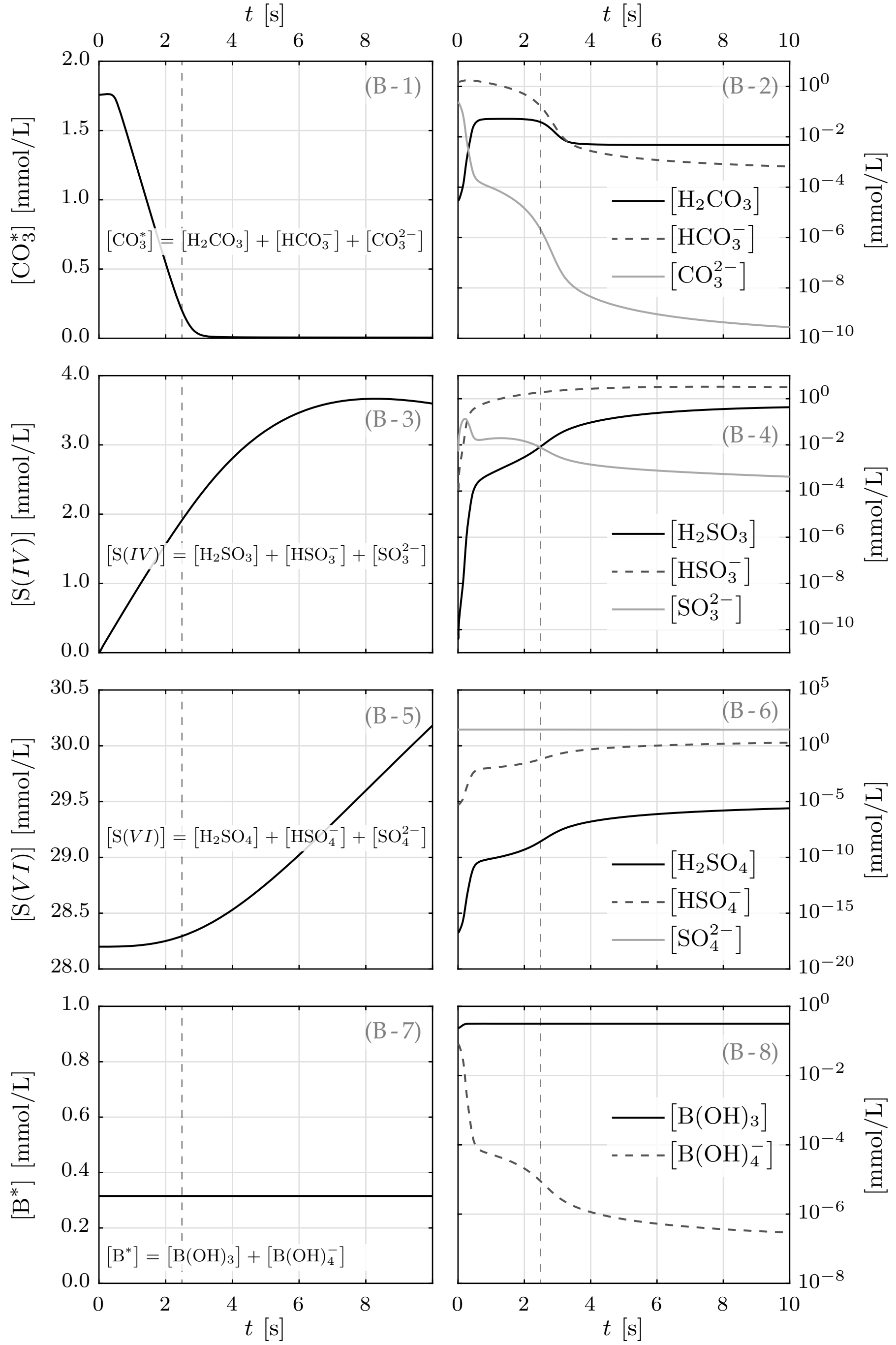

Figure 3.12: The concentrations of the different groups in the left column along with their respective species in the right column, which are in logarithmic scale. The vertical dashed lines are indicating $A_\mathrm{T} = 0$.

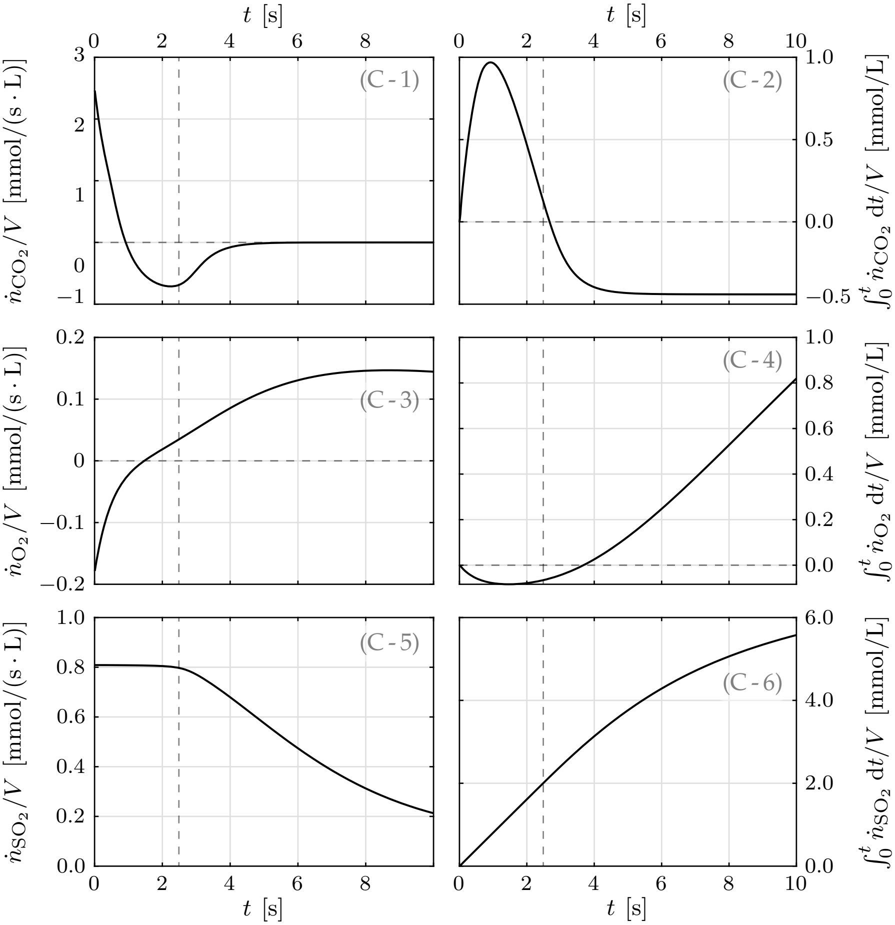

Figure 3.13: The mass transfer rates of CO_2(g), O_2(g), and SO_2(g) per unit volume in the left column, and the cumulative temporal integral of the rates in the right column. The vertical dashed lines are indicating $A_{\mathrm{T}} = 0$.

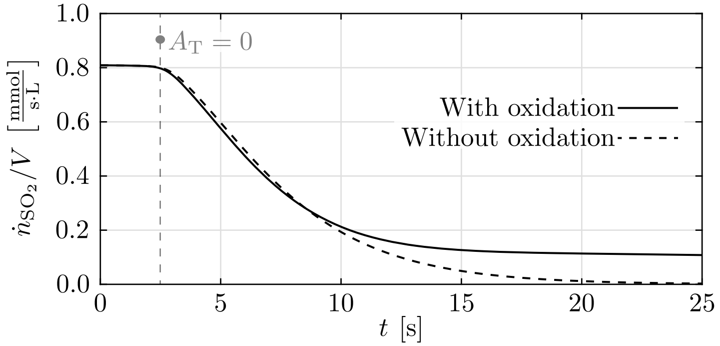

Figure 3.14: The effect of oxidation on the absorption rate of SO_2.

As seen in Figure 3.14, the absorption rate of SO_2 increases, when oxidation occurs. The effect is most apparent at low pH, where the concentration of H_2SO_3 is greatest, which is the driving force for SO_2 absorption.

3.8 Simplifications

The analyses carried out in the previous section were evaluated with all equilibria satisfied, which required solving a ninth-order polynomial in order to obtain equilibrium, which is computationally expensive. As not all equilibria are equally important, some can be removed without affecting the accuracy of the chemistry model significantly. It was described in *Section 3.3: Equilibria* that by only including the equilibria between the species in the CO_3^* group: H_2CO_3, HCO_3^- and CO_3^{2-}, the absorption rates could be captured accurately, even though the chemistry model would not satisfy all equilibria exactly.

3.8.1 $\mathrm{pK_a}$ tuning

When only including two equilibria when solving for $\left[\mathrm{H}^+\right]$ and thus pH, the absorption rate of $SO_2(\mathrm{g})$ deviates significantly from the full chemistry model, where all equilibria are satisfied. This is shown in Figure 3.15, where a comparison between the simplified and the full chemistry model is shown.

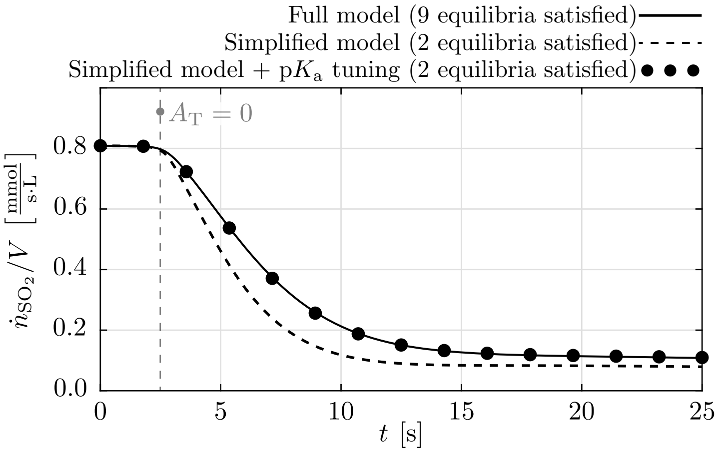

Figure 3.15: The absorption rate of SO_2 for the example case using the full, the simplified, and the simplified chemistry model + $\mathrm{p}K_\mathrm{a}$ tuning.

As seen in Figure 3.15, the absorption rate of $SO_2(\mathrm{g})$ is significantly reduced when using the simplified chemistry model, which is indicated by the black dashed line compared to the solid black line. However, by tuning the value of $\mathrm{p}K^\gamma_{SO_3,1}$ slightly, the absorption rate can be accurately captured. The correction applied is shown in (3.45).

$$\mathrm{p}K^{\gamma}_{\mathrm{SO_3,1,Tuned}} = \mathrm{p}K^{\gamma}_{\mathrm{SO_3,1}} \cdot 10^{-\Delta \mathrm{p}K_{\mathrm{SO_3,1}}} \tag{3.45}$$

Having tuned the value of $\mathrm{p}K^{\gamma}_{\mathrm{SO_3,1}}$ to $\mathrm{p}K^{\gamma}_{\mathrm{SO_3,1,Tuned}}$, the absorption rate is accurately captured, which is shown by the black dots in Figure 3.15, which follow the full chemistry model. The modified $\mathrm{p}K_{\mathrm{a}}$ value is visualized in Figure 3.16, where the species fractions, α, for the species in the $\mathrm{S}(IV)$ group are shown.

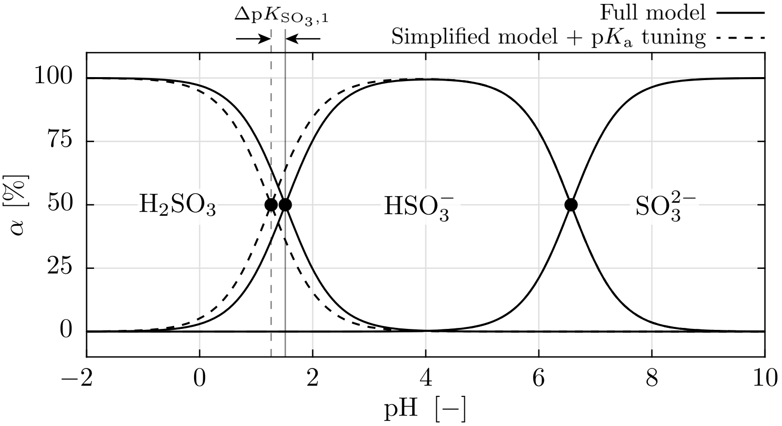

Figure 3.16: The species fractions, α, as a function of pH for the full model and the simplified chemistry model with $\mathrm{p}K_{\mathrm{a}}$ tuning shown with the solid and dashed lines respectively. The modified $\mathrm{p}K_{\mathrm{a}}$ value, $\mathrm{p}K^{\gamma}_{\mathrm{SO_3,1}}$, is adjusted with -0.24 units in this example, which simply moves it linearly to the left along the pH axis.

As seen in Figure 3.16, the adjustment made to $\mathrm{p}K^{\gamma}_{\mathrm{SO_3,1}}$ is very slight, but by doing so, the concentration of H_2SO_3 decreases, which increases the driving force for $SO_2(g)$ absorption. This will increase the absorption rate to that of the full chemistry model, which was shown in Figure 3.15.

The value of $\Delta \mathrm{p}K_{\mathrm{SO_3,1}}$ was determined by comparing the total absorption of $SO_2(g)$ for the full and the simplified chemistry model. It was found that $\Delta \mathrm{p}K_{\mathrm{SO_3,1}}$ was temperature dependent, which is shown in Figure 3.17.

As seen in Figure 3.17, the required value of $\Delta \mathrm{p}K_{\mathrm{SO_3,1}}$ to meet the absorption rate of the full chemistry model is a function of temperature. By solving for the intersections with the dotted line in Figure 3.17, the value of $\Delta \mathrm{p}K_{\mathrm{SO_3,1}}$ can be solved as a function of temperature. This is shown in Figure 3.18.

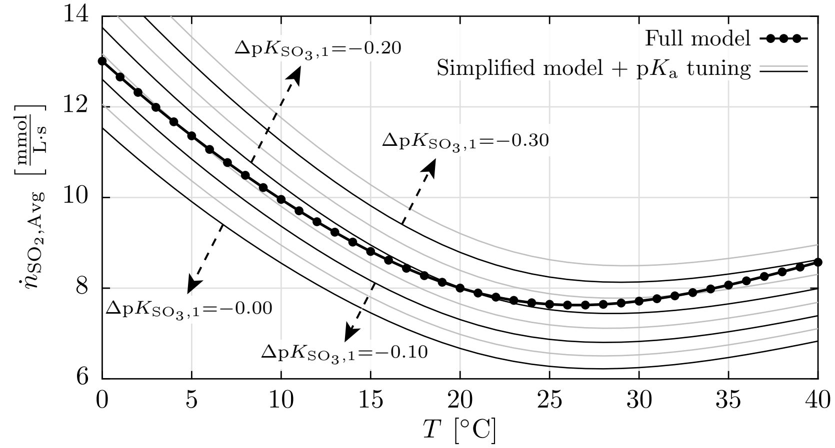

Figure 3.17: The average absorption rate for a typical scenario as a function of temperature. The black dotted line is the full chemistry model, whereas the thin lines are generated using the simplified chemistry model with varying values of $\Delta pK_{SO_3,1}$.

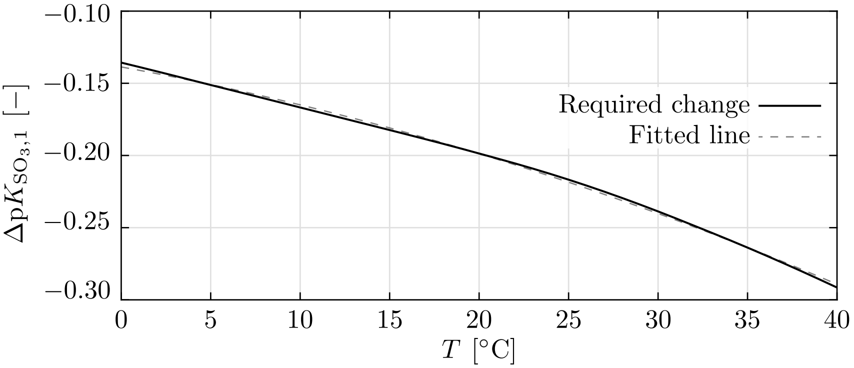

Figure 3.18: The required value of $\Delta pK_{SO_3,1}$ to meet the average absorption rate of the full chemistry model.

The curve in Figure 3.18 is fitted with a second-order polynomial, which is shown with the dashed line in the figure, and is defined in (3.46).

$$\begin{aligned}\Delta pK_{SO_3,1}(T) = & -3.79 \cdot 10^{-5} \cdot \left(\frac{T}{K} - 273.15\right)^2 + \\ & -2.246 \cdot 10^{-3} \cdot \left(\frac{T}{K} - 273.15\right) - 0.1387\end{aligned} \tag{3.46}$$

By tuning the value of $pK^{\gamma}_{SO_3,1}$ with the correlation for $\Delta pK_{SO_3,1}(T)$ shown in (3.46), the simplified chemistry model accurately captures the absorption rate of $SO_2(g)$ compared to the full chemistry model, despite only satisfying two equilibria exactly.

3.8.2 Solution procedure

The process of establishing equilibrium is to modify the concentrations of a given mixture, such that all equilibria are satisfied, while satisfying elementary mole balance and the electroneutrality principle. In case of the simplified chemistry model, only two equilibria are satisfied exactly. The solution procedure for calculating the equilibrium concentration of $\left[\mathrm{H}^+\right]$ is illustrated in Figure 3.19 on the next page, where the shaded areas indicate values or equations used in the full chemistry model, where all eight equilibria are satisfied. The six steps in the figure are described below:

Step (1): The concentrations of all species before equilibrium is defined as $\vec{c}_{\mathrm{Pre}}$. The mass of the solution is denoted m_{Pre}.

Step (2): The concentrations of the different groups are calculated using (3.15) on page 27. This step is a simple summation of different species concentrations.

Step (3): The concentration of H^+ is calculated using the group concentrations. The simplified chemistry model solves a third-order polynomial, where the roots were analytically derived in (3.24) on page 33. The full chemistry model solves a ninth-order polynomial using (3.22) on page 33, which is computationally expensive to evaluate.

Step (4): All remaining species are recovered from the group concentrations and the value of $\left[\mathrm{H}^+\right]$, which was found in Step (3), by using the species functions, f^{s}, previously described. The simplified model uses $K^{\gamma}_{\mathrm{SO_3,1,Tuned}}$, whereas the full model uses $K^{\gamma}_{\mathrm{SO_3,1}}$. All other $\mathrm{p}K_{\mathrm{a}}$ values are identical for the simple and the full chemistry model. The concentrations for the different species in Step (4) are denoted $\vec{c}_{\mathrm{Equil}}$, where $\left[\mathrm{H}^+_{\mathrm{E}}\right] = 0$.

Step (5): The simplified chemistry model does not calculate the same value for $\left[\mathrm{H}^+\right]$ as the full chemistry model does. Therefore, all species concentrations are slightly off, which causes an imbalance of H^+. In order to satisfy mass balance, the imbalance is calculated in Step (5), where $\vec{C}_{\mathrm{H}}$ was defined in (3.25). The full chemistry model does not need this step, as $\left[\mathrm{H}^+_{\mathrm{E}}\right] = 0$ will automatically be satisfied, when $\left[\mathrm{H}^+\right]$ is calculated using all eight equilibria, which required solving the roots of a ninth-order polynomial.

Step (6): The concentration of all species, after equilibrium is satisfied, is denoted $\vec{c}_{\mathrm{Equil}}$: $\left[\mathrm{H}^+\right]$ was found in Step (3); all species except $\mathrm{H}^+_{\mathrm{E}}$ in Step (4); and $\left[\mathrm{H}^+_{\mathrm{E}}\right]$ was found in Step (5). It should be noted that mass balance is enforced for the simplified model due to the introduction of $\mathrm{H}^+_{\mathrm{E}}$.

The values of $\left[\mathrm{Salt}\right]$, $\left[\mathrm{O_2}\right]$, and $\left[\mathrm{CO_2}\right]$ are copied directly from $\vec{c}_{\mathrm{Pre}}$, as these do not change during the procedure shown in Figure 3.19.

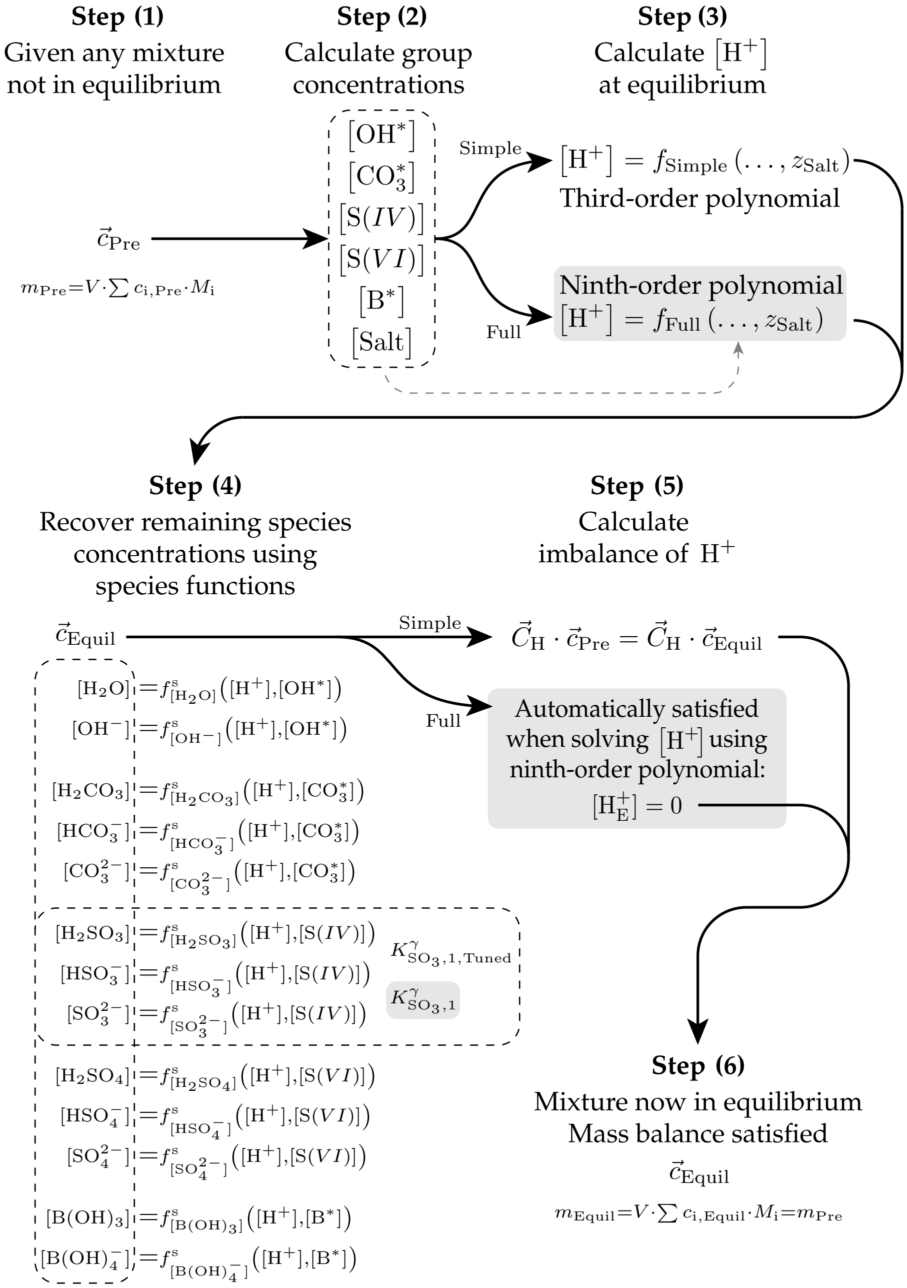

Figure 3.19: The procedure for satisfying equilibrium for both the simplified and the full chemistry model. The shaded areas indicate equations or values, which are used in the full chemistry model only.

It should be noted that the species concentration of any given mixture does not require all 18 concentrations to be specified. All six group concentrations, $\left[\mathrm{Salt}\right]$, $\left[\mathrm{O_2}\right]$, and $\left[\mathrm{CO_2}\right]$ are the only required values, as the equilibrium procedure in Figure 3.19 recovers the concentrations of all remaining individual species. Therefore, the number of degrees of freedoms is nine for each mixture, which can be a single droplet or a single wall film element.

3.8.3 Discussion

As the chemistry model is reduced to only include two equilibria when calculating pH, the computational requirements to satisfy equilibrium for a given mixture is significantly reduced. However, by reducing the model, some information is lost. By comparing the full and the simplified chemistry model, it was found that all species concentrations could be accurately recovered with minor differences, which are shown in Table 3.8.

Table 3.8: A comparison between the full and the simplified chemistry model at different times. The numbers indicate the relative deviations of the simplified model relative to the full chemistry model.

t	$5\,\mathrm{s}$	$10\,\mathrm{s}$	$15\,\mathrm{s}$	$20\,\mathrm{s}$	$25\,\mathrm{s}$
$\left[\mathrm{DIC}\right](t)$	$+0.11\%$	$+0.02\%$	$+0.02\%$	$+0.01\%$	$+0.01\%$
$\left[\mathrm{S}(IV)\right](t)$	-0.08%	$+0.25\%$	$+0.14\%$	-0.18%	-0.41%
$\left[\mathrm{S}(VI)\right](t)$	-0.00%	$+0.00\%$	$+0.02\%$	$+0.02\%$	$+0.00\%$
$n_{\mathrm{CO_2}}(t)$	-0.35%	-0.07%	-0.05%	-0.04%	-0.03%
$n_{\mathrm{O_2}}(t)$	-0.31%	$+0.03\%$	$+0.17\%$	$+0.13\%$	$+0.03\%$
$n_{\mathrm{SO_2}}(t)$	-0.10%	$+0.18\%$	$+0.15\%$	$+0.00\%$	-0.12%

Where $n_{\mathrm{CO_2}}$, $n_{\mathrm{O_2}}$, and $n_{\mathrm{SO_2}}$ are the temporal cumulative absorption rates. As seen in Table 3.8, all errors are below $1\ \%$, which indicate that the simplified chemistry model with $\mathrm{p}K_\mathrm{a}$ tuning accurately captures the dynamics of the full chemistry model for the typical pH span, which seawater scrubbers operate at.

A comparison of the pH between the simple and the full chemistry models is shown in Figure 3.20 on the next page for the example case previously investigated. The relative error is shown with the dashed grey line, which is related to the right y-axis. As seen in the figure, the pH error between the two chemistry models is minor, and does only differ slightly in some places. The simplifications to the chemistry model do induce errors, where some of these can be corrected by $\mathrm{p}K_\mathrm{a}$ tuning. Furthermore, for wet scrubber modelling, the most important aspect is the absorption of $\mathrm{SO_2(g)}$, which the simplified model with $\mathrm{p}K_\mathrm{a}$ tuning accurately captures. The advantage of simplifying the chemistry model is that equilibrium can be calculated by solving a third-order polynomial, whereas the full chemistry model requires solving a ninth-order polynomial. An overview of the chemistry model is shown in Figure 3.21.

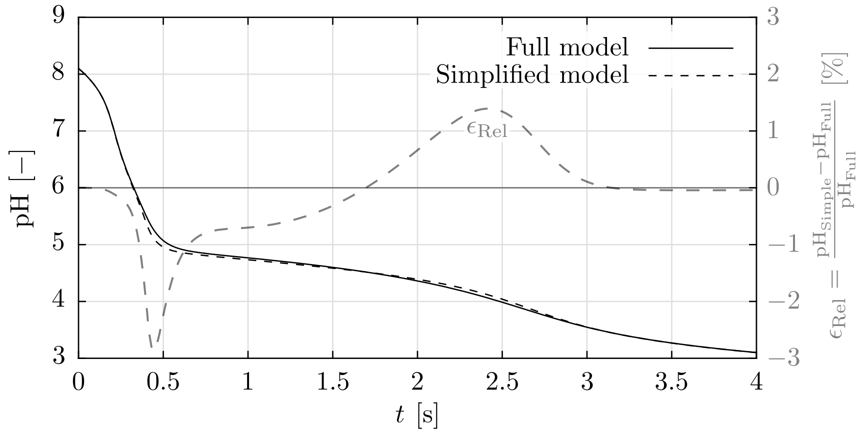

Figure 3.20: A comparison of pH between the full and the simplified chemistry model.

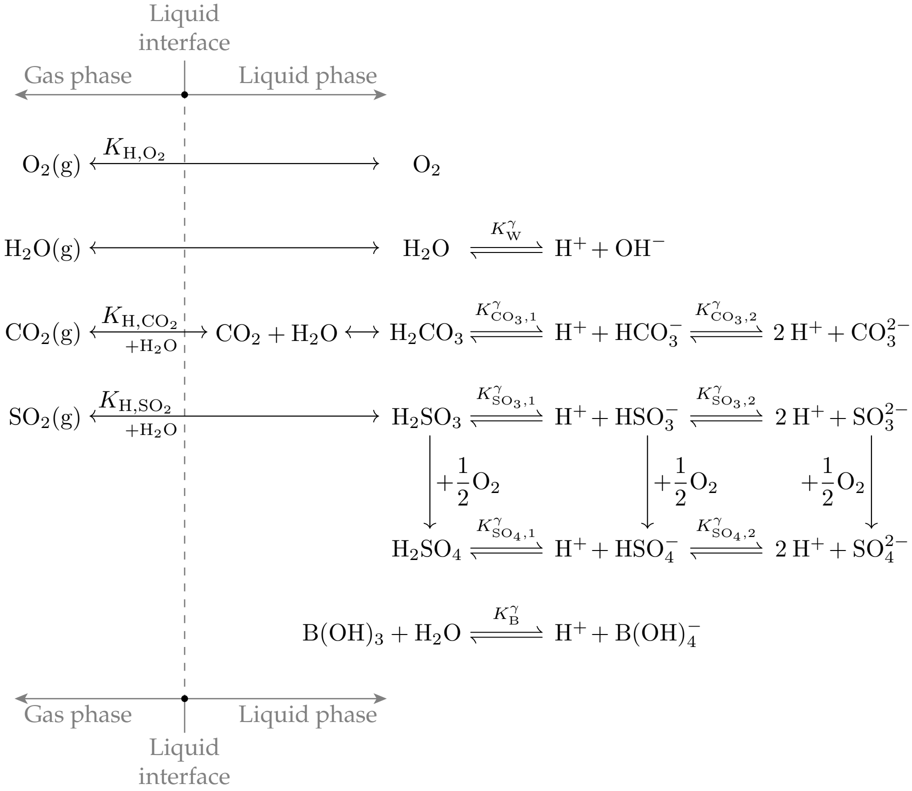

Figure 3.21: An overview of the chemistry model used in this study. The simplified chemistry model calculates pH using two equilibria, namely between H_2CO_3, $HCO_3{}^-$ and $CO_3{}^{2-}$, whereas the full chemistry model takes all equilibria into account. The simplified chemistry model adjusts the value of $K^\gamma_{SO_3,1}$ to match the absorption rate of $SO_2(g)$ of the full model.

4 DISCRETE PHASE

The liquid phase inside the scrubber is injected as small droplets through sprayer nozzles, which are located different places inside the scrubber as seen in Figure 1.4 on page 6. After being injected, the droplets experience numerous phenomena, which are resolved using sub-models. These are described in this chapter, where an overview is given in Figure 4.1.

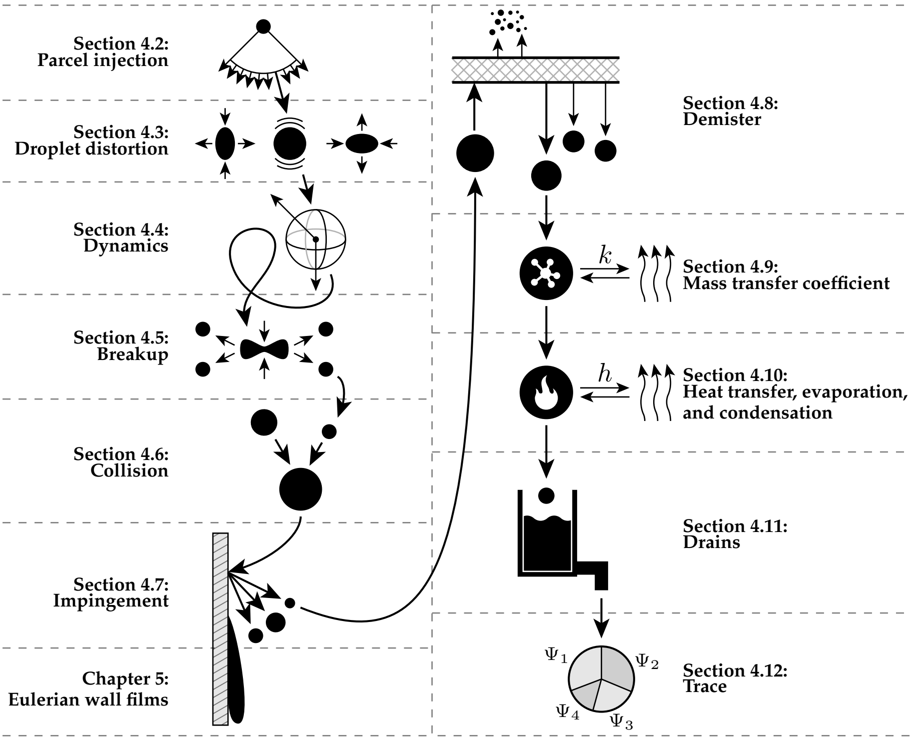

Figure 4.1: The sub-models to be covered in this chapter. The Eulerian wall film will be covered in the next chapter.

The sub-models included are chosen, as each of them are assumed necessary for accurate scrubber modelling. The discrete phase is based on a parcel representation, which is described in the next section.

4.1 Parcel representation

Millions of droplets are present inside an operating scrubber, which are all unique in terms of shape, species concentrations, temperature etc. If every single droplet is tracked and simulated, the computational requirements would be very large. The test scrubber located in the Alfa Laval Test & Training Centre in Aalborg, Denmark, is a small scrubber designed for $1.6\,\mathrm{MW}$ engine load with a diameter of $1.092\ \mathrm{m}$. A typical water flow for this scrubber is $16\ \mathrm{kg/s}$, and by assuming a mean droplet size of $1200\ \mu\mathrm{m}$, and an average residence time of $3\ \mathrm{s}$, the approximate number of droplets can be estimated using (4.1).

$$\begin{aligned} \dot{m} &\approx 16\,\mathrm{kg/s} \\ \tau &\approx 3\,\mathrm{s} \\ D &\approx 1200\,\mu\mathrm{m} \\ n_{\mathrm{Drops}} &\approx \frac{\dot{m}\cdot\tau}{{}^{4}\!/\!{}_{3}\cdot\pi\cdot\left(\frac{D}{2}\right)^{3}\cdot\rho_{\mathrm{l}}} \approx 50\cdot 10^{6}\ \text{droplets} \end{aligned} \tag{4.1}$$

The estimated droplet count shown in (4.1) is approximately $50\cdot 10^{6}$, although a large uncertainty is associated with this value. The high number of droplets is not feasible to resolve without a large computational cluster, so the droplets are instead represented by parcels.

A parcel is a collection of droplets, which share properties such as velocity, temperature, species concentration etc. This massively decreases computational requirements, as, for instance, 1000 droplets can be modelled simultaneously by assuming that they share properties [Zhou and Yao (145)]. The concept of a parcel is illustrated in Figure 4.2, where a single parcel is containing a finite number of smaller droplets.

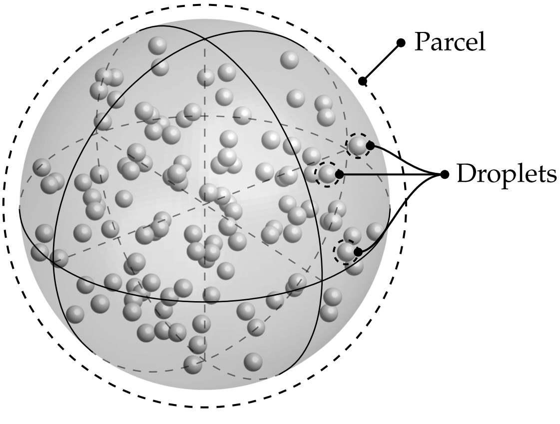

Figure 4.2: A parcel is a collection of a finite number of droplets, which share properties such as velocity, temperature, species concentration etc.

Each of the small droplets in Figure 4.2 share properties, so the temperature and species concentrations of all droplets inside the parcel are identical. The parcels are tracked instead of individual droplets, which reduced computational requirements. However, a large number of parcels is still required to resolve the dynamics of a wet scrubber, but instead of tracking $50 \cdot 10^6$ droplets, only approximately $50 \cdot 10^3$ parcels need to be tracked, which is three orders of magnitude smaller. Both steady- and unsteady parcel tracking can be applied, which is illustrated in Figure 4.3.

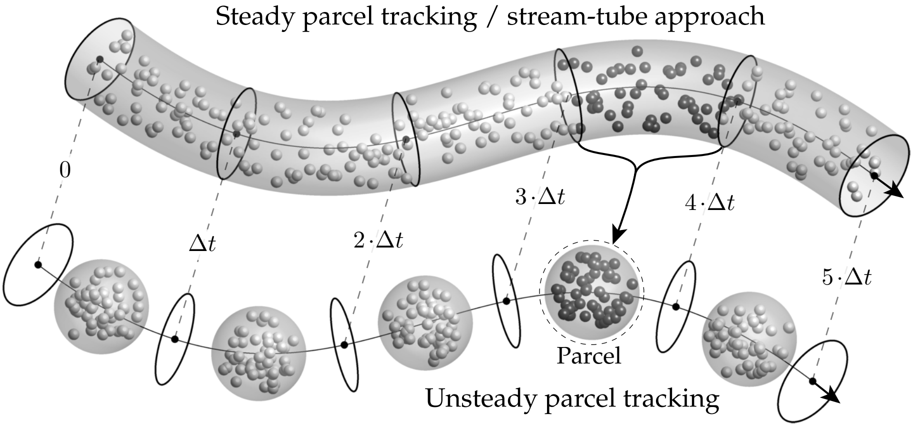

Figure 4.3: Steady parcel tracking computes the entire trajectory at once, whereas unsteady parcel tracking advances the parcels each time-step, Δt.

Figure 4.3 illustrates the two approaches, where the upper one is *steady parcel tracking*, which can be interpreted as a steam-tube approach. This method calculates the whole trajectory from injection to exit in one operation, where an arbitrary trajectory is shown in the figure. The mass flow can be calculated by summing the mass located within the steam-tube between two time-steps and dividing by Δt, where an example is shown in the figure by the black droplets, which are located between $3 \cdot \Delta t$ and $4 \cdot \Delta t$.

The other method is *unsteady parcel tracking*, where the stream-tube is sliced each time-step, and the droplets are collocated to parcels, which is illustrated by the parcel with the black droplets located between $3 \cdot \Delta t$ and $4 \cdot \Delta$. The choice of method affects the calculation of the source terms, which are required to resolve the continuous phase. This is illustrated in Figure 4.4 on the next page.

As seen in Figure 4.4, the continuous phase advances towards steady-state for n_{C} iterations. The steady parcel tracking method will then use the updated flow properties such as velocity, temperature etc. to compute new trajectories. These trajectories are then used to update the source terms, after which the loop continues until convergence.

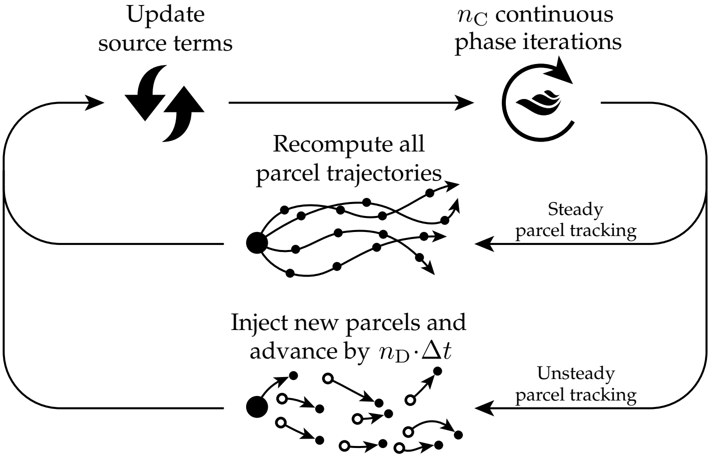

Figure 4.4: The solution method for both steady- and unsteady parcel tracking.

The unsteady parcel tracking method uses the updated flow properties to advance the parcels by n_D time-steps, Δt. The exchange rates between the continuous and discrete phase are integrated over time and relaxed to update the source terms. This method is advantageous when modelling complex discrete phase phenomena such as breakup, collision etc., which is not possible in practice for steady parcel tracking, as the number of parcels paths would increase exponentially, as they were calculated. This is illustrated in Figure 4.5.

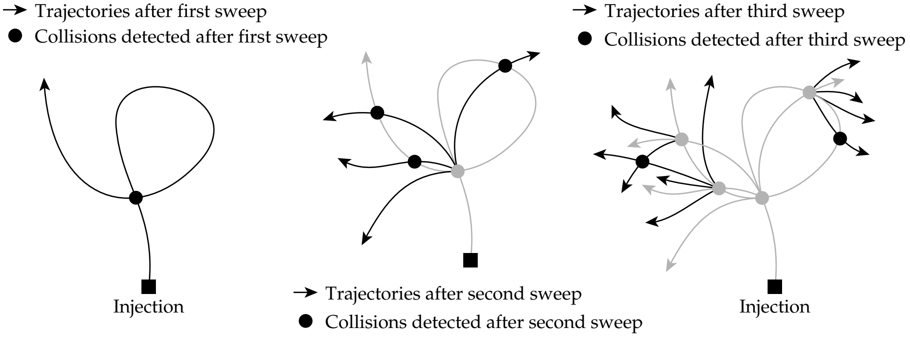

Figure 4.5: A fundamental problem arises, if steady parcel tracking is combined with collision and breakup models. The number of trajectories to investigate increases exponentially with the number of sweeps.

Figure 4.5 illustrates the problem with combining steady parcel tracking with a collision model. The example is in 2D, where a path collides with itself, which is indicated with the black circle. As a collision is detected, the outcome of this event has to be taken into account. This creates four new modified parcels, which intersect with the original path three times, which again has to be taken into account. The outcome of the three new collisions create six new parcels, which are illustrated in the third sweep. This process will continue, and the number of collisions will increase exponentially due to the number of paths. Therefore, the steady parcel tracking method is unsuitable for modelling a wet scrubber. The unsteady parcel tracking method does not suffer from this problem, as each parcel is free to move and collide with other parcels.

A parcel is a collection of droplets with identical diameter, velocity, temperature etc., so a parcel will have a total mass and a number of droplets, N. The properties of any single droplet within a parcel can be derived using this information, which is shown in (4.2) for some of the parcel variables.

$$\begin{aligned} m_{\text{Drop}} &= \frac{m_{\text{Parcel}}}{N_{\text{Parcel}}} \\ V_{\text{Drop}} &= \frac{V_{\text{Parcel}}}{N_{\text{Parcel}}} \\ \vec{x}_{\text{Drop}} &= \vec{x}_{\text{Parcel}} \\ E_{\text{Drop}} &= \frac{E_{\text{Parcel}}}{N_{\text{Parcel}}} \\ \frac{E_{\text{Drop}}}{m_{\text{Drop}} \cdot c_{\text{P}}} = T_{\text{Drop}} &= T_{\text{Parcel}} = \frac{E_{\text{Parcel}}}{m_{\text{Parcel}} \cdot c_{\text{P}}} \end{aligned} \tag{4.2}$$

Notice that some of the parcel and droplet properties are equal, such as temperature, T, and position, $\vec{x}$. The number of droplets within any given parcel is kept constant, so when water evaporates from the parcel, the droplet diameters will decrease as a consequence of the constant droplet count, N. A summary is given of all discrete phase properties in Table 4.1 on page 123.

4.2 Parcel injection

Seawater is injected into the scrubber through a number of sprayer nozzles. These are located various places inside the scrubber, which were illustrated in Figure 1.4 on page 6. Some of the nozzles are mounted on rings, such that water can be evenly distributed inside the scrubber, which is illustrated in Figure 4.6. The figure shows a ring inside the scrubber, where two rings are located in the absorber section. The remaining nozzles are simply located centrally in the scrubber, and are injecting water downwards.

The injected parcels must represent the whole range of droplet sizes and have some stochastic velocity distribution. These properties are described in the following subsections.

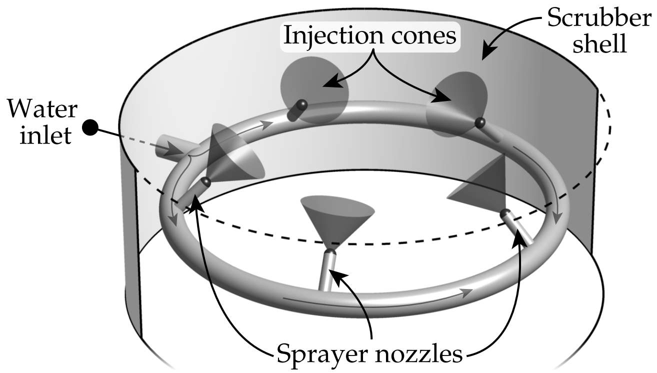

Figure 4.6: An illustration of a ring, where a number of nozzles are located. The nozzles are either tilted upwards or downwards dependent on the location inside the scrubber.

4.2.1 Sprayer nozzles

Water is injected into the scrubber through a number of sprayer nozzles, which come in many varieties, where both the geometry and the droplet size distribution varies. Some typical sprayer nozzle designs are shown in Figure 4.7, where the physical geometries and the computational analogies are shown.

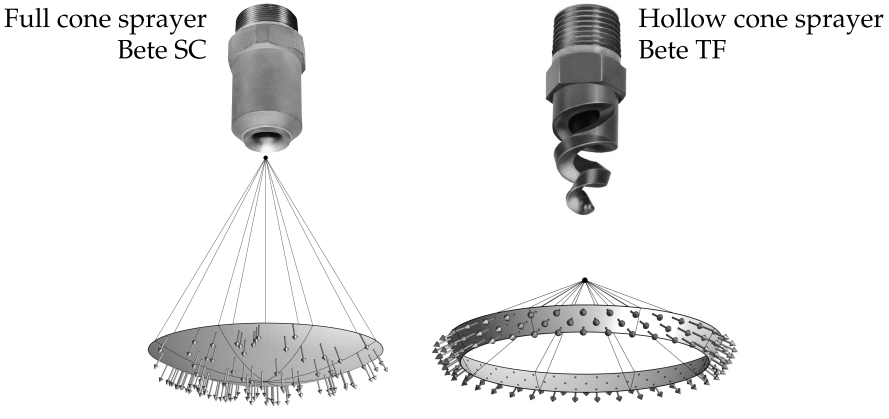

Figure 4.7: Two commonly used sprayer nozzles for wet scrubbers [BETE (15)]. The computational analogies are shown below each type, where the arrows indicate the direction of movement of the parcels, when they are injected.

It is assumed that the parcels are injected uniformly over the injection cones of the nozzles, which are indicated by the shaded grey areas in Figure 4.7. Equation (4.3) is used to sample uniformly over a capped spherical shell, which is illustrated in Figure 4.8. ζ are uniformly random numbers between 0 and 1.

$$
\begin{aligned}
\phi &= \operatorname{acos}\big(\cos(\phi_{\mathrm{Min}}) \cdot \zeta_\phi + \cos(\phi_{\mathrm{Max}}) \cdot (1 - \zeta_\phi)\big) \\
\theta &= \zeta_2 \cdot 2 \cdot \pi \\
x &= \sin(\phi) + \cos(\theta) + x_0 \\
y &= \sin(\phi) + \sin(\theta) + y_0 \\
z &= \cos(\phi) + z_0
\end{aligned} \tag{4.3}
$$

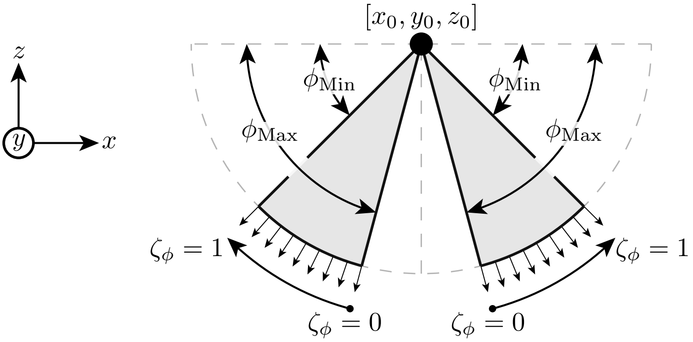

Figure 4.8: A 2D sketch of (4.3), where the injection points are uniformly sampled on a capped spherical shell.

4.2.2 Velocity

Having determined the direction of the injected parcels, the velocity magnitudes are randomly sampled from a truncated normal distribution, which ensures that no negative or infinitely high values are sampled. The normal distribution is shown in (4.4) [Walpole et al. (138)].

$$
\begin{aligned}
g(x) &= \frac{x - \mu}{\sigma} \\
y_{\mathrm{Norm}}(x) &= \frac{1}{\sqrt{2 \cdot \pi \cdot \sigma^2}} \cdot \exp\left(-\frac{1}{2} \cdot g(x)^2\right) \\
Y_{\mathrm{Norm}}(x) &= \frac{1}{2} \cdot \left(1 + \operatorname{erf}\left(\frac{g(x)}{\sqrt{2}}\right)\right)
\end{aligned} \tag{4.4}
$$

The truncated normal distribution is derived from (4.4) and is shown in (4.5) on the next page [Jawitz (74)], where y_{Trunc} and Y_{Trunc} are the probability and cumulative density functions, and Q_{Trunc} is the quantile function.

The truncated normal distribution ensures that $(\mu - \Delta \leq Q_{\mathrm{Trunc}}(\zeta) \leq \mu + \Delta)$, which cannot be achieved with the standard normal distribution given in (4.4). An example is shown in Figure 4.9, where $\mu = 15$ m/s, $\Delta = 2.5$ m/s and $\sigma = 1.5$ m/s.

$$
\begin{aligned}
Z &= \int_{\mu-\Delta}^{\mu+\Delta} y_{\mathrm{Norm}}\left(g\left(x\right)\right)\,\mathrm{d}x \\
&= Y_{\mathrm{Norm}}\left(g(\mu+\Delta)\right) - Y_{\mathrm{Norm}}\left(g(\mu-\Delta)\right) \\
y_{\mathrm{Trunc}}(x) &= \frac{y_{\mathrm{Norm}}\left(x\right)}{\sigma \cdot Z} \\
Y_{\mathrm{Trunc}}(x) &= \frac{Y_{\mathrm{Norm}}\left(x\right) - Y_{\mathrm{Norm}}\left(g\left(\mu-\Delta\right)\right)}{Z} \\
Q_{\mathrm{Trunc}}(\zeta) &= \mu + \sigma \cdot \sqrt{2} \cdot \mathrm{erf}^{-1}\left(\left(2\cdot\zeta - 1\right)\cdot Z\right)
\end{aligned}
\tag{4.5}
$$

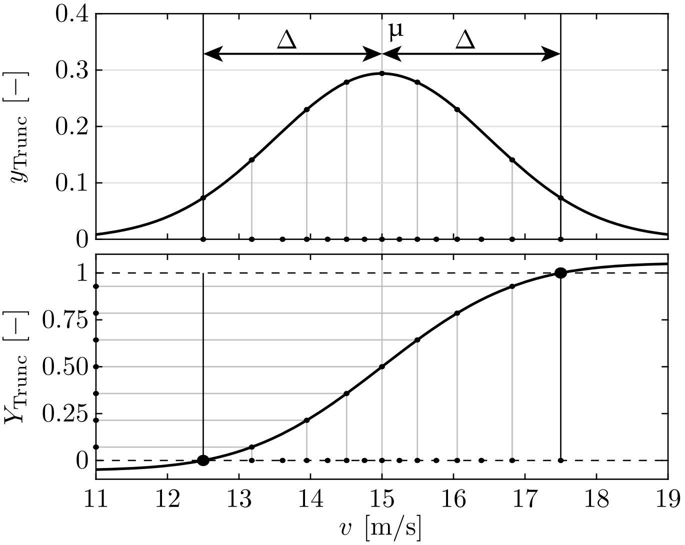

Figure 4.9: The truncated probability- and cumulative density functions shown in the upper and lower figure respectively. The thin vertical lines at $v = 12.5\mathrm{m/s}$ and $v = 17.5\ \mathrm{m/s}$ indicate the limits for the truncated distribution.

As seen in Figure 4.9, the values closest to μ are more frequent as expected. The quantile function at the limits are $Q_{\mathrm{Trunc}}(0) = 12.5\ \mathrm{m/s}$ and $Q_{\mathrm{Trunc}}(1) = 17.5\ \mathrm{m/s}$, which ensures that the velocity magnitude is bounded within these limits, as the input argument to Q_{Trunc} is a random uniformly sampled number between 0 and 1.

4.2.3 Droplet diameter distribution

When injecting water into the scrubber, small diameter droplets will exist in greater numbers compared to larger droplets. Furthermore, small droplets have a larger surface area per unit volume compared to larger ones, so it is advantageous to have small droplets inside the scrubber. However, if the droplets are too small, they will be carried upwards by the gas stream, which should be avoided. Therefore, the droplet size distribution is an important parameter, when designing a wet scrubber. A number of characterizing parameters are used when describing droplet size distributions, where the most commonly used is the Sauter Mean Diameter, D_{32}, which represents the volume to surface mean diameter. The general notation for deriving the characterizing diameters is shown in (4.6) in both a continuous and a discrete version [Finlay (50)]. It should be noted that n in this context is number density or number count.

$$\begin{aligned} &\text{(Continuous distribution)} \quad D_{\mathrm{pq}} = \left(\frac{\displaystyle\int_0^\infty n(D) \cdot D^p \,\mathrm{d}D}{\displaystyle\int_0^\infty n(D) \cdot D^q \,\mathrm{d}D} \right)^{\left(\frac{1}{p-q}\right)} \\ &\text{(Discrete distribution)} \quad D_{\mathrm{pq}} = \left(\frac{\displaystyle\sum_{\mathrm{i}} n_{\mathrm{i}} \cdot D_{\mathrm{i}}^p}{\displaystyle\sum_{\mathrm{i}} n_{\mathrm{i}} \cdot D_{\mathrm{i}}^q} \right)^{\left(\frac{1}{p-q}\right)} \end{aligned} \tag{4.6}$$

Another notation commonly used is $D_\phi(f)$, which is defined such that a given property, ϕ, has a fraction, f, of the total sample less than the value of $D_\phi(f)$ [ASTM International (11)]. This is defined in (4.7).

$$f = \frac{\displaystyle\int_0^{D_\phi(f)} n(D) \cdot \phi(D) \,\mathrm{d}D}{\displaystyle\int_0^\infty n(D) \cdot \phi(D) \,\mathrm{d}D} \tag{4.7}$$

ϕ can, for instance, be area or volume. Therefore, $D_{\mathrm{A}}(0.5)$ indicates the area median diameter, $D_{\mathrm{V}}(0.5)$ the volume median diameter, and $D_{\mathrm{V}}(0.9)$ the diameter where all droplets smaller than $D_{\mathrm{V}}(0.9)$ will account for $90\ \%$ of the total volume of the sample.

A typical sprayer nozzle is characterized by D_{32}. The injected droplets are not equal in size and will follow a distribution, where the Rosin-Rammler distribution [Bailey et al. (13)] is typically used, which originates from the Weibull distribution. The Rosin-Rammler distribution is shown in (4.8).

$$\begin{aligned} y_{\mathrm{RR}}(D) &= \frac{N_{\mathrm{RR}}}{D_{\mathrm{RR}}} \cdot \left(\frac{D}{D_{\mathrm{RR}}}\right)^{N_{\mathrm{RR}}-1} \cdot \exp\left(-\left(\frac{D}{D_{\mathrm{RR}}}\right)^{N_{\mathrm{RR}}}\right) \\ Y_{\mathrm{RR}}(D) &= 1 - \exp\left(-\left(\frac{D}{D_{\mathrm{RR}}}\right)^{N_{\mathrm{RR}}}\right) \\ Q_{\mathrm{RR}}(\zeta) &= \left(-\log_{\mathrm{e}}(1-\zeta)\right)^{1/N_{\mathrm{RR}}} \cdot D_{\mathrm{RR}} \end{aligned} \tag{4.8}$$

The Rosin-Rammler distribution has two parameters, which is the mean diameter, D_{RR}, and the spread parameter, N_{RR}. This distribution will be used for multiple sub-model, where the parameters will change depending on the model. D_{RR} is defined as $D_{\mathrm{V}}(f)$ where $f = 1 - 1/e = 63.2\,\%$. The relationship between D_{RR} and D_{32} can be analytically derived, which is shown in (4.9). $\Gamma(z)$ is the gamma function used in the field of statistics.

$$\begin{aligned} \frac{D_{\mathrm{RR}}}{D_{32}} &= \Gamma\left(1 - \frac{1}{N_{\mathrm{RR}}}\right) \\ \Gamma(z) &= \int_0^\infty x^{z-1} \cdot \exp(-x)\,\mathrm{d}x \end{aligned} \tag{4.9}$$

Some typical distributions are shown in Figure 4.10, where $D_{\mathrm{RR}} = 1800$ µm and N_{RR} is 1.5, 2.0, and 3.0.

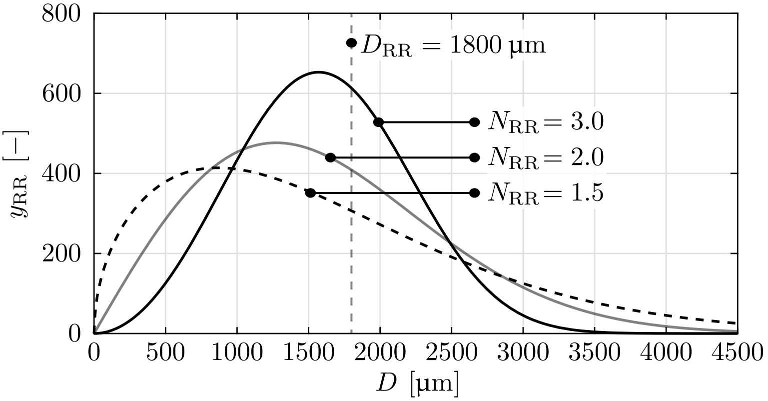

Figure 4.10: Three Rosin-Rammler distributions where N_{RR} is 1.5, 2.0, and 3.0. D_{RR} is kept constant at 1800 µm.

As seen in Figure 4.10, a lower value of N_{RR} results is smaller droplets. Figure 4.11 shows a distribution, where $D_{\mathrm{RR}} = 1800$ µm and $N_{\mathrm{RR}} = 2.0$. Some of the previously defined characterizing parameters are overlaid, which illustrates the relative magnitude of each metric, which are functions of N_{RR}.

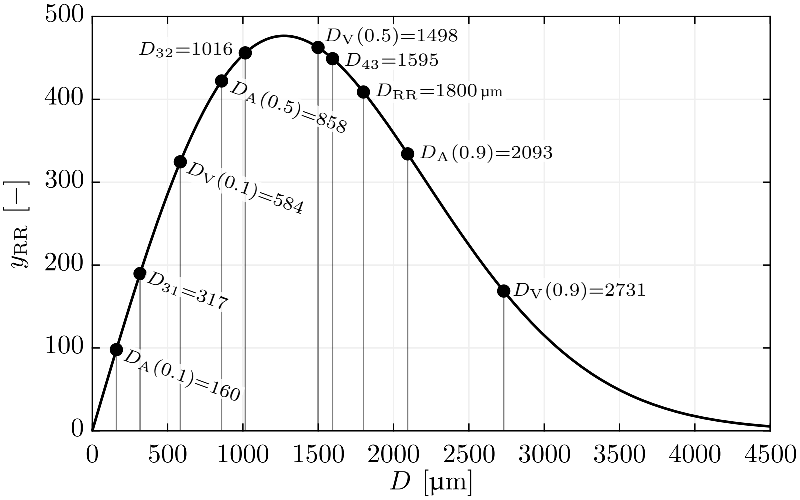

Figure 4.11: A Rosin-Rammler distribution with various characterizing metrics overlaid, where all numbers have units of µm.

4.3 Droplet distortion

Each droplet is subject to numerous forces: aerodynamic forces will deform the droplet, surface tension forces will act to restore the spherical shape of the droplet, and viscous forces will act to dampen the dynamics [Taylor (127)]. These forces combined create a dynamic system, where the shape of a droplet changes over time. Reference [O'Rourke and Amsden (101)] proposed a damped force oscillator for modelling droplet deformations, which is illustrated in Figure 4.12.

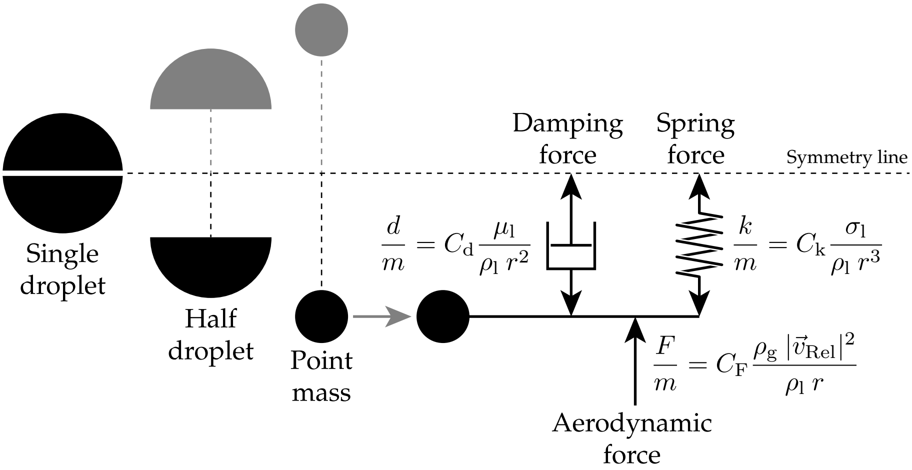

Figure 4.12: The principle of the droplet distortion model proposed by [O'Rourke and Amsden (101)]. Each droplet is divided into two point masses, where three forces are acting to deform or restore the droplet shape.

The model from [O'Rourke and Amsden (101)] assumes each droplet to be represented by two halves, which are modelled as point masses. The point masses are oscillating symmetrically relative to the centre line of the droplet, and are connected to this by a spring and a dashpot. The spring is analogous to the restoring surface tension force, and is proportional to the surface tension, σ_l. The dashpot is analogous to the viscous damping force, and is proportional to the viscosity, μ_l. The external force is analogous to the aerodynamic forces, and is proportional to the dynamic pressure, $1/2 \cdot \rho_\mathrm{g} \cdot |\vec{v}_\mathrm{Rel}|^2$, where $\vec{v}_\mathrm{Rel}$ is the relative velocity vector between the droplet and the gas.

The deformation is modelled as a second-order differential equation as shown in (4.10), where the three bottom terms are also shown in Figure 4.12. C_F, C_k, and C_d are model constants.

$$\begin{gathered}\frac{\mathrm{d}^2 x}{\mathrm{d}t^2} = \frac{F}{m} - \frac{k}{m} \cdot x - \frac{d}{m}\frac{\mathrm{d}x}{\mathrm{d}t} \\ \frac{F}{m} = C_\mathrm{F}\frac{\rho_\mathrm{g}\,|\vec{v}_\mathrm{Rel}|^2}{\rho_\mathrm{l}\,r} \qquad \frac{k}{m} = C_\mathrm{k}\frac{\sigma_\mathrm{l}}{\rho_\mathrm{l}\,r^3} \qquad \frac{d}{m} = C_\mathrm{d}\frac{\mu_\mathrm{l}}{\rho_\mathrm{l}\,r^2}\end{gathered} \tag{4.10}$$

x in (4.10) is the absolute deformation of the droplet from its spherical shape. By non-dimensioning this parameter, the resulting solution to the differential equation can be simplified. This is done by defining $\gamma = x/(C_\mathrm{b} \cdot r)$, where C_b is a model constant, which relates to the breakup criteria. This will be described in detail in *Section 4.5: Breakup*. The deformation is assumed to oscillate between a sphere and a spheroid, which is illustrated in Figure 4.13 along with (x/r) and γ.

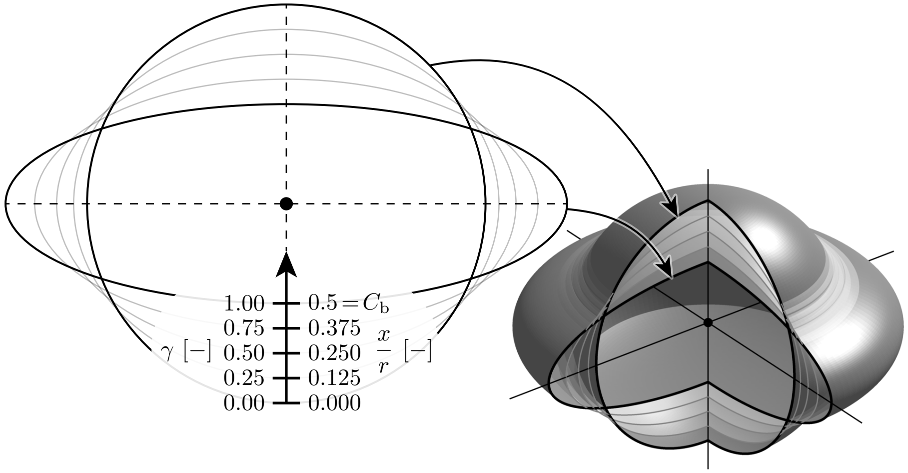

Figure 4.13: Examples of droplet deformation. x is the absolute deformation, and γ is the non-dimensional deformation. Notice that the spheroid bulge out at the equator due to volume conservation.

Substituting $x = \gamma \cdot (C_\mathrm{b} \cdot r)$ into (4.10), the differential equation in (4.11) is obtained.

$$\frac{\mathrm{d}^2\gamma}{\mathrm{d}t^2} = \underbrace{\left(\frac{C_\mathrm{F} \cdot \rho_\mathrm{g} \cdot |\vec{v}_\mathrm{Rel}|^2}{C_\mathrm{b} \cdot \rho_\mathrm{l} \cdot r^2}\right)}_{\text{Aerodynamic force}} - \underbrace{\left(\frac{C_\mathrm{k} \cdot \sigma_\mathrm{l}}{\rho_\mathrm{l} \cdot r^3}\right)}_{\text{Surface tension}}\gamma - \underbrace{\left(\frac{C_\mathrm{d} \cdot \mu_\mathrm{l}}{\rho_\mathrm{l} \cdot r^2}\right)}_{\text{Viscous damping}}\frac{\mathrm{d}\gamma}{\mathrm{d}t} \tag{4.11}$$

The differential equation in (4.11) is solved for $\gamma(t)$, which yields the expression shown in (4.12).

$$\begin{aligned}\gamma(t) = We_\mathrm{c} + \exp\left(-\frac{t}{t_\mathrm{d}}\right) \cdot \Bigg[& (\gamma(0) - We_\mathrm{c}) \cdot \cos(\omega\, t) + \\ & \frac{1}{\omega} \cdot \left(\left.\frac{\mathrm{d}\gamma}{\mathrm{d}t}\right|_{\mathrm{t}=0} + \frac{\gamma(0) - We_\mathrm{c}}{t_\mathrm{d}}\right) \cdot \sin(\omega\, t)\Bigg]\end{aligned} \tag{4.12}$$

$$We = \frac{\rho_\mathrm{g}\, |\vec{v}_\mathrm{Rel}|^2\, r}{\sigma_\mathrm{l}} \qquad We_\mathrm{c} = \frac{C_\mathrm{F}}{C_\mathrm{k}\, C_\mathrm{b}} We$$

$$\frac{1}{t_\mathrm{d}} = \frac{C_\mathrm{d}\, \mu_\mathrm{l}}{2\, \rho_\mathrm{l}\, r^2} \qquad \omega^2 = \frac{C_\mathrm{k}\, \sigma_\mathrm{l}}{\rho_\mathrm{l}\, r^3} - \frac{1}{t_\mathrm{d}^2}$$

We_c is the critical Weber number, which is related to the stationary value of γ, as $t \to \infty$ s. ω is related to the oscillation frequency, and t_d to the damping forces. The model constants are given in (4.13).

$$\begin{aligned} C_\mathrm{F} &= 1/3 & C_\mathrm{k} &= 8 \\ C_\mathrm{d} &= 5 & C_\mathrm{b} &= 0.5 \end{aligned} \tag{4.13}$$

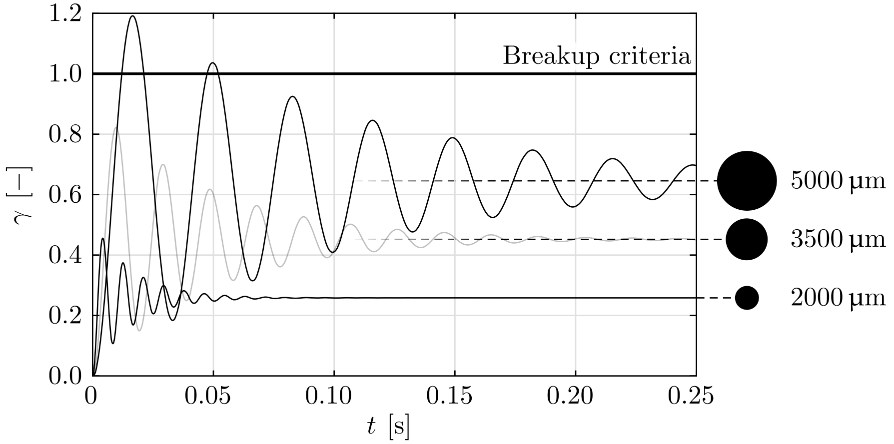

Figure 4.14: $\gamma(t)$ for three different sized droplets. It should be noted that C_d is increased to 100 for visualization purposes, which increases the damping effects and reduces the oscillation frequency.

$\gamma(t)$ is shown in Figure 4.14 on the previous page for three droplets subject to a relative velocity of $|\vec{v}_{\mathrm{Rel}}| = 15\,\mathrm{m/s}$ with diameters of 2000, 3500 and $5000\,\mathrm{\mu m}$. The figure shows that smaller droplets both oscillates with a higher frequency and settle faster compared to the larger droplets. The breakup criteria defined at $\gamma = 1.0$ will be described in detail in *Section 4.5: Breakup*.

4.4 Dynamics

The droplets injected into the scrubber will experience different forces acting on them. The drag force is a function of the droplet shape, which is modelled according to the previous section. The resulting force will accelerate the droplet, where this can be temporally integrated to yield an updated velocity and position. These phenomena are described in detail in this section.

4.4.1 Particle forces

The motion of a single droplet can be resolved by calculating all forces acting on the droplet along with the torques. Five forces are shown in Figure 4.15 [ANSYS Inc. (6)].

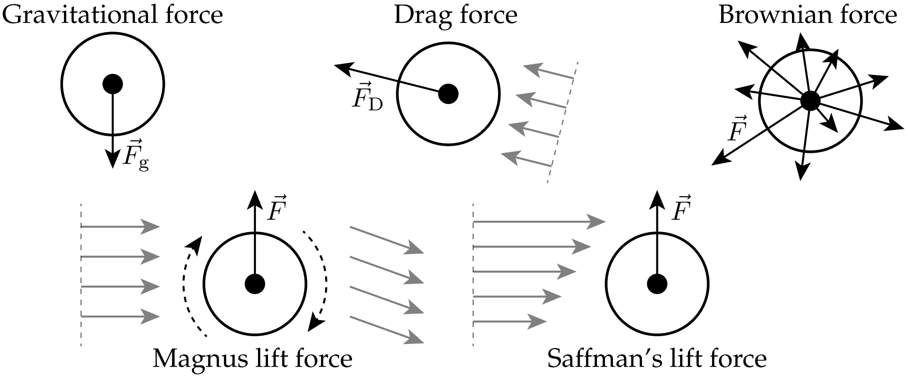

Figure 4.15: Five different forces acting on small particles, where the gravitational and the drag forces, $\vec{F}_g$ and $\vec{F}_D$ respectively, are the ones included in the model.

The *Gravitational force*, $\vec{F}_g$, is readily available, as it only depends on the gravitational acceleration vector and the mass of the droplet/parcel.

The *Brownian force* describes the force acting on a particle due to velocity fluctuation, and is dominant for sub-micron particles. Therefore, it can be neglected for larger particles, such as water droplets, with diameters greater than approximately $100\,\mathrm{\mu m}$.

The *Magnus lift force* describes the force acting on a droplet, when the rotation of the droplet imposes a significant acceleration of the fluid near the surface. This is neglected as the rotational rates of the droplets are not resolved.

The *Saffman's lift force* describes the force associated with shear flows. This force is only dominant for large velocity gradients, where the apparent velocity on two opposite sides of the droplet is significantly different. This force is not considered in this study, as its effect is assumed negligible.

The *Drag force*, $\vec{F}_{\mathrm{D}}$, is caused by the static pressure difference on the upstream and downstream sides of the droplet. This force and the gravitational force are shown in (4.14).

$$\begin{aligned}\vec{F}_{\mathrm{g}} &= m \cdot \vec{g} \\ \vec{F}_{\mathrm{D}} &= \underbrace{\frac{\vec{v}_{\mathrm{d}} - \vec{v}_{\mathrm{g}}}{|\vec{v}_{\mathrm{d}} - \vec{v}_{\mathrm{g}}|}}_{\substack{\text{Relative}\\ \text{normal}\\ \text{vector}}} \cdot \underbrace{\left(\frac{1}{2} \cdot \rho_{\mathrm{g}} \cdot |\vec{v}_{\mathrm{d}} - \vec{v}_{\mathrm{g}}|^2\right)}_{\substack{\text{Dynamic}\\ \text{Pressure}}} \cdot \underbrace{\left(r^2 \cdot \pi\right)}_{\substack{\text{Cross}\\ \text{sectional}\\ \text{area}}} \cdot c_{\mathrm{D}}\end{aligned} \tag{4.14}$$

The subscript $(...)_{\mathrm{d}}$ indicates the droplet or parcel, and c_{D} is the coefficient of drag, which is described in the next subsection.

4.4.2 Coefficient of drag

The coefficient of drag, c_{D}, is modelled using a correlation, which takes the sphericity into account, as the dynamic oscillations causes the droplet to be non-spherical. The correlation is shown in (4.15) [Haider and Levenspiel (65)].

$$\begin{aligned}c_{\mathrm{D}}(Re, \psi) &= \frac{24}{Re} \cdot \left(1 + b_1(\psi) \cdot Re^{b_2(\psi)}\right) + \frac{b_3(\psi) \cdot Re}{b_4(\psi) + Re} \\ b_1(\psi) &= \exp(2.3288 - 6.4581 \cdot \psi + 2.4486 \cdot \psi^2) \\ b_2(\psi) &= 0.0964 + 0.565 \cdot \psi \\ b_3(\psi) &= \exp(4.905 - 13.8944 \cdot \psi + 18.4222 \cdot \psi^2 - 10.2599 \cdot \psi^3) \\ b_4(\psi) &= \exp(1.4681 + 12.2584 \cdot \psi - 20.7322 \cdot \psi^2 + 15.8855 \cdot \psi^3)\end{aligned} \tag{4.15}$$

ψ is the sphericity of the droplet, which is defined as the ratio between the surface area of a sphere divided by the surface area of the deformed shape, while their volumes are equal [Wadell (136)]. This is defined in (4.16).

$$\begin{aligned}\psi = \frac{A_{\mathrm{Sphere}}}{A_{\mathrm{Deformed}}} \leq 1.0 \\ V_{\mathrm{Sphere}} = V_{\mathrm{Deformed}}\end{aligned} \tag{4.16}$$

The coefficient of drag, c_{D}, is shown as a function of both ψ and Re in Figure 4.16 according to the correlation in (4.15).

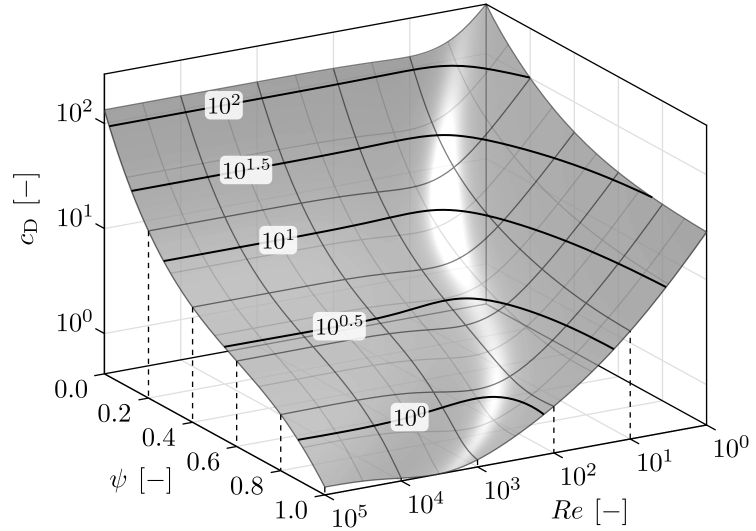

Figure 4.16: The coefficient of drag, c_D, as a function of ψ and Re. The solid lines are contour lines of c_D, where the contour values are highlighted.

As seen in Figure 4.16, c_D is a non-linear function of ψ and Re. The sphericity can be defined in terms of the deformation parameter, γ, from (4.12) on page 71. This transformation can be derived analytically, which is shown in *Chapter B: Sphericity*. The resulting function is defined in (4.17), where E_c is the eccentricity.

$$\begin{aligned} \psi(\gamma) &= \left(\log_e\left(\frac{E_c+1}{1-E_c}\right)\cdot\frac{(\gamma-2)^2}{16\,E_c}-\frac{1}{\gamma-2}\right)^{-1} \\ E_c &= \sqrt{1-\left(1-\frac{\gamma}{2}\right)^3} \end{aligned} \tag{4.17}$$

The function shown in (4.17) is shown in Figure 4.17 on the next page, where the cross sectional silhouette of the droplet is shown for selected values of γ.

The coefficient of drag is calculated based upon the average value of γ, within each time-step, $\bar{\gamma}$, as shown in (4.18). $\bar{c}_D$ is the value used during integration over the time-step.

$$\begin{aligned} \bar{\gamma} &= \frac{1}{\Delta t}\cdot\int_t^{t+\Delta t}\gamma(t)\,\mathrm{d}t \\ \bar{c}_D &= c_D\left(Re,\psi\left(\bar{\gamma}\right)\right) \end{aligned} \tag{4.18}$$

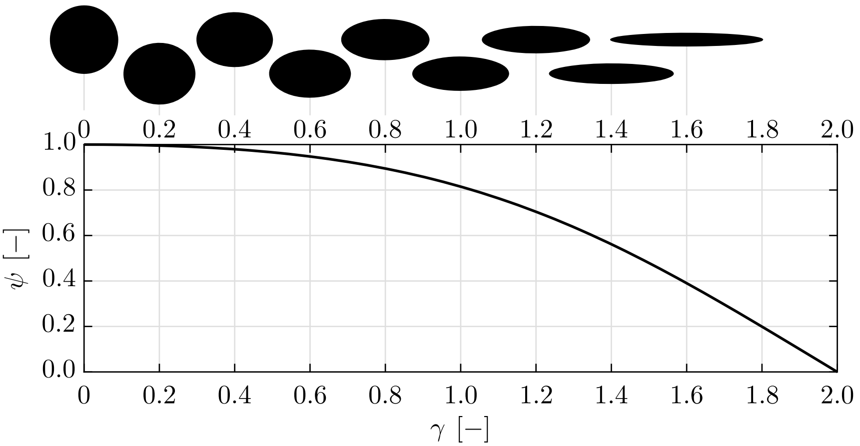

Figure 4.17: The sphericity, ψ, as a function of the deformation parameter, γ, as defined in (4.17). Spheroids silhouette can be seen for selected values of γ.

4.4.3 Integrating the equations of motion

Having calculated the coefficient of drag to be applied over the next timestep, $\bar{c}_\mathrm{D}$, the velocities and accelerations can be temporally integrated to yield an updated velocity and position. Numerous methods exist for calculating the trajectories with varying precision. Euler, trapezoidal, and Runge-Kutta are commonly used numerical integration methods, where this study will apply an analytical scheme to increase robustness of the model. The differential equation governing droplet motion is shown in (4.19) [ANSYS Inc. (6)], where τ_d is the characteristic time.

$$\begin{aligned} Re &= \frac{\rho_\mathrm{g}\, D\, |\vec{v}_\mathrm{g} - \vec{v}_\mathrm{d}|}{\mu_\mathrm{g}} \\ \tau_\mathrm{d} &= \frac{4\, \rho_\mathrm{l}\, D^2}{3\, \mu_\mathrm{g}\, \bar{c}_\mathrm{D}\, Re} \\ \vec{v}_\mathrm{g}(t) &= \vec{v}_\mathrm{g}(0) + \nabla \vec{v}_\mathrm{g} \cdot (\vec{v}_\mathrm{d}(0) \cdot t) \\ \frac{\mathrm{d}^2 \vec{x}_\mathrm{d}}{\mathrm{d}t^2} &= \frac{1}{\tau_\mathrm{d}} \cdot \left(\vec{v}_\mathrm{g}(t) - \frac{\mathrm{d}\vec{x}_\mathrm{d}}{\mathrm{d}t} \right) + \vec{a}_\mathrm{Ext} \end{aligned} \tag{4.19}$$

The gas velocity spatial gradient tensor, $\nabla \vec{v}_\mathrm{g}$, has size 3×3, and the apparent gas velocity experienced by the droplet is $\vec{v}_\mathrm{g}(t)$, which can be seen to vary as the droplet moves in time, $(\vec{v}_\mathrm{d}(0) \cdot t)$. Equation (4.19) yields three coupled differential equations, but in order to solve the equation, $\vec{v}_\mathrm{g}(t)$ must be modified to yield three uncoupled differential equations. This can be done by either assuming $\vec{v}_\mathrm{g}(t)$ to be constant, or to make it a function of time. Figure 4.18 shows different methods of uncoupling the differential equations.

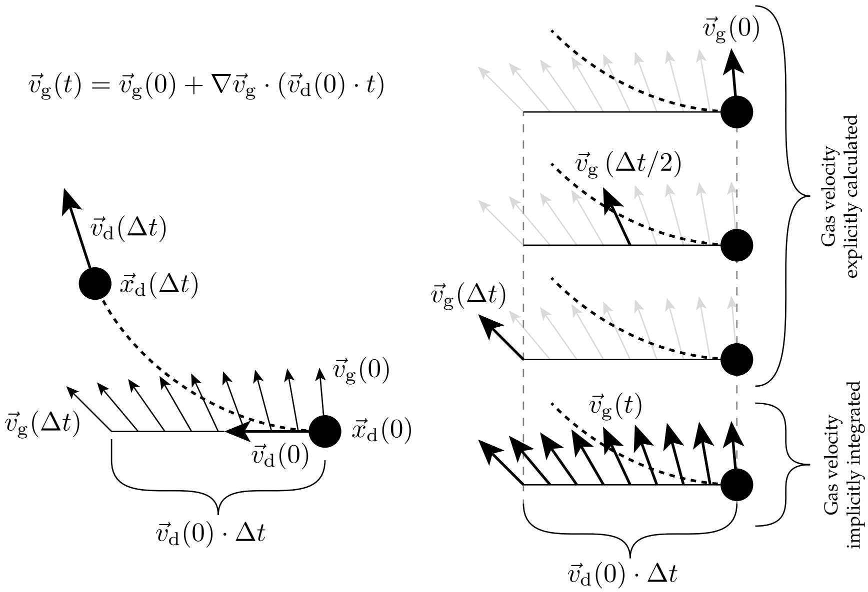

Figure 4.18: The surrounding gas velocity, $\vec{v}_\mathrm{g}$, varies in space, which must be taken into account when integrating the governing differential equation.

Figure 4.18 shows how the gas velocity in (4.19) can be modelled. The left figure shows a droplet, where its initial position and velocity at $t = 0$ are $\vec{x}_\mathrm{d}(0)$ and $\vec{v}_\mathrm{d}(0)$ respectively. The surrounding gas velocity at this point is $\vec{v}_\mathrm{g}(0)$, and the gas velocity tensor is $\nabla\vec{v}_\mathrm{g}$. As the new position and velocity of the particle, $\vec{x}_\mathrm{d}(\Delta t)$ and $\vec{v}_\mathrm{d}(\Delta t)$ respectively, are not known, the gas velocity used in (4.19) must be predicted. This is done by sampling from a line going from the current particle position, $\vec{x}_\mathrm{d}(0)$, to a point located at $(\vec{x}_\mathrm{d}(0) + \vec{v}_\mathrm{d}(0) \cdot \Delta t)$. The predicted gas velocity along this line is $\vec{v}_\mathrm{g}(t)$, and was shown in (4.19). This implies that the predicted velocity at the end point is $\vec{v}_\mathrm{g}(\Delta t)$.

The figures to the right show different ways of choosing the gas velocity to be inserted into (4.19). The upper three are showing explicit methods of evaluating the predicted gas velocity, as these are simply found by evaluating $\vec{v}_\mathrm{g}(t)$ with different values for t. The bottom figure to the right indicates that the full expression for $\vec{v}_\mathrm{g}(t)$ is used when solving the differential equation in (4.19) analytically. The solution to (4.19) using the explicit gas velocity method is shown in (4.20), where $\vec{e}$ is a support variable used multiple times in the equations.

$$\begin{aligned}
\vec{e} &= (\vec{v}_\mathrm{d}(0) + \nabla\vec{v}_\mathrm{g} \cdot \vec{v}_\mathrm{d}(0) \cdot \Delta t \cdot \phi) + \tau_\mathrm{d}\,\vec{a} \\
\vec{x}_\mathrm{d}(\Delta t) &= \vec{x}_\mathrm{d}(0) + \Delta t \cdot \vec{e} + \tau_\mathrm{d} \cdot (\vec{e} - \vec{v}_\mathrm{d}(0)) \cdot \left(\exp\left(-\frac{\Delta t}{\tau_\mathrm{d}}\right) - 1\right) \\
\vec{v}_\mathrm{d}(\Delta t) &= \vec{e} - \exp\left(-\frac{\Delta t}{\tau_\mathrm{d}}\right) \cdot (\vec{e} - \vec{v}_\mathrm{d}(0))
\end{aligned} \tag{4.20}$$

$\phi \in [0,1]$ is used to assign where the gas velocity is sampled from: $\phi = 0$ corresponds to $\vec{v}_{\mathrm{g}}(0)$, $\phi = 0.5$ corresponds to $\vec{v}_{\mathrm{g}}(\Delta t/2)$, and $\phi = 1$ corresponds to $\vec{v}_{\mathrm{g}}(\Delta t)$ in Figure 4.18.

The analytical solution to (4.19) using the implicit gas velocity method is shown in (4.21).

$$
\begin{aligned}
\vec{e} &= \vec{v}_{\mathrm{d}}(0) + \tau_{\mathrm{d}} \left(\vec{a} - \nabla \vec{v}_{\mathrm{g}} \cdot \vec{v}_{\mathrm{d}}(0) \right) \\
\vec{x}_{\mathrm{d}}(\Delta t) &= \vec{x}_{\mathrm{d}}(0) + \Delta t \cdot \left(\frac{\nabla \vec{v}_{\mathrm{g}} \cdot \vec{v}_{\mathrm{d}}(0) \cdot \Delta t}{2} + \vec{e} \right) + \\
&\qquad \tau_{\mathrm{d}} \cdot \left(\vec{v}_{\mathrm{d}}(0) - \vec{e} \right) \cdot \left(1 - \exp\left(-\frac{\Delta t}{\tau_{\mathrm{d}}} \right) \right) \\
\vec{v}_{\mathrm{d}}(\Delta t) &= \vec{e} + \Delta t \cdot \nabla \vec{v}_{\mathrm{g}} \cdot \vec{v}_{\mathrm{d}}(0) - \left(\vec{v}_{\mathrm{d}}(0) - \vec{e} \right) \cdot \exp\left(-\frac{\Delta t}{\tau_{\mathrm{d}}} \right)
\end{aligned}
\tag{4.21}
$$

The implicit method shown in (4.21) is well suited for gas flows, where strong velocity gradients are present such as a wet scrubber, so this will be used in this study to model the motion of the parcels.

The droplets/parcels exert forces on the continuous phase, which are expressed using the change in velocity divided by Δt, which ensures conservation of momentum. This is shown in (4.22).

$$
\vec{p}_{\mathrm{Gas}} = \left(\frac{\vec{v}_{\mathrm{d}}(\Delta t) - \vec{v}_{\mathrm{d}}(0)}{\Delta t} - \vec{g} \right) \cdot m \tag{4.22}
$$

The unit of $\vec{p}_{\mathrm{Gas}}$ is [N]. The term in the parenthesis is the apparent acceleration of the parcel relative to the continuous phase, which is the reason for subtracting $\vec{g}$.

4.5 Breakup

A liquid droplet oscillates and deforms in a gas stream due to aerodynamic and surface tension forces. If the deformation becomes too great, the droplet will experience breakup and shatter into smaller droplets. This phenomena has been investigated by numerous studies [O'Rourke and Amsden (101)] [Tanner (125)] [Tanner and Weisser (126)], where multiple models have been proposed. One of these is the Taylor Analogy Breakup model, TAB, which the spring-damper analogy in *Section 4.3: Droplet distortion* was based upon. The breakup process is shown as a flowchart in Figure 4.19. The different steps shown in the figure will be described in the following three subsections.

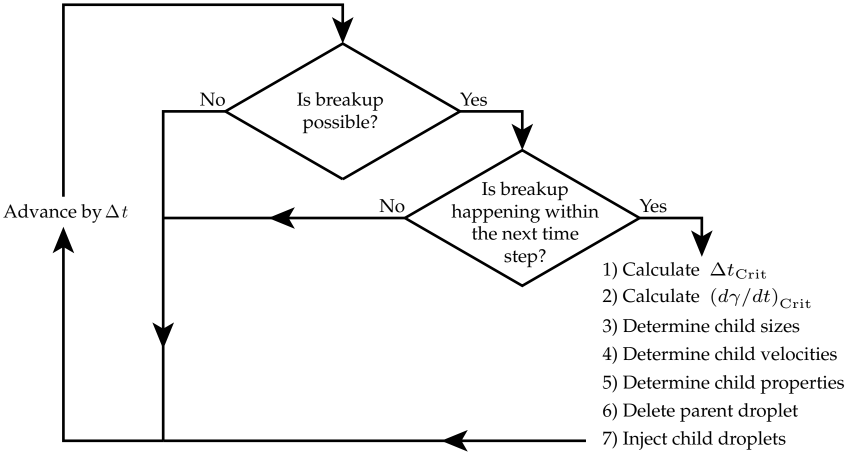

Figure 4.19: A flowchart of the breakup process, where the outer loop indicates each discrete time-step.

4.5.1 Breakup criteria

The breakup criteria is defined in (4.23) and is expressed both in terms of the absolute displacement, x, and the deformation parameter, γ, as defined in Figure 4.13 on page 70.

$$x > C_{\mathrm{b}} \cdot r \qquad \Rightarrow \qquad \gamma > 1 \tag{4.23}$$

In order to determine if a droplet is about to exceed the breakup criteria defined in (4.23) within the next time-step, Δt, the analytical solution to (4.12) on page 71 in its undamped version is used, where the viscous term is neglected, $C_{\mathrm{d}} = 0$. The amplitude of this function is given in (4.24), where the superscript $(...)^{\mathrm{n}}$ indicates the current time-step.

$$A_\gamma = \sqrt{\left(\gamma^{\mathrm{n}} - We_{\mathrm{c}}\right)^2 + \left(\frac{1}{\omega} \cdot \left(\frac{\mathrm{d}\gamma^{\mathrm{n}}}{\mathrm{d}t}\right)\right)^2} \tag{4.24}$$

We_{c} was defined in (4.12) and is the steady-state value of γ as $t \to \infty\,\mathrm{s}$. Therefore, breakup is only possible if (4.25) is satisfied.

$$A_\gamma + We_{\mathrm{c}} > 1 \tag{4.25}$$

If the inequality in (4.25) is satisfied, the time, at which breakup will occur using the undamped version of $\gamma(t)$, is found by solving for the smallest value of t_{BU} in (4.26).

$$\begin{gathered} We_{\mathrm{c}} + A_\gamma \cdot \cos(\omega \cdot t_{\mathrm{BU}} + \phi) = 1 \\ 0 \leq t_{\mathrm{BU}} \\ \text{Where:} \\ \cos(\phi) = \frac{\gamma^{\mathrm{n}} - We_{\mathrm{c}}}{A_\gamma} \quad \text{or} \quad \sin(\phi) = -\frac{\left(\frac{\mathrm{d}\gamma}{\mathrm{d}t}\right)^{\mathrm{n}}}{A_\gamma \cdot \omega} \end{gathered} \tag{4.26}$$

If $t_{\mathrm{BU}} < \Delta t$, breakup will occur within the next time-step. The process is illustrated in Figure 4.20, where both the damped and undamped functions are shown.

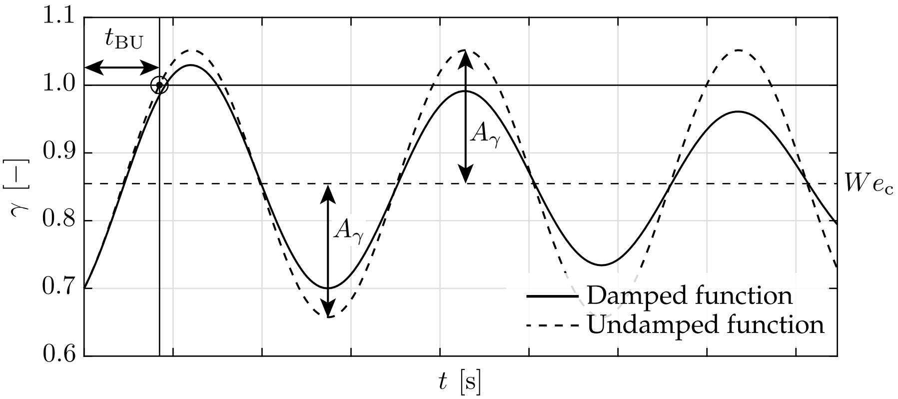

Figure 4.20: The method of evaluating t_{BU} using the undamped function for γ.

As seen in Figure 4.20, t_{BU} is evaluated for the undamped version when $\gamma = 1$. However, as the decay rate is significantly less than that illustrated in Figure 4.20, the difference between the damped and undamped versions is negligible on the short time scale of a few oscillations.

Small droplets have a higher restoring surface tension force relative to larger droplets due to the increase in surface curvature. Therefore, smaller droplets require a greater aerodynamic force to experience breakup, where this tendency is shown in Figure 4.21 on the next page according to the breakup model.

As seen in Figure 4.21, v_{Rel} decreases with diameter for breakup to occur. This tendency is also apparent in the governing differential equation, where aerodynamic forces are inversely proportional to r^2, and surface tension forces are inversely proportional with r^3. Therefore, the relative restoring surface tension force decreases relative to the aerodynamic force with increasing diameter.

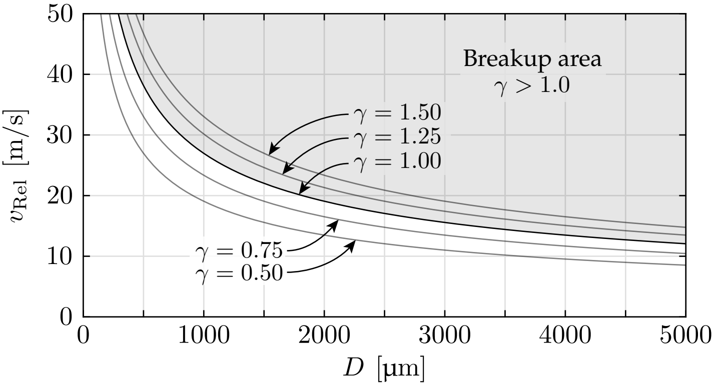

Figure 4.21: The required relative gas velocity, v_{Rel}, for droplets to break up as a function of droplet diameter, D. The analysis is based upon (4.24) and (4.25) assuming initial values of $\gamma = 0$ and $\mathrm{d}\gamma/\mathrm{d}t = 0$.

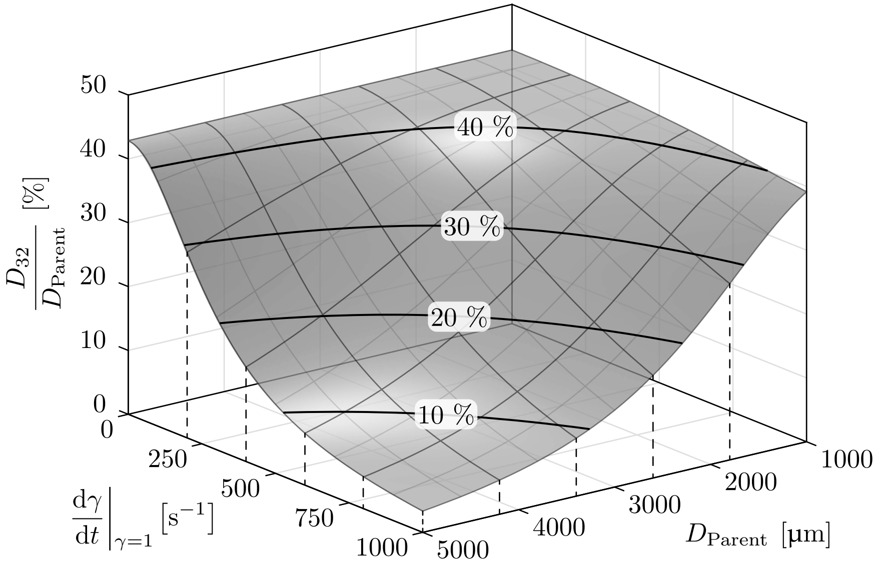

Figure 4.22: The ratio between the child and the parent droplet diameters as defined in (4.27). The solid black lines on the grey surface are contour lines of $(D_{32}/D_{\mathrm{Parent}})$.

4.5.2 Droplet sizes

When breakup occurs, the droplet will shatter into smaller droplets, which are denoted child droplets. The sizes of these are calculated using (4.27), where $K = 10/3$ is a model constant.

$$D_{32} = D_{\mathrm{Parent}} \cdot \left(1 + \frac{2\,K}{5} + \frac{\rho_{\mathrm{l}} \cdot r^3 \cdot \left(\frac{\mathrm{d}\gamma}{\mathrm{d}t}\right)^2}{\sigma_{\mathrm{l}}} \cdot \left(\frac{6\,K - 5}{120}\right)\right)^{-1} \tag{4.27}$$

Figure 4.22 on the previous page shows the relative size of the child droplets, $D_{32}/D_{\mathrm{Parent}}$, based upon (4.27). As seen in the figure, the relative child droplet sizes, $D_{32}/D_{\mathrm{Parent}}$, decreases with both D_{Parent} and $\mathrm{d}\gamma/\mathrm{d}t$. Having determined D_{32}, the child droplet sizes can be randomly sampled using the Rosin-Rammler distribution shown in (4.8) using $N_{\mathrm{RR}} = 3.5$ as the spread parameter [ANSYS Inc. (6)].

4.5.3 Droplet velocities

When breakup occurs, the equator of the spheroid moves with a velocity, which can be calculated using (4.28). A derivation of this term is shown in *Chapter B: Sphericity*.

$$|v_{\mathrm{Normal}}| = C_{\mathrm{v}} \cdot C_{\mathrm{b}} \cdot r \cdot \frac{\mathrm{d}\gamma}{\mathrm{d}t} \tag{4.28}$$

Where $C_{\mathrm{v}} = \sqrt{2}$ and is used to scale the equatorial velocity. The velocity of the child droplets is found by adding the velocity of the parent droplet, $\vec{v}_{\mathrm{Parent}}$, and the equatorial velocity multiplied with a random vector in the null space of $\vec{v}_{\mathrm{Parent}}$. The null space is defined as all vectors orthogonal to $\vec{v}_{\mathrm{Parent}}$. This is illustrated in Figure 4.23, where three child droplets are shown.

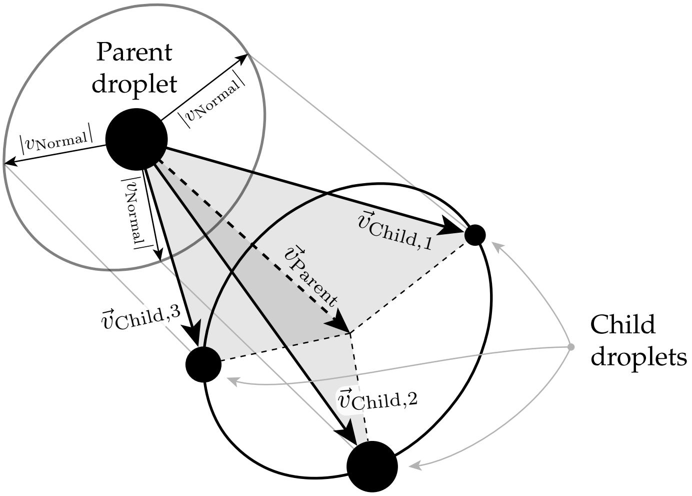

Figure 4.23: The velocity vectors of the child droplets, $\vec{v}_{\mathrm{Child}}$, relative to the parent droplet.

Having determined any null/orthogonal vector relative to $\vec{v}_{\mathrm{Parent}}$, this vector is rotated around $\vec{v}_{\mathrm{Parent}}$ by a random angle, θ. This rotation is carried out using *Rodrigues' rotation formula* [Rodrigues (111)]. The velocity is thus defined as shown in (4.29), where ζ is a uniform random number between 0 and 1.

$$
\begin{aligned}
\theta &= \zeta \cdot 2 \cdot \pi \\
\vec{e} &= \frac{\vec{v}_{\text{Parent}}}{|\vec{v}_{\text{Parent}}|} \\
\vec{n}_{\text{Rot}} &= \vec{n}_{\text{Null}} \cdot \cos(\theta) + (\vec{e} \times \vec{n}_{\text{Null}}) \cdot \sin(\theta) + \vec{e} \cdot (\vec{e} \cdot \vec{n}_{\text{Null}}) \cdot (1 - \cos(\theta)) \\
\vec{v}_{\text{Child}} &= \vec{v}_{\text{Parent}} + \vec{n}_{\text{Rot}} \cdot |v_{\text{Normal}}|
\end{aligned}
\tag{4.29}
$$

The properties of the parent parcel is evenly distributed to the child droplets, such that mass and energy balances are satisfied. Momentum balance is not completely satisfied, but this is assumed to only induce a negligible error.

4.6 Collision

When two droplets collide, the interaction between these can result in a number of different outcomes. They can either bounce off each other, coalesce, or separate after being fully or partially mixed [Ashgriz and Poo (10)], where the three latter phenomena are illustrated in Figure 4.24.

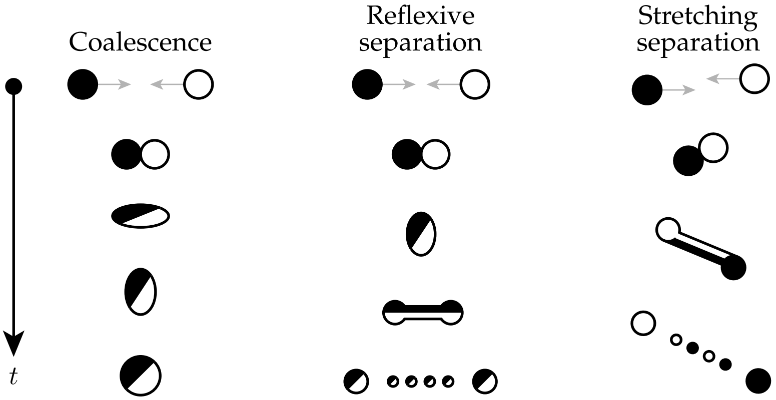

Figure 4.24: The different outcomes of two colliding droplets, where one is coloured black and one white, where the mixed droplets are coloured both black and white. The time axis increases downwards. The figure is based upon [Ko and Ryou (81)].

The collision outcomes shown in Figure 4.24, are droplet-droplet collisions. As the droplets are grouped together in parcels, where, for instance, 1000 droplets are modelled as a single parcel, the droplet-droplet collisions shown in Figure 4.24 cannot be directly applied. Instead, an alternative approach is employed, which is a parcel-parcel collision method, but in order to do so, each parcel must have some artificial volume associated with it. These volumes will be referred to as collision spheres, which are able to interact with each other. This section is divided into five subsections, which are illustrated in Figure 4.25.

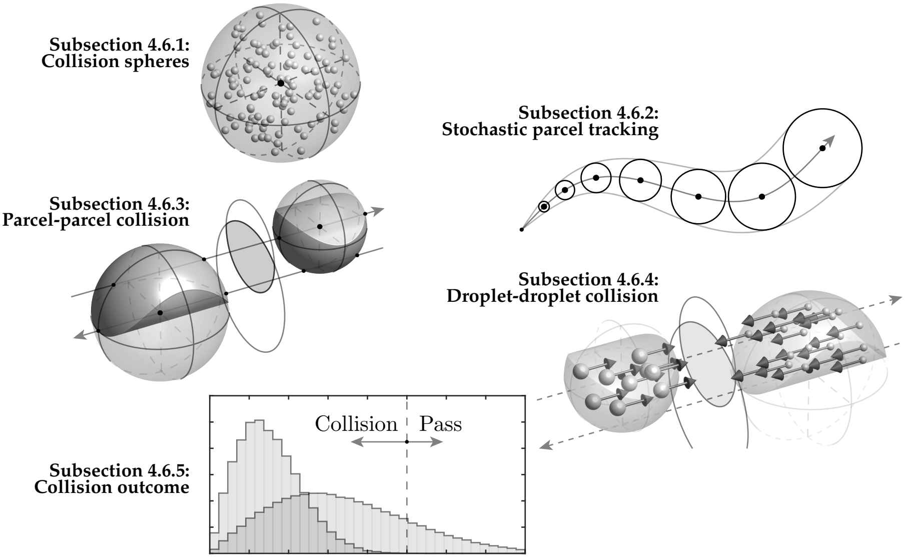

Figure 4.25: An overview of this section, which is divided into five subsections. Notice the difference between parcel-parcel collisions and droplet-droplet collisions.

4.6.1 Collision spheres

If the parcels were modelled as point masses, they would not occupy any volume, so the parcels would not be able to collide with each other. To overcome this, other studies have proposed methods where the probability of collision is calculated within each computational cell [O'Rourke (100)], but this approach is dependent on the mesh size. Therefore, another approach is proposed, where each parcel will have a collision sphere associated with it, where the radius will be referred to as the collision radius, r_c. The subscript $(...)_\mathrm{c}$ will be used throughout this section to indicate properties associated with the colli-

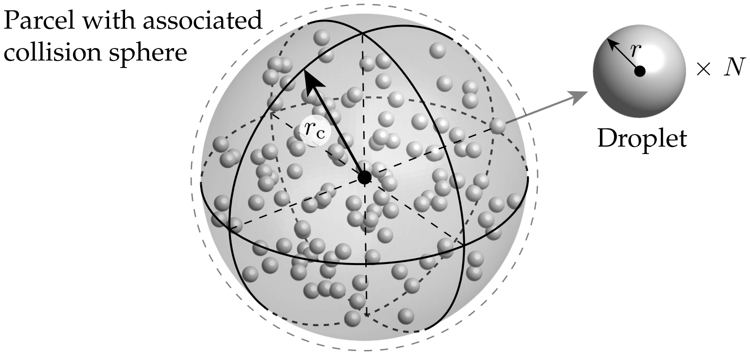

Figure 4.26: The principle of a collision sphere with radius r_c, in which all N identical droplets are located with radius r.

sion spheres or the collision itself. When associating a collision volume to each parcel, the parcels are able to interact with each other and collide, where the outcome can be determined using statistical methods. Each parcel has a total mass and a number of droplets associated with it, and each droplet within the parcel is identical, which is illustrated in Figure 4.26 on the previous page.

The collision radius, r_c, is a function of many parameters, where different existing models can be used to simulate the spread of the droplets within the parcel over time. A statistical method derived from an existing model called the *Discrete Random Walk Model* is used in this study, which is described in the next subsection.

4.6.2 Stochastic parcel tracking

The radius of a collision sphere, r_c, is changing over time, which is an analogy to the spreading of droplets due to turbulent fluctuations. This is illustrated in Figure 4.27.

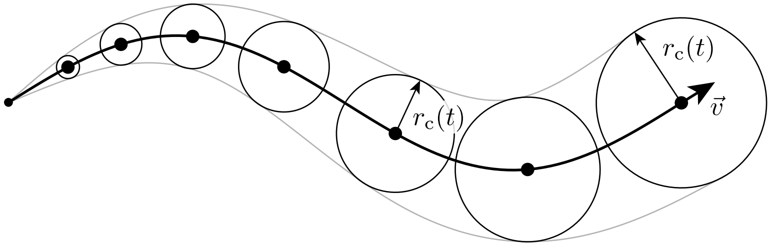

Figure 4.27: The radius of a collision sphere over time, $r_\mathrm{c}(t)$, where the black dots are indicating the position of the parcel as a function of time, which is moving according to the velocity vector, $\vec{v}$.

Various models exist for calculating the droplet dispersion, all of which have their advantages and disadvantages, where the *Discrete Random Walk Model* or *Eddy-lifetime model* is used in this study [Gosman and Loannides (62)]. This model tracks the parcels by adding random velocity components to the mean gas velocity, when integrating the equations of motion shown in (4.14) [ANSYS Inc. (6)], which is shown in (4.30). k_t is the turbulence kinetic energy, $\vec{v}$ is the relative velocity vector, and $\vec{v}'$ is the apparent velocity vector for any droplet.

$$\vec{v}' = \vec{v} + \underbrace{\begin{bmatrix} \zeta_\mathrm{x} \\ \zeta_\mathrm{y} \\ \zeta_\mathrm{z} \end{bmatrix} \cdot \sqrt{\frac{2 \cdot k_\mathrm{t}}{3}}}_{\text{Turbulent velocity fluctuations}} \tag{4.30}$$

Where ζ are normally distributed random numbers. $\vec{v}'$ is sampled repeatedly, and is constant between each sample. The effect of the sampling period is shown in Figure 4.28, where $\vec{v}'$ is sampled with three different rates.

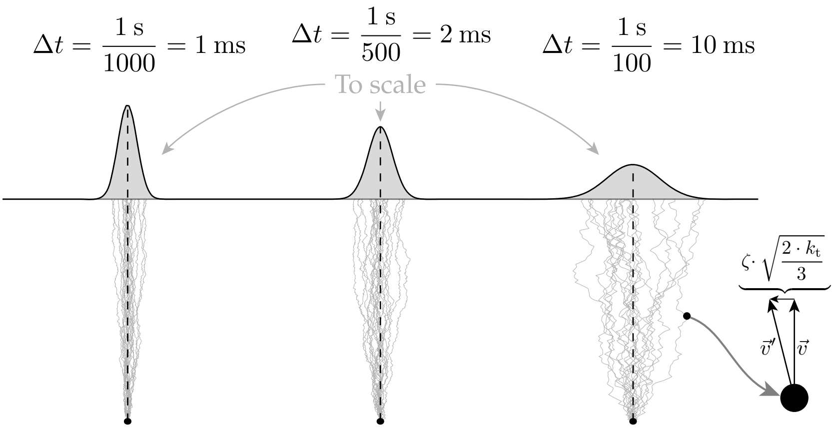

Figure 4.28: Three examples of Brownian motion with varying Δt, where the turbulent kinetic energy is kept constant and the total simulation period is 1 s. The probability density functions are to scale with each other.

The random walks shown in Figure 4.28 are commonly known as *Brownian motion*. As seen in Figure 4.28, the sampling period has a significant effect on the dispersion of the particles. The sampling period should reflect the local eddy lifetime, τ_e, where the *Eddy-lifetime model* calculates this scalar using the local value of turbulent kinetic energy, k_t, and the turbulent dissipation, ϵ_t, which is shown in (4.31).

$$\tau_e = 0.30 \cdot \frac{k_t}{\epsilon_t} \tag{4.31}$$

By applying (4.31) and sampling a new random velocity component with a period of τ_e, the dispersion is correctly captured. However, when sampling at a rate defined by the local flow properties, the time scales will not be similar to those of the solver, Δt, which is used for integrating all the other differential equations. This problem is illustrated in Figure 4.29.

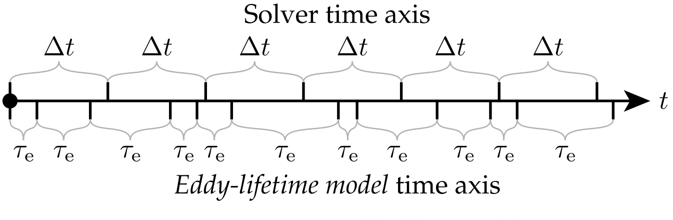

Figure 4.29: When using the *Eddy-lifetime model* the values of τ_e will not be equal to the solver time-step, Δt.

Figure 4.29 illustrates the requirement for two parallel time-axes, which increases the complexity of the model. τ_e is sampled using the local flow properties as defined in (4.31), so this value will constantly change, and will not coincide with the solver time axis, which advances by Δt for each iteration.

The problem can be overcome by integrating the dispersion continuously using the solver time-step, Δt.

Brownian motion can be described using the normal probability density function shown in (4.32), which describes the probability of finding a droplet located a distance, x, from the centre of the parcel.

$$y(x) = \frac{1}{\sqrt{4 \cdot \pi \cdot (D_{\mathrm{ST}} \cdot t)}} \cdot \exp\left(-\frac{x^2}{4 \cdot (D_{\mathrm{ST}} \cdot t)}\right) \tag{4.32}$$

D_{ST} in (4.32) is an analogy to mass diffusivity with units of $\left[\mathrm{m}^2/\mathrm{s}\right]$, where the subscript $(...)_{\mathrm{ST}}$ abbreviates *Stochastic Tracking*. When $t = 0$, the equation states that all particles are located at the same point in space, whereas when $t > 0$ the spread increases. The term in the parenthesis, $(D_{\mathrm{ST}} \cdot t)$, can be integrated continuously, which is shown in (4.33).

$$(D_{\mathrm{ST}} \cdot t) = C_{\mathrm{ST}} \cdot \int_0^t \frac{k_{\mathrm{t}}^2}{\epsilon_{\mathrm{t}}} \, \mathrm{d}t \tag{4.33}$$

Equation (4.33) is easily integrated using simple numerical methods, and the term $(D_{\mathrm{ST}} \cdot t)$ can be substituted into (4.32) to calculate the dispersion. Therefore, there is no need to have two parallel time axes when resolving the droplet dispersion within each parcel.

$C_{\mathrm{ST}} = 0.1$ is a model constant, which was found numerically. This was done by tuning C_{ST} for a given test case until the probability density functions for a numerical case and the continuous version coincide, which is illustrated in Figure 4.30 on the next page.

The top figure shows the probability density function for the continuous model, along with histograms of the numerical test. It can be seen that the histograms and the probability density functions are coinciding, which was achieved by tuning C_{ST} to 0.1. The solid black line goes through the peaks of the probability density functions as a function of time, t, and has also been projected onto the back-plane. The transparent top plane shows some of the sampled trajectories using the *Eddy-lifetime model*, which shows the spreading of the particles due to the random movement.

The example case was carried out using the values shown in the two bottom graphs of Figure 4.30, where the values of k_{t} and ϵ_{t} were varied arbitrarily. The lower graph shows the values of τ_{e}, which is used in the discrete model, and $(D_{\mathrm{ST}} \cdot t)$, which is used in the continuous model, where the latter can be seen to increase with time, which indicates spreading.

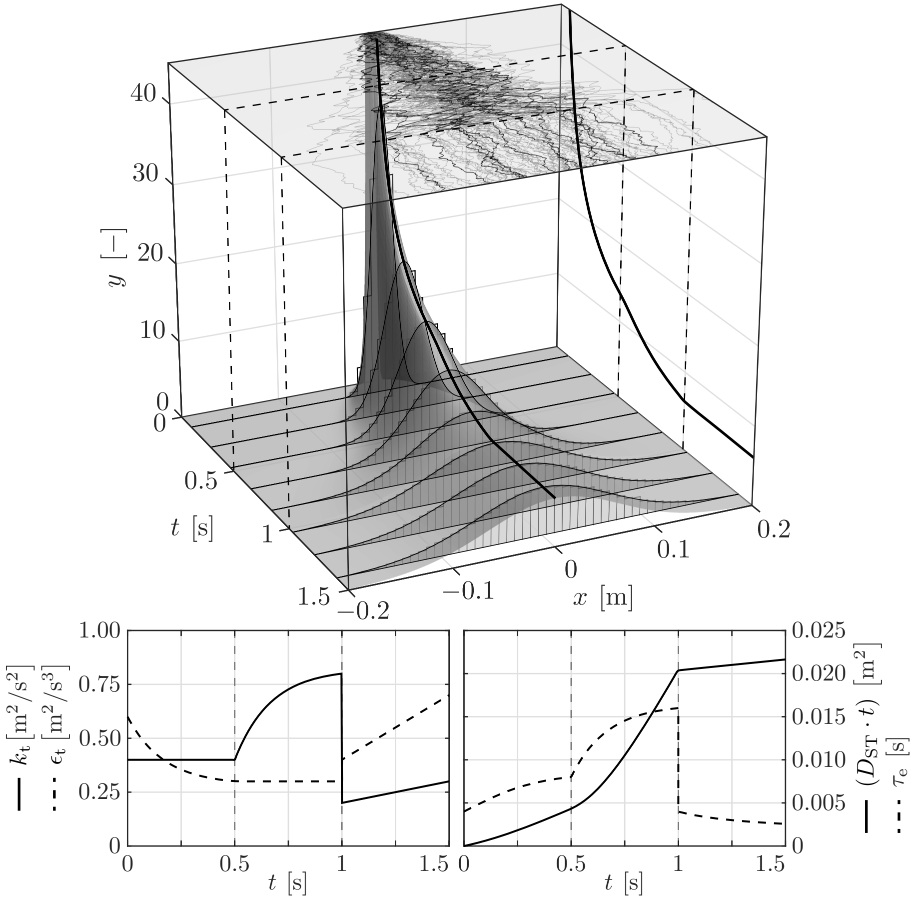

Figure 4.30: The test case used for tuning the continuous Eddy-Lifetime model. The lower left graph shows the inputs, k_{t} and ϵ_{t}, whereas the lower right graph shows the outputs, $(D_{\mathrm{ST}} \cdot t)$ and τ_{e}.

Having modelled the dispersion term, $(D_{\mathrm{ST}} \cdot t)$, the collision radius, r_{c}, can be calculated. This is defined as the radius, where 90 % of the droplets are enclosed, and is calculated using (4.34), which is derived from (4.32) and (4.33).

$$\begin{aligned} \beta &= \int_{-r_{\mathrm{c}}}^{r_{\mathrm{c}}} y(x)\,\mathrm{d}x \\ r_{\mathrm{c}}(D_{\mathrm{ST}} \cdot t) &= \sqrt{(D_{\mathrm{ST}} \cdot t)} \cdot \underbrace{2 \cdot \mathrm{erf}^{-1}\,(1-\beta)}_{=0.178 \text{ when } \beta=90\,\%} \\ V_{\mathrm{c}}(D_{\mathrm{ST}} \cdot t) &= \frac{32 \cdot \pi}{3} \cdot (D_{\mathrm{ST}} \cdot t)^{3/2} \cdot \mathrm{erf}^{-1}\,(1-\beta) \end{aligned} \tag{4.34}$$

The collision radius, r_{c}, and collision volume, V_{c}, are shown in Figure 4.31 as functions of $(D_{\mathrm{ST}} \cdot t)$.

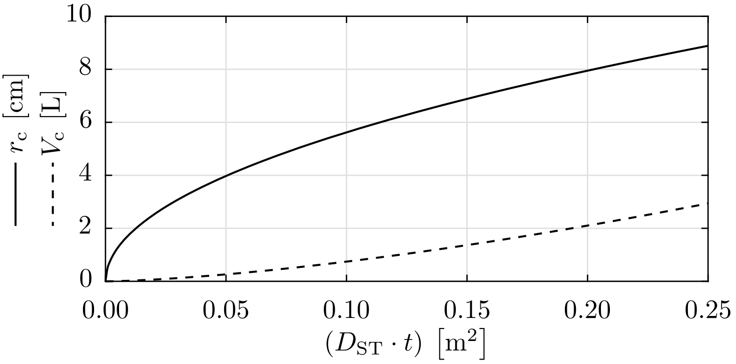

Figure 4.31: The collision radius, r_c, and collision volume, V_c, as functions of $(D_{ST} \cdot t)$.

4.6.3 Parcel-parcel collision

When two parcels get into close proximity to each other, their collision volumes may or may not overlap, which is illustrated in Figure 4.32. Notice that $r_{c,1} \leq r_{c,2}$, which applies throughout this section.

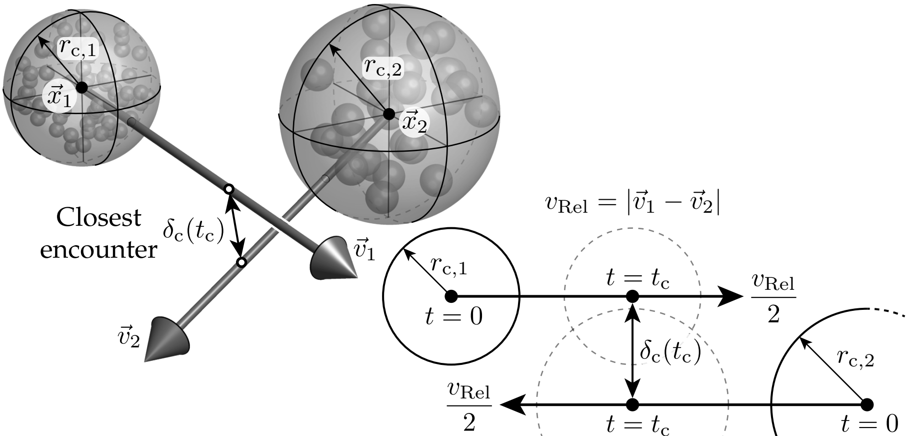

Figure 4.32: Two parcels in 3D space, each with an associated collision volume, coming in close proximity with each other. The closest encounter can be calculated using a 2D representation, which uses the relative velocity and position of the two parcels.

Figure 4.32 shows two parcels, where each contain a finite number of identical droplets, which are enclosed by the collision spheres with radii $r_{c,1}$ and $r_{c,2}$. As the two parcels approach each other, their collision volumes may overlap, which can be determined by using a 2D projection, which is shown in the lower right part of Figure 4.32. The distance between the two parcel centres, $\delta_c(t)$, reaches a minimum after $t = t_c$, which is determined using (4.35).

$$\begin{aligned}\delta_\mathrm{c}(t) &= \left|(\vec{x}_1 + \vec{v}_1 \cdot t) - (\vec{x}_2 + \vec{v}_2 \cdot t)\right| \\ \frac{\mathrm{d}\delta_\mathrm{c}(t)}{\mathrm{d}t} &= 0 \;\;\Rightarrow\;\; t_\mathrm{c} = -\frac{(\vec{x}_1 - \vec{x}_2)^\mathrm{T} \cdot (\vec{v}_1 - \vec{v}_2)}{(\vec{v}_1 - \vec{v}_2)^\mathrm{T} \cdot (\vec{v}_1 - \vec{v}_2)} \end{aligned} \tag{4.35}$$

$$\text{Collision occurs if: } (0 \leq t_\mathrm{c} \leq \Delta t) \text{ and } (\delta_\mathrm{c}(t_\mathrm{c}) \leq r_{\mathrm{c},1} + r_{\mathrm{c},2})$$

During a simulation with, for instance, $50 \cdot 10^3$ parcels, the collision conditions in (4.35) are computationally expensive to evaluate, if all possible collisions were to be investigated [J. G. M. Kuerten (73)]. Therefore, only the three closest parcels are identified using the *k-d tree* algorithm [Friedman et al. (54)], which is efficiently implemented in MATLAB. Equation (4.35) is subsequently only evaluated for these three possible candidates for each parcel.

If the collision conditions in (4.35) are both satisfied, the two collision volumes will overlap, which is illustrated in Figure 4.33.

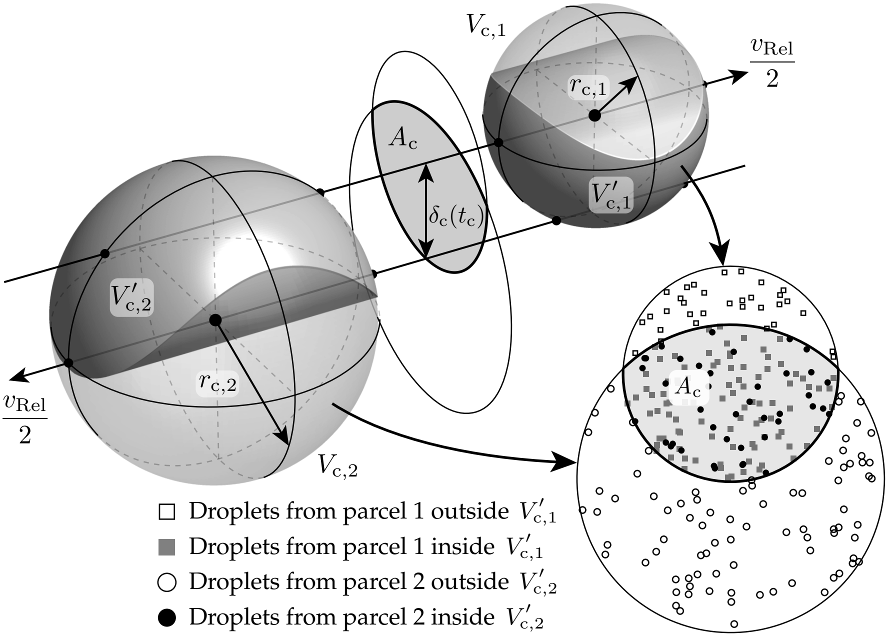

Figure 4.33: An illustration of the swept intersecting volumes of two collision spheres. V_c are the collision volumes, and V'_c are the swept overlapping volumes of the collision spheres. A_c is the intersecting area. Notice that the droplets inside the parcels are omitted in this illustration for visualization purposes.

Figure 4.33 shows two parcels colliding, which contain N_1 and N_2 droplets within their collision spheres respectively. The overlapping volume, as they sweep through one another, is highlighted as the solid regions in the figure, whose volumes are $V'_{\mathrm{c},1}$ and $V'_{\mathrm{c},2}$. The transparent surfaces indicate the collision spheres, whose volumes are $V_{\mathrm{c},1}$ and $V_{\mathrm{c},2}$. The lower right figure indicates the droplets within each parcel when seen in the direction of the collision, where the symbols are defined next to the figure. The overlapping area is denoted A_c, and the separation distance between the two trajectories at the closest encounter is $\delta_\mathrm{c}(t_\mathrm{c})$ as shown in Figure 4.32, where t_c was calculated in (4.35).

The parcel separation at the closest approach is defined in terms of two dimensionless numbers, which are defined in (4.36) and illustrated in Figure 4.34.

$$\phi_\mathrm{c} = \frac{r_{\mathrm{c},1}}{r_{\mathrm{c},2}} \qquad\qquad \Delta_\mathrm{c} = \frac{\delta_\mathrm{c}(t_\mathrm{c})}{r_{\mathrm{c},1} + r_{\mathrm{c},2}} \tag{4.36}$$

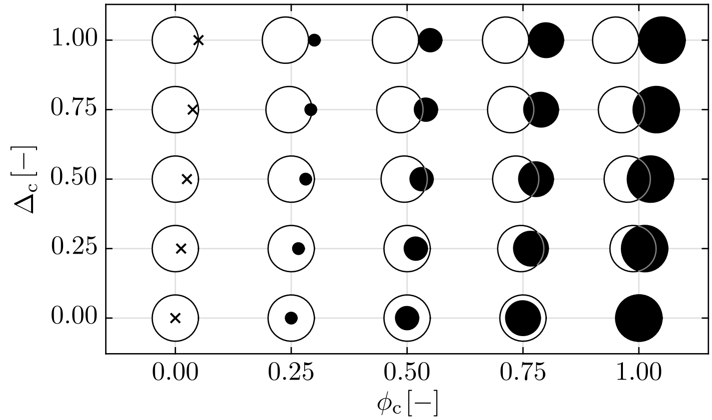

Figure 4.34: A graphical representation of the dimensionless numbers defined in (4.36). The white circles have constant radius, and the radii of the black circles vary with ϕ_c. Δ_c is the dimensionless separation distance.

As seen in Figure 4.34, $\Delta_\mathrm{c} = 0$ indicates that two parcels collide head on, whereas $\Delta_\mathrm{c} = 1$ indicates that they do not intersect and pass next to each other. The intersecting volume fractions, $V'_\mathrm{c}/V_\mathrm{c}$, in Figure 4.33 is found numerically, where the results are shown in Figure 4.35 on the next page as a function of Δ_c and ϕ_c. The upper and lower surfaces show $V'_{\mathrm{c},1}/V_{\mathrm{c},1}$ and $V'_{\mathrm{c},2}/V_{\mathrm{c},2}$ respectively. The dashed line separates the region, where the smaller droplet is completely absorbed by the larger droplet as $V'_{\mathrm{c},1}/V_{\mathrm{c},1} = 1$, which is derived using (4.37).

$$\begin{gathered} \delta_\mathrm{c} + r_{\mathrm{c},1} = r_{\mathrm{c},2} \\ \Downarrow \text{ Use (4.36)} \\ \Delta_\mathrm{c} \leq \frac{1 - \phi_\mathrm{c}}{1 + \phi_\mathrm{c}} \end{gathered} \tag{4.37}$$

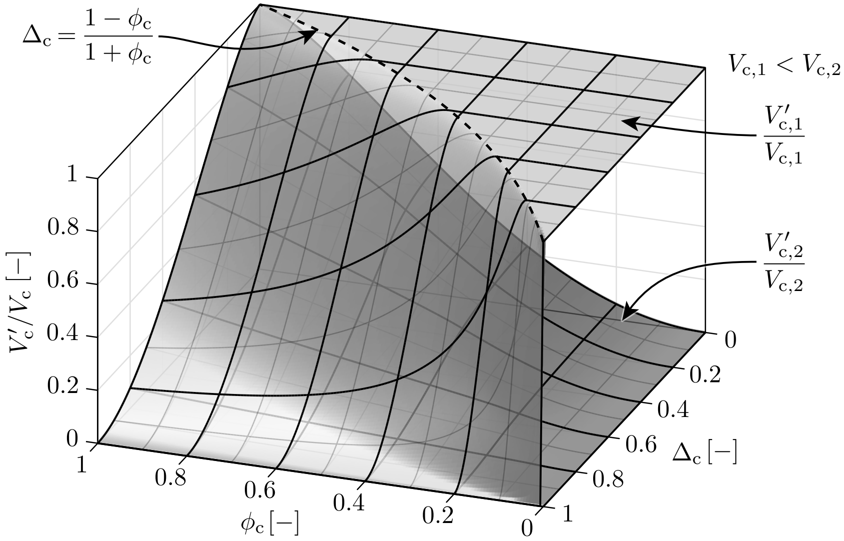

Figure 4.35: The intersecting volume ratios, V'_c/V_c, after two parcels are swept through each other.

When the volume fractions for each collision sphere is calculated, the number of droplets within each parcel under investigation for collision is found using (4.38). The mass of the colliding droplets, m', is also be found using V'_c/V_c as shown in the equation.

$$\begin{aligned} N'_1 &= \frac{V'_{c,1}}{V_{c,1}} \cdot N_1 \qquad & m'_1 &= \frac{V'_{c,1}}{V_{c,1}} \cdot m_1 \\ N'_2 &= \frac{V'_{c,2}}{V_{c,2}} \cdot N_2 \qquad & m'_2 &= \frac{V'_{c,2}}{V_{c,2}} \cdot m_2 \end{aligned} \tag{4.38}$$

The N'_1 and N'_2 droplets are meeting each other over a surface defined by the 2D projection of the sweeping action shown in Figure 4.33. This is further illustrated in Figure 4.36.

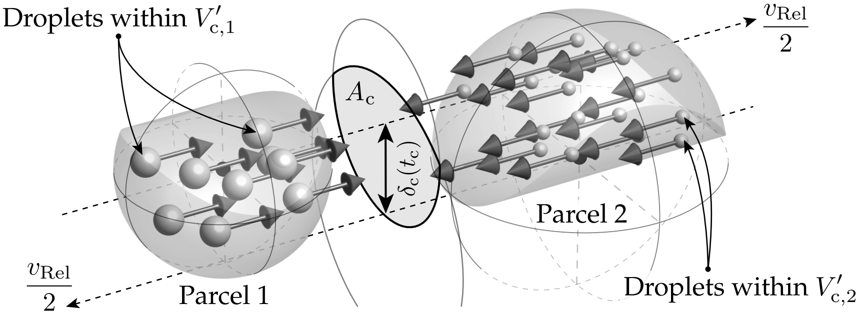

Figure 4.36: An illustration of the swept intersection volumes prior to collision in Figure 4.33, as parcel 2 is located to the right of parcel 1, which was the other way around in Figure 4.33.

As seen in Figure 4.36, the N'_1 and N'_2 droplets within the parcels are highlighted, where the arrows indicate their velocity and direction, which are identical for all droplets within each parcel respectively. Notice that the droplets inside parcel 1 and 2 are different in sizes, as the parcel assumption is that all droplets within a given parcel have common properties such as diameter, temperature, velocity etc.

4.6.4 Droplet-droplet collision

Having identified the droplets, which are located inside the swept intersection volumes for each parcel, N'_1 and N'_2, the probability of collisions between these droplets can be calculated. This is done using the impact Weber number, We, and another dimensionless separation distance, Δ_d, which are defined in (4.39) [Ashgriz and Poo (10)]. The subscript $(...)_\mathrm{d}$ indicates droplet-droplet collision properties.

$$\begin{aligned} \Delta_\mathrm{d} &= \frac{\delta_\mathrm{d}}{r_1 + r_2} \\ We &= \frac{\rho_\mathrm{l} \cdot D_1 \cdot |\vec{v}_1 - \vec{v}_2|^2}{\sigma_\mathrm{l}} \\ D_1 &\leq D_2 \end{aligned} \tag{4.39}$$

Δ_d is defined in a similar manner to the parcel-parcel collision separation distance in (4.36), but Δ_d is the dimensionless separation distance between two individual droplets, where δ_d is the distance between the droplets. r and D are the droplet radii and diameters of the droplets within the parcels, and are not related to the collision spheres. The collision outcome is determined from Figure 4.37 [Ashgriz and Poo (10)].

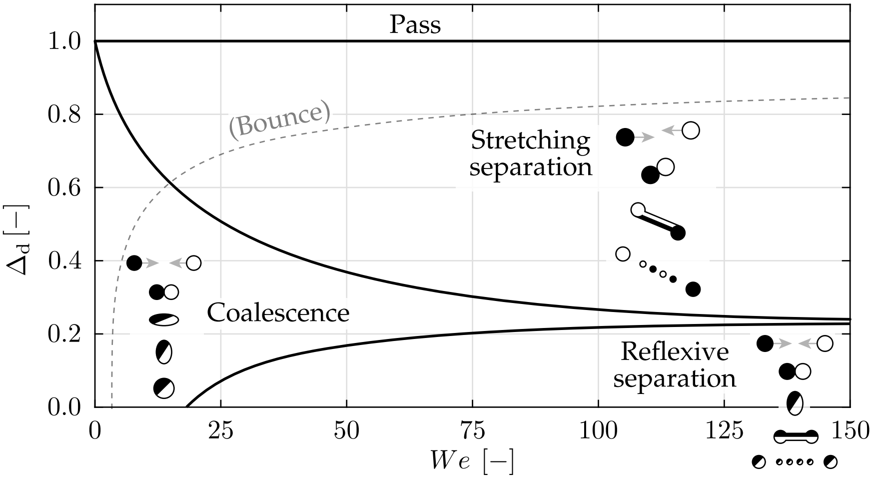

Figure 4.37: The outcome of a droplet collision is determined from the dimensionless separation distance, Δ_d, and the collision Weber number, We [Ashgriz and Poo (10)].

The dashed line in Figure 4.37 indicates a region (Bounce) [Pawar et al. (106)], which was not taken into account in this study, where two droplets bounce off each other. The reason for omitting this region is that [Ashgriz and Poo (10)] did not report this region, which the droplet-droplet collision model is based upon. Notice that when $\Delta_\mathrm{d} > 1$, the droplets are passing each other.

A problem arises when using parcels to define the discrete phase. As a parcel is a collection of a large number of droplets, the outcome of a parcel-parcel collision might consist of all three outcomes shown in Figure 4.37. A new method of dealing with parcel-parcel collisions is therefore proposed in this study. It is assumed that the droplets meeting at the intersection area, A_c, are uniformly distributed, although this is not completely true due to the spherical shape of the collision volumes. The droplet packing densities, ρ_c, describe how tightly the droplets are located, and are calculated using (4.40) for the two colliding parcels.

$$\begin{aligned}\rho_{\mathrm{c},1} &= \frac{N_1'}{A_\mathrm{c}} \\ \rho_{\mathrm{c},2} &= \frac{N_2'}{A_\mathrm{c}}\end{aligned} \tag{4.40}$$

The droplet packing density, ρ_c, is used to calculate the outcomes of the droplet collisions. Figure 4.38 shows the overlapping intersection area from Figure 4.33 with area A_c, where $N_1' = 175$ and $N_2' = 250$ droplets are randomly distributed and are shown as black and grey circles respectively.

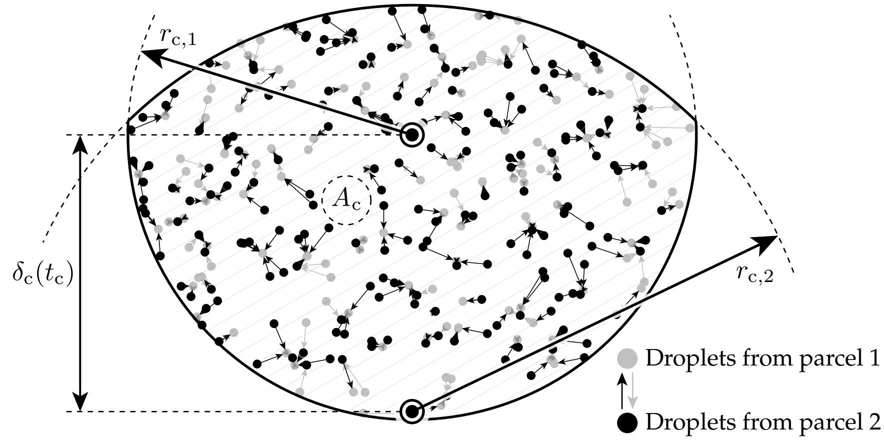

Figure 4.38: The overlapping intersection area for a parcel-parcel collision, where the droplets from the two parcels are shown with the black and grey dots. The small black arrows indicate the closest droplets in parcel 1 for all droplets within parcel 2 - and vice versa for the grey arrows.

Figure 4.38 shows the overlapping area from Figure 4.36, where the droplets from the two parcels are shown with black and grey. The arrows indicate the nearest neighbour for each droplet, where the grey arrows are associated with the grey droplets, and are thus pointing towards the closest black droplets, and vice versa for the black arrows. The nearest neighbours form droplet pairs, which are most likely to take part in droplet-droplet collisions, as they are closest to each other. In order to determine the outcome of each collision/arrow pair, the dimensionless separation distance, Δ_d, is calculated using (4.39), where a histogram of the separation distances is seen in Figure 4.39 for a given example.

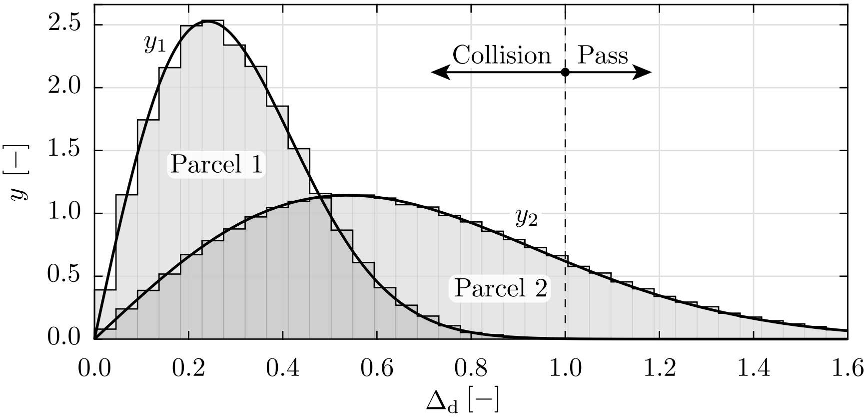

Figure 4.39: Histograms for the dimensionless droplet-droplet separation distance, Δ_d, for two parcels with $\rho_{\mathrm{c},1} = 10^6\,\mathrm{droplets/m^2}$, $D_1 = 800\,\mathrm{\mu m}$, $\rho_{\mathrm{c},2} = 2\cdot 10^5\,\mathrm{droplets/m^2}$ and $D_2 = 2500\,\mathrm{\mu m}$. Two Weibull distributions are fitted to the histograms, y_1 and y_2.

The shaded grey areas are the numerical histograms, whereas the solid thick lines are the fitted Weibull distributions. As seen in Figure 4.39, the values for Δ_d distribute according to a Weibull distribution, which is shown in (4.41), where both the probability and cumulative density functions are shown.

$$\begin{aligned} y(\Delta_\mathrm{d}, \lambda, k_\mathrm{d}) &= \frac{k_\mathrm{d}}{\lambda} \cdot \left(\frac{\Delta_\mathrm{d}}{\lambda}\right)^{k_\mathrm{d}-1} \cdot \exp\left(-\left(\frac{\Delta_\mathrm{d}}{\lambda}\right)^{k_\mathrm{d}}\right) \\ Y(\Delta_\mathrm{d}, \lambda, k_\mathrm{d}) &= 1 - \exp\left(-\left(\frac{\Delta_\mathrm{d}}{\lambda}\right)^{k_\mathrm{d}}\right) \end{aligned} \tag{4.41}$$

The probability, y, and cumulative, Y, density functions are functions of Δ_d, λ, and k_d, where the latter two parameters are shown in (4.42). These correlations were found by carrying out numerical studies and fitting the Weibull distribution to the histograms of Δ_d. Notice that λ_1 is a function of $\rho_{\mathrm{c},2}$ and vice versa for λ_2, as any single droplet from parcel 1 can only collide with the droplets from parcel 2.

$$
\begin{aligned}
k_{\mathrm{d}} &= 2.0 \\
\lambda_1(\rho_{\mathrm{c},2}) &= \frac{0.5636}{\sqrt{\rho_{\mathrm{c},2}} \cdot (r_1 + r_2)} \\
\lambda_2(\rho_{\mathrm{c},1}) &= \frac{0.5636}{\sqrt{\rho_{\mathrm{c},1}} \cdot (r_1 + r_2)}
\end{aligned}
\tag{4.42}
$$

Having determined the probability density functions for the dimensionless distance, Δ_{d}, for each parcel relative to the other parcel, the outcome of the collision can be determined. The critical values for Δ_{d} in Figure 4.37 are interpolated as function of We, where the critical values are denoted $\Delta_{\mathrm{d}}^{\text{RS-Co}}$ and $\Delta_{\mathrm{d}}^{\text{Co-SS}}$, where the superscripts RS, Co, SS, and Pa abbreviates *Reflexive Separation*, *Coalescence*, *Stretching Separation*, and *Pass* respectively. These values are overlaid with y_1 and y_2 from Figure 4.39 in Figure 4.40.

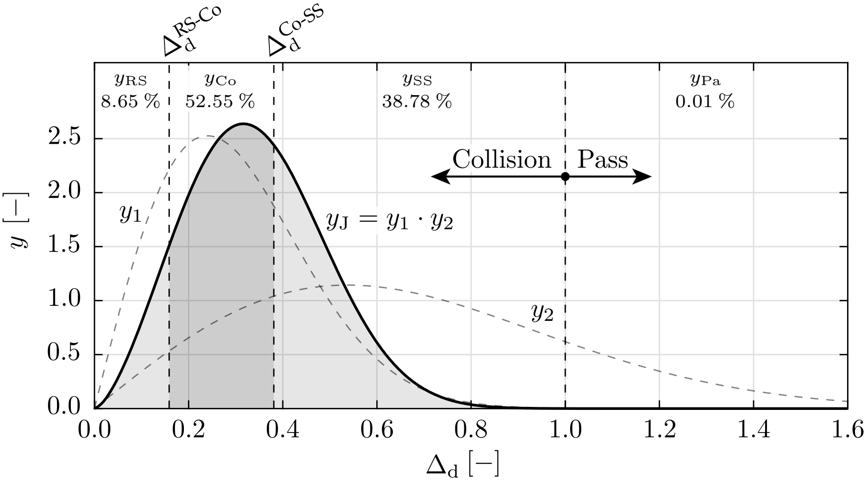

Figure 4.40: The probability density function for both parcels, y_1 and y_2, along with the joint probability, $y_{\mathrm{J}} = y_1 \cdot y_2$, as a function of Δ_{d}. $\Delta_{\mathrm{d}}^{\text{RS-Co}}$ and $\Delta_{\mathrm{d}}^{\text{Co-SS}}$ are interpolated from Figure 4.37 at $We = 44$ for the given example.

The outcome of the collision is the integral of the joint probability between each critical value for Δ_{d}. The joint probability density function is a product of two Weibull distributions, which is evaluated numerically in the model. The joint distribution is shown in (4.43).

$$
\begin{aligned}
y_{\mathrm{J}}(\Delta_{\mathrm{d}}) &= y_1(\Delta_{\mathrm{d}}) \cdot y_2(\Delta_{\mathrm{d}}) \\
Y_{\mathrm{J}}(\Delta_{\mathrm{d}}) &= \int_0^x y_1(x) \cdot y_2(\Delta_{\mathrm{d}}) \, \mathrm{d}x
\end{aligned}
\tag{4.43}
$$

The joint probability density function, y_{J}, is shown with the thick black line in Figure 4.40, where the shaded areas indicate the probability of each type of collision, which are evaluated according to (4.44).

$$
\begin{aligned}
y_{\mathrm{RS}} &= \int_0^{\Delta_{\mathrm{d}}^{\text{RS-Co}}} y_{\mathrm{J}}(\Delta_{\mathrm{d}})\,\mathrm{d}\Delta_{\mathrm{d}} = Y_{\mathrm{J}}(\Delta_{\mathrm{d}}^{\text{RS-Co}}) \\
y_{\mathrm{Co}} &= \int_{\Delta_{\mathrm{d}}^{\text{RS-Co}}}^{\Delta_{\mathrm{d}}^{\text{Co-SS}}} y_{\mathrm{J}}(\Delta_{\mathrm{d}})\,\mathrm{d}\Delta_{\mathrm{d}} = Y_{\mathrm{J}}(\Delta_{\mathrm{d}}^{\text{Co-SS}}) - Y_{\mathrm{J}}(\Delta_{\mathrm{d}}^{\text{RS-Co}}) \\
y_{\mathrm{SS}} &= \int_{\Delta_{\mathrm{d}}^{\text{Co-SS}}}^{1} y_{\mathrm{J}}(\Delta_{\mathrm{d}})\,\mathrm{d}\Delta_{\mathrm{d}} = Y_{\mathrm{J}}(1) - Y_{\mathrm{J}}(\Delta_{\mathrm{d}}^{\text{Co-SS}}) \\
y_{\mathrm{Pa}} &= \int_{1}^{\infty} y_{\mathrm{J}}(\Delta_{\mathrm{d}})\,\mathrm{d}\Delta_{\mathrm{d}} = 1 - Y_{\mathrm{J}}(1)
\end{aligned}
\tag{4.44}
$$

The probabilities in (4.44) were evaluated for the example case in Figure 4.40, and were shown in the upper part of Figure 4.40, where, for example, the probability of coalescence is $y_{\mathrm{Co}} = 52.55\,\%$.

4.6.5 Collision outcome

Having determined the probabilities for each collision type according to (4.44), new parcels are created to reflect the physics of collision. The properties of these new parcels are described in the following four paragraphs.

Reflexive separation

The outcome of a reflexive separation is assumed to be two equal sized droplet, where the parent properties are distributed evenly, which indicates complete mixing during collision. This is shown in (4.45), where $m_{\mathrm{RS},1}$ and $m_{\mathrm{RS},2}$ are the total masses of the two child parcels, and $D_{\mathrm{RS},1}$ and $D_{\mathrm{RS},2}$ are the diameters.

$$
\begin{aligned}
m_{\mathrm{RS},1} = m_{\mathrm{RS},2} &= \frac{(m_1' + m_2') \cdot y_{\mathrm{RS}}}{2} \\
D_{\mathrm{RS},1} = D_{\mathrm{RS},2} &= \frac{\left(D_1^3 + D_2^3\right)^{1/3}}{2}
\end{aligned}
\tag{4.45}
$$

The number of droplets within each of the new parcels after collision are determined using (4.46), which ensures mass balance.

$$
\dot{N}_{\mathrm{i}} = m_{\mathrm{i}} \cdot \left(\frac{4}{3} \cdot \pi \cdot \left(\frac{D_{\mathrm{i}}}{2}\right)^3 \cdot \rho_{\mathrm{l}}\right)^{-1} \tag{4.46}
$$

Coalescence

When two droplets coalesce, the properties after collision are determined by conserving all properties including momentum. This is shown in (4.47).

$$
\begin{aligned}
m_{\mathrm{Co}} &= (m_1' + m_2') \cdot y_{\mathrm{Co}} \\
D_{\mathrm{Co}} &= \left(D_1^3 + D_2^3\right)^{1/3} \\
\vec{v}_{\mathrm{Co}} &= \frac{\vec{v}_1 \cdot m_1' + \vec{v}_2 \cdot m_2'}{m_1' + m_2'}
\end{aligned}
\tag{4.47}
$$

All other properties are simply summed. The number of droplets within the parcel after collision is determined similar to (4.46) in order to ensure mass balance.

Stretching separation

The outcome of a stretching separation is assumed to be two different sized droplets. This is shown in (4.45), where ζ is a random uniform number between 0 and 1, which imposes the stochastic nature of stretching separation collisions.

$$
\begin{aligned}
m_{\mathrm{SS},1} &= (m_1' \cdot \zeta \qquad\;\; + m_2' \cdot (1-\zeta)) \cdot y_{\mathrm{SS}} \\
m_{\mathrm{SS},2} &= (m_1' \cdot (1-\zeta) + m_2' \cdot \zeta) \cdot y_{\mathrm{SS}} \\
D_{\mathrm{SS},1} &= (D_1^3 \cdot \zeta \qquad\;\; + D_2^3 \cdot (1-\zeta))^{1/3} \\
D_{\mathrm{SS},2} &= (D_1^3 \cdot (1-\zeta) + D_2^3 \cdot \zeta)^{1/3}
\end{aligned}
\tag{4.48}
$$

All other conserved properties are distributed according to the same procedure, and the number of droplets within the parcels after collision are determined similar to (4.46) in order to ensure mass balance.

Pass

The droplets, which are passing each other, do not exchange properties, as they are not colliding with any droplets. Therefore, they are simply added to the fractions of the parcels, which are not taking part in the collision.

4.7 Impingement

Upon impact with a solid surface, a droplet will typically deposit some of its mass and shed some smaller droplets into the gas stream again. This phenomenon was studied by [Kuhnke (84)], where the proposed model from this study was chosen for implementation, and is based on experimental studies. This model takes thermal breakup into account, where the surface temperature is significantly greater than the liquid itself. However, this will never be the case for a wet scrubber, so this part of the model is not implemented. This reduces the impingement model, where either complete deposition, or partial deposition along with a splash occurs, which is illustrated in Figure 4.41.

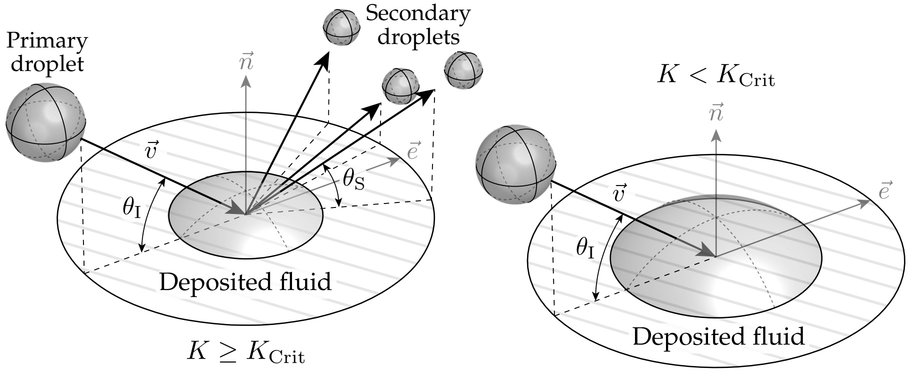

Figure 4.41: The legend associated with this section. When the primary droplet impinge a wall, it will either deposit some fluid and shed secondary droplets back into the domain, or experience complete deposition.

Figure 4.41 shows a droplet impinging a wall with velocity $\vec{v}$ and a normal impact angle of θ_I. The left figure shows partial deposition, where some secondary droplets are shed with a normal angle of θ_S. The right figure shows complete deposition, where no droplets are shed into the scrubber again. $\vec{e}$ is the normal vector along the surface of the wall in the direction of $\vec{v}$. The impingement model uses three dimensionless numbers, which are shown in (4.49).

$$La = \frac{\sigma_\mathrm{l} \cdot \rho_\mathrm{l} \cdot D}{\mu_\mathrm{l}^2} \qquad We = \frac{\rho_\mathrm{l} \cdot (\vec{v} \cdot \vec{n})^2 \cdot D}{\sigma_\mathrm{l}} \qquad K = We^{5/8} \cdot La^{1/8} \tag{4.49}$$

La is the *Laplace number*, which is relating surface tension to viscous forces, and is commonly used to characterize free surfaces in fluid dynamics. The outcome of the impingement is determined using (4.50).

$$\begin{aligned} K_\mathrm{Crit} &= f\left(H_\mathrm{F}/D, La\right) \\ \text{Deposition:} \quad K &< K_\mathrm{Crit} \\ \text{Splash:} \quad K &\geq K_\mathrm{Crit} \end{aligned} \tag{4.50}$$

Where H_F is the wall film height, which is described in detail in *Chapter 5: Eulerian wall films*. The critical value of K, K_Crit, is a function of H_F, D, and La, and can be seen in reference [Kuhnke (84)]. For complete deposition, where $K < K_\mathrm{Crit}$, the droplet will be absorbed by the wall film, and act as a source term for the Eulerian wall film. In case of partial deposition and a splash, where $K \geq K_\mathrm{Crit}$, a fraction of the droplet will be deposited on the wall film, and the remaining mass will be re-injected as secondary droplets. The velocity, diameter, and direction of the secondary droplets are function of D, θ_I, and We, where the reader is referred to [Kuhnke (84)] for the derivation of the different functions and correlations.

4.8 Demister

A demister is present in the top of the absorber section of a wet scrubber. A classical design is a wave-plate demister, where alternating bends force the droplets to hit the surfaces and flow along the demister to the bottom, where the liquid is re-injected into the scrubber again. This ensures that a minimum of water escapes the scrubber, which is most important for closed-loop scrubber operation, where fresh water is generated on-board, which required energy. Therefore, a demister must efficiently separate the droplets, while not induce a high pressure loss, as this decreases the efficiency of the engine.

4.8.1 Collection efficiency

When a parcel hits the demister, most of the liquid will be collected by the demister, whereas a small fraction will pass through and exit the scrubber through the outlet. Numerous model exists for calculating this fraction, where this study uses the model proposed by [Bürkholz (19)], where the demister collection efficiency is calculated using (4.51).

$$
\begin{aligned}
\eta_{\text{Demister}} &= 1 - \left(1 - \eta_{\text{Bend}}\right)^{n_{\text{Bend}}} \\
\eta_{\text{Bend}} &= \min\left(\frac{\rho_{\text{l}}\, v_{\text{g}}\, D^2}{18\, \mu_{\text{g}}\, w_{\text{Demister}}} \cdot \alpha_{\text{Bend}}, 1\right)
\end{aligned}
\tag{4.51}
$$

η_{Demister} is the overall collection efficiency, η_{Bend} is the collection efficiency for a single bend, n_{Bend} is the number of bends, w_{Demister} is the channel width, and α_{Bend} is the bend angle. This is illustrated in Figure 4.42.

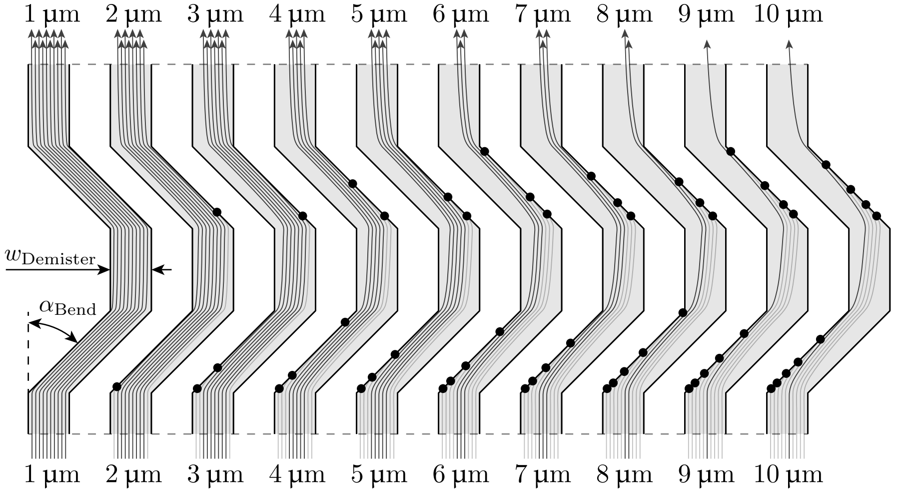

Figure 4.42: An illustration of a wave plate demister, where small droplets pass through, whereas larger droplets do not. The black dots indicate collisions with the walls of the demister.

As seen in the figure, the small droplets pass through the demister, whereas the larger ones do not. The scrubber used to verify the model in *Part II: Verification* uses a demister with $n_{\mathrm{Bend}} = 3$, $\alpha_{\mathrm{Bend}} = 45^\circ$, and $w_{\mathrm{Demister}} = 20\,\mathrm{mm}$.

A large number of droplet sizes are present in the scrubber model, but as the droplets with $D \lesssim 25\,\mu\mathrm{m}$ only exist in very small fractions of the overall mass, these are not resolved. A consequence of this is that by using the droplet diameters within each parcel directly in (4.51), the efficiency would be approximately $100\,\%$, and no water would escape through the demister. Therefore, an alternative approach is used, where it is assumed that each parcel hitting the demister is constructed of different sized droplets, where the Sauter Mean Diameter, D_{32}, is equal to the droplet diameter of the parcel, which was described in *Section 4.2: Parcel injection*. This process is illustrated in Figure 4.43.

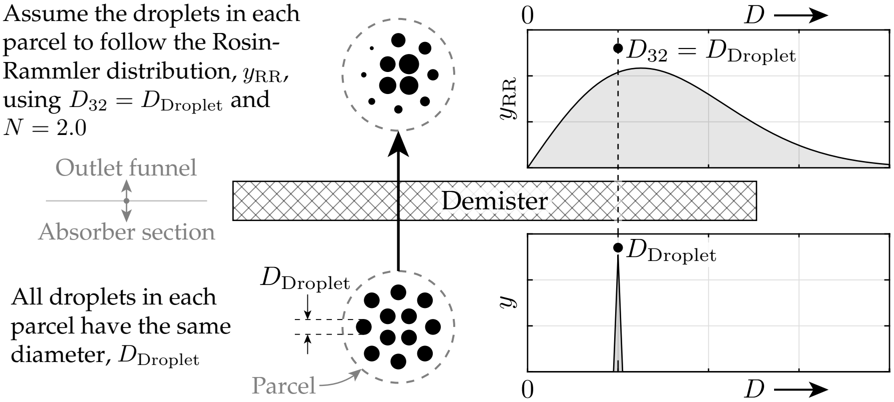

Figure 4.43: When a parcel hits the demister, it is assumed that the droplets within each parcel follow the Rosin-Rammler distribution, y_{RR}, which allows for analytical integration of the demister efficiency.

Figure 4.43 shows the process of assuming the droplet diameters within each parcel to distribute according to the Rosin-Rammler distribution, y_{RR}, which was shown in (4.8) on page 67. This method is used, as droplets with a diameter less than $25\,\mu\mathrm{m}$ are not resolved in the model, as they only represent a small fraction of the overall liquid mass. The lower right graph in Figure 4.43 illustrates the distribution of diameters, where only a single diameter is present in the parcel. As the parcel impact the demister, the distribution is assumed to follow the graph in the upper right part of the figure, where $D_{32} = D_{\mathrm{Droplet}}$ by assumption.

By assuming the droplets to follow the Rosin-Rammler distribution, the probability density function, y_{RR}, can be analytically integrated, which is shown in (4.52).

$$\begin{aligned}\eta_{\text{Parcel}} &= \int_0^{\infty} y_{\text{RR}}(D)\cdot\eta_{\text{Demister}}(D)\,\mathrm{d}D \\ &= 1-\int_0^{D_{\text{Lim}}} y_{\text{RR}}(D)\cdot\left(1-\eta_{\text{Demister}}(D)\right)\,\mathrm{d}D \\ D_{\text{Lim}} &= \sqrt{\frac{18\cdot\mu_{\text{g}}\cdot w_{\text{Demister}}}{\alpha_{\text{Bend}}\cdot\rho_{\text{l}}\cdot v_{\text{g}}}}\end{aligned} \tag{4.52}$$

As seen in (4.52), the collection efficiency for a single parcel, η_{Parcel}, can be evaluated using two different integrals, where the integration limits differ. D_{Lim} is the diameter, at which $\eta_{\text{Bend}} = \eta_{\text{Demister}} = 100\ \%$, which is derived from (4.51). An example is shown in Figure 4.44, where a parcel hits the demister with $D = 40\ \mu\text{m}$, where the gas velocity is $v_{\text{g}} = 5\ \text{m/s}$ and the demister properties are those previously described.

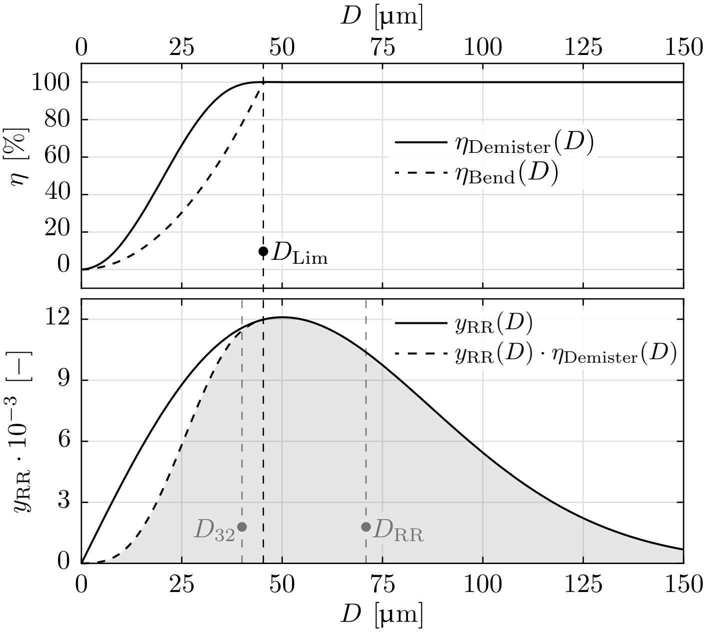

Figure 4.44: The collection efficiencies for a typical demister in the upper figure. The lower figure shows the assumed droplet diameter distribution, where the shaded area is the collected fraction, which is integrated to yield η_{Parcel}.

As seen in Figure 4.44, the collection efficiency is $100\ \%$ when $D \geq D_{\text{Lim}}$. The lower figure shows the assumed droplet diameter distribution, where D_{32} and D_{RR} are shown according to (4.9). In the example shown, $\eta_{\text{Parcel}} = 90.6\%$, which means that 9.4% of the parcel mass passes through the demister and escapes the scrubber through the outlet. The overall collection efficiency, η_{Parcel}, as a function of both D and v_{g} is shown in Figure 4.45.

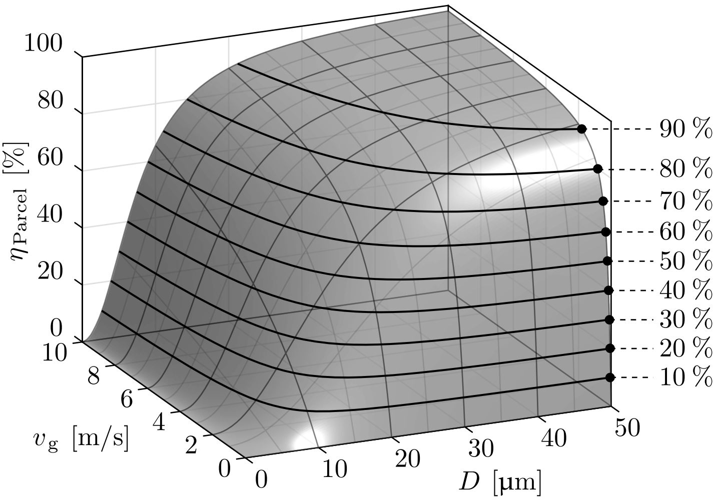

Figure 4.45: The overall collection efficiency, η_{Parcel} in (4.52) as a function of D and v_{g}.

As seen in Figure 4.45, the collection efficiency is, as expected, 0% when $D = 0$. When $D > 50\,\mu\text{m}$ and $v_{\text{g}} > 2\,\text{m/s}$, the collection efficiency is $\eta_{\text{Parcel}} > 90\,\%$, so almost no droplets escape the scrubber. The escaping mass flow is logged in the computational model of the scrubber, and the collected mass flow is mixed and re-injected into the scrubber. A low pass filter is applied to all properties, such that steady-state values can be obtained. The diameters of the re-injected parcels follow the truncated normal distribution shown in (4.5) with a mean diameter of $3000\,\mu\text{m}$ and a span of $1500\,\mu\text{m}$ such that all the diameters are between 1500 and $4500\,\mu\text{m}$.

4.8.2 Pressure loss

The demister will invoke a pressure loss, as the gas has to follow the bends, while the droplets exert forces on the gas. The specific pressure loss is modelled according to *Darcy's law*, which describes the pressure loss over a porous material [Darcy (31)]. The governing equation is shown in (4.53).

$$\begin{aligned} \nabla P &= -\frac{\vec{v}_{\text{g}} \cdot \mu_{\text{g}}}{\kappa_{\text{Demister}}} \\ \kappa_{\text{Demister}} &= \begin{bmatrix} 0.1 & 0 & 0 \\ 0 & 0.1 & 0 \\ 0 & 0 & 1.0 \end{bmatrix} \cdot \widetilde{\kappa}_{\text{Demister}} \end{aligned} \tag{4.53}$$

The pressure loss over the demister is implemented as a momentum source term in the CFD model. Therefore, the geometry of the demister is not resolved, but rather the demister is modelled as a porous zone, where the permeability is κ_{Demister}. The definition of κ_{Demister} in (4.53) has three components, where a low value indicates greater resistance. Therefore, the x and y components are $1/10$ of the z component, as the demister has almost no radial or tangential flow components, where the flow is limited due to the vanes shown in Figure 4.42. The value of the scalar $\widetilde{\kappa}_{\text{Demister}}$ is tuned to match specifications from the demister supplier, where the pressure loss per unit distance is shown in Figure 4.46 [Munters (97)].

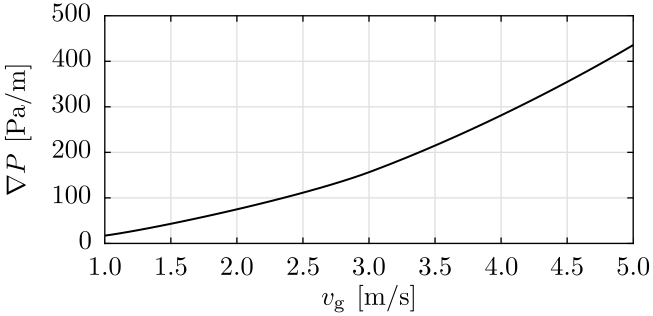

Figure 4.46: The specific pressure loss of the demister [Munters (97)].

4.9 Mass transfer coefficient

The overall mass transfer coefficient for the i^{th} species, $\bar{k}_{\text{i}}$, was shown in (3.9) on page 25, and is repeated in (4.54).

$$\bar{k}_{\text{i}} = \frac{k_{\text{g,i}} \cdot k_{\text{l,i}}}{k_{\text{l,i}} + \dfrac{k_{\text{g,i}}}{K_{\text{H,i}} \cdot R \cdot T}} \tag{4.54}$$

$\bar{k}_{\text{i}}$ is a function of both the inside/liquid and outside/gas mass transfer coefficient, $k_{\text{l,i}}$ and $k_{\text{g,i}}$ respectively, which are described in the following subsections.

4.9.1 External mass transfer coefficient

The external mass transfer coefficient is dependent on the thickness of the boundary layer [Bird et al. (17)]. However, these are not resolved in this study, so correlations are instead used to calculate the mass exchange rates. $k_{\text{g,i}}$ is calculated using three dimensionless numbers, which are shown in (4.55) [Bird et al. (17)].

$$
\begin{aligned}
Re &= \frac{D \cdot v_{\mathrm{Rel}} \cdot \rho_{\mathrm{g}}}{\mu_{\mathrm{g}}} \\
Sc &= \frac{\mu_{\mathrm{g}}}{\rho_{\mathrm{g}} \cdot \mathscr{D}_{\mathrm{g,i}}} \\
Sh &= \frac{k_{\mathrm{g,i}} \cdot D}{\mathscr{D}_{\mathrm{g,i}}} = f\left(Re, Sc\right)
\end{aligned}
\tag{4.55}
$$

Where Sh is the *Sherwood number*, which is a function of the *Reynolds number*, Re, and the *Schmidt number*, Sc, where the correlation from [Frossling (57)] is shown in (4.56), which applies to spheres.

$$
Sh = 2.0 + 0.552 \cdot \sqrt{Re} \cdot Sc^{1/3} \quad , \quad \begin{pmatrix} 2 < Re < 12000 \\ 0.6 < Sc < \ \ 2.7 \end{pmatrix}
\tag{4.56}
$$

Having calculated Sh, the external mass transfer coefficient, $k_{\mathrm{g,i}}$, can be determined using the definition of Sh in (4.55). The gas mass diffusivity, $\mathscr{D}_{\mathrm{g}}$, for the different gas phase species are shown in *Chapter A: Constants and correlations*.

The external mass transfer coefficient can be sufficient in some cases to calculate the flux of species, but this requires the internal mass transfer coefficient to be orders of magnitude greater compared to the external. The *mass transfer Biot number*, Bi_{m}, is the ratio of resistances to mass transfer, and indicates if a lumped assumption is valid [Welty et al. (140)], and is shown in (4.57).

$$
Bi_{\mathrm{m}} = \frac{k_{\mathrm{g,i}} \cdot D}{\mathscr{D}_{\mathrm{l,i}}}
\tag{4.57}
$$

The liquid mass diffusivity, $\mathscr{D}_{\mathrm{l}}$, is typically of the order of $2 \cdot 10^{-9}\,\mathrm{m^2/s}$, and the external mass transfer coefficient is of the order of approximately $0.15\,\mathrm{m/s}$, so for a typical droplet with $D = 1500\,\mu\mathrm{m}$, the value of Bi_{m} in (4.57) is approximately 10^5. This indicates that a droplet cannot be assumed to have a uniform species concentration. However, the Biot analysis assumes that all internal species transfer is due to diffusion, and circulation within the droplet is not considered. Therefore, a correlation for the internal mass transfer coefficient is required, which is described in the next subsection.

4.9.2 Internal mass transfer coefficient

The internal mass transfer coefficient is difficult to determine, as it depends on shape, viscosity, oscillations, velocity, mass diffusivity etc. Therefore, different approaches have been used throughout the literature to approximate the internal mass transfer coefficient, which will be covered in this section.

Mass transfer in a liquid phase is governed by diffusion and convection, which can be modelled by the general transport equation shown in (4.58) [Versteeg and Malalasekera (135)] [ANSYS Inc. (6)].

$$\frac{\partial c_\mathrm{i}}{\partial t} + \overbrace{\nabla \cdot (\vec{v}\, c_\mathrm{i})}^{\substack{\text{Convective}\\ \text{term}}} = \overbrace{-\nabla \cdot \vec{J_\mathrm{i}}}^{\substack{\text{Diffusive}\\ \text{term}}} + \overbrace{S_\mathrm{i}}^{\substack{\text{Source}\\ \text{term}}} \tag{4.58}$$

The units of (4.58) is $\mathrm{mol}/(\mathrm{m}^3 \cdot \mathrm{s})$. The diffusive term in (4.58) is modelled according to *Fick's law of diffusion* [Fick (49)], which is shown in (4.59).

$$\vec{J_\mathrm{i}} = -\left(\mathscr{D}_\mathrm{l,i} + \mathscr{D}_\mathrm{t}\right) \nabla c_\mathrm{i} - \mathscr{D}_\mathrm{T,i} \cdot \frac{\nabla T}{T} \tag{4.59}$$

Where $\vec{J_\mathrm{i}}$ is the diffusion flux vector, $\mathscr{D}_\mathrm{l,i}$ is the mass diffusivity for the i^th species, and $\mathscr{D}_\mathrm{t}$ is the turbulent mass diffusivity. $\mathscr{D}_\mathrm{T,i}$ is the thermal diffusion coefficient, also known as the Soret coefficient, which relates the spatial temperature gradient to species flux. However, this effect is not considered in this project, so $\mathscr{D}_\mathrm{T,i} = 0$.

The turbulent diffusivity, $\mathscr{D}_\mathrm{t}$, is a function of the turbulent viscosity, which is used within CFD analyses. $\mathscr{D}_\mathrm{t}$ can be greater than $\mathscr{D}_\mathrm{l,i}$ for highly turbulent flows [Henschke and Pfennig (68)], so its effect is important for evaluating the internal mass transfer coefficient.

Internal circulation

The fluid inside a droplet circulates due to shear forces at the surface of the droplet, which result in internal vortices. At low Reynold numbers, the vortices resemble *Hill's vortices* [Hill (69)] [Edelmann et al. (41)], where an analytical solution exists for the flow field, which satisfies the Navier-Stokes equations. This solution is derived by applying the *Stokes stream function* [Stokes (123)] while assuming axial symmetry in the flow field, which is shown in spherical coordinates in (4.60).

$$v_\mathrm{r} = \frac{1}{r'^2 \cdot \sin(\theta)} \cdot \frac{\partial \psi}{\partial \theta} \qquad v_\theta = \frac{-1}{r' \cdot \sin(\theta)} \cdot \frac{\partial \psi}{\partial r'} \tag{4.60}$$

The flow field was solved by [Hadamard (63)], where the stream function, ψ, is shown in (4.61). r' is the input argument to the functions, and r is the radius of the droplet.

$$\begin{aligned}
\mu^* &= \mu_\mathrm{l}/\mu_\mathrm{g} \\
\psi_\mathrm{Out}(r',\theta) &= \frac{v_\mathrm{Rel} \cdot r^2 \cdot \sin(\theta)^2}{4} \cdot \left(\left(\frac{\mu^*}{1+\mu^*} \right) \frac{r}{r'} - \left(\frac{2 + 3\,\mu^*}{1+\mu^*} \right) \frac{r'}{r} + 2 \left(\frac{r'}{r} \right)^2 \right) \\
\psi_\mathrm{In}(r',\theta) &= \frac{v_\mathrm{Rel} \cdot r^2 \cdot \sin(\theta)^2}{4} \cdot \left(\left(\frac{1}{1+\mu^*} \right) \left(\frac{r'}{r} \right)^2 \left(1 - \left(\frac{r'}{r} \right)^2 \right) \right) \\
\psi(r',\theta) &= \begin{cases} \psi_\mathrm{Out}(r',\theta) & \text{if} \quad (r' \geq r) \\ \psi_\mathrm{In}(r',\theta) & \text{if} \quad (r' < r) \end{cases}
\end{aligned} \tag{4.61}$$

Where μ^* is the viscosity ratio between the liquid and gas phase, and v_{Rel} is the magnitude of the relative velocity vector, $|\vec{v}_{\mathrm{Rel}}|$. Two different functions apply based upon whether the radial distance, r', is smaller or greater compared to the droplet radius, r. The stream function in (4.61) is visualized in Figure 4.47.

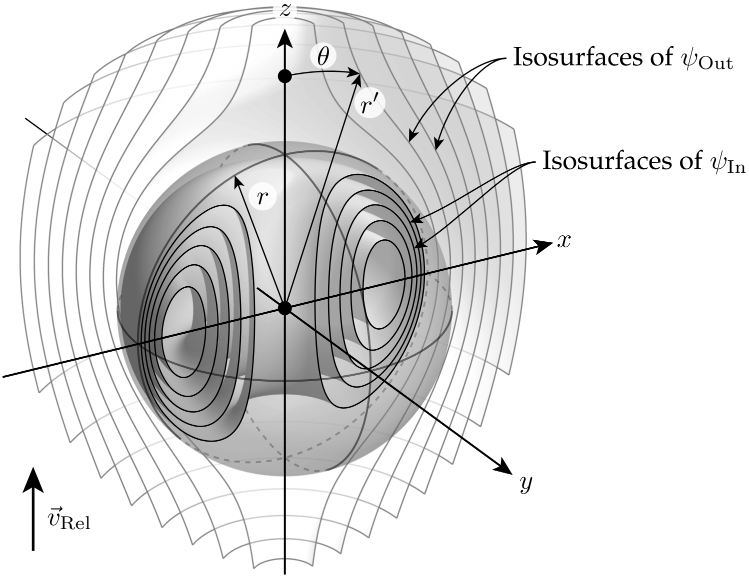

Figure 4.47: A visualization of the internal circulation of a single droplet using the *Stokes stream function*. The isosurfaces are generated using (4.61).

The velocities of the local flow field inside the droplet can be derived from (4.60) and converted to Cartesian coordinates using (4.62), where the coordinate system is shown in Figure 4.47.

$$\begin{aligned}
v_{\mathrm{x}}(r',\theta) &= \left(v_{\mathrm{r}}\frac{\partial x}{\partial r'} + v_\theta \frac{\partial x}{\partial \theta}\right) \cdot \cos(\phi) \\
v_{\mathrm{y}}(r',\theta) &= \left(v_{\mathrm{r}}\frac{\partial x}{\partial r'} + v_\theta \frac{\partial x}{\partial \theta}\right) \cdot \sin(\phi) \\
v_{\mathrm{z}}(r',\theta) &= \left(v_{\mathrm{r}}\frac{\partial z}{\partial r'} + v_\theta \frac{\partial z}{\partial \theta}\right)
\end{aligned} \tag{4.62}$$

The internal flow is idealized and will in reality be turbulent due to oscillations and velocity shear. However, the flow field can be used to derive analytical approximations to the internal mass transfer coefficient, which can be tuned to match experimental data. Different analytical solutions exist, where a brief overview is given in the following subsections. In order to compare the different methods, the *Fourier number*, Fo, and a dimensionless concentration, $\eta(t)$, are introduced, which are shown in (4.63).

$$Fo(t) = \frac{\mathscr{D}_{\mathrm{l,i}} \cdot t}{r^2} \qquad \eta(t) = \frac{c_{\mathrm{l,i}}(t) - c_{\mathrm{l,i}}(0)}{c_{\mathrm{l,i}}^{\mathrm{Eq}} - c_{\mathrm{l,i}}(0)} \tag{4.63}$$

Where $c_{\mathrm{l,i}}^{\mathrm{Eq}} = c_{\mathrm{g,i}} \cdot (K_{\mathrm{H,i}} \cdot R \cdot T) = c_{\mathrm{l,i}}(t \to \infty\,\mathrm{s})$, and is the concentration of the liquid, when it is in equilibrium with the continuous phase, which has a concentration of $c_{\mathrm{g,i}}$.

Spherical shell assumption

Reference [Newman (98)] investigated the internal mass transfer coefficient of spheres, where the species transport was governed by diffusion. The internal circulation shown in Figure 4.47 was ignored, and the radial species concentration was calculated by combining a finite number of spherical shells, which are illustrated in Figure 4.48.

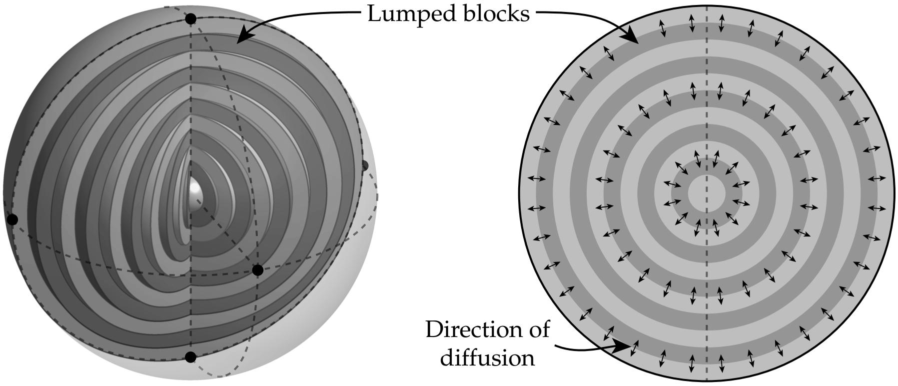

Figure 4.48: The approach used in [Newman (98)], where n spherical lumped shells are used to calculate the radial concentration over time.

As seen in Figure 4.48, the sphere is divided into n spherical shells, where each of these are assumed lumped. By assuming zero resistance to mass transfer in the continuous phase, the outermost shell will have a constant concentration of $c_{\mathrm{l,i}}^{\mathrm{Eq}}$. Using this assumption, the overall concentration within the droplet, $c_{\mathrm{l,i}}(t)$, can be modelled according to (4.64) [Newman (98)], where the driving force is the radial concentration gradient, which was indicated by the small arrows in Figure 4.48.

$$\eta_{\mathrm{Shell}}(Fo) = 1 - \frac{6}{\pi^2} \sum_{\mathrm{n=1}}^{\infty} \frac{1}{n^2} \exp\Big(- (n \cdot \pi)^2 \cdot Fo \Big) \tag{4.64}$$

Equation (4.64) can be simplified to (4.65), which introduces a maximum error of $0.1\,\%$, but does not required an infinite sum to be evaluated [Henschke and Pfennig (68)].

$$\eta_{\text{Shell}}(Fo) \approx \begin{cases} 1 - 6 \cdot \sqrt{\frac{Fo}{\pi}} + 3 \cdot Fo & \text{if} \quad (Fo \leq 0.15) \\ \frac{6}{\pi^2} \cdot \exp\left(-\pi^2 \cdot Fo\right) & \text{if} \quad (Fo > 0.15) \end{cases} \tag{4.65}$$

Fo in (4.63) was defined based on the liquid mass diffusivity, $\mathscr{D}_{\text{l,i}}$, and does therefore not take turbulent mixing into account, which implies $\mathscr{D}_{\text{t}} = 0$. Reference [Henschke and Pfennig (68)] proposed a term for modelling the turbulent diffusivity, $\mathscr{D}_{\text{t}}$, which is shown in (4.66).

$$\begin{aligned} Fo_{\text{t}}(t) &= \frac{(\mathscr{D}_{\text{l,i}} + \mathscr{D}_{\text{t}}) \cdot t}{r^2} \\ \mathscr{D}_{\text{t}} &= \frac{v_{\text{Rel}} \cdot D}{C_{\text{IP}} \cdot (1 + \mu^*)} \end{aligned} \tag{4.66}$$

C_{IP} is an instability constant, which defines the turbulent mixing between any two lumped shells, and Fo_{t} is the associated turbulent Fourier number. It should be noted that $\mathscr{D}_{\text{t}}$ increases with decreasing C_{IP}. The method described is based upon the spherical shell assumption, and does not take the internal circulation into account, which was shown in Figure 4.47.

Lumped flow assumption

The flow field calculated using the stream function shown in (4.61) was used by [Kronig and Brink (83)] to derive an analytical expression of mass absorption. The spherical shells in Figure 4.48 are replaced by lumped masses, which are separated by the streamlines in Figure 4.47. This is visualized in Figure 4.49.

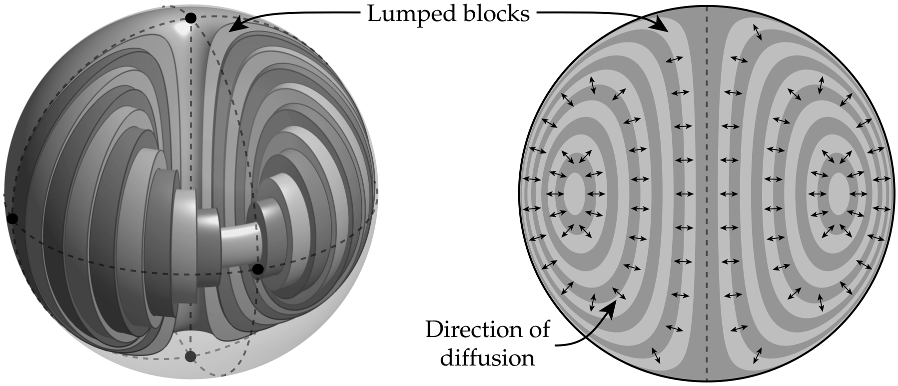

Figure 4.49: The approach used by [Kronig and Brink (83)], where n lumped masses are separated by the streamlines derived using (4.61).

Each alternating shaded block in Figure 4.49 is assumed lumped, and thus to have uniform properties. By again assuming zero resistance to mass transfer in the continuous phase, the outermost block has a constant concentration of

$c_{\mathrm{l,i}}^{\mathrm{Eq}}$. An analytical expression was derived by [Kronig and Brink (83)], which is shown in (4.67), where the driving force is the concentration gradient normal to the streamlines, which was shown by the arrows in Figure 4.49.

$$\begin{aligned} \eta_{\mathrm{Flow}}(Fo) &= 1 - \frac{3}{8}\sum_{\mathrm{n}=1}^{\infty} A_{\mathrm{n}}^{2} \cdot \exp\left(-\lambda_{\mathrm{n}} \cdot 16 \cdot Fo\right) \\ A = [1.32, 0.73, \ldots] &\qquad \lambda = [1.678, 9.83, \ldots] \end{aligned} \tag{4.67}$$

$\eta_{\mathrm{Flow}}(Fo)$ in (4.67) is derived by solving an eigenvalue problem, where the first two eigenvalues are shown in the equation.

Comparison between the shell model and the flow model

$\eta_{\mathrm{Shell}}(Fo)$ will be referred to as the *shell model*, and $\eta_{\mathrm{Flow}}(Fo)$ will be referred to as the *flow model*, where analytical expressions were given to these in (4.64) and (4.67) respectively. The spherical shell and flow models both assume infinitely fast mixing, as each block was assumed lumped, which means that the transient dynamics are not taken into account. This is illustrated in Figure 4.50, where $\eta_{\mathrm{Shell}}(Fo)$ and $\eta_{\mathrm{Flow}}(Fo)$ are shown as well, where $\eta_{\mathrm{Flow}}(Fo)$ can be seen to increase more rapidly compared to $\eta_{\mathrm{Shell}}(Fo)$.

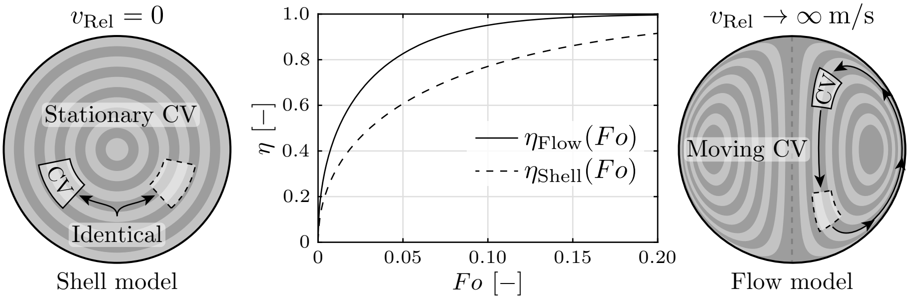

Figure 4.50: The two extrema where $v_{\mathrm{Rel}} = 0$ and $v_{\mathrm{Rel}} \to \infty$ m/s. $\eta_{\mathrm{Flow}}(Fo)$ and $\eta_{\mathrm{Shell}}(Fo)$ are shown in the middle figure.

The spherical shell model is analogous to $v_{\mathrm{Rel}} = 0$, as no internal circulation exists in this case, and mass diffuses into the droplet in the radial direction only. This means that any control volume, CV, will remain stationary, and is not moving over time. Only the concentration of the control volume will change, so a control volume rotated around the centre will be indistinguishable from the other.

The flow model is analogous to $v_{\mathrm{Rel}} \to \infty$m/s, as each lumped block separated by the streamlines is completely mixed. This can be in interpreted by considering a control volume, which will move infinitely fast along the streamlines. Therefore, the dashed control volume to the right in Figure 4.50 is also indistinguishable from the other.

The reason why $\eta_{\text{Flow}}(Fo)$ increases more rapidly compared to $\eta_{\text{Shell}}(Fo)$ is that the apparent internal surface area, over which diffusion acts to transfer species, are different for the two models. This is illustrated in Figure 4.51.

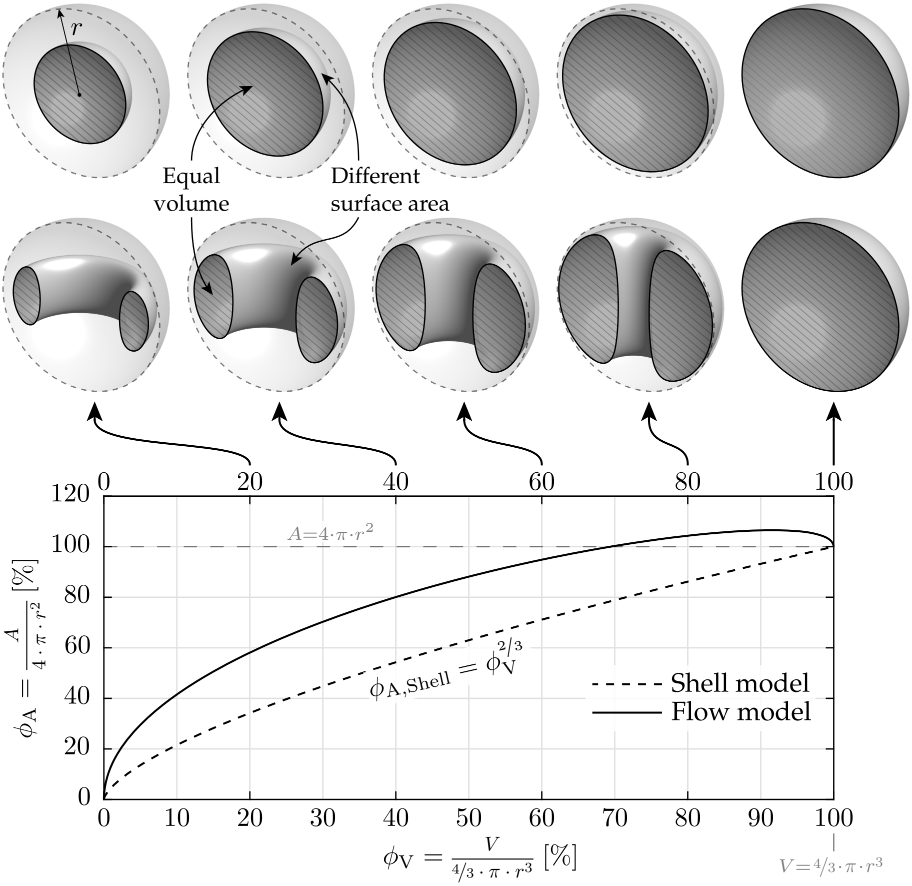

Figure 4.51: A comparison between the internal surface area as a function of the encapsulated volume fraction, where both the shell and flow models are normalized to the area and volume of a sphere. The figures above the graph show graphical comparisons between the two models at specified values for ϕ_{V}, where the upper and lower rows are the shell and flow models respectively.

As seen in Figure 4.51, the surface area compared to a sphere, ϕ_{A}, is plotted as a function of the encapsulated volume compared to that of a sphere, ϕ_{V}. The shell model can be showed to increase with $\phi_{\text{A,Shell}} = \phi_{\text{V}}^{2/3}$, and will never exceed $\phi_{\text{A}} > 100\ \%$. An interesting tendency can be seen for the flow model, which does exceed $\phi_{\text{A}} > 100\ \%$. This occurs at approximately $\phi_{\text{V}} > 70\ \%$, where the surface area exceeds that of a sphere with radius r. Generally, the surface area is greater for the flow model compared to the shell model, which is the reason for $\eta_{\text{Flow}}(Fo)$ to increase more rapidly compared to $\eta_{\text{Shell}}(Fo)$.

Between the two extrema, $v_{\text{Rel}} = 0$ and $v_{\text{Rel}} \to \infty$ m/s, a regime exists, where the transient effects affect the concentration profile as a function of time, $\eta(Fo)$. This is investigated in the next subsection.

Proposed transient model

In order to resolve the transient tendencies for mass absorption, a computational model is required, where the governing transport equation can be solved on a mesh. However, special care must be taken, as mesh induced diffusion / false diffusion can invalidate the results [Versteeg and Malalasekera (135)], which is a result of the flow field not being aligned with the mesh. Therefore, the mesh is constructed by using the streamlines in Figure 4.47 in combination with the velocity potential, which is perpendicular to the streamlines. The required functions are shown in (4.68), where, again, r' is the input argument to the functions and r is the radius of the droplet.

$$\begin{aligned} \xi(r',\theta) &= 4 \cdot \left({}^{r'}\!/_{r}\right)^2 \cdot \left(1 - \left({}^{r'}\!/_{r}\right)^2\right) \cdot \sin(\theta)^2 \\ \beta(r',\theta) &= \frac{\left({}^{r'}\!/_{r}\right)^4 \cdot \cos(\theta)^4}{2 \cdot \left({}^{r'}\!/_{r}\right)^2 - 1} \end{aligned} \tag{4.68}$$

The two functions are plotted using contour lines in Figure 4.52 on the next page, where the intersections define the mesh nodes, which makes a conformal mesh, where ξ and β are orthogonal. The conformal mesh ensures that no flow exist in the directions of changing ξ, so no false diffusion will exist in the solution. The volume of each cell is calculated by revolving the cell around the z-axis, and a total of 7500 cells were used in the transient model.

The species transport inside a droplet is governed by both diffusion and convection, which can be solved using the general transport equation, which was defined in (4.58) on page 105. The *Finite Volume Method* is used to solve this equation, where an upwind scheme was used to resolve the convective term, a linear first-order scheme was used to resolve the diffusive term, and the temporal integration was carried out using an implicit method. An example is shown in Figure 4.53 on the next page, where the initial concentration of a given species starts at a point and spreads out due to convection and diffusion. This numerical model will be referred to as the *transient model*, where the subscript $(...)_{\text{Trans}}$ applies.

The transient model was verified against the analytical solutions of the shell and flow models previously described, and the results were identical. The advantage of the transient model is that the temporal effects are taken into account, whereas the analytical shell and flow models do not.

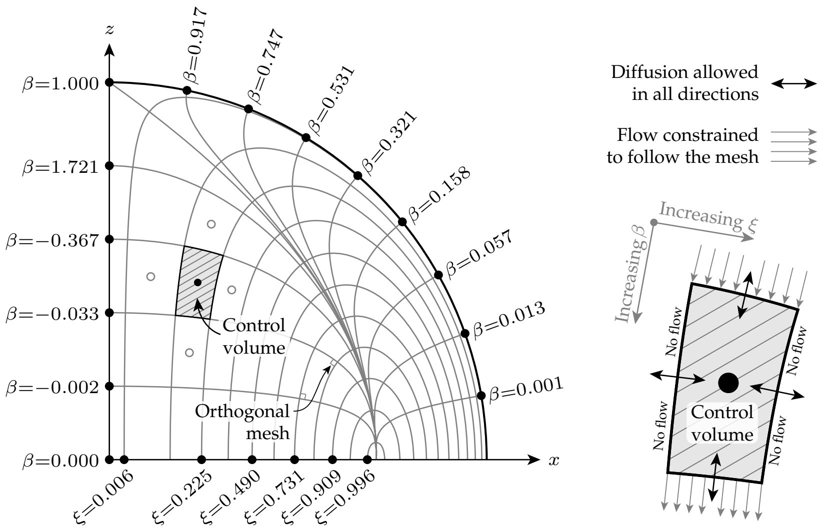

Figure 4.52: A mesh with no false diffusion can be generated by exploiting the streamlines of the ideal flow solution. β and ξ were shown in (4.68), and are orthogonal to each other.

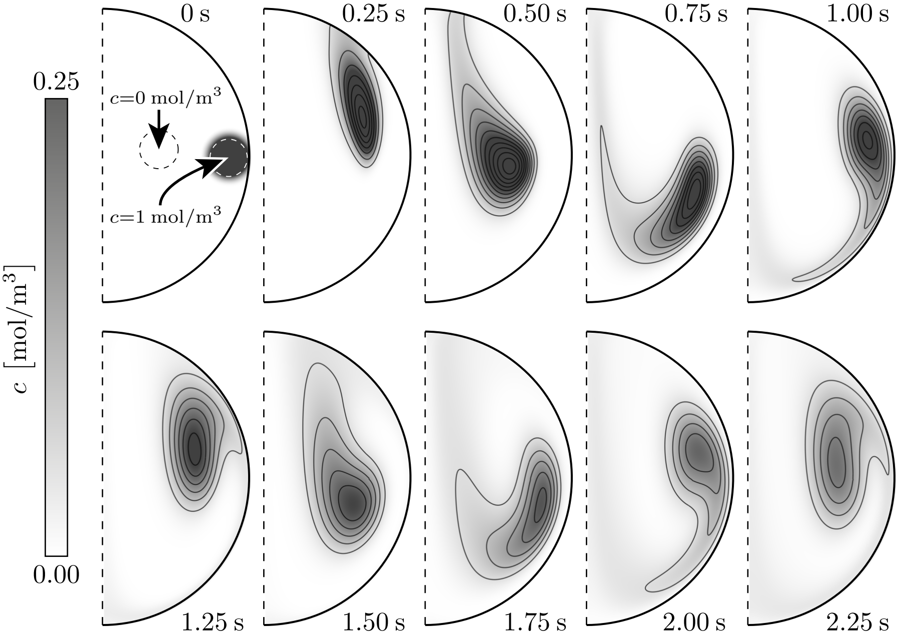

Figure 4.53: An example of the transient model. The initial concentration of a given species is a point, as shown in the upper left part of the figure, where $t = 0$. As time advances, both convective and diffusive phenomena spread out the species.

In order to compare the transient model against the shell and flows models, the resistance to mass transfer in the continuous phase is again assumed to be zero, so the outermost cells in the transient model are assigned a constant concentration of $c_{1,\mathrm{i}}^{\mathrm{Eq}}$. The overall absorption over time is defined in (4.69), where i is the i^{th} mesh cell in the transient model.

$$\eta_{\mathrm{Trans}}(Fo, Pe, \mu^*) = \frac{\sum_{\mathrm{i}} n_{\mathrm{i}}(Fo)}{\sum_{\mathrm{i}} V_{\mathrm{i}}} = \frac{\sum_{\mathrm{i}} n_{\mathrm{i}}(Fo)}{{}^4\!/_3 \cdot \pi \cdot r^3} \tag{4.69}$$

It was found that $\eta_{\mathrm{Trans}}(Fo, Pe, \mu^*)$ was a function of the *Fourier number*, Fo, the viscosity ratio, μ^*, and the *Peclet number*, Pe where the latter is defined in (4.70).

$$Pe = \frac{D \cdot v_{\mathrm{Rel}}}{\mathscr{D}_1} = Re \cdot Sc \tag{4.70}$$

$\eta_{\mathrm{Trans}}(Fo, Pe, \mu^*)$ is shown in Figure 4.54 for varying values of Pe and with a constant value for $\mu^* = 50$, where $\eta_{\mathrm{Shell}}(Fo)$ and $\eta_{\mathrm{Flow}}(Fo)$ are shown as well.

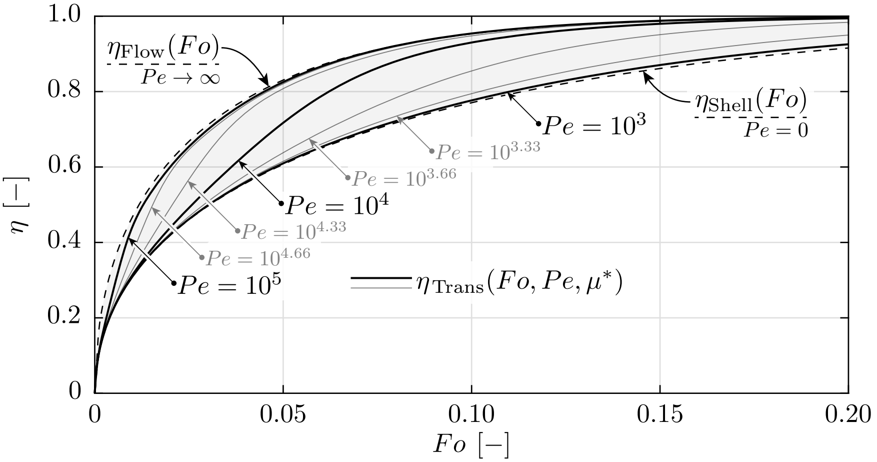

Figure 4.54: Example of $\eta_{\mathrm{Trans}}(Fo, Pe, \mu^*)$ for different values of Pe with a constant viscosity ratio of $\mu^* = 50$. The dashed lines are indicating $\eta_{\mathrm{Shell}}(Fo)$ and $\eta_{\mathrm{Flow}}(Fo)$, which corresponds to $Pe = 0$ and $Pe \to \infty$ respectively. $\eta_{\mathrm{Trans}}(Fo, Pe, \mu^*)$ lies in-between these curves as seen in the figure, which is shown with the shaded area.

Figure 4.54 shows $\eta_{\mathrm{Trans}}(Fo, Pe, \mu^*)$ for different values of Pe, where these can be seen to be bound between $\eta_{\mathrm{Shell}}(Fo)$ and $\eta_{\mathrm{Flow}}(Fo)$, where the latter two are shown with the dashed lines. This is stated in (4.71).

$$\begin{aligned} \lim_{Pe \to \infty} \eta_{\mathrm{Trans}}(Fo, Pe, \mu^*) &\to \eta_{\mathrm{Flow}}(Fo) \\ \lim_{Pe \to 0} \eta_{\mathrm{Trans}}(Fo, Pe, \mu^*) &\to \eta_{\mathrm{Shell}}(Fo) \end{aligned} \tag{4.71}$$

$\eta_{\mathrm{Trans}}(Fo, Pe, \mu^*)$ can be used to model the species absorption for a droplet with internal circulation, where the transient tendencies are taken into account. However, the absorption rates are defined according to (4.54) on page 103, where the driving force is the concentration difference between the gas and the surface of the droplet: $(c_{\mathrm{g,i}} - \frac{c_{\mathrm{l,i}}}{K_{\mathrm{H,i}} \cdot R \cdot T})$. Therefore, due to the nature of the driving force, the tendency of η must be an exponential function, which is derived in (4.72).

$$\begin{aligned}
\frac{\partial n(t)}{\partial t} &= A \cdot k_{\mathrm{l,i}} \cdot \left(c_{\mathrm{l,i}}^{\mathrm{Eq}} - \frac{n(t)}{V} \right) \\
&\Downarrow \text{Analytical solution} \\
\eta_{\mathrm{Model}}(t) &= \frac{n(t) - n(0)}{c_{\mathrm{l,i}}^{\mathrm{Eq}} \cdot V - n(0)} = 1 - \exp\left(-\frac{3 \cdot k_{\mathrm{l,i}} \cdot t}{r} \right) \\
&\Downarrow \text{Substitute } t = \frac{Fo \cdot r^2}{\mathscr{D}} \\
\eta_{\mathrm{Model}}(Fo, \tau) &= 1 - \exp\left(-\frac{Fo}{\tau} \right) \quad \text{where} \quad \tau = \frac{\mathscr{D}}{3 \cdot k_{\mathrm{l,i}} \cdot r}
\end{aligned} \tag{4.72}$$

As seen in (4.72), the analytical solution to the decaying driving force is an exponential function, so $\eta_{\mathrm{Trans}}(Fo, Pe, \mu^*)$ cannot be used directly. The exponential function is characterized by a time constant, τ, which is a function of $\mathscr{D}$, r, and $k_{\mathrm{l,i}}$. τ is found by fitting exponential functions to the results from the transient model, which is illustrated in Figure 4.55.

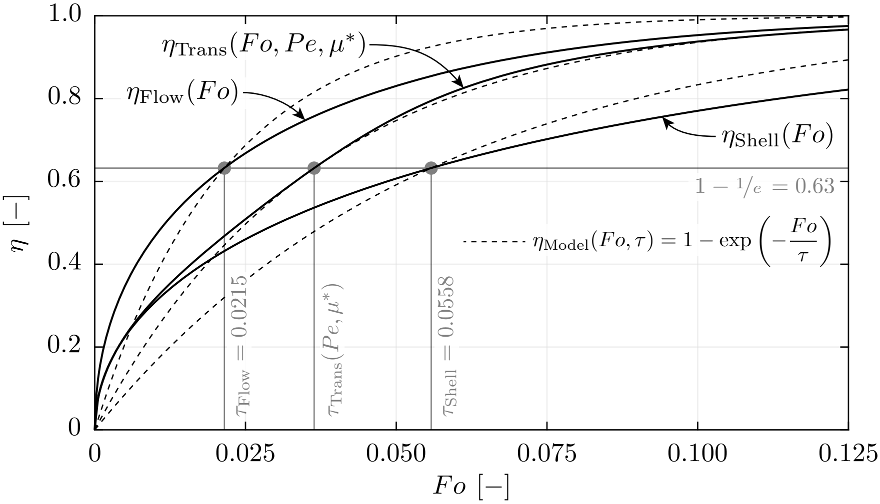

Figure 4.55: The tendency for $\eta_{\mathrm{Trans}}(Fo, Pe, \mu^*)$ is not an exponential decaying function. Therefore, the results from the transient model is fitted to an exponential function, where the time constant, τ, is found when $\eta_{\mathrm{Trans}}(Fo = \tau) = 1 - 1/e \approx 0.63$. The time constants for the shell and flow models are shown as well.

Figure 4.55 shows the three models with the solid lines: $\eta_{\text{Shell}}(Fo)$, $\eta_{\text{Flow}}(Fo)$, and $\eta_{\text{Trans}}(Fo, Pe, \mu^*)$, where the latter is bound between the two first. The tendency for the transient model is not an exponential function, which is required in the scrubber model, as the absorption rate is defined according to (4.54) on page 103. Therefore, exponential functions are fitted to the results, which are shown with the dashed lines in Figure 4.55. These are fitted by solving for Fo when $\eta(Fo = \tau) = 1 - {}^1\!/_e$. τ is the time constant, which are shown in grey in the figure. The time constants are shown in (4.73).

$$\begin{aligned} \eta_{\text{Shell}}(\tau_{\text{Shell}}) &= 1 - {}^1\!/_e & \rightarrow \quad \tau_{\text{Shell}} &= 0.0558 \\ \eta_{\text{Flow}}(\tau_{\text{Flow}}) &= 1 - {}^1\!/_e & \rightarrow \quad \tau_{\text{Flow}} &= 0.0215 \\ \eta_{\text{Trans}}(\tau_{\text{Trans}}) &= 1 - {}^1\!/_e & \rightarrow \quad \tau_{\text{Trans}} &= f(Pe, \mu^*) \end{aligned} \tag{4.73}$$

τ_{Shell} and τ_{Flow} are derived analytically, whereas τ_{Trans} is found numerically, which is a function of both Pe and μ^*. As the transient model is bound between the shell and the flow models it follows that $\tau_{\text{Flow}} \leq \tau_{\text{Trans}}(Pe, \mu^*) \leq \tau_{\text{Shell}}$, so the time constant for the transient model, $\tau_{\text{Trans}}(Pe, \mu^*)$, is defined as a fraction between τ_{Flow} and τ_{Shell}, which is defined in (4.74).

$$\phi_{\text{Trans}}(Pe, \mu^*) = \frac{\tau_{\text{Trans}}(Pe, \mu^*) - \tau_{\text{Shell}}}{\tau_{\text{Flow}} - \tau_{\text{Shell}}} \tag{4.74}$$

When $\phi_{\text{Trans}} = 0$ the value of $\tau_{\text{Trans}} = \tau_{\text{Shell}}$, whereas when $\phi_{\text{Trans}} = 1$ the value of $\tau_{\text{Trans}} = \tau_{\text{Flow}}$. Having defined $\phi_{\text{Trans}}(Pe, \mu^*)$, a numerical study was carried out where Pe and μ^* were varied. The results are shown in Figure 4.56.

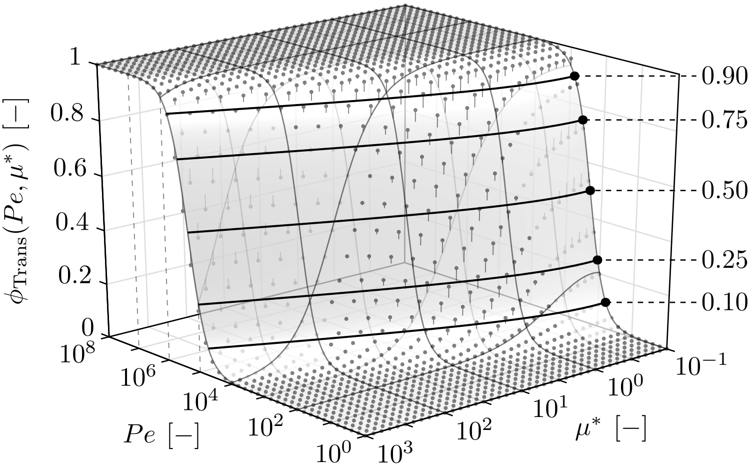

Figure 4.56: The values of $\phi_{\text{Trans}}(Pe, \mu^*)$ from the transient model shown as the grey dots. A surface was fitted to the data points, where the errors between the data points and the surface are shown with the small vertical grey lines. Five contour lines of the fitted surface are shown with the thick black lines.

As seen in Figure 4.56, $\phi_{\text{Trans}}(Pe, \mu^*)$ is a non-linear function of both Pe and μ^*. A surface is fitted to the data points, where the expression for the surface is shown in (4.75), which is a logistic function [Verhulst (134)].

$$\begin{aligned}\phi_{\text{Trans}}(Pe, \mu^*) &= \frac{1}{1+\exp(\Delta(Pe, \mu^*))} \quad , \quad \begin{pmatrix} 1 < Pe < 10^8 \\ 0.1 < \mu^* < 1000 \end{pmatrix} \\ \Delta(Pe, \mu^*) &= \Big(\log_{10}(\mu^*) + \exp\left(-\log_{10}(\mu^*)\right) \cdot 0.4 + 2.25 - \log_{10}(Pe) \Big) \cdot 4.0 \end{aligned} \tag{4.75}$$

The fitted surface has a maximum deviation of 0.057, which is reasonable for the large span in Pe and μ^*. Having defined an expression for $\tau_{\text{Trans}}(Pe, \mu^*)$, the internal mass transfer coefficient can be calculated using (4.72) on page 114, which is stated in (4.76). It should be noted that the liquid mass diffusivity, $\mathscr{D}_{\text{l}}$, is defined such that the turbulent effects are included, so $\mathscr{D}_{\text{l}} = \mathscr{D}_{\text{l,i}} + \mathscr{D}_{\text{t}}$, where $\mathscr{D}_{\text{l,i}}$ is the mass diffusivity of the i^{th} species, and $\mathscr{D}_{\text{t}}$ is the turbulent mass diffusivity, which was defined in (4.66) on page 108.

$$\begin{aligned} k_{\text{l,i}}(Pe, \mu^*) &= \frac{\mathscr{D}_{\text{l,i}} + \mathscr{D}_{\text{t}}}{3 \cdot r \cdot \tau_{\text{Trans}}(Pe, \mu^*)} \\ \tau_{\text{Trans}}(Pe, \mu^*) &= \tau_{\text{Shell}} + \phi_{\text{Trans}}(Pe, \mu^*) \cdot (\tau_{\text{Flow}} - \tau_{\text{Shell}}) \end{aligned} \tag{4.76}$$

$k_{\text{l,i}}$ is shown in Figure 4.57 for varying v_{Rel}, D and C_{IP}, where $\mu^* = 50$ and $\mathscr{D}_{\text{l,i}} = 2 \cdot 10^{-9}\ \text{m}^2/\text{s}$, which are typical values for a liquid droplet inside a wet scrubber.

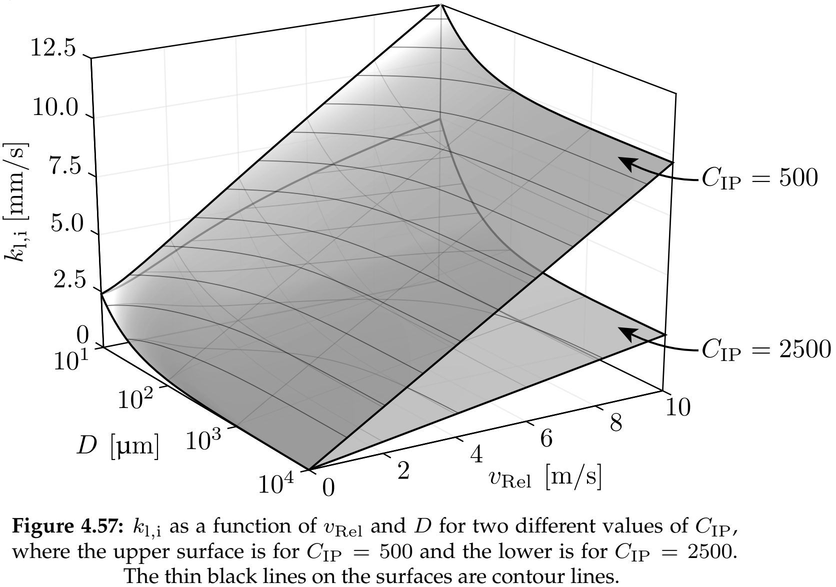

Figure 4.57: $k_{\text{l,i}}$ as a function of v_{Rel} and D for two different values of C_{IP}, where the upper surface is for $C_{\text{IP}} = 500$ and the lower is for $C_{\text{IP}} = 2500$. The thin black lines on the surfaces are contour lines.

As seen in Figure 4.57, the values of $k_{\text{l,i}}$ increases with decreasing C_{IP}, as the upper surface is for $C_{\text{IP}} = 500$ and the lower surface is for $C_{\text{IP}} = 2500$. This value is tuned in *Chapter 10: Model tuning* to match the absorption rate of $SO_2(g)$ from the experimental data described in *Chapter 9: Experiments*. Furthermore, the instability constant, C_{IP}, is used for calculating the overall heat transfer coefficient, which is described in the next section.

4.9.3 Summary

The overall mass transfer coefficient, $\bar{k}_{\text{i}}$, is determined according to the seven steps shown below:

1) Determine the visosity ratio and the turbulent diffusivity using (4.66):

$$\mu^* = \frac{\mu_{\text{l}}}{\mu_{\text{g}}} \qquad \mathscr{D}_{\text{t}} = \frac{v_{\text{Rel}} \cdot D}{C_{\text{IP}} \cdot (1+\mu^*)}$$

2) Calculate the tubulent Peclet number using (4.70):

$$Pe_{\text{t}} = \frac{D \cdot v_{\text{Rel}}}{\mathscr{D}_{\text{l,i}} + \mathscr{D}_{\text{t}}}$$

3) Evaluate (4.75) to obtain $\phi_{\text{Trans}}(Pe_{\text{t}}, \mu^*)$.

4) Calculate the time constant for the transient model using (4.76):

$$\tau_{\text{Trans}}(Pe_{\text{t}}, \mu^*) = \tau_{\text{Shell}} + \phi_{\text{Trans}}(Pe_{\text{t}}, \mu^*) \cdot (\tau_{\text{Flow}} - \tau_{\text{Shell}})$$

5) Use $\tau_{\text{Trans}}(Pe_{\text{t}}, \mu^*)$ and (4.76) to calculate the internal mass transfer coefficient:

$$k_{\text{l,i}}(Pe_{\text{t}}, \mu^*) = \frac{\mathscr{D}_{\text{l,i}} + \mathscr{D}_{\text{t}}}{3 \cdot r \cdot \tau_{\text{Trans}}(Pe_{\text{t}}, \mu^*)}$$

6) Calculate the external mass transfer coefficient using (4.55) and (4.56):

$$k_{\text{g,i}} = \frac{Sh(Re, Sc) \cdot \mathscr{D}_{\text{g,i}}}{D}$$

7) Detemine the overall mass transfer coefficient using (4.54):

$$\bar{k}_{\text{i}} = \frac{k_{\text{g,i}} \cdot k_{\text{l,i}}}{k_{\text{l,i}} + \dfrac{k_{\text{g,i}}}{K_{\text{H,i}} \cdot R \cdot T}}$$

The mass transfer coefficient is tuned by adjusting the instability constant, C_{IP}, which is explained in detail in *Chapter 10: Model tuning*. The method of simulating the internal circulation using the proposed method is valid at low Reynolds numbers, where the described models are most applicable. However, by tuning C_{IP}, the effects of the internal circulation is assumed to be captured despite not taking oscillations and other turbulent phenomena into account.

4.10 Heat transfer, evaporation, and condensation

The droplets within the scrubber are subject to heating, cooling, evaporation and condensation. In order to capture these effects in the scrubber model, correlations must be implemented to calculate the overall heat transfer coefficient, $\bar{h}$, where the heat flux is defined in (4.77).

$$\dot{Q} = A \cdot \bar{h} \cdot (T_\mathrm{g} - T_\mathrm{l}) \tag{4.77}$$

4.10.1 Heat transfer coefficient

The heat transfer coefficient, h, is modelled using the correlation provided by [Ahmed and Yovanovich (1)], which is an extension of the well known correlation from [Ranz and Marshall (110)]. These correlations map the *Nusselt number*, Nu, as a function of the *Prandtl number*, Pr, and the *Reynolds number*, Re, and are shown in (4.78).

$$\begin{gathered}
\text{Ranz \& Marshall:} \\
Nu = 2.0 + 0.6 \cdot \sqrt{Re} \cdot Pr^{1/3} \\[2ex]
\text{Ahmed \& Yovanovich:} \\
Nu = 2.0 + 0.775 \cdot \sqrt{Re} \cdot \frac{Pr^{1/3}}{\sqrt{2 \cdot Re^{-0.25} + 1} \cdot \left(1 + \frac{1}{(2\,Re^{-0.25}+1)^3 \cdot Pr}\right)^{0.17}}
\end{gathered} \tag{4.78}$$

Having calculated Nu in (4.78), the external heat transfer coefficient, h_g, is calculated using (4.79).

$$h_\mathrm{g} = \frac{Nu \cdot \kappa_\mathrm{g}}{D} \tag{4.79}$$

Where κ_g is the thermal conductivity of the gas, which is a function of temperature. Similar to the mass transfer coefficient, the thermal Biot number, which is defined as $Bi_\mathrm{T} = D \cdot h_\mathrm{g}/\kappa_\mathrm{g}$. This evaluates to $Bi_\mathrm{T} \approx 1.0$ for typical values, which indicates that a lumped assumption is not valid as $Bi_\mathrm{T} > 0.1$. This indicates that an internal heat transfer coefficient is required in order to accurately capture the overall heat transfer coefficient, which is defined in (4.80). T_s is the surface temperature, T_l is the bulk temperature of the droplet, and T_g is the bulk gas temperature.

$$\begin{gathered}
\dot{Q} = A \cdot h_\mathrm{g} \cdot (T_\mathrm{g} - T_\mathrm{s}) = A \cdot h_\mathrm{l} \cdot (T_\mathrm{s} - T_\mathrm{l}) = A \cdot \bar{h} \cdot (T_\mathrm{g} - T_\mathrm{l}) \\
\Downarrow \\
\bar{h} = \frac{h_\mathrm{l} \cdot h_\mathrm{g}}{h_\mathrm{l} + h_\mathrm{g}} \\
T_\mathrm{s} = \frac{h_\mathrm{l} \cdot T_\mathrm{l} + h_\mathrm{g} \cdot T_\mathrm{g}}{h_\mathrm{l} + h_\mathrm{g}}
\end{gathered} \tag{4.80}$$

In a similar manner to the overall mass transfer coefficient, a surface temperature is introduced, T_s, which is between T_l and T_g. The internal heat transfer coefficient is modelled using the same proposed model for the mass transfer coefficient described in the previous section, but instead of mass diffusivity, the thermal diffusivity, α, is used instead, which is shown in (4.81).

$$\alpha = \frac{\kappa_{\mathrm{l}}}{\rho_{\mathrm{l}} \cdot c_{\mathrm{P}}} \tag{4.81}$$

The units of α is $\left[\mathrm{m}^2/\mathrm{s}\right]$, which is also the units of the mass diffusivity, $\mathscr{D}$. h_{l} is derived by using the exponential function, which was the same for the mass transfer coefficient. This is derived in (4.82).

$$\begin{gathered}
\frac{\partial E(t)}{\partial t} = A \cdot h_{\mathrm{l}} \cdot \Bigg(T_{\mathrm{g}} - \overbrace{\frac{E(t)}{m \cdot c_{\mathrm{P}}}}^{T_{\mathrm{l}}(t)}\Bigg) \\
\Downarrow \text{Analytical solution} \\
\eta_{\mathrm{Model}}(t) = \frac{T_{\mathrm{l}}(t) - T(0)}{T_{\mathrm{g}} - T(0)} = 1 - \exp\left(-\frac{3 \cdot h_{\mathrm{l}} \cdot t}{c_{\mathrm{P}} \cdot \rho_{\mathrm{l}} \cdot r}\right) \\
\Downarrow \text{Substitute } t = \frac{Fo \cdot r^2}{\alpha + \mathscr{D}_{\mathrm{t}}} \\
\eta_{\mathrm{Model}}(Fo, \tau) = 1 - \exp\left(-\frac{Fo}{\tau}\right) \quad \text{where} \quad \tau = \frac{(\alpha + \mathscr{D}_{\mathrm{t}}) \cdot c_{\mathrm{P}} \cdot \rho_{\mathrm{l}}}{3 \cdot h_{\mathrm{l}} \cdot r}
\end{gathered} \tag{4.82}$$

Having defined $\eta_{\mathrm{Model}}(Fo, \tau)$, the internal heat transfer coefficient, h_{l}, can be calculated by setting $\tau = \tau_{\mathrm{Trans}}(Pe, \mu^*)$, where the correlation used was shown in (4.76) on page 116. h_{l} is therefore defined according to (4.83).

$$h_{\mathrm{l}} = \frac{(\alpha + \mathscr{D}_{\mathrm{t}}) \cdot c_{\mathrm{P}} \cdot \rho_{\mathrm{l}}}{3 \cdot \tau_{\mathrm{Trans}}(Pe, \mu^*) \cdot r} \tag{4.83}$$

The overall heat transfer coefficient, $\bar{h}$, is determined using the seven steps on page 117 previously described for the mass transfer coefficient, where the following changes are required:

- $\mathscr{D}_{\mathrm{l,i}}$ is replaced with α as defined in (4.81)
- $k_{\mathrm{l,i}}$ is replaced with h_{l} as defined in (4.83)
- $k_{\mathrm{g,i}}$ is replaced with h_{g} as defined in (4.79)
- $\bar{k}_{\mathrm{i}}$ is replaced with $\bar{h}$ as defined in (4.80)

The turbulent diffusivity, $\mathscr{D}_{\mathrm{t}}$, is defined similar to the mass transfer coefficient, but its effect will not be as apparent for the heat transfer coefficient as it is for the mass transfer coefficient, as $\alpha/\mathscr{D}_{\mathrm{l,i}} \approx 70$.

4.10.2 Evaporation and condensation

Having determined the overall heat and mass transfer coefficients, the thermal energy transfer rate can be calculated using (4.77). The latent heat of evaporation must be taken into account for correct modelling, but due to the magnitudes of the absorption rates of the different species, only the latent heat of H_2O is taken into account in this project. This is due to the small absorption rates of CO_2, O_2, and SO_2, and that the latent heat of evaporation for these species are significantly smaller compared to that of H_2O. The driving force for the absorption rate of H_2O is the partial pressure of water in the continuous gas phase, $P_{\mathrm{g,H_2O}}$, and the saturation vapour pressure at the surface, $P_{\mathrm{Sat}}(T_{\mathrm{s}})$, where the temperature is T_{s} as defined in (4.80). The mass transfer rate of H_2O is shown in (4.84).

$$\dot{m}_{\mathrm{H2O}} = M(\mathrm{H_2O}) \cdot A \cdot k_{\mathrm{g,H_2O}} \cdot \left(\frac{P_{\mathrm{g,H_2O}}}{T_{\mathrm{g}} \cdot R} - \frac{P_{\mathrm{Sat}}(T_{\mathrm{s}})}{T_{\mathrm{s}} \cdot R} \right) \tag{4.84}$$

Notice that the mass transfer rate, $\dot{m}_{\mathrm{H_2O}}$, is calculated using the external mass transfer coefficient, $k_{\mathrm{g,H_2O}}$, as the concentration of H_2O within the droplet is not changing, so an internal mass transfer coefficient is not required. The saturation pressure is calculated using the *Antoine equation* [Antoine (8)], which is shown in (4.85) along with the derivative with respect to temperature.

$$\begin{aligned} P_{\mathrm{Sat}}(T) &= 10^{\left(C_1 - \frac{C_2}{C_3 + T}\right)} \cdot \frac{101325\,\mathrm{Pa}}{760} \\ \frac{\partial P_{\mathrm{Sat}}}{\partial T} &= P_{\mathrm{Sat}}(T) \cdot \frac{C_2 \cdot \log_{\mathrm{e}}(10)}{(C_3 + T)^2} \end{aligned} \tag{4.85}$$

$$C_1 = 8.07131 \qquad C_2 = 1730.63\,\mathrm{K} \qquad C_1 = 233.426\,\mathrm{K}$$

When taking the latent heat of evaporation into account, the thermal energy gradient in the liquid phase is expressed according to (4.86) [ANSYS Inc. (6)].

$$m \cdot c_{\mathrm{P}} \cdot \frac{\mathrm{d}T}{\mathrm{d}t} = \dot{Q} - \dot{m}_{\mathrm{H_2O}} \cdot h_{\mathrm{fg,H_2O}} \tag{4.86}$$

Equation (4.86) is a function of both T and m, and no analytical solutions exists for this, when integrating both mass, m, and thermal energy, E, with respect to time. Furthermore, $\dot{m}_{\mathrm{H_2O}}$ can be relatively large, which affects the temperature. This makes the equation stiff to solve, and therefore, an implicit method is used, which is shown in (4.87). n and $n + 1$ are the current and next time-step respectively.

$$
\begin{aligned}
T_{\mathrm{l}}^{\mathrm{n+1}} &= \frac{E^{\mathrm{n+1}}}{c_{\mathrm{P}} \cdot m^{\mathrm{n+1}}} \\
T_{\mathrm{s}}^{\mathrm{n+1}} &= \frac{h_{\mathrm{l}} \cdot T_{\mathrm{l}}^{\mathrm{n+1}} + h_{\mathrm{g}} \cdot T_{\mathrm{g}}}{h_{\mathrm{l}} + h_{\mathrm{g}}} \\
c_{\mathrm{s}}^{\mathrm{n+1}} &= \frac{P_{\mathrm{Sat}}(T_{\mathrm{s}}^{\mathrm{n}}) + \left(\partial P_{\mathrm{Sat}}/\partial T\right)^{\mathrm{n}} \cdot \left(T_{\mathrm{s}}^{\mathrm{n+1}} - T_{\mathrm{s}}^{\mathrm{n}}\right)}{R \cdot T_{\mathrm{s}}^{\mathrm{n}}} \\
\dot{m}_{\mathrm{H_2O}}^{\mathrm{n+1}} &= M(\mathrm{H_2O}) \cdot k_{\mathrm{g,H_2O}} \cdot A \cdot \left(c_{\mathrm{g}} - c_{\mathrm{s}}^{\mathrm{n+1}}\right) \\
\dot{Q}^{\mathrm{n+1}} &= A \cdot \bar{h} \cdot \left(T_{\mathrm{g}} - T_{\mathrm{l}}^{\mathrm{n+1}}\right) \\
m_{\mathrm{H_2O}}^{\mathrm{n+1}} &= m_{\mathrm{H_2O}}^{\mathrm{n}} + \Delta t \cdot \dot{m}_{\mathrm{H_2O}}^{\mathrm{n+1}} \\
E^{\mathrm{n+1}} &= E^{\mathrm{n}} + \Delta t \cdot \left(\dot{Q}^{\mathrm{n+1}} + \dot{m}_{\mathrm{H_2O}}^{\mathrm{n+1}} \cdot h_{\mathrm{fg,H_2O}}\right)
\end{aligned}
\tag{4.87}
$$

The seven equations and unknowns in (4.87) can be solved analytically, where the resulting expressions are too extensive to display, but are used in the scrubber model. The implicit method improves stability, but introduced small errors, which can be minimized by keeping the time-step, Δt, small.

4.11 Drains

The seawater injected into the scrubber absorbs $\mathrm{SO_2(g)}$ among others, so the pH will decrease as the acid buffer capacity is depleted. This reduces the absorption rate of $\mathrm{SO_2(g)}$, which was described in *Chapter 3: Chemistry*. The low pH water is removed from the scrubber via the drains, which are located in the jet and absorber sections as shown in Figure 1.4 on page 6. The drains each have two sources, which are direct parcel impacts and the wall film mass rates. This are shown in (4.88) and illustrated in Figure 4.58 on the next page.

$$
\dot{m}_{\mathrm{Drain}} = \dot{m}_{\mathrm{Parcel}} + \dot{m}_{\mathrm{Film}} \tag{4.88}
$$

When a parcel hits a drain, the parcel is eliminated from the simulation, and the mass rate is logged, such that mass and energy balances for the overall model can be monitored. The total mass rate, $\dot{m}_{\mathrm{Drain}}$, has a low pass filter applied to it, such that a steady-state value can be obtained. After having applied the low pass filter, equilibrium is satisfied, such that the mixture of wall films and parcels results in a single stream. This allows for evaluating the overall performance of the scrubber, and to track mass, mole, and energy balances.

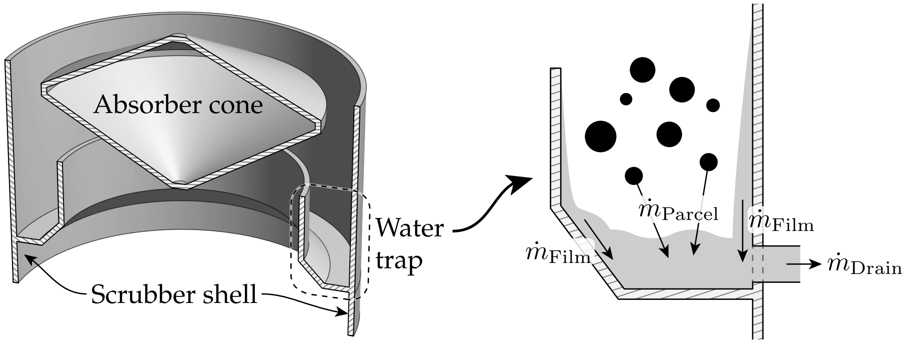

Figure 4.58: An illustration of the absorber water traps and the sources from the wall films and the parcels.

4.12 Trace

Water is injected different places inside the scrubber as previously described. Ultimately, this water will leave the scrubber through the drains, the demister, or via the gas phase as water vapour. In order to track the water, extra components are added to the liquid phase, which are denoted *trace components*. Each sprayer nozzle will have its own trace component, so a scrubber having four sprayer nozzles will have four trace components, which are tracked in each of the sub-models previously described. When post-processing the results of the simulation, the outlet flow from the drains can be traced back to the sprayer nozzles. This allows for evaluating the amount of water flowing from the jet section to the absorber section and vice versa, which is an important parameter when optimizing the scrubber. The trace components, Ψ, are illustrated in Figure 4.59.

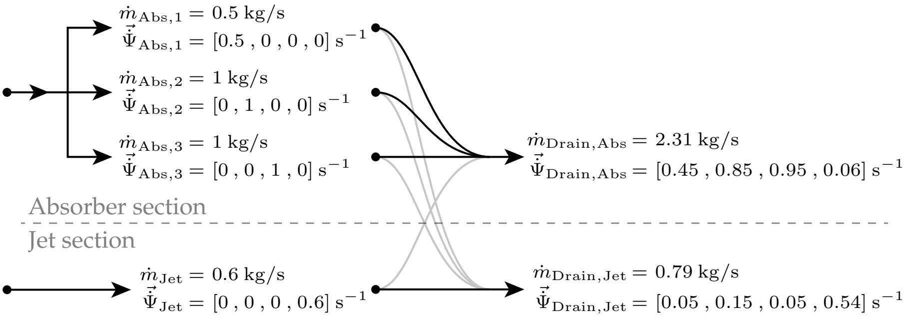

Figure 4.59: An illustration of the trace components, $\vec{\Psi}$, which are different for each of the sprayer nozzles within the scrubber. The example illustrates how water from the absorber section enters the jet section and exists via the jet drain, and vice versa from the jet to the absorber section, which is indicated by the grey lines.

As seen in Figure 4.59, $\vec{\Psi}$ are treated as extra mass flow components, but it should be noted that the trace components do not contribute to the mass of each parcel. The trace components are only tracked in the liquid phase, so no extra scalar fields are introduced in the continuous phase, as this only increases the complexity of the model without providing any critical information.

4.13 Parcel variables

The discrete phase consists of a number of parcel, where each of these are modelled using the sub-models described in this chapter. In order to fully describe a parcel at any given time, 24 variables are required, which are shown in Table 4.1.

Table 4.1: Each parcel has 24 degrees of freedom, which are listed in this table. Notice that $\vec{m}$ theoretically only requires nine variables to be specified, but in practice all 18 components are included (17 species and $\mathrm{H}_{\mathrm{E}}^{+}$).

Name	Unit	Variables	Description
E	J	1	Thermal energy
N	–	1	Droplet count
$\vec{m}$	kg	18 (9)	Species masses
$\vec{x}$	m	3	Position
$\mathrm{d}\vec{x}/\mathrm{d}t$	m/s	3	Velocity
γ	–	1	Deformation parameter
$\mathrm{d}\gamma/\mathrm{d}t$	–/s	1	Deformation velocity
$(D_{\mathrm{ST}} \cdot t)$	m^2	1	Growth parameter
$\vec{\Psi}$	–	4	Trace components
$\sum$		33 (24)	

As seen in Table 4.1, 24 independent values are required in order to fully define the state of any given parcel. The species masses, $\vec{m}$, theoretically only requires nine variables to fully define all 18 species masses, which was described in *Section 3.8.2: Solution procedure*. However, it was found easier to model all 18 species (17 species and $\mathrm{H}_{\mathrm{E}}^{+}$), so in practice each parcel has 33 associated variables. All other variables such as droplet diameter, temperature etc. can be derived from the independent variables in Table 4.1.

5 | EULERIAN WALL FILMS

Liquid films flow along the inner structures of the scrubber, as the injected water impacts the surfaces and sticks to it as described in *Section 4.7: Impingement*. The wall films will accelerate due to gravity, whilst different mechanisms will atomize or separate some of the liquid into the scrubber again as droplets. This wall films are subject to the gas phase reactions, the internal chemistry, and the equilibria described in *Chapter 3: Chemistry*. The wall films are described in eight sections, which are illustrated in Figure 5.1.

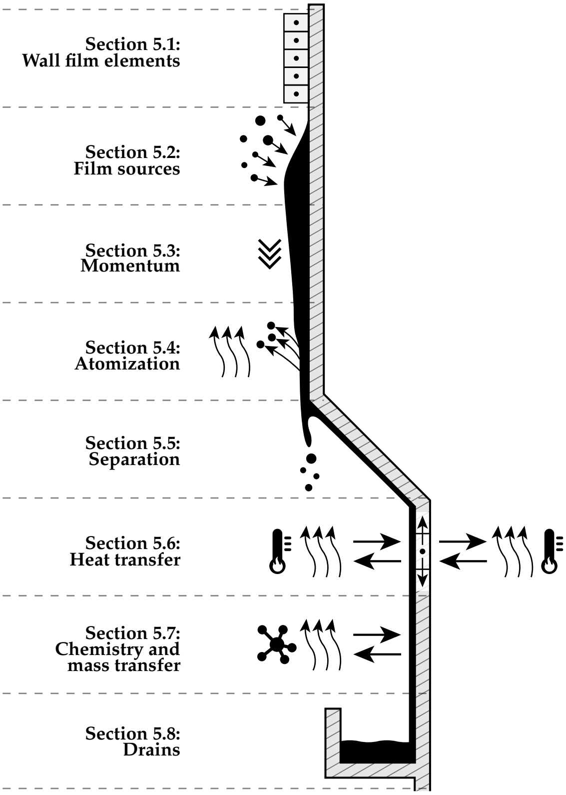

Figure 5.1: An overview of the eight sections in this chapter.

5.1 Wall film elements

A wet scrubber has numerous surfaces, on which water is flowing along. For the scrubber investigated in this study, which is described in *Chapter 9: Experiments*, 15 different wall films are modelled, where nine of these are shown with the arrows following the surfaces in Figure 5.2. The wall films are treated in a 2D manner, as the tangential components are assumed negligible. Each wall film is discretized into a number of wall film elements, where the properties of the films are stored, so an Eulerian approach is used to model the wall films. An example of the wall film elements is illustrated to the right in Figure 5.2.

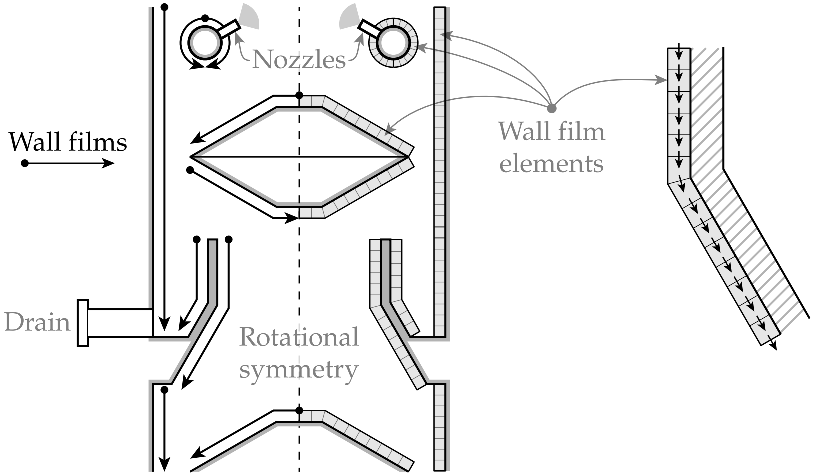

Figure 5.2: Nine of the 15 wall films in the scrubber model are shown to the left by the arrows following the surfaces. Each wall film is discretized into a number of *wall film elements*, where the properties are stored. Mass and energy is propagated from element to element as indicated by the small arrows to the right.

Each of the wall film elements has an associated area, A_{F}, which is the swept area when revolving the element by 360° around the axial direction of the scrubber. The subscript $(...)_{\mathrm{F}}$ will be used throughout this chapter to indicate wall film properties.

5.2 Film sources

When a parcel impacts a solid surface, some fluid will be deposited, which was described in *Section 4.7: Impingement*, where a fraction of the parcel mass was deposited on the wall. This acts like a source term on the wall film, where a low pass filter is used to obtain steady-state values. The filter has an adjustment parameter, ϕ_{LP}, which assigns the fraction of the new value to be used, which is shown in (5.1), where n and $n-1$ assign the current and previous time-steps respectively.

$$\overline{\dot{m}}_{\mathrm{F}}^{\mathrm{n}} = \overline{\dot{m}}_{\mathrm{F}}^{\mathrm{n-1}} \cdot (1 - \phi_{\mathrm{LP}}) + \dot{m}_{\mathrm{F}}^{\mathrm{n}} \cdot \phi_{\mathrm{LP}} \tag{5.1}$$

The reason for filtering is that the discrete phase is modelled in an unsteady manner, where the discrete phase is advanced by Δt, and during each time-step, some of the parcels will impinge the wall films. However, as the number of parcels hitting the wall films will fluctuate, a filter is required. An example is shown in Figure 5.3, where the number of parcels hitting a wall film element varies between time-steps, so the apparent mass source terms varies as well.

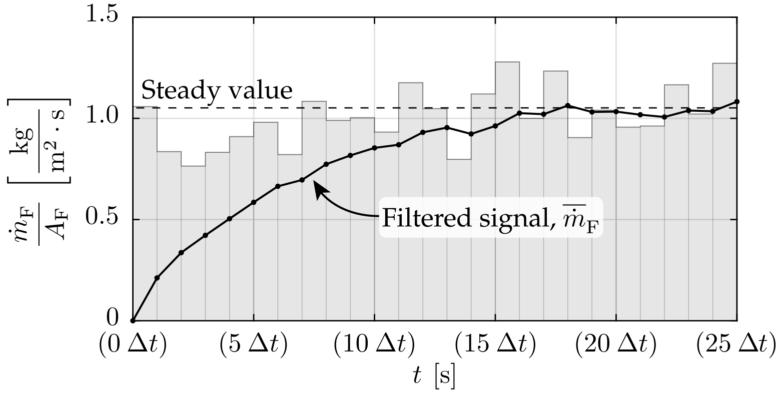

Figure 5.3: An example of the mass sources acting on a wall film element, and how a low pass filter is used to obtain a steady value.

It can be seen in Figure 5.3 that the filtered signal, $\overline{\dot{m}}_{\mathrm{F}}$, tends towards a steady-state value. The mass source term contains the mass flows of all 18 species, and in addition to this, a thermal energy source term, and four trace component source terms are also stored. These are shown in Table 5.1 on page 142, where an overview of the independent variables for each wall film element is shown.

5.3 Momentum

When mass accumulates on the wall, gravitational and shear forces act on each wall film element, which cause the wall films to accelerate and flow along the surfaces. Three forces are taken into account in this project: the gravitational force, F_{g}, the wall shear stress, τ_{W}, and the gas shear stress, τ_{g}. These are illustrated in Figure 5.4, where H_{F} is the film height, and ΔL_{F} is the wall film length along the shell. The velocity along the wall film is shown to the right.

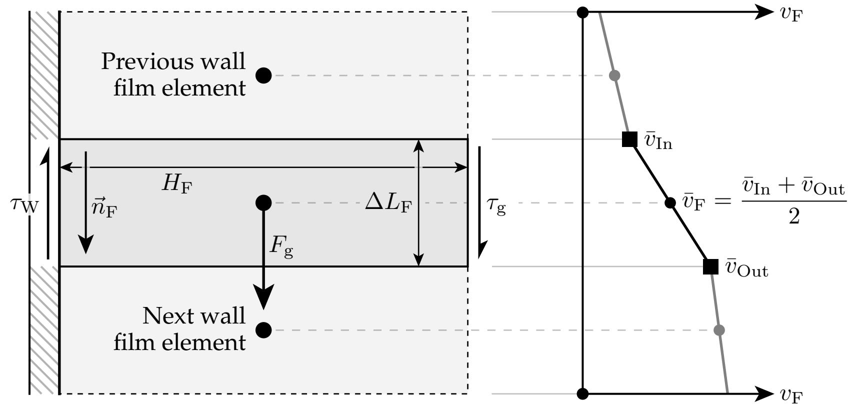

Figure 5.4: An overview of the different forces and shear stresses acting on a wall film element to the left, and an illustration of the velocities associated with a single wall film element to the right.

As seen in Figure 5.4, three forces are acting on each wall film element. The gravitational force, F_g, can be defined per unit area, which transforms the force to a shear stress. This is shown in (5.2), where $\vec{n}_F$ is the normal vector along the wall in the direction of the flow, as seen in Figure 5.4.

$$\tau_{\text{Gravity}} = \rho_l \cdot H_F \cdot (\vec{g} \cdot \vec{n}_F) \tag{5.2}$$

The gas shear stress, τ_g, is calculated from within OpenFOAM, and is transferred to MATLAB, such that it can be used in the wall film calculations.

The wall shear stress, τ_W, is calculated using the velocity gradient at the wall, $(\mathrm{d}v_F/\mathrm{d}x)$. By assuming a parabolic velocity profile, which is a solution to the Navier-Stokes equations under ideal conditions, the wall shear stress, τ_W, can be calculated analytically. The assumed parabolic velocity profile is illustrated in Figure 5.5.

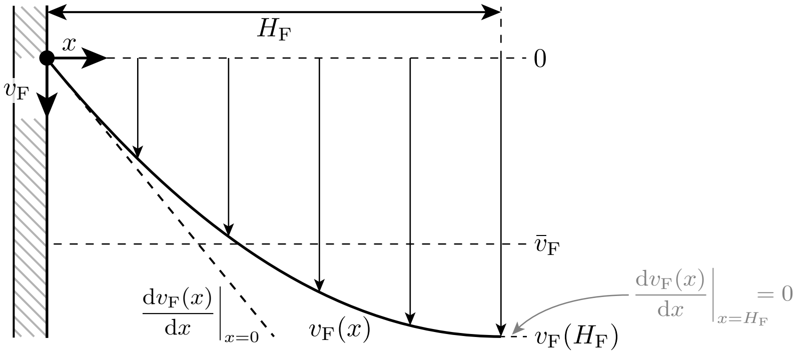

Figure 5.5: The assumed parabolic velocity profile for a wall film element. $\bar{v}_F$ is the average film velocity. The normal velocity gradient is shown as well by the inclined dashed line.

The no-slip condition is applied to the surface of the wall, and the velocity gradient at $x = H_\mathrm{F}$ is assumed zero. This results in the velocity profile shown in (5.3).

$$v_\mathrm{F}(x) = v_\mathrm{F}(H_\mathrm{F}) \cdot \left(1 - \left(\frac{H_\mathrm{F} - x}{H_\mathrm{F}}\right)^2\right) \tag{5.3}$$

Given the velocity profile in (5.3), the average film velocity, $\bar{v}_\mathrm{F}$, is calculated along with the velocity gradient at the wall, which is shown in (5.4).

$$\begin{aligned} \bar{v}_\mathrm{F} &= \frac{1}{H_\mathrm{F}} \cdot \int_0^{H_\mathrm{F}} v_\mathrm{F}(x)\,\mathrm{d}x = \frac{2 \cdot v_\mathrm{F}(H_\mathrm{F})}{3} \\ \left.\frac{\mathrm{d}v_\mathrm{F}(x)}{\mathrm{d}x}\right|_{\mathrm{x=0}} &= \frac{3 \cdot \bar{v}_\mathrm{F}}{H_\mathrm{F}} \end{aligned} \tag{5.4}$$

Having calculated the velocity gradient at the wall, the wall shear stress, τ_W, is determined using (5.5).

$$\tau_\mathrm{W} = \left.\frac{\mathrm{d}v_\mathrm{F}(x)}{\mathrm{d}x}\right|_{\mathrm{x=0}} \cdot \mu_\mathrm{l} = \frac{3 \cdot \mu_\mathrm{l} \cdot \bar{v}_\mathrm{F}}{H_\mathrm{F}} \tag{5.5}$$

Due to conservation of mass, the film height is calculated according to (5.6). r_F is the radial distance from the wall film element to the centre axis of the scrubber. The film height is assumed small compared to the radius of the scrubber, $H_\mathrm{F} \ll r_\mathrm{F}$, so the cross sectional area is approximated by the product between the circumference and the wall film height.

$$\begin{aligned} \dot{V}_\mathrm{F} &= \dot{m}_\mathrm{F} \cdot \rho_\mathrm{l} \\ H_\mathrm{F} &= \frac{\dot{V}_\mathrm{F}}{\underbrace{r_\mathrm{F} \cdot 2 \cdot \pi}_{\text{Circumference}} \cdot \bar{v}_\mathrm{F}} \end{aligned} \tag{5.6}$$

The three shear forces acting on each wall film element causes an acceleration, which is shown in (5.7).

$$a_\mathrm{F} = \frac{\tau_\mathrm{W} + \tau_\mathrm{Gravity} + \tau_\mathrm{g}}{H_\mathrm{F} \cdot \rho_\mathrm{l}} \tag{5.7}$$

Having obtained an expression for a_F, the velocity of the film is calculated. This is done in a sequential manner along the wall film length. The velocity out of each wall film element, $\bar{v}_\mathrm{Out}$, is calculated based on the velocity from the previous wall film element, $\bar{v}_\mathrm{In}$. These velocities were illustrated in Figure 5.5. $\bar{v}_\mathrm{Out}$ is calculated by solving the system of equations shown in (5.8).

$$\begin{aligned}
\bar{v}_{\mathrm{F}} &= \frac{\bar{v}_{\mathrm{In}} + \bar{v}_{\mathrm{Out}}}{2} \\
\bar{v}_{\mathrm{Out}} &= \bar{v}_{\mathrm{In}} + a_{\mathrm{F}} \cdot \Delta t_{\mathrm{F}} \\
\Delta t_{\mathrm{F}} &= \frac{\Delta L_{\mathrm{F}}}{\bar{v}_{\mathrm{F}}} \\
a_{\mathrm{F}} &= \frac{\tau_{\mathrm{W}}(\bar{v}_{\mathrm{F}}, H_{\mathrm{F}}) + \tau_{\mathrm{Gravity}}(H_{\mathrm{F}}) + \tau_{\mathrm{g}}}{H_{\mathrm{F}} \cdot \rho_{\mathrm{l}}} \\
H_{\mathrm{F}} &= \frac{\dot{V}_{\mathrm{F}}}{r_{\mathrm{F}} \cdot 2 \cdot \pi \cdot \bar{v}_{\mathrm{F}}}
\end{aligned} \tag{5.8}$$

Where Δt_{F} is the time required to pass the wall film element with length ΔL_{F}. The solution to $\bar{v}_{\mathrm{Out}}$ is the root of a third-order polynomial, where the analytical expression is too extensive to display, but is used in the scrubber model.

5.4 Atomization

Atomization occurs when the shear stresses from the gas exceeds a certain threshold. This causes waves to form at the surface, which eventually breaks off into small droplets. The model used in this study is based upon [Mayer (93)], and is illustrated in Figure 5.6.

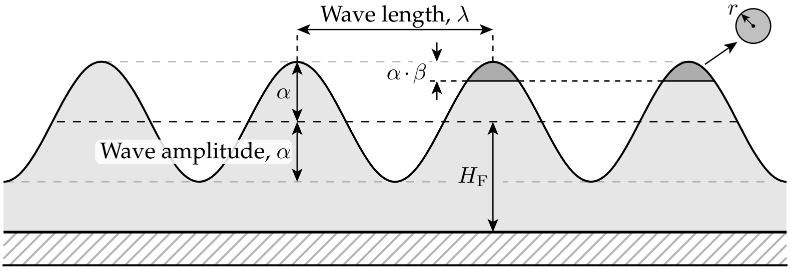

Figure 5.6: An illustration of atomization of a wall film, which breaks off the crests of the waves and creates small droplets, which are re-injected into the scrubber.

The surface waves on the wall films are formed due to Kelvin-Helmholtz instabilities [Helmholtz (67)], which are modelled linearly with small permutations. The wave amplitude growth is related to its wave length, which is shown in (5.9) [ANSYS Inc. (6)] [Mayer (93)].

$$\begin{aligned}
\frac{1}{\tau_{\mathrm{Atom}}} = \omega &= \frac{f}{\sqrt{\lambda}} - \frac{\nu_{\mathrm{D}}}{\lambda^2} \\
f &= \sqrt{\frac{\pi}{2}} \cdot \frac{\beta\, \rho_{\mathrm{g}}\, v_{\mathrm{g}}^2}{\sqrt{\sigma_{\mathrm{l}}\, \rho_{\mathrm{l}}}} \\
\nu_{\mathrm{D}} &= \frac{8\, \pi^2\, \mu_{\mathrm{l}}}{\rho_{\mathrm{l}}}
\end{aligned} \tag{5.9}$$

Where τ_{Atom} is the time constant for the exponential growth and is the inverse of its frequency, ω, and ν_{D} is a viscous damping parameter. β is the fraction of the wave, which breaks off the waves to create small droplets, and is a model constant with value $\beta = 0.3$. In order for the waves to experience atomization, the wave amplitude growth must increase over time, which implies $\omega > 0$. By solving for λ in (5.9) when $\omega = 0$, the minimum wave length for atomization to occur, λ_{Min}, can be found, which is shown in (5.10).

$$\begin{aligned}\lambda_{\text{Min}} &= 2\,\pi\,\sqrt[3]{16}\cdot\left(\frac{\mu_{\text{l}}\,\sqrt{\sigma_{\text{l}}/\rho_{\text{l}}}}{\beta\,\rho_{\text{g}}\,v_{\text{g}}^{2}}\right)^{2/3}\\ \lambda_{\text{Crit}} &= \sqrt[3]{16}\cdot\lambda_{\text{Min}}\\ \bar{\lambda} &= \frac{9}{2}\cdot\lambda_{\text{Min}}\end{aligned} \tag{5.10}$$

It follows that all wavelengths greater than λ_{Min} will experience atomization. The values of τ_{Atom} is shown in Figure 5.7, where typical values are used in (5.9) and (5.10).

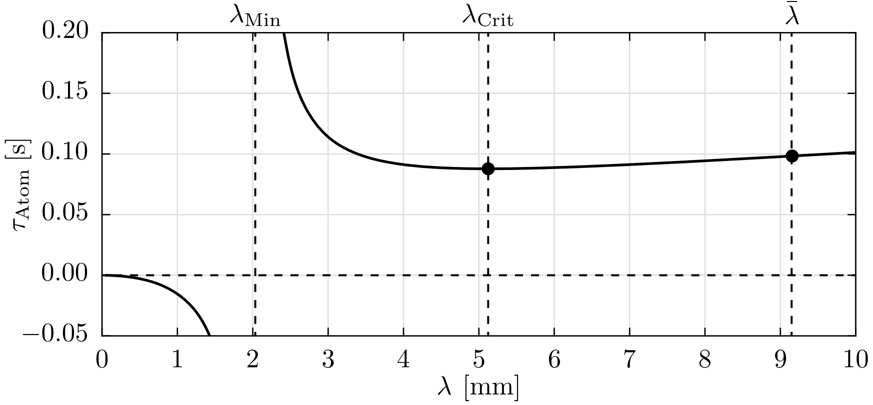

Figure 5.7: The time constant, τ_{Atom}, as a function of the wavelength, λ. The graph is made using typical values for the terms in (5.10).

As seen in Figure 5.7, the time constant, τ_{Atom}, is negative when $\lambda < \lambda_{\text{Min}}$, which indicates a damped wave. τ_{Atom} is positive when $\lambda > \lambda_{\text{Min}}$, which is indicating an exponential growth, which is required for atomization to occur. This is illustrated in Figure 5.8 on the next page, where the relative amplitudes of the surface waves after certain times are shown. It can be seen that waves with $\lambda < \lambda_{\text{Min}}$ are damped waves, which will decrease in amplitude over time due to viscous dissipation. This is related to the negative time constant, τ_{Atom}, in Figure 5.7. When $\lambda = \lambda_{\text{Min}}$ where $\tau_{\text{Atom}} \to \pm\infty\,\text{s}$, the amplitude will remain constant and thus yields a standing wave. When $\lambda > \lambda_{\text{Min}}$, where $\tau_{\text{Atom}} > 0$, the waves will experience exponential growth and eventually atomize.

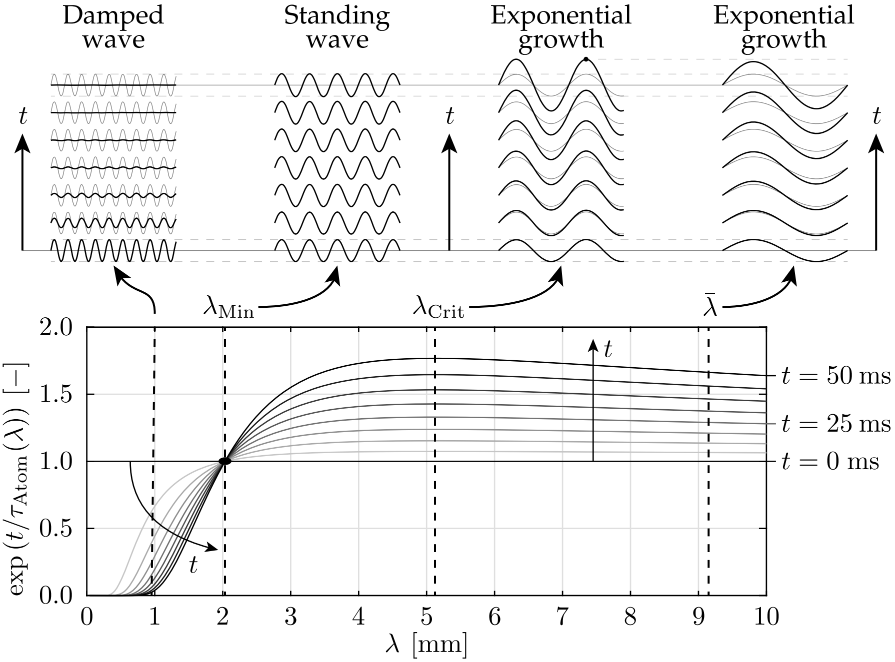

Figure 5.8: An example of wave growth over time, and is using the same typical values, which were used in Figure 5.7. The waves in top of the figure indicate the wave growth over time with the solid black curved. The grey curves are the original wave at $t = 0$.

When atomization occurs, the atomization mass rate is calculated using (5.11), where an expression for ω was derived by [de Bertodano et al. (32)], which is shown in (5.11) as well.

$$\begin{gathered}\dot{m}_{\mathrm{Atom}} = C_{\mathrm{Atom}} \cdot \rho_{\mathrm{l}} \cdot \bar{\lambda} \cdot \omega \cdot dA \\ \omega = 0.384 \cdot \frac{\rho_{\mathrm{g}} \cdot v_{\mathrm{g}}^{3}}{\sigma_{\mathrm{l}}} \sqrt{\frac{\rho_{\mathrm{g}}}{\rho_{\mathrm{l}}}}\end{gathered} \tag{5.11}$$

Where C_{Atom} is a model constant with a value of 0.5 [ANSYS Inc. (5)]. The average diameter of the atomized droplets is shown in (5.12).

$$\bar{D}_{\mathrm{Atom}} = F_{\mathrm{Atom}} \cdot \bar{\lambda} \tag{5.12}$$

Where F_{Atom} is a model constant with a value of $0.3^{5/3}$ [Mayer (93)]. The average droplet diameter upon atomization, $\bar{D}_{\mathrm{Atom}}$, is used in combination with the truncated normal distribution in (4.5) on page 66 to reflect the stochastic nature of atomization, where the injected droplet diameters are sampled between $0.75 \cdot \bar{D}_{\mathrm{Atom}}$ and $1.25 \cdot \bar{D}_{\mathrm{Atom}}$ according to the distribution.

The wall film is modelled in a 2D manner, where the mass flow is assumed to be evenly distributed around the circumference of the scrubber shell. This implies that 3D phenomena are not taken into account, which was found to cause stability problems in the model, as some regions experienced $100\ \%$ atomization due to large gas velocities, so no liquid could pass these regions. This resulted in mass accumulation inside the scrubber, which did not reflect reality. During the experimental tests it was observed that rivulets formed on the shell. Furthermore, if the flow inside the scrubber is not axis symmetric, the wall films will distribute unevenly around the circumference of the scrubber. These two phenomena are illustrated in Figure 5.9.

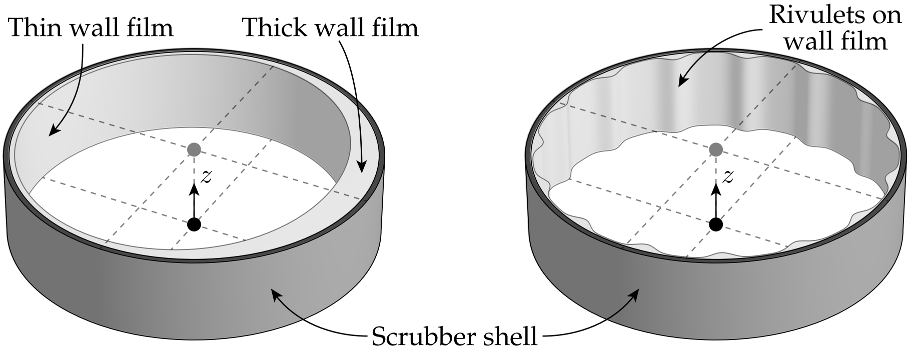

Figure 5.9: An illustration of an uneven distribution of a wall film along the circumference shows to the left, and an example of rivulet formation along the shell to the right.

The left figure in Figure 5.9 shows an uneven film distribution, which can occur if the gas velocity is significantly greater on one side compared to the other. This causes one side to be atomized, whereas the other will not. The right figure shows rivulets on the inside of the shell, which are caused by film instabilities [Singh et al. (118)].

Rivulets can be modelled using correlations. However, no model was implemented to model these in this study, so instead a simple approach was applied, where only a fraction, ϕ_{Rivulet}, of the calculated mass rate in (5.11), $\dot{m}_{\text{Atom}}$, could be atomized. This is shown in (5.13), where $\dot{m}_{\text{Atom,Limit}}(L)$ indicates the limited atomization rate. L is the length along the wall film in the direction of motion.

$$\begin{aligned}\dot{m}_{\text{Accumulated}}(L) &= \int_0^L \frac{\dot{m}_{\text{Sources}}}{dA} \cdot (2 \cdot \pi \cdot r(x))\ \mathrm{d}x \\ \dot{m}_{\text{Rivulet}}(L) &= \dot{m}_{\text{Accumulated}}(L) \cdot \phi_{\text{Rivulet}} \\ \dot{m}_{\text{Atom,Limit}}(L) &= \min\left(\dot{m}_{\text{Atom}}(L), \max\left(\dot{m}_{\text{F}}(L) - \dot{m}_{\text{Rivulet}}(L), 0\right)\right)\end{aligned} \tag{5.13}$$

ϕ_{Rivulet} adjusts the fraction of the accumulated mass flows, which is not susceptible to atomization. The method is crude in terms of accuracy, as rivulet formation is a complex phenomena, but this is beyond the scope of this study.

A value of $\phi_{\text{Rivulet}} = 0.5$ was chosen for implementation in the scrubber model. A constructed example of (5.13) is shown in Figure 5.10.

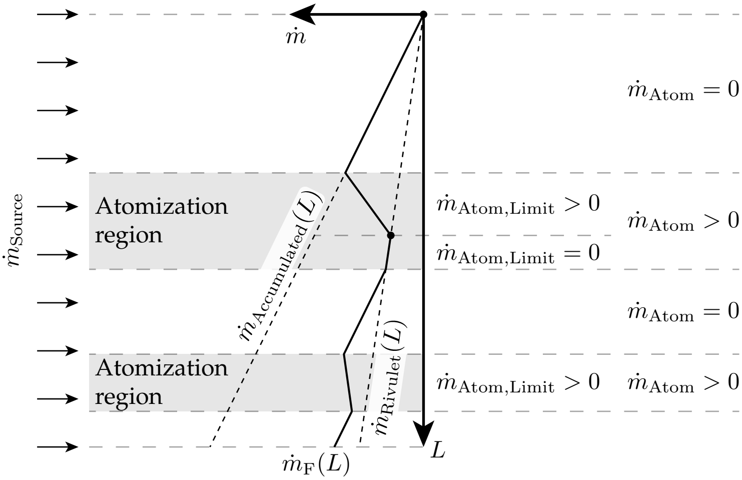

Figure 5.10: An example of how $\dot{m}_{\text{Atom}}(L)$ is limited to $\dot{m}_{\text{Atom,Limit}}(L)$ according to (5.13).

Figure 5.10 shows a wall film, which has a constant mass source along its entire length, $\dot{m}_{\text{Source}}$. The mass flow along the wall film is shown as the solid line, $\dot{m}_{\text{F}}(L)$, which can be seen to increase in the upper region, where $\dot{m}_{\text{F}}(L)$ is following $\dot{m}_{\text{Accumulated}}(L)$, as no atomization occurs. $\dot{m}_{\text{Rivulet}}(L)$ is proportional to $\dot{m}_{\text{Accumulated}}(L)$, where the proportionality factor is ϕ_{Rivulet}. A region with atomization is shown in grey, where $\dot{m}_{\text{F}}$ decreases. However, at some point $\dot{m}_{\text{F}}(L) = \dot{m}_{\text{Rivulet}}(L)$, which is shown with the black dot. At this point the atomization mass rate is limited and set to zero. When the atomization region is passed, $\dot{m}_{\text{F}}$ increases again, as no atomization occurs. Finally, another atomization region is shown in the bottom of the figure, where no limiting occurs.

Having calculated both $\dot{m}_{\text{Atom,Limit}}$ and $\bar{D}_{\text{Atom}}$, the number rate of droplets is calculated using (5.14). Recall that the number of droplets in each parcel, N, is an independent variable, and D is a derived variable as described in *Section 4.13: Parcel variables*.

$$\dot{N}_{\text{Atom}} = \frac{\dot{m}_{\text{Atom,Limit}}}{\frac{4}{3} \cdot \pi \cdot \left(\frac{\bar{D}_{\text{Atom}}}{2}\right)^3 \cdot \rho_{\text{l}}} \tag{5.14}$$

All other properties of the atomized droplets are those of the film at the current position such as temperature, species concentrations etc. A first-order filter is applied to $\dot{m}_{\text{Atom,Limit}}$ to ensure a steady-state solution in the same manner as done with the wall film source terms described in *Section 5.2: Film sources*.

5.5 Separation

When the wall film reaches a sharp edge, the film might not stay attached to the surface, and the liquid film re-enters the domain as droplets. This phenomena was investigated by [O'Rourke and Amsden (102)] and [Friedrich et al. (55)], where the model proposed by the latter study is chosen for implementation in this study, and was derived empirically. An illustration of the phenomenon is illustrated in Figure 5.11.

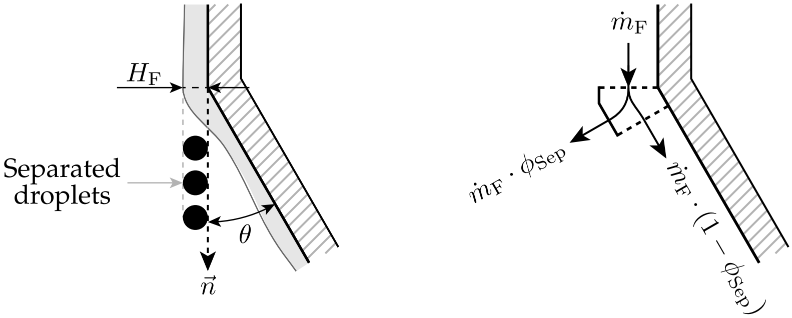

Figure 5.11: When a wall film reaches a sharp edge, a fraction of the mass flow, ϕ_Sep, will re-enter the domain as droplets.

Figure 5.11 illustrates a wall film with thickness H_F and mass flow $\dot{m}_\mathrm{F}$. When encountering a sharp corner inclined at an angle, θ, a fraction of the mass flow, ϕ_Sep, will re-enter the domain. The diameters of the injected droplets are assumed to be equal to the height of the wall film, $D = H_\mathrm{F}$. The model proposed by [Friedrich et al. (55)] is shown in (5.15).

$$\begin{aligned} D &= H_\mathrm{F} & \vec{v}_\mathrm{D} &= \vec{n}_\mathrm{F} \cdot v_\mathrm{F} \\ We_\mathrm{F} &= \frac{\rho_\mathrm{l}\, H_\mathrm{F}\, v_\mathrm{F}^2}{\sigma_\mathrm{l}} & F_\mathrm{Ratio} &= \frac{We_\mathrm{F}}{1 + \frac{1}{\sin(\theta)}} \\ \phi_\mathrm{Sep} &= 1 - \exp\left(0.411544 \cdot \left(\frac{1 - F_\mathrm{Ratio}^2}{F_\mathrm{Ratio}}\right)\right) \end{aligned} \tag{5.15}$$

The velocity of the injected droplets, $\vec{v}_\mathrm{D}$, is the wall film velocity, whereas the position of the injected droplets are randomly seeded from the edge, where separation occurs. In order for separation to occur, a criteria must be satisfied, which is shown in (5.16) [ANSYS Inc. (6)].

$$\theta > \theta_\mathrm{Crit} = 20^\circ \tag{5.16}$$

Separation occurs if the criteria in (5.16) is satisfied. ϕ_Sep is clipped at $5\ \%$ [ANSYS Inc. (6)], and the values of ϕ_Sep are shown as a function of θ and We_F in Figure 5.12 according to (5.15).

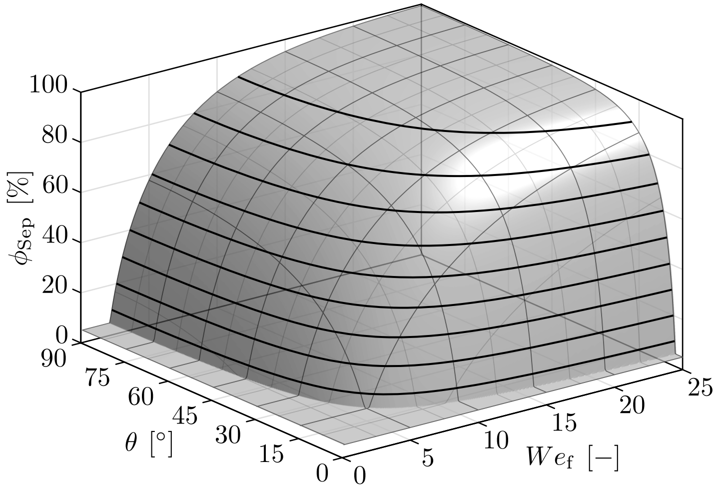

Figure 5.12: The separation fraction, ϕ_{Sep}, as a function of θ and We_{F}. It should be noted that separation only occurs, if $\theta > 20°$ as stated in (5.16).

As seen in Figure 5.12, the separation fraction, ϕ_{Sep}, increases with both θ and We_{F}, while being clipped at $5\ \%$. Some of the wall films in the scrubber are terminated at an edge. These will inject the whole wall film into the domain again, which is shown in Figure 5.13. The diameter and the velocity of the injected droplets are again calculated using (5.15).

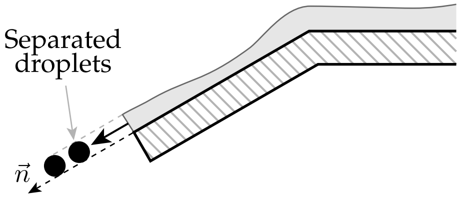

Figure 5.13: When a wall film terminates at an edge, the remaining mass flow will re-enter the domain as droplets. This implies that $\phi_{\mathrm{Sep}} = 1$.

5.6 Heat transfer

Each wall film element is coupled with the surrounding gas phase, and with the shell surfaces within the scrubber, on which the wall films are flowing along. Therefore, each wall film elements exchanges both thermal energy and mass with the gas phase, and thermal energy with the shell. The shell both conducts thermal energy, but is also coupled with the surrounding ambient air, where natural convection governs. These four thermal energy flows are described in this section, where an overview is shown in Figure 5.14. The subscripts $(...)_{\mathrm{g}}$, $(...)_{\mathrm{F}}$, $(...)_{\mathrm{S}}$, and $(...)_{\mathrm{A}}$ abbreviates *Gas*, *Film*, *Shell*, and *Ambient air* respectively.

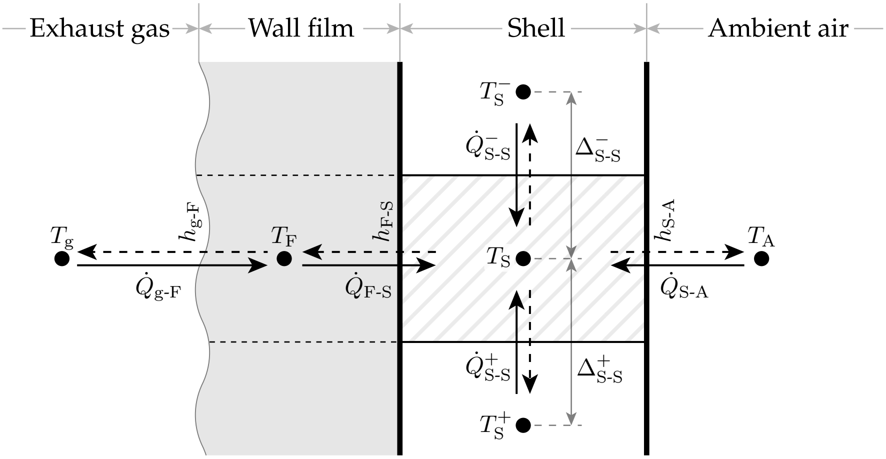

Figure 5.14: An overview of the different heat flows for a single wall film element. The solid arrows indicate the direction of positive $\dot{Q}$, whereas the dashed arrows indicate negative values.

As seen in Figure 5.14, each liquid wall film element exchanges heat with the gas phase and the solid shell, $\dot{Q}_{\text{g-F}}$ and $\dot{Q}_{\text{F-S}}$ respectively. Each shell element is connected to its neighbouring shell elements, where the superscripts $(...)^-$ and $(...)^+$ indicate the previous and next shell element respectively. The shell elements exchange thermal energy by conduction, $\dot{Q}_{\text{S-S}}$, and each shell element also exchanges heat with the surrounding ambient air by natural convection, $\dot{Q}_{\text{S-A}}$. The heat flows are calculated using (5.17).

$$\begin{aligned}
\dot{Q}_{\text{g-F}} &= A_{\text{g-F}} \cdot h_{\text{g-F}} \cdot (T_{\text{g}} - T_{\text{F}}) & \dot{Q}_{\text{S-S}}^- &= A_{\text{S-S}}^- \cdot \frac{\kappa_{\text{S}}}{\Delta_{\text{S-S}}^-} \cdot \left(T_{\text{S}}^- - T_{\text{S}}\right) \\
\dot{Q}_{\text{F-S}} &= A_{\text{F-S}} \cdot h_{\text{F-S}} \cdot (T_{\text{F}} - T_{\text{S}}) & \dot{Q}_{\text{S-S}}^+ &= A_{\text{S-S}}^+ \cdot \frac{\kappa_{\text{S}}}{\Delta_{\text{S-S}}^+} \cdot \left(T_{\text{S}}^+ - T_{\text{S}}\right) \\
\dot{Q}_{\text{S-A}} &= A_{\text{S-A}} \cdot h_{\text{S-A}} \cdot (T_{\text{A}} - T_{\text{S}})
\end{aligned} \tag{5.17}$$

κ_{S} is the thermal conductivity of the steel, where the scrubber in the Alfa Laval Test & Training Centre is built from $4\,\text{mm}$ 316L grade stainless steel, which has a thermal conductivity of approximately $14\ \text{W}/(\text{m} \cdot \text{K})$ [Nickel Institute (99)]. Under steady-state conditions, the net heat flow for each shell control volume is zero, which is stated in (5.18).

$$\dot{Q}_{\text{F-S}} + \dot{Q}_{\text{S-A}} + \dot{Q}_{\text{S-S}}^- + \dot{Q}_{\text{S-S}}^+ = 0 \tag{5.18}$$

In order to calculate the different heat flows, the heat transfer coefficients for the different energy flows, $h_{\text{g-F}}$, $h_{\text{F-S}}$, and $h_{\text{S-A}}$, are required, which are described in the following subsection.

5.6.1 Heat transfer coefficients

Gas-film heat transfer coefficient

$h_{\text{g-F}}$ is the heat transfer coefficient between the gas phase and the wall film as seen in Figure 5.14. This heat transfer coefficient is governed by the law-of-the-wall, which resolves the near wall properties of the continuous phase. The heat transfer coefficient is calculated in a similar manner to ANSYS Fluent, which requires multiple support variables, which are shown in (5.19) [ANSYS Inc. (6)] [Jayatilleke (75)].

$$\begin{aligned}
u^\star &= C_\mu^{0.25} \cdot \sqrt{k_\mathrm{t}} \\
y^\star &= \frac{\rho_\mathrm{g} \cdot u^\star \cdot y_\mathrm{P}}{\mu_\mathrm{g}} \\
Pr &= \frac{\mu_\mathrm{g} \cdot c_\mathrm{P}}{\kappa_\mathrm{g}} \\
P &= 9.24 \cdot \left(\left(\frac{Pr}{Pr_\mathrm{t}} \right)^{0.75} - 1 \right) \cdot \left(1 + 0.28 \cdot \exp\left(-0.007 \cdot \frac{Pr}{Pr_\mathrm{t}} \right) \right) \\
T_\mathrm{c} &= Pr_\mathrm{t} \cdot \left(\frac{1}{\kappa'} \cdot \log_\mathrm{e}\left(E \cdot y^\star \right) + P \right)
\end{aligned} \tag{5.19}$$

Where k_t is the turbulent kinetic energy, and y_P is the normal distance from the cell centre to the wall. The constants in (5.19) are shown in (5.20).

$$\begin{aligned}
y_\mathrm{T}^\star &= 11.63 & C_\mu &= 0.09 \\
Pr_\mathrm{t} &= 0.85 & \kappa' &= 0.4187 \\
E &= 9.794
\end{aligned} \tag{5.20}$$

The heat transfer coefficient is calculated based upon the location of the first cell in the computational domain, where two different correlations apply based on $y^\star$, which are shown in (5.21).

$$h_{\text{g-F}} = \begin{cases} \kappa_\mathrm{g} / y_\mathrm{P} & \text{if } \left(y^\star < y_\mathrm{T}^\star\right) \\ \dfrac{\rho_\mathrm{g} \cdot c_\mathrm{P} \cdot u^\star}{T_\mathrm{c}} & \text{if } \left(y^\star >= y_\mathrm{T}^\star\right) \end{cases} \tag{5.21}$$

$h_{\text{g-F}}$ is of the order of $50\ \mathrm{W}/\left(\mathrm{m}^2 \cdot \mathrm{K}\right)$. It should be noted that an extensive study was carried out in ANSYS Fluent to verify the implementation in OpenFOAM. $h_{\text{g-F}}$ is calculated from within OpenFOAM, and is subsequently transferred to MATLAB, where the wall films are modelled.

Film-shell heat transfer coefficient

$h_{\text{F-S}}$ is the heat transfer coefficient between the wall film and the shell as seen in Figure 5.14. The heat transfer coefficient is governed by forced convection, where the correlation used is shown in (5.22) [Cimbala et al. (25)].

$$\begin{aligned} Re_{\mathrm{x}} &= \frac{\rho_{\mathrm{l}} \cdot \bar{v}_{\mathrm{F}} \cdot x}{\mu_{\mathrm{l}}} \\ Pr_{\mathrm{l}} &= f(T) \\ Nu_{\text{F-S}} &= 0.037 \cdot Re_{\mathrm{x}}^{0.8} \cdot Pr_{\mathrm{l}}^{(1/3)} \\ h_{\text{F-S}} &= \frac{Nu_{\text{F-S}} \cdot \kappa_{\mathrm{l}}}{x} \end{aligned} \tag{5.22}$$

x is the characteristic length, and is the running length along the wall film. μ_{l} and Pr_{l} are evaluated as functions of the liquid temperature of the wall film based upon data from the software program *Engineering Equation Toolbox, EES* [F-Chart (47)], where the correlations are shown in *Chapter A: Constants and correlations*. $h_{\text{F-S}}$ is of the order of $2500\ \mathrm{W}/\left(\mathrm{m}^2 \cdot \mathrm{K}\right)$.

Shell-ambient air heat transfer coefficient

$h_{\text{S-A}}$ is the heat transfer coefficient between the shell and surrounding ambient air as seen in Figure 5.14, where the correlation used in this study is shown in (5.23) [Cimbala et al. (25)].

$$\begin{aligned} Gr &= \frac{g \cdot \beta \cdot (T_{\mathrm{S}} - T_{\mathrm{A}}) \cdot L^3}{\nu_{\mathrm{g}}^2} \\ Ra &= Gr \cdot Pr \\ Nu_{\text{S-A}} &= \left(0.825 + \frac{0.387 \cdot Ra^{(1/6)}}{\left(1 + (0.492/Pr)^{(9/16)}\right)^{(8/27)}}\right)^2 \\ h_{\text{S-A}} &= \frac{Nu_{\text{S-A}} \cdot \kappa_{\mathrm{g}}}{L} \end{aligned} \tag{5.23}$$

Where Gr is the *Grashof number*, and Ra is the *Rayleigh number*. For ideal gases, $\beta = 1/T$ apply, where the average temperature between the shell and the ambient air was used. The characteristic length, L, was chosen to be $3\ \mathrm{m}$, and the correlation for Nu is based upon natural convection for vertical surfaces. $h_{\text{S-A}}$ is of the order of $5\ \mathrm{W}/\left(\mathrm{m}^2 \cdot \mathrm{K}\right)$, so its effect is not significant.

5.6.2 Matrix algorithm

Having determined the three required heat transfer coefficients, the temperature of the shell can be determined. This is done using an iterative method, where each iteration solves a linear system of equations, which is formed by combining (5.17) and (5.18) for all shell elements. The linear equations for a single shell element is shown in (5.24).

$$\begin{bmatrix} \left(\frac{A^{-}_{\text{S-S}}\cdot\kappa_{\text{S}}}{\Delta^{-}}\right) \\ -\left((h\cdot A)_{\text{F-S}} + (h\cdot A)_{\text{S-A}} + \frac{A^{-}_{\text{S-S}}\cdot\kappa_{\text{S}}}{\Delta^{-}} + \frac{A^{+}_{\text{S-S}}\cdot\kappa_{\text{S}}}{\Delta^{+}}\right) \\ \left(\frac{A^{+}_{\text{S-S}}\cdot\kappa_{\text{S}}}{\Delta^{+}}\right) \end{bmatrix}^{\text{T}} \cdot \begin{bmatrix} T_{\text{S}}^{-} \\ T_{\text{S}} \\ T_{\text{S}}^{+} \end{bmatrix} = \\ -\left((h\cdot A)_{\text{F-S}}\cdot T_{\text{F}} + (h\cdot A)_{\text{S-A}}\cdot T_{\text{A}}\right) \tag{5.24}$$

Equation (5.24) can be defined for all shell elements, which yields a set of linear equation, that can be solved using Gauss elimination. The wall film temperature is updated for each iteration, and will thus yield the correct temperature, when steady-state has been achieved. Thus, the non-linear functions for $Pr_{\text{l}}(T)$ and $\mu_{\text{l}}(T)$ will be updated iteratively. The heat flux from the shell to the film, $\dot{Q}_{\text{F-S}}$, is implemented as a source term, so this term will also reach steady values as the simulation advances. A low pass filter is, again, used to increase stability for this sub-model, and this is defined in (5.25).

$$\overbrace{T_{\text{S}}^{\text{n}}}^{\substack{\text{Updated}\\\text{shell temperature}}} \leftarrow \underbrace{T_{\text{S}}^{\text{n}-1}}_{\substack{\text{Previous}\\\text{shell temperature}}} \cdot (1-\phi_{\text{LP}}) + \overbrace{T_{\text{S}}^{\text{n}}}^{\substack{\text{Solved}\\\text{shell temperature}\\\text{from (5.24)}}} \cdot \phi_{\text{LP}} \tag{5.25}$$

As seen in (5.25), only a fraction, ϕ_{LP}, of the new calculated value from (5.24) is used for each iteration, n. As the simulation is advanced, a steady-state solution is thus obtained.

5.7 Chemistry and mass transfer

The wall film chemistry is modelled according to *Chapter 3: Chemistry*, where all effects are taken into account for the films as well. However, the wall films are not solved in a transient manner, as is the discrete phase. Rather, it is steady-state solutions that are solved for. Therefore, the time-step, Δt, is not used for the wall films, but instead the local time-step is used, Δt_{F}, which was defined in (5.8) on page 130. This time-step is used in the governing chemistry equations described in *Chapter 3: Chemistry*, which makes the derived chemistry model applicable for the wall films as well.

Each wall film is coupled to the gas phase, where both thermal energy and species are transferred across the liquid interfaces of the wall films. The mass transfer of different species is calculated according to (3.9) on page 25, where the only unknown is the overall mass transfer coefficient, $\bar{k}_{\text{i}}$. This coefficient is a function of both the internal, $k_{\text{l,i}}$, and the external, $k_{\text{g,i}}$, mass transfer coefficients.

$k_{\mathrm{l,i}}$ is calculated in a similar manner to the discrete phase, which was described in *Section 4.9: Mass transfer coefficient*. Instead of using the droplet diameter as the characteristic length in the equations, the wall film height, H_{F}, is used instead. A more correct approach would be to derive correlations for a wall film, but it is assumed that the internal mass transfer coefficient, $k_{\mathrm{l,i}}$, will be in the correct range by using this approach.

$k_{\mathrm{g,i}}$ is calculated by using a *heat & mass transfer analogy*. This approach is used, as the gas-film heat transfer coefficient, $h_{\mathrm{g\text{-}F}}$, is calculated from within OpenFOAM using the law-of-the-wall. Therefore, this value takes the continuous phase turbulence into account, which was seen in (5.19) through (5.21) on page 138. The *Chilton and Colburn J-factor analogy* [Geankoplis (58)] is commonly used to relate mass and heat transfer coefficient, but the more generally applicable *Friend–Metzner analogy* is used in this study. This analogy is shown in (5.26) [Friend and Metzner (56)].

$$\frac{Sh}{Re \cdot Sc^{1/3}} = \frac{Nu}{Re \cdot Pr^{1/3}} \tag{5.26}$$

Equation (5.26) states that the Sh and Nu are related with $(Sc/Pr)^{1/3}$. Therefore, the mass transfer coefficient can be expressed in terms of the heat transfer coefficient, which is shown in (5.27).

$$\begin{aligned} Nu &= \frac{h_{\mathrm{g}} \cdot L}{\kappa_{\mathrm{g}}} \\ Sh &= \frac{k_{\mathrm{g,i}} \cdot L}{\mathscr{D}_{\mathrm{g,i}}} \\ &\Downarrow \text{Substitute into (5.26) and solve for } k_{\mathrm{g,i}} \\ k_{\mathrm{g,i}} &= h_{\mathrm{g}} \cdot \left(\frac{\mathscr{D}_{\mathrm{g,i}}}{\kappa_{\mathrm{g}}}\right) \cdot \left(\frac{Sc}{Pr}\right)^{1/3} \end{aligned} \tag{5.27}$$

The method of using the *Friend–Metzner analogy* is considered to be more accurate compared to a general correlation for liquid wall films, as the continuous phase turbulence is taken into account. Having obtained expressions for both $k_{\mathrm{l,i}}$ and $k_{\mathrm{g,i}}$, the overall mass transfer coefficient for the wall films, $\bar{k}_{\mathrm{i}}$, is calculated using the expression shown in (3.9) on page 25.

5.8 Drains

The drains for the wall film were described in *Section 4.11: Drains*, where $\dot{m}_{\mathrm{Film}}$ represents the mass flow of the final wall film element for any given wall film. The majority of the liquid exiting the scrubber is via the wall films, as most parcels hit the wall at some point before hitting the drain. However, if they do reach the drains, the parcels are eliminated from the simulation, where the removed mass and energy is stored such that mass and energy balances can be monitored.

5.9 Wall film variables

Each wall film element has a number of defining independent variables, which are listed in Table 5.1.

Table 5.1: Each wall film element has 14 degrees of freedom, which are listed in this table. Notice that $\vec{m}_{\text{Source}}$ theoretically only requires nine variables to be specified, but in practice all 18 components are included.

Name	Unit	Variables	Description
$\dot{E}_{\text{Source}}$	J/s	1	Thermal energy source term
$\vec{m}_{\text{Source}}$	kg/s	18 (9)	Species masses source terms
$\vec{\Psi}_{\text{Source}}$	$-/\text{s}$	4	Trace component source terms
$\sum$		23 (14)	

As seen in Table 5.1, 14 independent variables are required to fully define each wall film element. All of the independent variables are source terms from the discrete phase, which are calculated when the parcels are impinging the wall and depositing mass and energy as described in *Section 5.2: Film sources*. All other wall film properties, such as velocity, thickness etc., can be derived based on the independent variables. Once again, the mass source terms can be represented by only nine variables, but in practice all 18 species masses are used, as this was found easier to implement. Therefore, 23 variables are used in the scrubber model instead of the required minimum of 14.

6 CONTINUOUS PHASE

The exhaust gas passing through the scrubber consists of five major species: CO_2, H_2O, O_2, SO_2, and N_2. These components are assumed not to react with each other, although a slight oxidation of SO_2 with O_2 forms SO_3, but this is not included in this study, as previously described. The gas phase is governed by the Navier-Stokes equations, where both convection and diffusion transports the species inside the scrubber. In order to resolve the concentrations of the different species, a computational mesh is required, where the partial differential equations can be solved. The software package used in this study for solving these equations is OpenFOAM, where a custom solver was implemented for scrubber modelling. These three topics will be described in this chapter, which are illustrated in Figure 6.1.

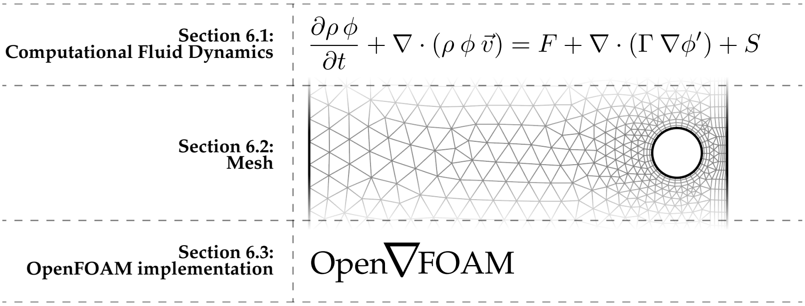

Figure 6.1: An overview of the three sections in this chapter.

Similar to the liquid phase, a component matrix for the gas phase can be defined, which is shown in (6.1).

$$\mathbf{C}_g = \begin{bmatrix} \vec{C}_C \\ \vec{C}_H \\ \vec{C}_O \\ \vec{C}_S \\ \vec{C}_N \\ \vec{C}_B \\ \vec{C}_{Na} \\ \vec{C}_{Cl} \end{bmatrix} = \left[\begin{array}{ccccc} CO_2 & H_2O & O_2 & SO_2 & N_2 \\ 1 & 0 & 0 & 0 & 0 \\ 0 & 2 & 0 & 0 & 0 \\ 2 & 1 & 2 & 2 & 0 \\ 0 & 0 & 0 & 1 & 0 \\ 0 & 0 & 0 & 0 & 2 \\ 0 & 0 & 0 & 0 & 0 \\ 0 & 0 & 0 & 0 & 0 \\ 0 & 0 & 0 & 0 & 0 \end{array}\right] \tag{6.1}$$

The component matrix for the gas phase, $\mathbf{C}_g$, in (6.1) will be used later in this study to evaluate the mole balance for each elementary component.

6.1 Computational Fluid Dynamics

The continuous phase is governed by the Navier-Stokes equations, which describe the motion of a fluid. These equations solve for a given set of scalars, where turbulence can be modelled by using a turbulence model. These scalars and equations are described in this section along with the applied boundary conditions in the continuous phase.

6.1.1 Scalars

The continuous phase is governed by the Navier-Stokes equation, which are solved on a mesh. Species fractions, momentum, energy, and turbulence is modelled, which results in 11 degrees of freedom for each computational cell, which are listed in Table 6.1.

Table 6.1: Each cell has 11 degrees of freedom, which are shown in this table.

Name	Unit	Scalars	Description
$\vec{v}_\mathrm{g}$	m/s	3	Velocity
$\vec{w}_\mathrm{g}$	kg/kg	4	Mass fractions
i	$\mathrm{J/(kg \cdot K)}$	1	Internal energy
P	Pa	1	Pressure
ω_t	1/s	1	Specific rate of dissipation
k_t	$\mathrm{m^2/s^2}$	1	Turbulent kinetic energy

All other continuous phase variables can be derived from the 11 independent variables in Table 6.1. The gas phase is assumed ideal, so the equation of state is used to couple temperature, pressure, and density, which is shown in (6.2).

$$\begin{gathered} P \cdot V = n \cdot R \cdot T_\mathrm{g} \\ \Downarrow \\ \rho_\mathrm{g} = \frac{P \cdot M_\mathrm{Mixture}}{R \cdot T_\mathrm{g}} \end{gathered} \tag{6.2}$$

Where M_Mixture is the molar mass of the mixture of species. By using (6.2), the density can be calculated from the independent variables within each computational cell. The internal energy is a function of density and temperature, where the enthalpy of the mixture is calculated according to *Chapter A: Constants and correlations*.

6.1.2 Turbulence modelling

Turbulence is modelled using the *k-ω-SST*, *Shear Stress Transport*, turbulence model [Menter (94)], which blends the k-ω and the k-ϵ models to utilize the strengths of both. The k-ω model is used in the inner region of the boundary layer, and switches to the k-ϵ in the outer regions and in shear flows. The turbulence model requires k_t and ω_t to be specified at the inlet, where the correlations in (6.3) are used to calculate these [ANSYS Inc. (6)]. The subscripts $(...)_\mathrm{t}$ indicate variables related to turbulence modelling.

$$\begin{aligned} Re_\mathrm{D} &= \frac{D_\mathrm{Inlet} \cdot v_\mathrm{Inlet} \cdot \rho_\mathrm{g}}{\mu_\mathrm{g}} & k_\mathrm{t} &= \frac{3}{2} \cdot \left(v_\mathrm{Inlet} \cdot I_\mathrm{t}\right)^2 \\ I_\mathrm{t} &= 0.16 \cdot \left(Re_\mathrm{D}\right)^{-1/8} & \omega_\mathrm{t} &= \frac{\sqrt{k_\mathrm{t}}}{l_\mathrm{t}} \\ l_\mathrm{t} &= \frac{0.07 \cdot D_\mathrm{Inlet}}{C_\mu^{3/4}} & \mu_\mathrm{t} &= \frac{\rho_\mathrm{g} \cdot k_\mathrm{t}}{\omega_\mathrm{t}} \end{aligned} \tag{6.3}$$

Re_D is calculated using the inlet properties measured during the experimental tests, and the diameter of the inlet pipe. I_t is the turbulent intensity, where the correlation in (6.3) is valid for fully developed pipe flows. l_t is the turbulent length scale, and is again a correlation, which is suitable for pipe flows. k_t, ω_t, and μ_t are all calculated based on the previous values in (6.3). The values of the different parameters are shown in Figure 6.2 for a typical exhaust gas stream, where the inlet velocity is varied and thus Re_D.

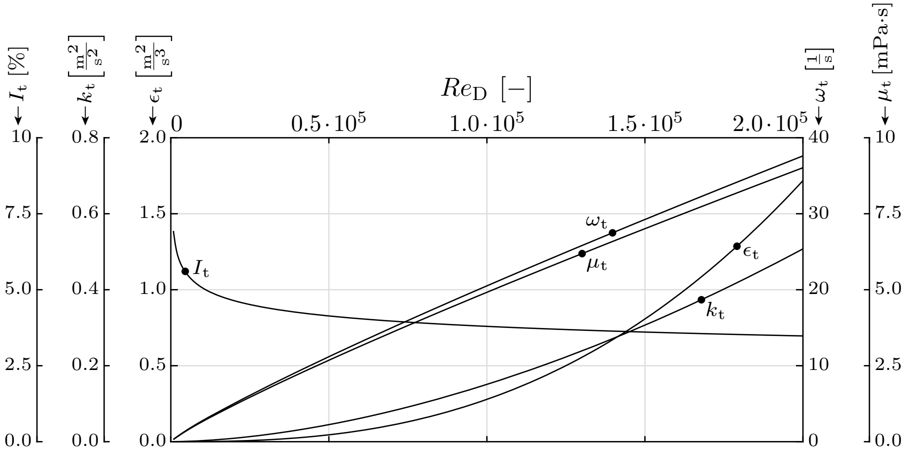

Figure 6.2: The turbulent inlet parameters as functions of Re_D for a typical exhaust gas stream, where D_Inlet is that of the scrubber used to verify the model.

As seen in Figure 6.2, the turbulent intensity decreases as a function of Re_D, as the relative velocity fluctuations decrease. ω_t and μ_t change with similar tendencies, but their values are, naturally, different, which can be seen on the two axes to the right of the figure.

6.1.3 Equations

The governing equations for the continuous gas phase can be stated in a single equation, which is the general transport equation, and is shown in (6.4) [Ferziger and Peric (48)].

$$\frac{\partial \rho \, \phi}{\partial t} + \nabla \cdot (\rho \, \phi \, \vec{v}) = F + \nabla \cdot (\Gamma \, \nabla \phi') + S \tag{6.4}$$

ϕ is any quantity or scalar, F is a force term, Γ is a diffusivity constant, ϕ' is a diffusivity scalar, and S is a source term. The equation stated in (6.4) can be used to define any of the governing equations by substituting ϕ, F, Γ, ϕ', and S with the specified terms shown in Table 6.2.

Table 6.2: The terms used to form the governing equations for the continuous gas phase. Each equation can be formed by substituting the terms in the table into (6.4) [Versteeg and Malalasekera (135)] [Ferziger and Peric (48)].

Equation	Scalar	Force term	Diffusivity constant	Diffusivity scalar	Source term
	ϕ	F	Γ	ϕ'	S
Continuity	1	0	0	0	$\sum \dot{m}_{\text{i}}/V$
x-Momentum	v_{x}	$-\frac{\partial P}{\partial x}$	μ_{Eff}	$v_{\text{x}} = \phi$	p_{x}
y-Momentum	v_{y}	$-\frac{\partial P}{\partial y}$	μ_{Eff}	$v_{\text{y}} = \phi$	p_{y}
z-Momentum	v_{z}	$-\frac{\partial P}{\partial z}$	μ_{Eff}	$v_{\text{z}} = \phi$	p_{z}
Energy	i	$-P \, \nabla \cdot \vec{v} + \Theta$	k	T	$\dot{Q}$
Species	y_{i}	0	μ_{Eff}	ϕ	$\dot{m}_{\text{i}}$

The two equations related to turbulence, k_{t} and ω_{t}, are not included in Table 6.2, as they include long terms, which are too extensive to display. Θ is a dissipation function, which contains all the effects due to viscous stresses in the internal energy equation [Versteeg and Malalasekera (135)], and μ_{Eff} is the effective viscosity, which takes the turbulent diffusivity into account.

6.1.4 Boundary conditions

Four different boundary types are present in the model, which are the inlet, the outlet, the shell, and the periodic boundaries, where the latter is explained in detail in the next section. The boundary conditions applied to each of the scalars shown in Table 6.1 are shown in Table 6.3, where the internal energy is expressed in terms of the gas temperature, T_{g}.

Table 6.3: The boundary conditions at the four different boundary types in the model.

Variable	Inlet	Outlet	Shell
P	Zero gradient	Fixed value ($1\ \mathrm{atm}$)	Zero gradient
T_g	Fixed value	Zero gradient	Zero gradient
$\vec{v}_\mathrm{g}$	Fixed value	Zero gradient	No-slip
$\vec{w}_\mathrm{g}$	Fixed value	Zero gradient	Zero gradient
k_t	Fixed value	Zero gradient	k_t wall function
ω_t	Fixed value	Zero gradient	ω_t wall function

As seen in Table 6.3, all scalars except P have fixed values at the inlet. A small error is induced for $\vec{v}_\mathrm{g}$, as the velocity is not uniform at the inlet, but this error is assumed negligible. The pressure at the inlet has a zero gradient boundary condition applied, as the pressure is fixed at the outlet, where the value of the static pressure is $1\ \mathrm{atm}$. All other scalars at the outlet have a zero gradient boundary condition applied, which acts normal to the mesh faces, which is in the axial direction of the scrubber. The no-slip condition is applied to $\vec{v}_\mathrm{g}$ at the surfaces, whereas wall functions are used for the two turbulence scalars. The remaining scalars have a zero gradient boundary condition applied at the shells.

6.2 Mesh

In order to solve the governing partial differential equations using the finite volume method, the scrubber domain is meshed into a finite number of cells. ANSYS Fluent Meshing is used for this purpose, as it allows for scripting the meshing process. This is beneficial, as a large number of meshes has to be generated for the mesh independence studies in *Chapter 8: Independence studies*.

6.2.1 Procedure

The automated meshing process consists of seven steps, which are illustrated in Figure 6.3 on the next page.

Step (1): The first step takes the defining parameters for the scrubber geometry, such as diameters, lengths, angles etc., and generates a geometry file based on these inputs. The geometry is saved as a .stl, *sterolithography*, file, which is a basic geometry format, where the geometry is defined using triangles only. A journal file, .jou, is generated as well, which contains the meshing commands to be executed by ANSYS Fluent Meshing. This file also holds information about the mesh sizes, refinement areas, inflation, prism layers etc.

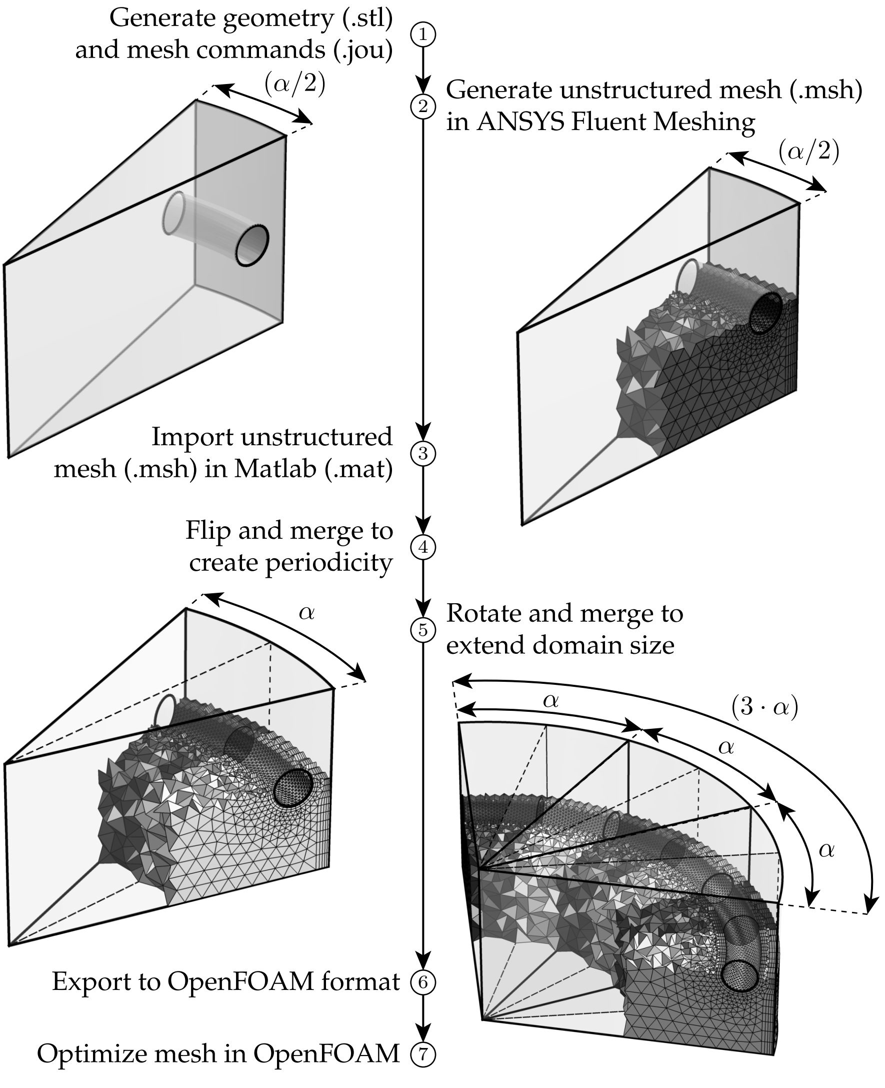

Figure 6.3: The process of creating the mesh illustrated in seven steps. An example geometry is used to illustrate this, where one of the rings leading to the sprayer nozzles is shown. The ring was illustrated in Figure 4.6 on page 64.

Step (2): This step launches ANSYS Fluent Meshing, which reads the .jou file. A series of commands are then executed automatically, which generates the volumetric mesh along with the prism layers. The final command saves the mesh as a .msh file, which is the default mesh format used by ANSYS Fluent for CFD calculations.

Step (3): The .msh file is imported into MATLAB by reading the raw ASCII formatted file. The mesh is subsequently saved as a .mat file, which is the data file format supported by MATLAB.

Step (4): This step reads the .mat file in MATLAB, and flips the mesh as shown in Figure 6.3. The shared faces are merged to create a single consistent mesh. By doing so, the periodic faces match each other, which ensures consistent results.

Step (5): This step duplicates the merged mesh generated in the fourth step and rotates it a number of times. The separate meshes are then merged, after which a consistent extended mesh is obtained. The different boundaries are subsequently identified and stored.

Step (6): This step exports the final mesh as an OpenFOAM supported mesh, which is again done from MATLAB, where routines were coded to do this process.

Step (7): This step executes an OpenFOAM command, which renumbers the mesh. This reduces the bandwidth of the mesh, which decreases the memory requirements and increases convergence rates [Sloan (120)].

6.2.2 Quality

The procedure described results in a mesh, which can be modified in both extent and quality. A number of different metrics can be used to evaluate the quality, where four common metrics are shown in (6.5) [ANSYS Inc. (7)].

$$\begin{aligned}
\text{Orthogonal quality} &= C_{\text{Type}} \cdot \text{Volume}/\sqrt{\left(\sum (\text{Edge length})^2\right)^3} \\
\text{Cell equiangle skew} &= \max\left(\frac{\theta_{\text{Max}} - \theta_{\text{e}}}{\pi - \theta_{\text{e}}}, \frac{\theta_{\text{e}} - \theta_{\text{Min}}}{\theta_{\text{e}}}\right) \\
\text{Cell equivolume skew} &= \frac{\text{Optimal cell size} - \text{Cell size}}{\text{Optimal cell size}} \\
\text{Cell volume change} &= \max\left(\frac{\text{Neighbour cell volume}}{\text{Cell volume}}\right)
\end{aligned} \tag{6.5}$$

Where C_{Type} is a constant, which is different for each cell type. θ_{e} is the equiangular angle for the face type, and θ_{Max} and θ_{Min} are the largest and smallest angles for each face. The different metrics in (6.5) are evaluated for a typical mesh generated using the procedure described, where a histogram of the orthogonal quality is shown in Figure 6.4.

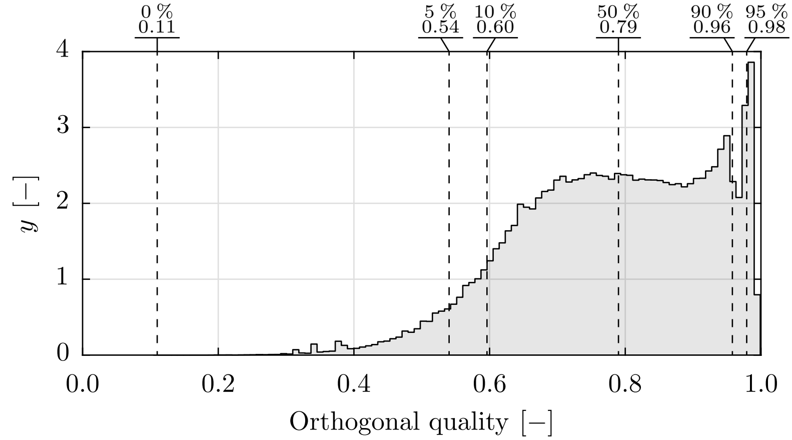

Figure 6.4: A histogram for the orthogonal quality for a typical mesh generated using the described procedure.

As seen in Figure 6.4, the orthogonal quality spans between 0 and 1, where a value of 1 indicates the best quality. The vertical dashed lines indicate the 5, 10, 50, 90 and 95 $\%$ fractiles, which are shown for each metric in Table 6.4.

Table 6.4: The mesh quality for a typical mesh reported using fractiles as shown in Figure 6.4. The values in parentheses are indicating the optimal values, where the mesh quality is the best.

	Fractile						
Metric	0 %	5 %	10 %	50 %	90 %	95 %	100%
Orthogonal quality	0.11	0.54	0.60	0.79	0.96	0.98	(1.00)
Cell equiangle skew	(0.00)	0.02	0.04	0.30	0.45	0.49	0.84
Cell equivolume skew	(0.00)	0.02	0.03	0.21	0.40	0.46	0.89
Cell volume change	1.00	1.00	1.01	1.22	1.68	1.95	12.48

As seen in Table 6.4, most cells have a good quality, although some cells do not. This can be seen for the skewness parameters for the 100% fractiles, which are the largest overall values. The 95 $\%$ fractile indicates that the fraction of bad cells is minor, and simulations proved to converge well, which indicates a good overall mesh.

The k-ω-SST model is used to model turbulence in this study, as previously described, where wall functions are used to model different flow scalars near the wall. This requires the cell heights close to the wall to be small, where the dimensionless y^+ parameter is commonly used to quantify these distance, and is shown in (6.6).

$$y^+ = \frac{v_\tau \cdot y}{\nu_\mathrm{g}} \qquad v_\tau = \sqrt{\frac{\tau_\mathrm{W}}{\rho_\mathrm{g}}} \tag{6.6}$$

The first prism layer near the shell was defined with a height of $3\,\mathrm{mm}$, which should result in $y^+ = 30$ for a velocity of approximately $4\,\mathrm{m/s}$. The y^+ parameter was analysed in the scrubber model for a typical case, where the results are shown in Figure 6.5.

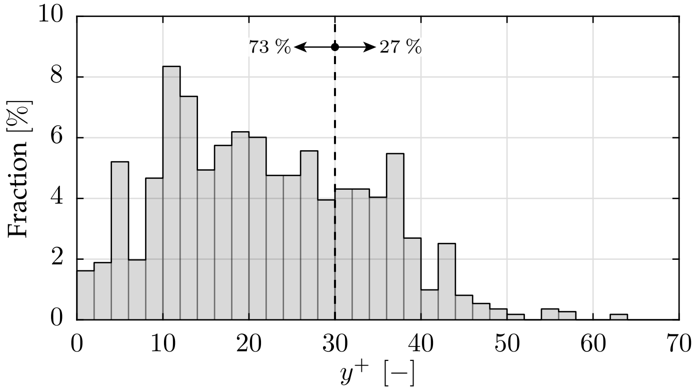

Figure 6.5: A histogram of y^+ for a typical simulation.

As seen in Figure 6.5, 73 % of the y^+ face values are below 30, whereas the remaining faces span up to approximately 65. However, only a small fraction is greater than $y^+ > 45$.

6.3 OpenFOAM implementation

OpenFOAM is a freeware product released under the *General Public License* [Free Software Foundation, Inc. (53)] by the OpenFOAM Foundation [The OpenFOAM Foundation (130)]. OpenFOAM allows the user to define their own solvers, which are specialized to solve a specific problem. The usual procedure, when coding a solver, is to modify an existing one. The *reactingFoam* solver was used as a template in this study, where descriptions of the changes made are shown below:

- **Disabled combustion**
  The *reactingFoam* solver is used for combustion of species. However, no combustion is present in a wet scrubber, so this model was removed to decrease computational requirements.
- **Heat transfer coefficient calculations**
  The heat transfer coefficient on each wall face needed to be calculated in order to evaluate the heat flux from the wall film to the continuous phase. The correlations implemented are the same used in ANSYS Fluent, which were described in *Section 5.6: Heat transfer*.

- **Timing controls**
  The solver was divided into several parts, which could timed during execution, such that the time-consuming portion of the code could be optimized. The time consumption of the different parts are shown in *Chapter 11: Example case*.
- **Cell specific source terms**
  A standard library for defining the source terms for each individual cell was not available. Therefore, a procedure for doing this was implemented, such that the source terms from MATLAB could be assigned for each cell.
- **Link library**
  The link structure is a significant part of the model, as it allows OpenFOAM to be coupled with MATLAB. This part needed to be coded *ab initio* and implemented in parallel for the model to work.
  Parallel considerations were required to defined the link structure, as MATLAB requires information about the computational core association of each cell and face of the mesh to write the source terms in the correct order, such that OpenFOAM could interpret these correctly. This is further described in *Chapter 7: Phase coupling*.

7 PHASE COUPLING

The liquid phase is modelled in MATLAB, and the continuous phase is modelled in OpenFOAM, so when carrying out a simulation, both programs run simultaneously. These two software packages must be able to communicate, such that the phases can interact. The liquid dispersed and wall film phases require data values from the continuous phase, which are defined on the mesh, and the continuous phase requires source terms for each cell. These data must be efficiently communicated between the programs in order to decrease computational requirements.

This chapter describes the method of distributing the source terms from the discrete phase and the wall film to the CFD mesh, and how the source terms are smoothed and linearised to increase stability. Mass, energy, and mole balances must be satisfied, which required summing all flows going in and out of the scrubber, and is described in *Section 7.3: Mass, energy, and mole balances*. The method, at which the two software programs are communicating, is explained as well, and, lastly, an overview of the complete scrubber model is visualized, where the interactions between all sub-models are shown.

7.1 Source terms

The source terms are calculated from within MATLAB and are sent to OpenFOAM, where the continuous phase is modelled. Both the discrete phase and the wall film phase contribute to the summed source terms, which is shown in (7.1) for any given cell.

$$\begin{aligned} \varphi_{\sum}^{\mathrm{n}} &= \varphi_{\mathrm{D}}^{\mathrm{n}} + \varphi_{\mathrm{F}}^{\mathrm{n}} \\ \bar{\varphi}_{\sum}^{\mathrm{n}} &\leftarrow \bar{\varphi}_{\sum}^{\mathrm{n}-1} \cdot (1 - \phi_{\mathrm{LP}}) + \varphi_{\sum}^{\mathrm{n}} \cdot \phi_{\mathrm{LP}} \end{aligned} \tag{7.1}$$

Where φ_{D} and φ_{F} are the source terms for the discrete phase and the wall film phase respectively, and $\varphi_{\sum}$ is the sum of these. For each iteration, n, a low pass filter ensures, that the source terms communicated to OpenFOAM from MATLAB are filtered, which is shown in the lower equation, where ϕ_{LP} is a relaxation factor. φ_{D} and φ_{F} are described in the following two subsections.

7.1.1 Discrete phase source terms

In order to couple the discrete phase with the continuous phase, source terms between these phases must be calculated, φ_{D}. This requires the mass, energy, and momentum rates for all parcels to be calculated and distributed to the mesh cells. A typical approach to execute this task is to consider the time each parcel resides inside each cell, which is illustrated in Figure 7.1.

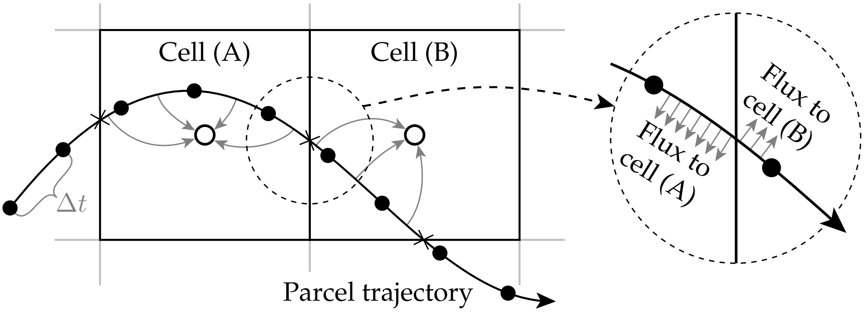

Figure 7.1: The method of distributing the parcel flux to the computational CFD mesh. The flux is either mass, energy, or momentum rates.

Figure 7.1 shows a parcel moving through a computational CFD mesh, where two cells, A and B, are shown. The black dots indicate different discrete time-steps, which are separated by Δt in time. The exchange rates of mass, momentum, and energy is temporally integrated, where the resulting flux is distributed to the current cell, in which the parcel is located. This is indicated by the thin grey arrows. When the parcel moves from cell A to cell B during a time-step, the intersection with the shared face is calculated, and the parcel flux is integrated to cell B instead of cell A. This is illustrated in the right part of the figure. The distribution of flux to either of the cells is shown in Figure 7.2, where an example related to heat flux, $\dot{Q}$, is shown

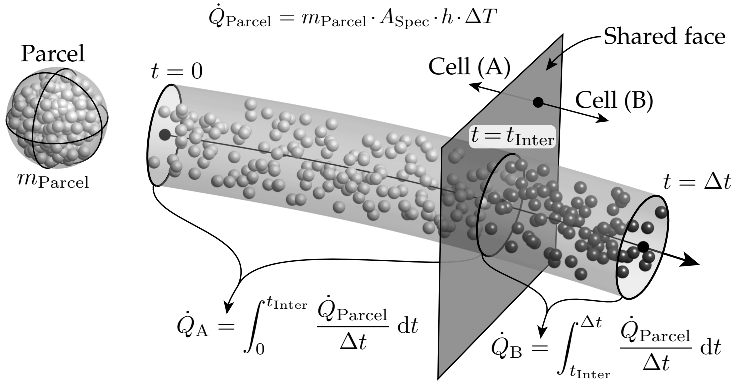

Figure 7.2: An example of the integration of flux, which is distributed to either cell A or B dependent on the position of the parcel.

As seen in Figure 7.2, a parcel, which contains a finite number of identical droplets, is moving from cell A to cell B. The parcel can be interpreted as a streamtube during a time-step, where the droplets are distributed over the trajectory between $t = 0$ and $t = \Delta t$. The flux of thermal energy, $\dot{Q}_{\mathrm{Parcel}}$, is shown in the top, where A_{Spec} $\left[\mathrm{m}^2/\mathrm{kg}\right]$ is the specific surface area, which is a function of the droplet size. The flux of thermal energy to cell A, $\dot{Q}_{\mathrm{A}}$, is calculated by integrating $\dot{Q}_{\mathrm{Parcel}}/\Delta t$ from $t = 0$ to $t = t_{\mathrm{Inter}}$, where t_{Inter} is the time, where the parcel intersects the shared face between the two cells. The same can be done for cell B, where the integrated heat flux is $\dot{Q}_{\mathrm{B}}$.

This method is accurate for calculating source terms within each cell, but typically a smoothing term is applied, such that the source terms are distributed to the surrounding cells in order to increase stability [ANSYS Inc. (6)], as otherwise spikes in the sources terms are likely to occur. A drawback of the method is that the intersections with all the faces must be calculated, which is computationally expensive - especially for 3D simulations. Therefore, this study proposes an alternative approach, which sums the parcel source terms on the mesh nodes, and subsequently distribute the source terms to the cells connected. This induces a small error, but the calculation of the face intersections can be omitted, so instead, the nearest node is the only requirement for this approach, which is illustrated in Figure 7.3.

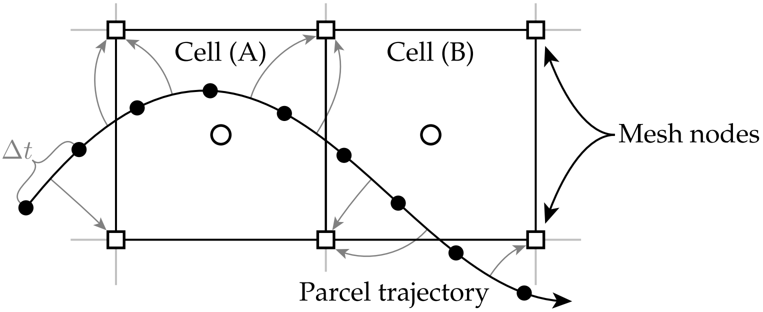

Figure 7.3: The method of distribution the parcel flux to the nearest node of the CFD mesh, which are shown as the white squares.

As the parcel travels through the computational CFD mesh, the closest mesh node is located, which is computationally cheap to find using the *k-d tree* algorithm [Friedman et al. (54)], which is efficiently implemented in MATLAB. The flux is distributed to the mesh nodes using a similar approach to Figure 7.2, but no mesh intersection detection is required. Having distributed the flux to the nodes, the rates are redistributed to the connected cells of each mesh node. This is shown in (7.2), where $\vec{\varphi}_{\mathrm{N}}$ is the node flux vector, $\vec{\varphi}_{\mathrm{C}}$ is the distributed cell flux vector, and $\vec{\bar{\varphi}}_{\mathrm{C}}$ is the smoothened cell flux vector.

$$\begin{aligned}
&\text{(Project node flux to connected cells)} && \vec{\varphi}_{\mathrm{C}} = \mathbf{K}_{\mathrm{N}\rightarrow\mathrm{C}} \cdot \vec{\varphi}_{\mathrm{N}} \\
&\text{(Smooth cell sources)} && \bar{\vec{\varphi}}_{\mathrm{C}} = \mathbf{K}_{\mathrm{C}\rightarrow\bar{\mathrm{C}}} \cdot \vec{\varphi}_{\mathrm{C}} \\
& && \Downarrow \\
&\text{(Project and smooth)} && \bar{\vec{\varphi}}_{\mathrm{C}} = \underbrace{\mathbf{K}_{\mathrm{C}\rightarrow\bar{\mathrm{C}}} \cdot \mathbf{K}_{\mathrm{N}\rightarrow\mathrm{C}}}_{\mathbf{K}_{\mathrm{N}\rightarrow\bar{\mathrm{C}}}} \cdot \vec{\varphi}_{\mathrm{N}}
\end{aligned} \tag{7.2}$$

The matrices, $\mathbf{K}$, are large sparse matrices, which are pre-computed, as the mesh is stationary and does not change over time. The matrix $\mathbf{K}_{\mathrm{N}\rightarrow\bar{\mathrm{C}}}$ indicates which cells to redistribute the node flux to. It takes the distance from the node to the cell centres into account along with the cell volumes, which is shown in (7.3). I_{Sub} is the subset of cells, which are connected to the node, and the subscripts iC and iN indicate the i^{th} cell and node respectively. $\vec{X}$ is the position of the cell or node.

$$\begin{aligned}
&\text{(Volume weight)} && w_{\mathrm{iC}}^{\mathrm{Vol}} = V_{\mathrm{iC}} \\
&\text{(Distance weight)} && w_{\mathrm{iN}\rightarrow\mathrm{iC}}^{\mathrm{Dist}} = \frac{1}{\sqrt{2\cdot\pi\cdot\sigma^2}} \cdot \exp\left(-\frac{\left|\vec{X}_{\mathrm{iN}} - \vec{X}_{\mathrm{iC}}\right|^2}{2\,\sigma^2} \right) \\
&\text{(Product weight)} && w_{\mathrm{iN}\rightarrow\mathrm{iC}}^{\mathrm{Prod}} = w_{\mathrm{iN}\rightarrow\mathrm{iC}}^{\mathrm{Vol}} \cdot w_{\mathrm{iN}\rightarrow\mathrm{iC}}^{\mathrm{Dist}} \\
&\text{(Normalized weight)} && w_{\mathrm{iN}\rightarrow\mathrm{iC}} = \frac{w_{\mathrm{iN}\rightarrow\mathrm{iC}}^{\mathrm{Prod}}}{\sum\limits_{\mathrm{iC}\in\mathrm{I_{Sub}}} w_{\mathrm{iN}\rightarrow\mathrm{iC}}^{\mathrm{Prod}}}
\end{aligned} \tag{7.3}$$

The weights, w, are assigned to $\mathbf{K}_{\mathrm{N}\rightarrow\bar{\mathrm{C}}}$ such that (7.2) is satisfied. σ is found by solving the equation stated in (7.4), which is illustrated in Figure 7.4.

$$\frac{1}{2} \cdot \left(1 + \operatorname{erf}\left(\frac{x_{\mathrm{Target}}}{\sigma\cdot\sqrt{2}} \right) \right) = Y_{\mathrm{Target}} \tag{7.4}$$

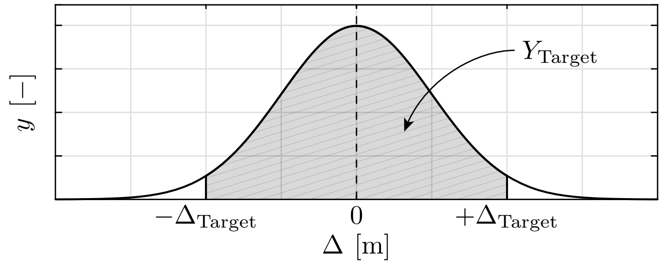

Figure 7.4: The method of determining σ, where the integral of the probability density function between $-\Delta_{\mathrm{Target}}$ and $+\Delta_{\mathrm{Target}}$ is Y_{Target}.

The value of σ is calculated using the cumulative density function, which is shown in (7.4). Using $Y_{\mathrm{Target}} = 90\ \%$ and $x_{\mathrm{Target}} = 10\ \mathrm{cm}$, the standard deviation is $\sigma = 0.432$, which is used in this study. This indicates that the node flux is distributed to the cells within a distance of 10 cm around each node, where the fraction is determined using (7.3). Therefore, the nodes closest to the parcel receives significantly more flux compared to those, which are located farther away. It should be noted that the proposed method is independent of the mesh size.

7.1.2 Eulerian wall film source terms

The wall films are coupled with the continuous phase, where thermal energy and species are transferred through the liquid interface as described in *Section 5.6: Heat transfer* and *Section 5.7: Chemistry and mass transfer*. In order to couple the wall films with the continuous phase, the source terms in the cells near the walls must be altered. Ideally, only the source term of the cells closest to the wall should be modified. However, in reality it is assumed that the films are more chaotic compared to the computational analogy, so the source terms are distributed around each wall film element, which also increases the stability of the overall model, as large source terms are avoided near the wall. A sketch of the wall film influencing the continuous phase is shown in Figure 7.5.

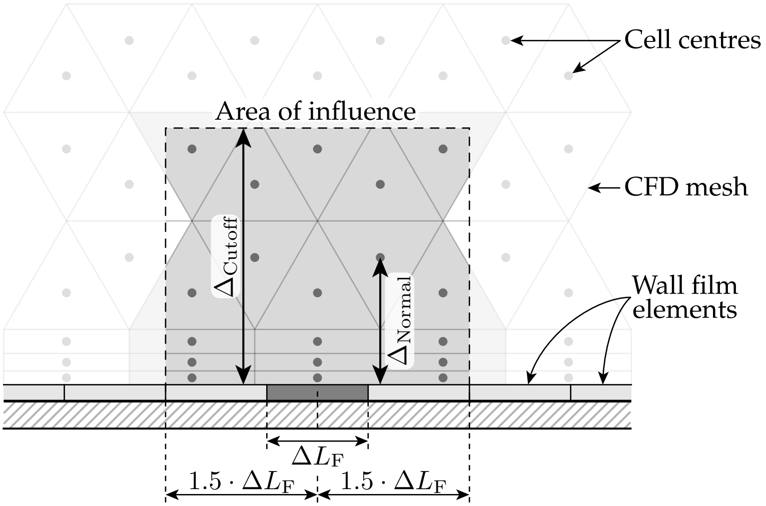

Figure 7.5: The method of coupling a wall film with the continuous phase. Each wall film element influences the cells closest to the wall within a normal distance of Δ_{Cutoff}.

Figure 7.5 shows a number of wall film elements, where the middle one is highlighted. This single element has an area of influence, which is defined relative to the centre of the element. The area spans $3 \cdot \Delta L_{\mathrm{F}}$ along the shell, and Δ_{Cutoff} into the continuous domain, which was chosen to be $\Delta_{\mathrm{Cutoff}} = 2.5$ cm in the model. Each cell within this area is affected by the source terms from the highlighted wall film element with a given weight, $w_{\mathrm{iF}\to\mathrm{iC}}$, where the normal distance, Δ_{Normal}, is used to calculate this. 19 cells are located within the area of influence for the highlighted wall element in Figure 7.5, where the weights are calculated using a Gaussian smoothing kernel, which is shown in (7.5). iC and iF are the i^{th} cell and wall film element respectively.

$$\begin{aligned} w'_{\text{iF}\rightarrow\text{iC}} &= \frac{1}{\sqrt{2\cdot\pi\cdot\sigma^2}}\cdot\exp\left(-\frac{\Delta_{\text{Normal}}}{2\cdot\sigma^2}\right) \\ w_{\text{iF}\rightarrow\text{iC}} &= \frac{w'_{\text{iF}\rightarrow\text{iC}}}{\sum_{\text{iC}} w'_{\text{iF}\rightarrow\text{iC}}} \\ &\Downarrow \\ \sum_{\text{iC}} w_{\text{iF}\rightarrow\text{iC}} &= 1.0 \end{aligned} \tag{7.5}$$

The first equation calculates the weight for the iC^{th} cell for the iF^{th} wall film element. The sum of the weights from the first step does not equal unity, which is required for mass and energy balances to be satisfied. Therefore, the weights are normalized in the second equation, such that the sum equals unity.

The weights are stored in a large matrix, $\mathbf{K}_{\text{F}\rightarrow\text{C}}$. 15 wall films are present in the model, where these have a total of approximately 600 wall film elements. Assuming a 3D mesh with approximately 10^6 cells, the weight matrix would have a size of $\left(600 \times 10^6\right)$, so in order to reduce the computational memory required, the weights are stored in a sparse matrix, which mainly consists of zeros. Having defined $\mathbf{K}_{\text{F}\rightarrow\text{C}}$, the source terms for a given scalar for all cells, $\vec{\varphi}_{\text{C}}$, is calculated using (7.6), where $\vec{\varphi}_{\text{F}}$ is the source terms from the wall film.

$$\vec{\varphi}_{\text{C}} = \mathbf{K}_{\text{F}\rightarrow\text{C}}\cdot\vec{\varphi}_{\text{F}} \tag{7.6}$$

In order to model the wall films according to *Chapter 5: Eulerian wall films*, various continuous phase properties are required, such a temperature, viscosity, density etc. These must be projected from the continuous phase to the wall film elements, which is simply done by using the weight matrix transposed, $\mathbf{K}^{\text{T}}_{\text{F}\rightarrow\text{C}}$. This is shown in (7.7), where λ is any given flow property.

$$\begin{aligned} \mathbf{K}_{\text{C}\rightarrow\text{F}} &= \mathbf{K}^{\text{T}}_{\text{F}\rightarrow\text{C}} \\ \vec{\lambda}_{\text{F}} &= \mathbf{K}_{\text{C}\rightarrow\text{F}}\cdot\vec{\lambda}_{\text{C}} \end{aligned} \tag{7.7}$$

The matrix $\mathbf{K}_{\text{F}\rightarrow\text{C}}$ is calculated for each of the 15 wall films prior to starting the simulation, so these matrices are only computed once.

7.2 Linearisation and damping

When solving the governing equations of fluid dynamics, the equations are defined as linear systems of equations, which are solved iteratively. In order to increase stability, when solving these equations, the source terms can be linearised. This is common practice, as it increases convergence rate and stability. A linear system of equation is shown in (7.8), which can be any of the equations to be solved during a CFD simulation, which were shown in Table 6.2 on page 146.

$$\begin{aligned} \mathbf{A} \cdot \vec{x}^{n+1} &= \vec{b} + \vec{\varphi} \\ \mathbf{A} \cdot \vec{x}^{n+1} &= \vec{b} + \vec{\varphi}_{\mathrm{u}} + \vec{\varphi}_{\mathrm{p}} \cdot \vec{x}^{n+1} \end{aligned} \tag{7.8}$$

The source term vector in (7.8) is $\vec{\varphi}$, and holds information about the source terms in each of the cells. $\vec{\varphi}$ can be divided into a constant term, φ_{u}, and a linearised term, φ_{p}. $\vec{x}$ is updated for each iteration, as it is the variable, which is solved for. However, the source terms are not recalculated for each iteration, as this requires MATLAB to advance the discrete phase and give back control to OpenFOAM. Instead, OpenFOAM performs a number of iterations before writing the updated data and giving control to MATLAB again. Therefore, the linearised source term, $\vec{\varphi}_{\mathrm{p}}$, is calculated and sent to OpenFOAM from MATLAB. An example is given for heat transfer in (7.9).

$$\begin{aligned} \dot{Q} &= h \cdot A \cdot (T_{\mathrm{g}} - T_{\mathrm{l}}) \\ \varphi_{\mathrm{u}} &= -\dot{Q} \\ \varphi_{\mathrm{p}} &= -\frac{\partial \dot{Q}}{\partial T_{\mathrm{g}}} = -h \cdot A \end{aligned} \tag{7.9}$$

$\dot{Q}$ is positive when the liquid phase is increasing in temperature, which is consistent with the previous chapters. The values of φ_{u} and φ_{p} are calculated from within MATLAB for each parcel, and are distributed to the cells similar to the source terms described in *Section 7.1: Source terms*. The inclusion of the linearised source terms increases stability and convergence rate. It should be noted that only the thermal energy rate and the momentum sources are linearised, whereas the mass sources are not. Therefore, the source files sent to OpenFOAM from MATLAB contains the following 12 values for each cell: $\dot{Q}, p_{\mathrm{x}}, p_{\mathrm{y}}, p_{\mathrm{z}}, \dot{m}_{\mathrm{CO_2}}, \dot{m}_{\mathrm{H_2O}}, \dot{m}_{\mathrm{O_2}}, \dot{m}_{\mathrm{SO_2}}, \frac{\partial \dot{Q}}{\partial T_{\mathrm{g}}}, \frac{\partial p_{\mathrm{x}}}{\partial v_{\mathrm{x}}}, \frac{\partial p_{\mathrm{y}}}{\partial v_{\mathrm{y}}}$, and $\frac{\partial p_{\mathrm{y}}}{\partial v_{\mathrm{z}}}$.

7.3 Mass, energy, and mole balances

Numerous sub-models make up the scrubber model, which were implemented in MATLAB, and a solver was developed in OpenFOAM. In order to validate the implementation, mass, elementary mole components, and energy balances must be ensured, so these parameters are continuously evaluated during simulation. The overall mass flows going in and out of the scrubber are illustrated in Figure 7.6, where the components of the liquid, $\vec{\dot{m}}_{\mathrm{l}}$, and gas, $\vec{\dot{m}}_{\mathrm{g}}$, vectors are shown as well.

$$\vec{\dot{m}}_{\mathrm{l}} = \begin{bmatrix} \dot{m}_{\mathrm{l,H_2O}} \\ \dot{m}_{\mathrm{l,H^+}} \\ \dot{m}_{\mathrm{l,OH^-}} \\ \dot{m}_{\mathrm{l,O_2}} \\ \dot{m}_{\mathrm{l,CO_2}} \\ \dot{m}_{\mathrm{l,H_2CO_3}} \\ \dot{m}_{\mathrm{l,HCO_3^-}} \\ \dot{m}_{\mathrm{l,CO_3^{2-}}} \\ \dot{m}_{\mathrm{l,H_2SO_3}} \\ \dot{m}_{\mathrm{l,HSO_3^-}} \\ \dot{m}_{\mathrm{l,SO_3^{2-}}} \\ \dot{m}_{\mathrm{l,H_2SO_4}} \\ \dot{m}_{\mathrm{l,HSO_4^-}} \\ \dot{m}_{\mathrm{l,SO_4^{2-}}} \\ \dot{m}_{\mathrm{l,B(OH)_3}} \\ \dot{m}_{\mathrm{l,B(OH)_4^-}} \\ \dot{m}_{\mathrm{l,Salt}} \\ \dot{m}_{\mathrm{l,H_E^+}} \end{bmatrix} \qquad \vec{\dot{m}}_{\mathrm{g}} = \begin{bmatrix} \dot{m}_{\mathrm{g,CO_2}} \\ \dot{m}_{\mathrm{g,H_2O}} \\ \dot{m}_{\mathrm{g,O_2}} \\ \dot{m}_{\mathrm{g,SO_2}} \\ \dot{m}_{\mathrm{g,N_2}} \end{bmatrix}$$

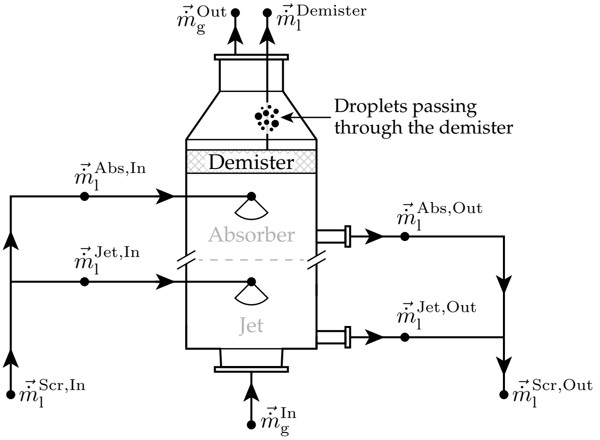

Figure 7.6: The flows going in and out of the scrubber. The mass flow vectors $\vec{\dot{m}}_{\mathrm{l}}$ and $\vec{\dot{m}}_{\mathrm{g}}$ are shown to the left, where all components in the two phases are shown.

As seen in Figure 7.6, multiple flows are entering and exiting the scrubber. It should be noted that $\vec{\dot{m}}_{\mathrm{l}}^{\mathrm{Demister}}$ is the liquid droplets, which are passing through the demister, which was described in *Section 4.8: Demister*. At steady-state, the mass flow going in and out should be equal, which is stated in (7.10).

$$\begin{aligned}
\dot{m}_{\Sigma}^{\mathrm{In}} &= \sum\left(\overbrace{\vec{\dot{m}}_{\mathrm{l}}^{\mathrm{Jet,In}} + \vec{\dot{m}}_{\mathrm{l}}^{\mathrm{Abs,In}}}^{\vec{\dot{m}}_{\mathrm{l}}^{\mathrm{Scr,In}} = \vec{\dot{m}}_{\mathrm{l}}^{\mathrm{In}}}\right) + \sum \vec{\dot{m}}_{\mathrm{g}}^{\mathrm{In}} \\
\dot{m}_{\Sigma}^{\mathrm{Out}} &= \sum\left(\underbrace{\overbrace{\vec{\dot{m}}_{\mathrm{l}}^{\mathrm{Jet,Out}} + \vec{\dot{m}}_{\mathrm{l}}^{\mathrm{Abs,Out}}}^{\vec{\dot{m}}_{\mathrm{l}}^{\mathrm{Scr,Out}}} + \vec{\dot{m}}_{\mathrm{l}}^{\mathrm{Demister}}}_{\vec{\dot{m}}_{\mathrm{l}}^{\mathrm{Out}}}\right) + \sum \vec{\dot{m}}_{\mathrm{g}}^{\mathrm{Out}} \\
\dot{m}_{\Sigma}^{\mathrm{In}} &= \dot{m}_{\Sigma}^{\mathrm{Out}}
\end{aligned} \tag{7.10}$$

Equation (7.10) applies to the overall mass flow, but as each stream is a vector of different species, the elementary components can be calculated using the component matrices, $\mathbf{C}_{\mathrm{l}}$, and $\mathbf{C}_{\mathrm{g}}$, which were defined in (3.26) on page 35 and (6.1) on page 143 respectively. Elementary component balance should also be satisfied at steady-state, which is stated in (7.11), where $\vec{\dot{m}}_{\mathrm{l}}^{\mathrm{In}}$ and $\vec{\dot{m}}_{\mathrm{l}}^{\mathrm{Out}}$ are the overall liquid mass flows, which were defined in (7.10).

$$
\begin{aligned}
\vec{\dot{n}}^{\mathrm{In}}_{\sum} &= \begin{bmatrix} \dot{n}_{\mathrm{C}} \\ \dot{n}_{\mathrm{H}} \\ \dot{n}_{\mathrm{O}} \\ \dot{n}_{\mathrm{S}} \\ \dot{n}_{\mathrm{N}} \\ \dot{n}_{\mathrm{B}} \\ \dot{n}_{\mathrm{Na}} \\ \dot{n}_{\mathrm{Cl}} \end{bmatrix}^{\mathrm{In}}_{\sum} = \mathbf{C}_{\mathrm{l}} \cdot \overbrace{\left(\vec{\dot{m}}^{\mathrm{In}}_{\mathrm{l}} \oslash \vec{M}_{\mathrm{l}}\right)}^{\vec{\dot{n}}^{\mathrm{In}}_{\mathrm{l}}} + \mathbf{C}_{\mathrm{g}} \cdot \overbrace{\left(\vec{\dot{m}}^{\mathrm{In}}_{\mathrm{g}} \oslash \vec{M}_{\mathrm{g}}\right)}^{\vec{\dot{n}}^{\mathrm{In}}_{\mathrm{g}}} \\
\vec{\dot{n}}^{\mathrm{Out}}_{\sum} &= \begin{bmatrix} \dot{n}_{\mathrm{C}} \\ \dot{n}_{\mathrm{H}} \\ \dot{n}_{\mathrm{O}} \\ \dot{n}_{\mathrm{S}} \\ \dot{n}_{\mathrm{N}} \\ \dot{n}_{\mathrm{B}} \\ \dot{n}_{\mathrm{Na}} \\ \dot{n}_{\mathrm{Cl}} \end{bmatrix}^{\mathrm{Out}}_{\sum} = \mathbf{C}_{\mathrm{l}} \cdot \overbrace{\left(\vec{\dot{m}}^{\mathrm{Out}}_{\mathrm{l}} \oslash \vec{M}_{\mathrm{l}}\right)}^{\vec{\dot{n}}^{\mathrm{Out}}_{\mathrm{l}}} + \mathbf{C}_{\mathrm{g}} \cdot \overbrace{\left(\vec{\dot{m}}^{\mathrm{Out}}_{\mathrm{g}} \oslash \vec{M}_{\mathrm{g}}\right)}^{\vec{\dot{n}}^{\mathrm{Out}}_{\mathrm{g}}} \qquad (7.11) \\
\vec{\dot{n}}^{\mathrm{In}}_{\sum} &= \vec{\dot{n}}^{\mathrm{Out}}_{\sum}
\end{aligned}
$$

The operator $\oslash$ is the *Hadamard division operator*, which performs element-wise division for the components in the two vectors. Each components in $\vec{\dot{n}}^{\mathrm{In}}_{\sum}$ should equal $\vec{\dot{n}}^{\mathrm{Out}}_{\sum}$ at steady-state, which is stated in the last equation of (7.11). The remaining balance applies to thermal energy, which is stated in (7.12).

$$
\begin{aligned}
\dot{Q}^{\mathrm{In}}_{\sum} = {} & \sum\left(\vec{\dot{m}}^{\mathrm{Jet,In}}_{\mathrm{l}}\right) \cdot c_{\mathrm{P}} \cdot T^{\mathrm{Jet,In}}_{\mathrm{l}} + \sum\left(\vec{\dot{m}}^{\mathrm{Abs,In}}_{\mathrm{l}}\right) \cdot c_{\mathrm{P}} \cdot T^{\mathrm{Abs,In}}_{\mathrm{l}} + \\
& \left(\vec{\dot{m}}^{\mathrm{In}}_{\mathrm{g}} \cdot \vec{h}_{\mathrm{g}}(T^{\mathrm{In}}_{\mathrm{g}}) + \dot{m}^{\mathrm{In}}_{\mathrm{g,H_2O}} \cdot h_{\mathrm{fg,H_2O}}\right) \\
\dot{Q}^{\mathrm{Out}}_{\sum} = {} & \sum\left(\vec{\dot{m}}^{\mathrm{Jet,Out}}_{\mathrm{l}}\right) \cdot c_{\mathrm{P}} \cdot T^{\mathrm{Jet,Out}}_{\mathrm{l}} + \sum\left(\vec{\dot{m}}^{\mathrm{Abs,Out}}_{\mathrm{l}}\right) \cdot c_{\mathrm{P}} \cdot T^{\mathrm{Abs,Out}}_{\mathrm{l}} + \qquad (7.12) \\
& \sum\left(\vec{\dot{m}}^{\mathrm{Demister}}_{\mathrm{l}}\right) \cdot c_{\mathrm{P}} \cdot T^{\mathrm{Demister}}_{\mathrm{l}} + \left(\vec{\dot{m}}^{\mathrm{Out}}_{\mathrm{g}} \cdot \vec{h}_{\mathrm{g}}(T^{\mathrm{Out}}_{\mathrm{g}}) + \dot{m}^{\mathrm{Out}}_{\mathrm{g,H_2O}} \cdot h_{\mathrm{fg,H_2O}}\right) \\
\dot{Q}^{\mathrm{In}}_{\sum} = {} & \dot{Q}^{\mathrm{Out}}_{\sum}
\end{aligned}
$$

As seen in (7.12), the thermal energy of the liquid phase is assumed to change linearly with temperature, so a constant value of c_{P} applies, as this does not change significantly between 0 and 80°C. The gas phase enthalpy vector, $\vec{h}_{\mathrm{g}}(T_{\mathrm{g}})$ is a non-linear function of the gas temperature, which can be seen in *Chapter A: Constants and correlations*. Furthermore, the enthalpy of evaporation for the water vapour is included, $h_{\mathrm{fg,H_2O}}$, as this has a significant contribution, as previously stated. The continuous phase variables in the previous equations are integrated over the surfaces of the inlet and the outlet, whereas the liquid phase variables are directly available from the MATLAB results.

The overall balance parameters, $\dot{m}^{\mathrm{In}}_{\sum}$, $\dot{m}^{\mathrm{Out}}_{\sum}$, $\vec{\dot{n}}^{\mathrm{In}}_{\sum}$, $\vec{\dot{n}}^{\mathrm{Out}}_{\sum}$, $\dot{Q}^{\mathrm{In}}_{\sum}$, and $\dot{Q}^{\mathrm{Out}}_{\sum}$ are monitored during simulation and are shown for a typical simulation in *Chapter 11: Example case*.

7.4 Link structure

When a simulation is running, the two software programs, OpenFOAM and MATLAB, exchange information. In order to manage the data, the file hierarchy shown in Figure 7.7 is used.

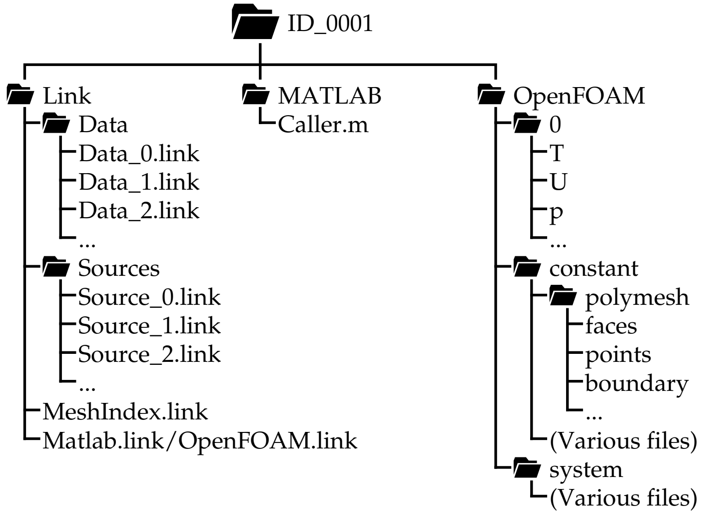

Figure 7.7: The hierarchy of a simulation, where three main directories are present: *Link*, *MATLAB* and *OpenFOAM*.

The main directory for a single simulation is identified with ID_xxxx, where a unique ID is given. This is used for the experimental tuning as described in *Chapter 10: Model tuning*, where a large number of simulations are carried out and stored. Three sub-directories are present within the main directory: *Link*, *MATLAB* and *OpenFOAM*.

The *Link* directory contains two sub-directories, where *Data* contains the .link files written by OpenFOAM, which are read by MATLAB. The *Sources* sub-directory contains the cell source terms written by MATLAB, and are read by OpenFOAM.

The *MATLAB* directory contains a simple script, *Caller.m*, which executes the main program, where the discrete phase and the wall films are modelled. The MATLAB model is located in an upper directory.

The *OpenFOAM* directory contains the initial conditions, such as temperature, pressure etc., in the *0* directory. The directory *constants* contains the mesh in *polymesh* along with various files containing definitions of the link, thermo-physical, and turbulence parameters. The directory *system* contains files, which are used to define the solver methods, damping etc., along with the schemes used to resolve each continuous scalar.

When a simulation is started, *Caller.m* will launch OpenFOAM, and a continuous loop starts, which is illustrated in Figure 7.8. Source_x.link indicates the source terms for the x^{th} processor, which are written separately to each processor to increase speed, and the same applies to Data_x.link.

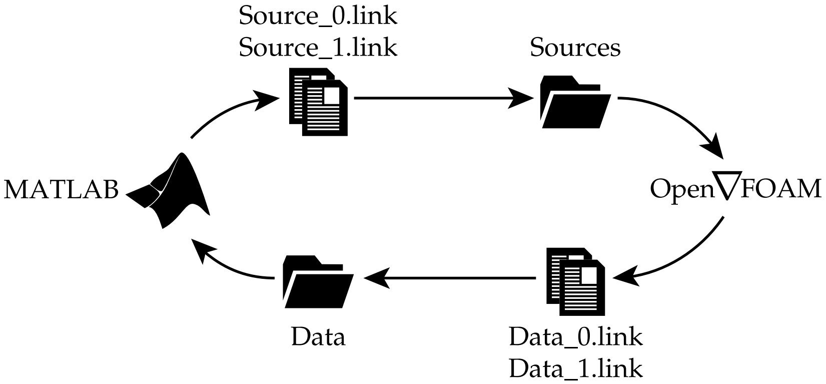

Figure 7.8: The procedure of switching between the two software programs, MATLAB and OpenFOAM, where the programs write and read sources and data. Only one of the two software packages are advancing the simulation at any given time.

As seen in Figure 7.8, OpenFOAM and MATLAB switches between iterating the continuous phase, and advancing the discrete phase and updating the wall films respectively. Sources and data are written to the respective directories, each time control is given to the other program. These files are binary formatted in order to increase write and read speeds. The software in control is identified with a simple dummy file, which is successively created, renamed, and deleted between each passing of the control. An alternative approach would be to let both programs run at the same time, but it was found that no benefit could be obtained this way.

The overhead associated with the reading and writing of data and sources was found to be small compared to the overall simulation time. This was timed, where the results are shown in *Chapter 11: Example case*.

7.5 Modelling overview

The scrubber model consists of the discrete phase, the wall film phase, and the continuous phase. These were all described in the previous chapters along with the coupling between the phases. A complete overview of the model is shown in Figure 7.9 on the next page, which illustrates the flow of species and energy in both the liquid and gas phase. Three grey boxes are shown, which are labelled *Parcels*, *Wall films*, and *Gas phase*.

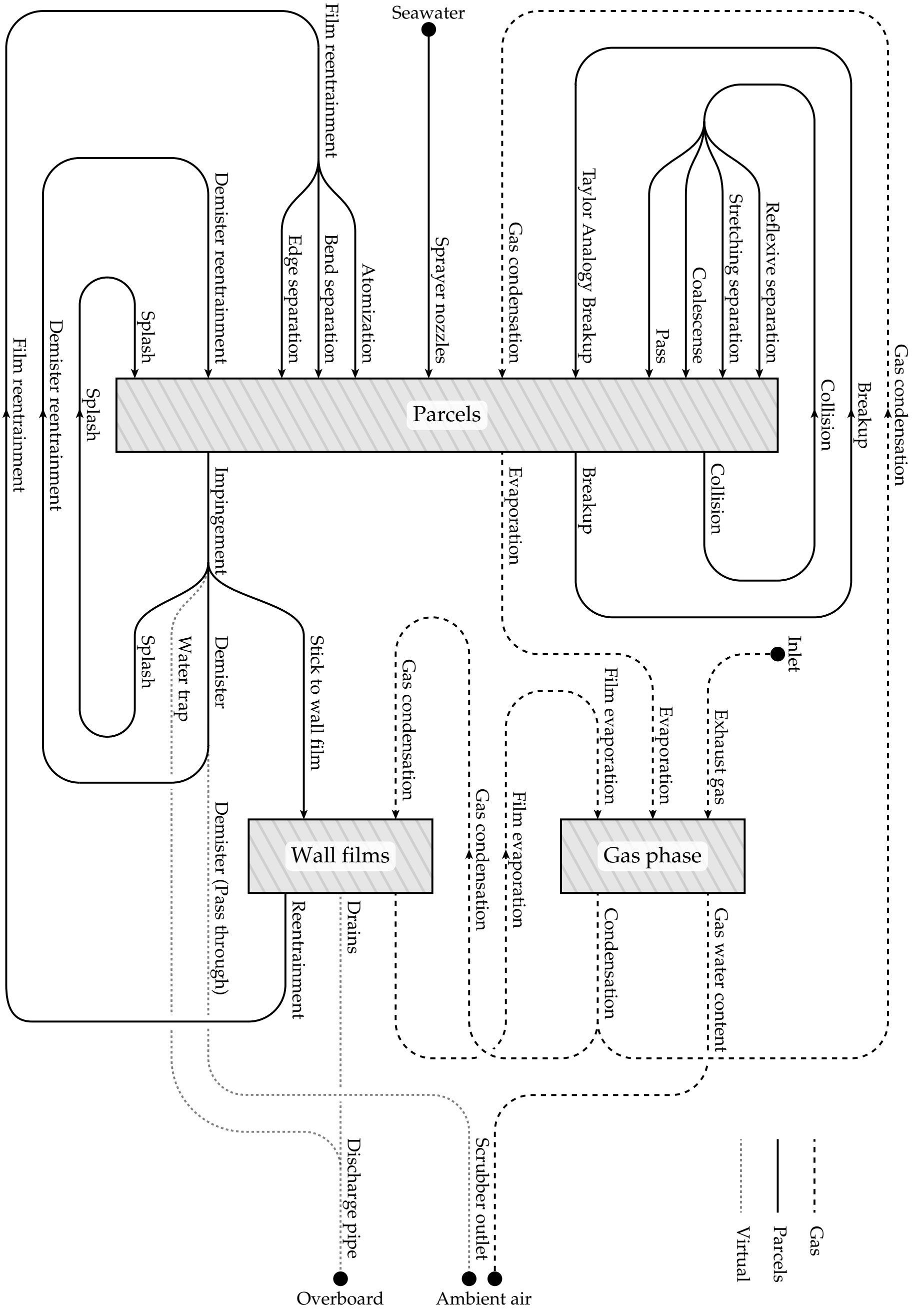

Figure 7.9: A flow chart of all flows within the model. The solid lines are indicating discrete parcels, whereas the black dashed lines are indicating gas phase streams. The grey dashed lines indicate virtual streams, which are logged, such that mass and energy balance can be ensured in the model.

The liquid phase, which is seawater, is injected via the sprayer nozzles inside the scrubber, and is represented by parcels. The dashed black lines are indicating gas streams, and the solid black lines are indicating liquid streams. The grey dashed lines are virtual, which means that they are not represented by either the continuous phase, via parcels, or by the wall film - instead they are simply numbers in the model, such that the mass streams can be tracked.

The box labelled *Parcels* illustrates the part of the liquid phase, which is represented by the discrete parcels. A number of sub-models is coupled to this phase, which are indicated by the lines and arrows. Arrows going into the labelled box illustrate parcels, which are created in the domain or adding mass to existing parcels, whereas arrows leaving the box on the right-hand side are illustrating parcels, which are eliminated from the domain/simulation or losing mass to the gas phase.

The box labelled *Wall films* illustrates the part of the liquid phase, which is represented by the wall films, which are located along the surfaces of the scrubber. The arrows going into this box are either parcels/droplets, which are hitting the wall and sticking to it, or condensing water from the continuous phase. The arrows leaving this box are either evaporating water, re-entrained parcels, or the drains, where the water is ejected overboard.

The box labelled *Gas phase* illustrates water present in the gas as vapour. Arrows going into this box are the evaporation of the droplets and the wall film, along with the water content from the inlet. The arrows going out are condensing water going to the droplets or the wall films. The outlet gas contains water, which is going to the ambient air.

8 INDEPENDENCE STUDIES

In order to ensure consistent results from the model, independence studies are carried out. These studies examine the results, when certain key parameters are changed in the model. In order for the model to be independent, the results from the model must be invariant to changes in the key parameters [Casey and Wintergerste (21)]. Five difference independence studies are carried out, which are illustrated in Figure 8.1.

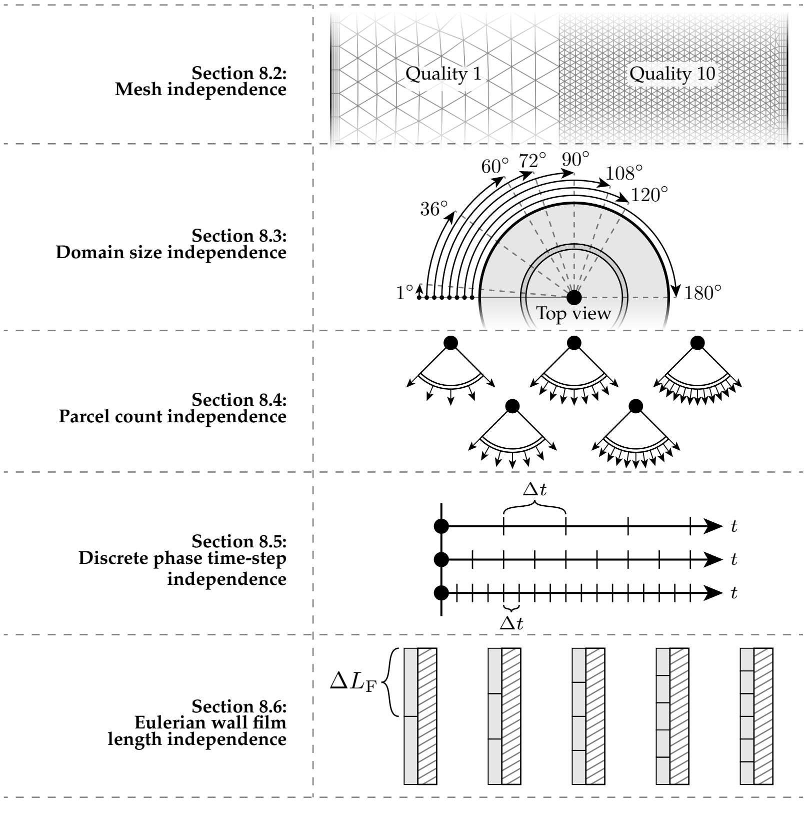

Figure 8.1: An overview of the five independence studies carried out in this study.

The first independence study is a mesh independence study, where the cell count is varied with 10 different steps. The second independence study is a domain size independence study, where the periodic angle is varied from 1° to 180° with eight different steps. The first of these steps is a 2D axis-symmetric case, where the periodic angle is 1°. The third independence study is a parcel count independence study, where the parcel count is varied with 16 different steps, which results in a maximum of $80 \cdot 10^3$ parcels. The fourth independence study is a time-step independence study, where the time-step used for the discrete phase is varied from 0.25 to $10\ \mathrm{ms}$ with nine different steps. The fifth independence study is a wall film length independence study, where the average wall film element length along the shell is varied from 5 to $40\ \mathrm{mm}$ with eight different steps.

8.1 Reference case

As multiple independence studies are carried out, the number of possible permutations is large, if all parameters are varied simultaneously. Therefore, it is assumed that each of the independence studies are independent of the others, so each study can be carried out on its own. A reference case is defined, which is the baseline case for all the independence studies. The key parameters to be changed are all shown in Figure 8.2, where the reference case is composed of the highlighted values.

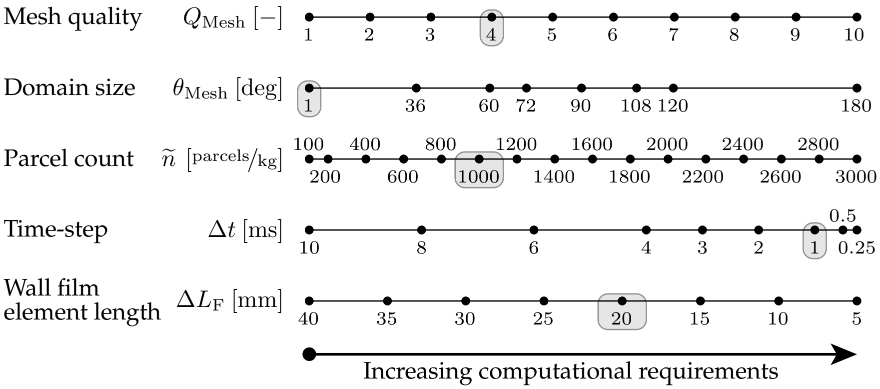

Figure 8.2: The values for the five different independence studies. The highlighted values indicate the ones used for the reference case.

The reference case is defined using $Q_{\text{Mesh}} = 4$, $\theta_{\text{Mesh}} = 1^\circ$, $\widetilde{n} = 1000 \text{parcels/kg}$, $\Delta t = 1\,\text{ms}$, and $\Delta L_{\text{F}} = 20\,\text{mm}$. Each simulation is carried out for $20\,\text{s}$ in the discrete phase, where steady-state is achieved after approximately $7\,\text{s}$. Therefore, the simulations are guaranteed to be fully converged. A single case is used for the independence studies, which is the seventh test from the experimental tests shown in Table 9.1 on page 182. This case was chosen, as all sprayer layers were active, and the load was in the mid range.

8.2 Mesh independence

The mesh independence study investigates the effect of varying the cell count and thus the average cell size. This is changed by adjusting the meshing parameters, when generating the mesh as shown in Figure 6.3 on page 148. 10 different mesh qualities were generated, where the resulting number of nodes, faces and cells are shown in Table 8.1.

Table 8.1: The 10 different mesh qualities, where the number of nodes, faces and cells are represented per 1°, where the values in the parentheses shows the percentage compared to the finest mesh.

Quality	n_{Nodes} [nodes/1°]	n_{Faces} [faces/1°]	n_{Cells} [cells/1°]
1	1574 (13.0%)	10475 (11.0%)	4621 (10.5%)
2	2126 (17.6%)	14580 (15.3%)	6481 (14.8%)
3	2534 (20.9%)	17604 (18.4%)	7847 (17.9%)
4	3044 (25.1%)	21457 (22.4%)	9599 (21.9%)
5	3573 (29.5%)	25488 (26.7%)	11434 (26.0%)
6	4378 (36.2%)	31803 (33.3%)	14328 (32.6%)
7	5341 (44.1%)	39356 (41.2%)	17788 (40.5%)
8	6790 (56.1%)	50908 (53.3%)	23102 (52.6%)
9	8809 (72.8%)	67568 (70.7%)	30828 (70.2%)
10	12107 (100.0%)	95601 (100.0%)	43916 (100.0%)

Table 8.1 shows the node, face and cell counts per 1°. Therefore, the fifth mesh quality for $\theta_{\mathrm{Mesh}} = 60°$ has $(11434\,\mathrm{cells}/1° \cdot 60° \approx 686040\,\mathrm{cells})$. The results from the 10 simulations are shown in Figure 8.3.

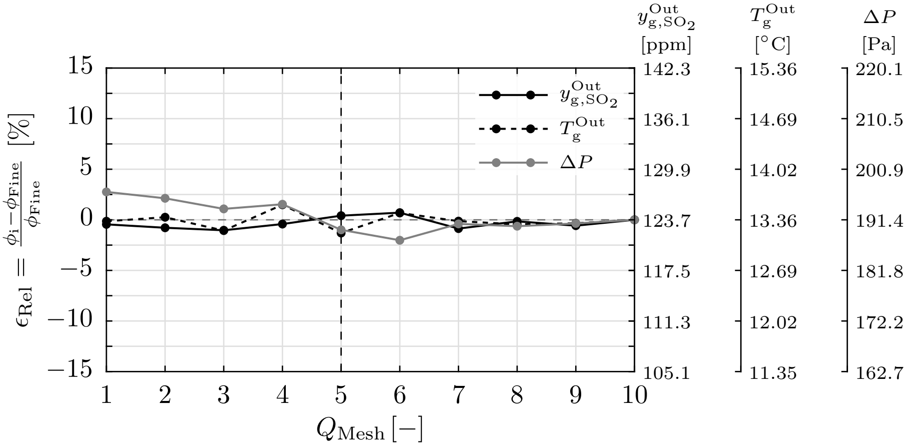

Figure 8.3: The results from the mesh independence analysis.
The vertical dashed line is the value chosen for further analyses.

As seen in Figure 8.3 three values are presented, which are the sulfur concentration, $y_{\mathrm{g,SO_2}}^{\mathrm{Out}}$, and temperature, $T_{\mathrm{g}}^{\mathrm{Out}}$, at the outlet, and the pressure loss over the scrubber, ΔP. These values are normalized relative to the finest quality, ϕ_{Fine}, which is defined in (8.1)

$$\epsilon_{\mathrm{Rel}} = \frac{\phi_{\mathrm{i}} - \phi_{\mathrm{Fine}}}{\phi_{\mathrm{Fine}}} \tag{8.1}$$

The relative errors, ϵ_{Rel}, are shown on the left axis of Figure 8.3, which spans between -15 % and 15 %, which will be common for all independence studies in this chapter, such that the graphs throughout this chapter are comparable. The actual values within the presented span are shown on the three right axes. Notice that the actual values presented are those before the model is tuned to the experimental values, which is done in *Chapter 10: Model tuning*.

The relative errors seen in Figure 8.3 fluctuate between -2.5 and 2.5 %, where the errors become smaller with increasing quality. As the errors are relatively small, the fifth mesh quality $Q_{\mathrm{Mesh}} = 5$ is used in the scrubber model, as this was relatively cheap in terms of computational requirements, while the errors are below approximately 2 %.

8.3 Domain size independence

As described in *Chapter 6: Continuous phase*, rotational symmetry was exploited to reduce computational requirements. Therefore, only a fraction of the scrubber is simulated, as the tangential components are assumed to cancel out, where the domain size independence study serves to validate this assumption. Eight different simulations are carried out, where θ_{Mesh} is varied from 1° to 180° with eight different steps. The results are shown in Figure 8.4 on the next page, where the upper axis shows the fraction of a full circle, $\theta_{\mathrm{Mesh}}/360°$.

As seen in Figure 8.4, the relative error, ϵ_{Rel}, is below 5 % for $y_{\mathrm{g,SO_2}}^{\mathrm{Out}}$ and $T_{\mathrm{g}}^{\mathrm{Out}}$ relative to the values at $\theta_{\mathrm{Mesh}} = 180°$, although these fluctuate slightly. However, the pressure loss, ΔP, is approximately 15 % lower for $\theta_{\mathrm{Mesh}} = 1°$ compared to $\theta_{\mathrm{Mesh}} = 180°$, where the general tendency is that the pressure loss increases with increasing θ_{Mesh}. One reason for this tendency is that a 3D simulation allows for tangential flows, which are not present in the 2D simulation, where $\theta_{\mathrm{Mesh}} = 1°$. These tangential flows might result in large eddies, which will increase the overall pressure loss. The tangential variations were investigated, where an example is shown in Figure 8.5 for the gas temperature, $T_{\mathrm{g}}(\theta)$, for the finest simulation, where $\theta_{\mathrm{Mesh}} = 180°$.

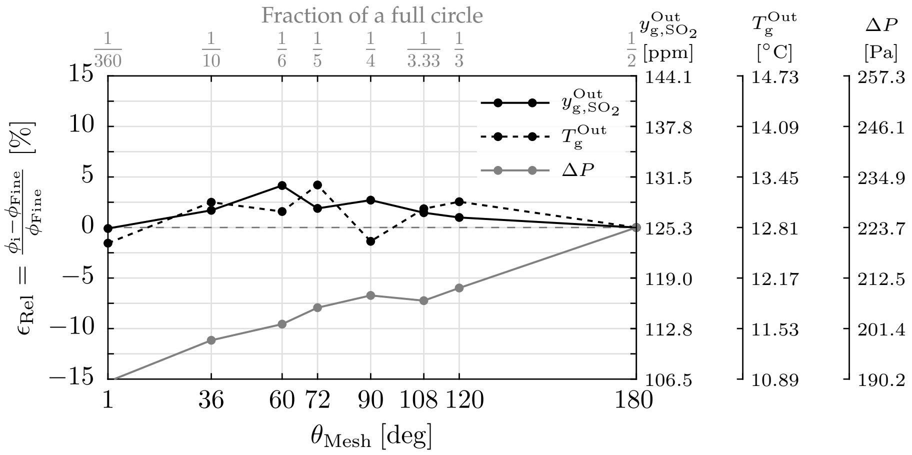

Figure 8.4: The results from the domain size independence study. The results are presented in a similar manner to Figure 8.3. The upper axis shows the fractions of a full circle.

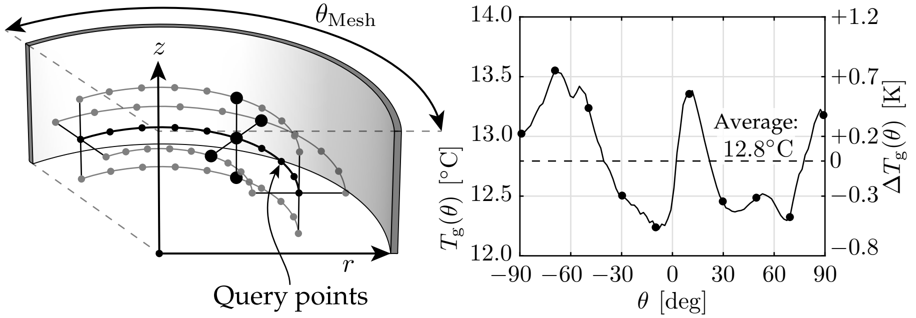

Figure 8.5: An example of the tangential variations for the gas temperature. The graph to the right is constructed by probing the temperature along the highlighted lines in the illustration to the left, where the query/probing points are shown with the black dots.

Figure 8.5 shows an illustration of the scrubber to the left, which spans θ_{Mesh}. The dotted lines are indicating query points, where the flow variables are interpolated on the mesh. An example is shown to the right, where the temperature, $T_{\mathrm{g}}(\theta)$, can be seen to vary as a function of θ. The average temperature for this example is 12.8°C, where the differences from the average are shown on the right axis, $\Delta T_{\mathrm{g}}(\theta)$.

By sampling a large number of query points over the whole continuous phase domain, the general tangential variations can be estimated. This was done by generating 20000 interpolation lines similar to the one shown in Figure 8.5, where $\Delta T_{\mathrm{g}}(\theta)$ was evaluated for a single line. For each discrete value of θ, all values of ΔT_{g} were gathered, and the 5, 25, 50, 75, and 90 % fractiles were calculated. The results from this analysis are shown in Figure 8.6.

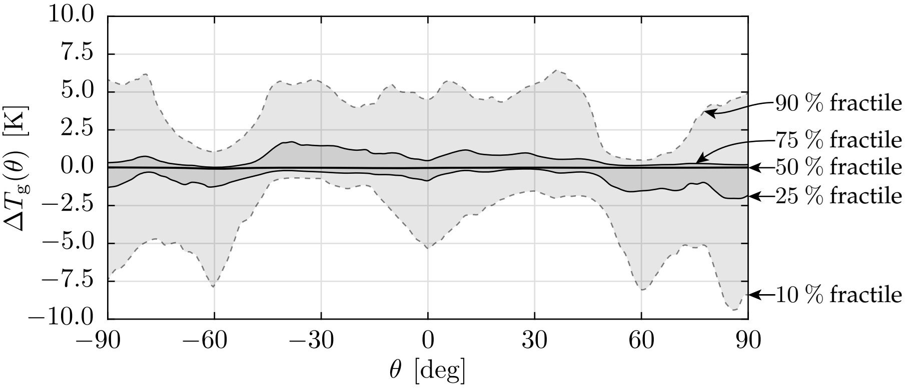

Figure 8.6: The average tangential variations of $\Delta T_\text{g}(\theta)$, where five different fractiles are shown.

For each value of θ in Figure 8.6, ΔT_g was evaluated for all 20000 query points, where an example of this was shown in Figure 8.5 by the big black dots along the interpolation lines. Having done so, the fractiles were calculated, which are shown in Figure 8.6. As seen in the figure, the average tangential variations are mostly below 7.5 K for the 90 % fractile. The 75 % fractiles are all below approximately 2 K, and the 50 % fractile is practically 0. Therefore, the assumption about the tangential variations to cancel out on average is supported by these results, where other flow variables were investigated as well.

Based on the results in Figure 8.4, the domain size used for the model tuning in *Chapter 10: Model tuning* is chosen to be $\theta_\text{Mesh} = 1°$. This is primarily based on the massively reduced computational requirements, which the 2D mesh will results in. The relatively large error for the overall pressure loss will be further addressed in *Chapter 10: Model tuning*.

8.4 Parcel count independence

The parcel count independence study is carried out by varying the typical mass of each parcels. The parameter used for this analysis is $\widetilde{n}$, which defines the number of parcels per kilogram of water. This parameters is used by all sub-models, which are injecting droplets into the domain, which are: sprayer injection, demister re-injection, film atomization, and film separation. Each of these sub-models are injecting a given mass flow into the scrubber, $\dot{m}_\text{Model}$. This mass flow is distributed over a number of parcels, which is calculated using (8.2).

$$n_\text{Model} = \text{round}\Big((\dot{m}_\text{Model} \cdot \Delta t) \cdot \widetilde{n} \Big) \tag{8.2}$$

n_Model is the number of parcels injected by a given sub-model per time-step. For instance, a sprayer nozzle injecting 7.5 $^\text{kg}/_\text{s}$ will inject 15 parcels per time-step assuming $\Delta t = 1$ ms and $\widetilde{n} = 2000$ $^\text{parcels}/_\text{kg}$.

During any simulation, the total number of parcels will increase until steady-state is achieved, where the number of seeded parcels is equal to the number of eliminated parcels per time-step. The values of $\widetilde{n}$ are varied from 100 to 3000 $^{\text{parcels}}/_{\text{kg}}$ with 16 different values, where the results are shown in Figure 8.7.

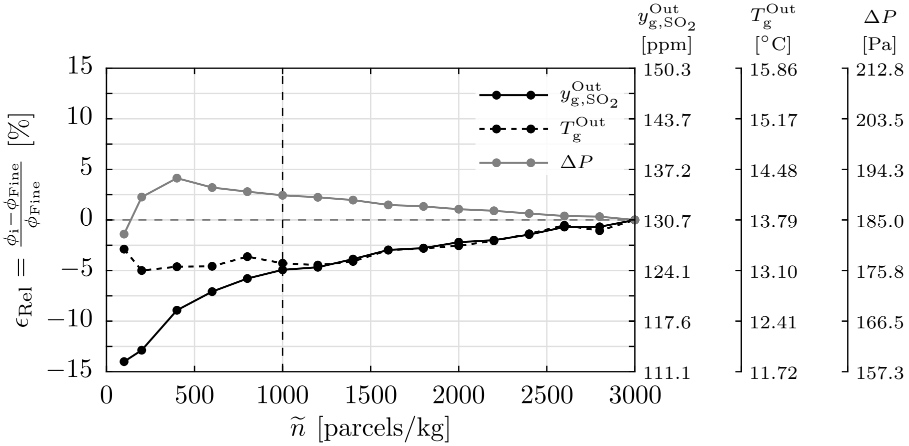

Figure 8.7: The results from the parcel count independence study, where $\widetilde{n}$ is varied between 100 and 3000 $^{\text{parcels}}/_{\text{kg}}$ with 16 different values. The vertical dashed line is the value chosen for further analyses.

Figure 8.7 shows ϵ_{Rel}, where the error values can be seen to deviate significantly at $\widetilde{n} = 100$ $^{\text{parcels}}/_{\text{kg}}$, but converges towards finite values as $\widetilde{n}$ increases. The total number of parcels, when steady-state is achieved, n_{Parcels}, is shown in Figure 8.8, where the liquid accumulation within the scrubber is shown as well, m_{Accu}.

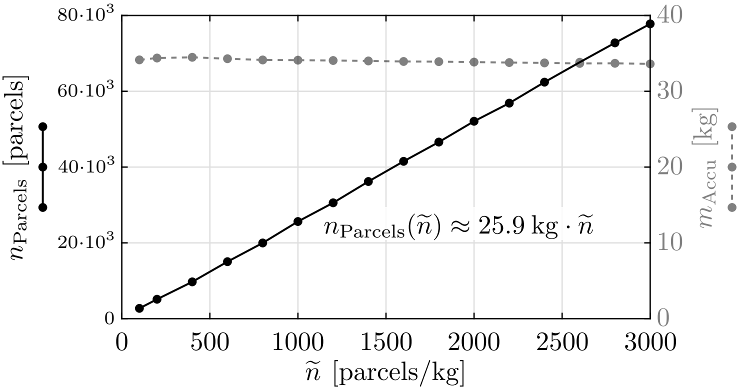

Figure 8.8: The total number of parcels when steady-state has been achieved during the parcel count independence study. The liquid accumulation, m_{Accu}, is shown in grey, where the right y-axis applies.

Figure 8.8 shows the total number of parcels at steady-state, which can be seen to increase proportional to $\widetilde{n}$ with a proportionality factor of 25.9kg. The liquid accumulation, m_{Accu}, which is simply the sum of all wall film elements and all suspended droplets, is shown in the figure as well as the grey line, which corresponds to the right axes. The liquid accumulation should be constant with changing $\widetilde{n}$, which can be seen to be the case in the figure, where the liquid accumulation is $m_{\text{Accu}} \approx 34\,\text{kg}$.

Based on the results in Figure 8.7, $\widetilde{n} = 1000\ ^{\text{parcels}}/_{\text{kg}}$ is used in the model despite $\epsilon_{\text{Rel}} \approx 5\,\%$, as this was found to be a good compromise between accuracy and computational requirements.

8.5 Discrete phase time-step independence

The discrete phase is advanced with each iteration, which is defined using a specified time-step, Δt. This constant is varied from 0.25 to 10 ms with eight different steps, where the results are shown in Figure 8.9.

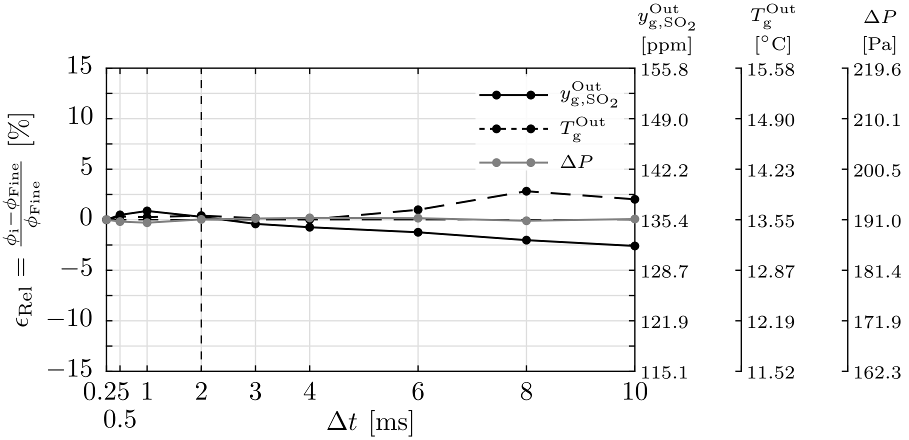

Figure 8.9: The results from the time-step independence study. The vertical dashed line indicates the value chosen for further analyses.

As seen in Figure 8.9, the finest time-step is $0.25\,\text{ms}$, so all data are normalized relative to this point. The errors for $\Delta t = 10$ ms, which is the coarsest time-step, are all below 3 %, so the model is not sensitive to Δt within this span. The time-step chosen for further analyses is $\Delta t = 2$ ms, which is indicated by the vertical dashed line in the figure.

8.6 Eulerian wall film length independence

The Eulerian wall film requires all surfaces to be meshed into a finite number of wall film elements, on which the models described in *Chapter 5: Eulerian* *wall films* are solved. The average wall film length is varied from $5\mathrm{mm}$ to $40\mathrm{mm}$ in increments of 5 mm, which resulted in eight different values of ΔL_F. The results are shown in Figure 8.10, where the total number of wall film elements is shown on the upper axis.

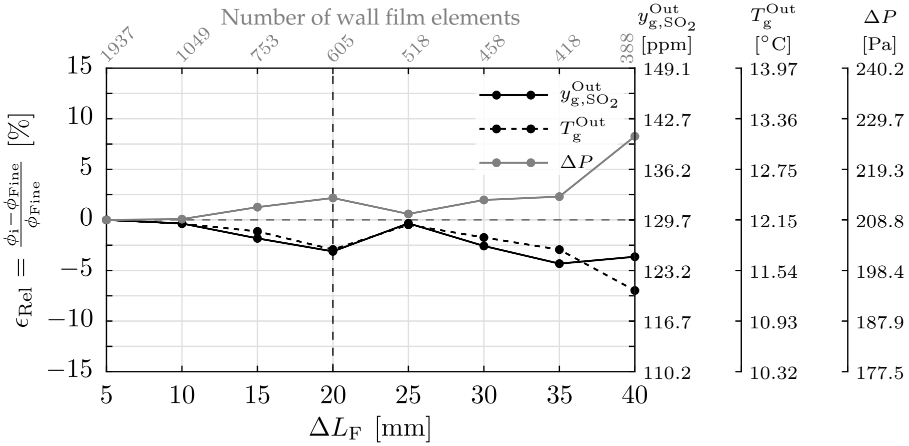

Figure 8.10: The results from the Eulerian wall film length independence study. The vertical dashed line indicates the value chosen for further analyses.

As seen in Figure 8.10, the relative errors compared to the finest wall film length, $\Delta_\mathrm{F} = 5$ mm, are fluctuating. All relative errors are below 5 % except for $\Delta L_\mathrm{F} = 40$ mm, where the errors start to increase significantly. The value of ΔL_F chosen for further analyses is $\Delta L_\mathrm{F} = 20$ mm, where the errors are approximately 3 %.

8.7 Summary

Based on the five independence studies, the values chosen for further analyses are those shown in Table 8.2.

Table 8.2: An overview of the results from the independence studies. The relative errors, ϵ_{Rel}, for the selected values are shown in the table.

		ϵ_{Rel} [%]		
Variable	**Value used**	$y_{\mathrm{g,SO_2}}$	$T^{\mathrm{g}}_{\mathrm{Out}}$	ΔP
Q_{Mesh}	5	$+0.4$	-1.3	-1.0
θ_{Mesh}	1°	-0.1	-1.6	-15.3
$\widetilde{n}$	1000 $^{\mathrm{parcels}}/_{\mathrm{kg}}$	-4.9	-4.3	$+2.4$
Δt	2 ms	$+0.3$	$+0.4$	$+0.0$
ΔL_F	20 mm	-3.1	-2.9	$+2.2$

As seen in Table 8.2, all relative errors are below 5% except ΔP for θ_{Mesh}. However, due to the massive reduction in computational requirements, a value of $\theta_{\mathrm{Mesh}} = 1^{\circ}$ was chosen. The large error of $-15.3\ \%$ will be further addressed in *Section 10.4: Results*.

PART II

VERIFICATION

9 EXPERIMENTS

In order to validate and tune the scrubber model, a set of experimental tests were carried out at the Alfa Laval Test & Training Centre under varying conditions, such that the scrubber model can be verified and tuned to different operating scenarios. A description of the test centre and the experimental setup along with the experimental methods and procedures are given in the first two sections in this chapter. The results from the tests are presented in the third section, where a *Least Squares Adjustment* technique is applied to the results in order to have consistent measurements, which can be used to validate the computational scrubber model.

9.1 Test centre and setup

The Alfa Laval Test & Training Centre facilitates $1350\ \mathrm{m}^2$ of testing area [Alfa Laval (4)]. The centre features all components on-board an operating ship, where a 9 cylinder 4-stroke dual fuel $2\ \mathrm{MW}$ 28/32 MAN engine is installed capable of running on both HFO and MGO [MAN Diesel & Turbo (90)]. A sketch of the test centre is shown in Figure 9.1.

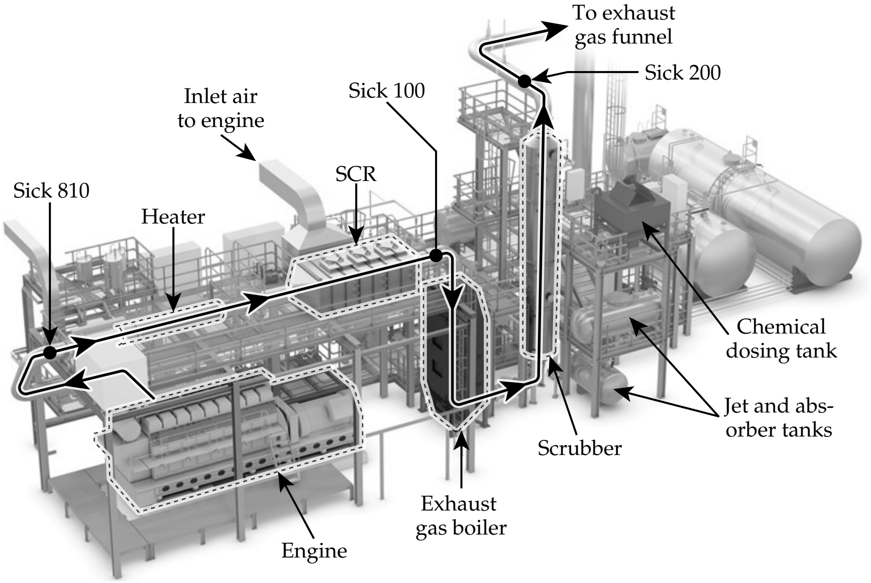

Figure 9.1: The experimental setup used for verifying and modelling the scrubber model. The image is from [Alfa Laval (4)]. The gas stream from the engine to the exhaust funnel is highlighted with five major components, and three gas analysers are present in the exhaust gas line, which are indicated with the black circles.

9.1.1 Components

The gas stream passes through five major components, which are described below:

Engine: The engine is a MAN 28/32 engine with 9 cylinders capable of providing 2 MW shaft power [MAN Diesel & Turbo (90)]. The engine can operate on both MGO and HFO, where HFO was used during the tests. It is connected to a generator, which can provide 1.8 MW electrical power at full load, and is connected to the electrical grid of Aalborg, such that it can support the demand from the city when running.

Heater: Six electrical heaters are located after the engine, which serve to heat the exhaust gas, such that different inlet temperatures can be tested for the remaining components. Each of the heaters has a capacity of 50 kW allowing for a total of 300 kW, if all heaters are active. It should be noted that the heaters are not present on-board an operating ship, but are only used for testing purposes.

SCR: The *Selective Catalytic Reduction*, SCR, unit is used for removing NO_x from the exhaust gas. The unit is a Haldor Topsøe DNX catalyst [Haldor Topsoe (66)], and removes NO_x by injecting urea into the exhaust gas stream, which reacts on the catalytic surfaces within the unit.

Exhaust gas boiler: An Alfa Laval XW exhaust gas boiler is installed after the SCR unit, which extracts heat from the exhaust gas to produce steam. It operates at 7 bar, and has a steam capacity of 600 kg/h. The steam line is also connected to the district heating of Aalborg to support the demand when running.

Scrubber: The *Alfa Laval Experimental Scrubber*, ALES, is a wet inline scrubber designed for 1.6 MW with a diameter of 1.092 m and a height of 5.96 m from the jet water trap to the bottom of the demister, and features both closed-loop and open-loop operation. Different chemicals can be added to the water during closed-loop operation. The jet and absorber tanks can be seen in Figure 9.1 to the right of the scrubber inlet, and the chemical dosing tank used during closed-loop operation is shown above the tanks.

9.1.2 Sensors

Hundreds of sensors are installed at the test centre, which are logging values every 10 s. Three gas analysers are present on the exhaust gas line, where two are placed before the scrubber and one after. An overview of the sensors related to scrubber operation is shown in Figure 9.2.

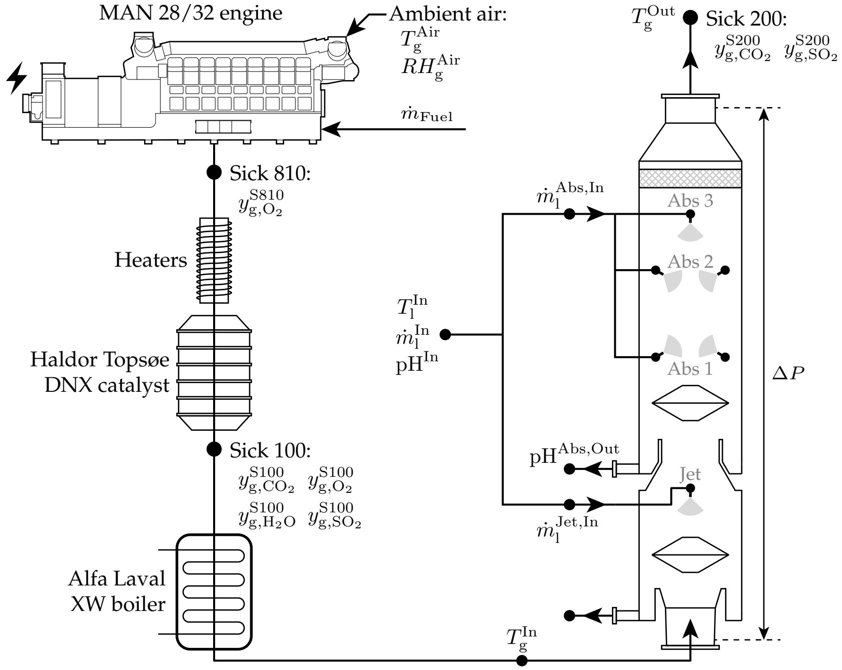

Figure 9.2: The sensors related to scrubber operation. The three gas analysers measure different values, which are all used in this study.

Figure 9.2 shows some of the sensors related to scrubber operation. The exhaust gas flow from the engine is calculated using the values from the two gas analysers located before the scrubber, Sick 810 and Sick 100, along with the fuel flow. The performance of the scrubber is evaluated using the differential pressure transmitter, ΔP, along with the inlet and outlet sensors, where y_{g,SO_2} is measured before and after the scrubber, y_{g,SO_2}^{S100} and y_{g,SO_2}^{S200} respectively. Notice that $y_{g,i}$ is the mole fraction of the i^{th} species in the exhaust gas. All subscripts for the gas and liquid values are shown with $(...)_g$ or $(...)_l$ respectively, and the superscripts show the locations of the measured values, such as $\dot{m}_l^{Jet,In}$, which is the inlet liquid mass flow to the jet.

9.2 Method and procedure

The tests were carried out by operating the engine at different loads while activating or deactivating different sprayer layers, which were shown as *Abs 1*, *Abs 2*, *Abs 3*, and *Jet* in Figure 9.1. An overview of the different tests carried out is shown in Table 9.1, where both the engine loads and the scrubber loads are shown. The scrubber is designed for 1.6MW, which is below the maximum electrical power of the engine of 1.8 MW.

Table 9.1: An overview of the different tests. The target power was 800 and 1600 kW, which can be seen to fluctuate slightly during the tests. The crosses indicate which sprayer layers are activated, where the names refer to Figure 9.2.

Test [−]	**Engine load** [%]	**Scrubber load** [%]	**Power** [kW]	$\dot{m}_{\mathrm{l}}^{\mathrm{In}}$ [kg/s]	**Jet** [−]	**Abs 1** [−]	**Abs 2** [−]	**Abs 3** [−]
1	44.9	50.5	809	9.9	×	×		
2	44.9	50.5	808	7.6		×		
3	44.9	50.5	808	9.5	×		×	
4	45.0	50.7	811	7.1			×	
5	45.1	50.7	811	14.6	×	×	×	
6	45.2	50.8	813	12.3		×	×	
7	44.7	50.3	805	18.6	×	×	×	×
8	45.3	50.9	815	16.4		×	×	×
9	88.8	99.9	1598	9.8	×	×		
10	89.2	100.3	1605	7.5		×		
11	88.8	100.0	1599	9.4	×		×	
12	88.3	99.4	1590	7.1			×	
13	88.4	99.4	1591	14.5	×	×	×	
14	88.6	99.7	1595	12.2		×	×	
15	88.8	99.8	1598	18.4	×	×	×	×
16	88.8	99.9	1598	16.3		×	×	×

As seen in Table 9.1, all sprayer layers are activated for the seventh test, and the load is approximately 50 % of the design load for the scrubber. This test was used for the independence studies in *Chapter 8: Independence studies*. Steady-state values were ensured by monitoring different process parameters during the test, which settled after a few minutes. The ambient air properties during the tests were found using the national weather service [Danish Meteorological Institute (29)], and the seawater properties were determined from laboratory analyses [EKOKEM (44)]. These values are shown in (9.1).

$$\begin{aligned} T_{\mathrm{g}}^{\mathrm{Air}} &= 5^{\circ}\mathrm{C} & \mathrm{pH}^{\mathrm{In}} &= 8.1 \\ RH_{\mathrm{g}}^{\mathrm{Air}} &= 95\ \% & S &= 20.8\ \mathrm{g/kg} \\ T_{\mathrm{l}}^{\mathrm{In}} &= 8.06^{\circ}\mathrm{C} & I &= 0.423\ \mathrm{mol/L} \\ A_{\mathrm{T}} &= 2.1\ \mathrm{mmol/L} \end{aligned} \tag{9.1}$$

It should be noted that the salinity, S, is significantly lower compared to typical seawater, which is caused by brackish water inflows to *Limfjorden*, which is the fjord passing through Aalborg. The ionic strength, I, was not measured, but instead calculated using (3.5) on page 23 based on the salinity.

9.2.1 Filtering

All sensors have some associated uncertainty with the logged values, which causes the signals to fluctuate around mean values [Antoine et al. (9)]. This can be seen in Figure 9.3, where various values from Figure 9.2 are shown.

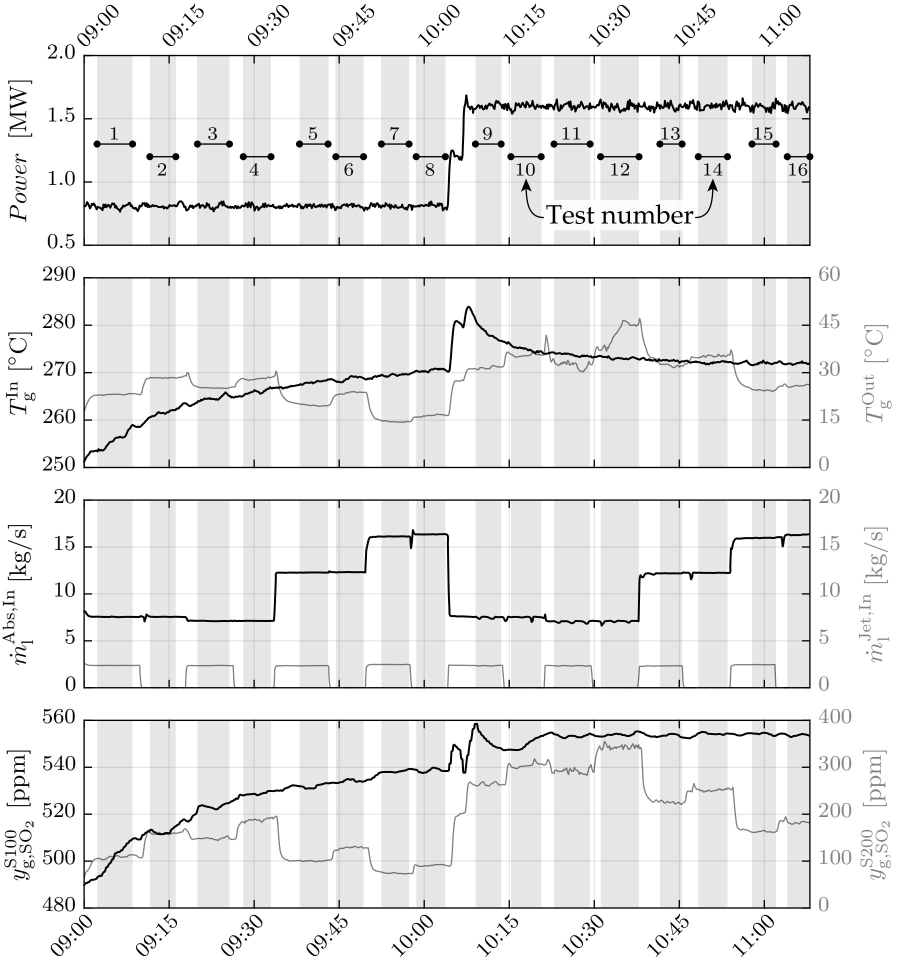

Figure 9.3: Seven of the main parameters during the 16 tests, which are indicated by the shaded areas and the numbers in the upper figure. The black and grey lines are linked to the left and right axes respectively.

Each test in Table 9.1 is highlighted with the shaded areas in Figure 9.3 according to the numbers in the top figure. As seen in the figure, most values fluctuate slightly, which is caused by measurement uncertainties, so a filter was applied to obtain steady-state values. This filter first removed the outliers, after which the median value was found. This simple method proved suitable for the signals shown in Figure 9.3.

It should be noted that the sulfur concentration measured between the engine and the scrubber, $y^{\mathrm{S100}}_{\mathrm{g,SO_2}}$, can be seen to increase from approximately 490 to 540 ppm between 09:00 and 10:00. This is caused by a fuel switch, where the engine had been running with MGO prior to carrying out the experiments for this study, where HFO was used. Due to the installation of the fuel line at the test centre, the fuel switch takes several hours of running.

9.3 Least squares adjustment

The filtered signals for each test can be used to tune and verify the computational scrubber model. However, as the signals are noisy, and some sensors might not be fully calibrated or accurate, the resulting signals will not yield physical results. A simple example of this is a pipe with two mass flow sensors. These should both yield the same mass flow, but due to the mentioned uncertainties, the signals will most likely be different. Therefore, the mass flows must be adjusted, which, in this simple example, is simply done by calculating the average value. This is illustrated in Figure 9.4.

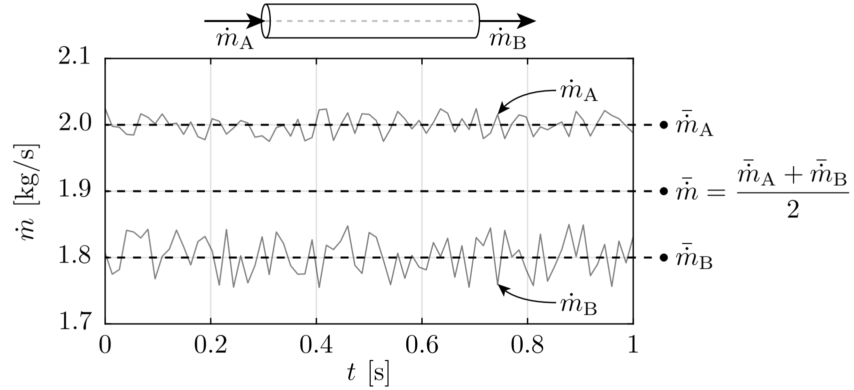

Figure 9.4: An illustration of the fundamental measurement problem when having multiple sensors, which should yield identical values. Both measurement errors and calibration errors pose problems.

In the case of multiple sensors with numerous logged values, such as mass flow, mole fractions etc., the problem becomes more complex, where each sensor value must be adjusted in order to ensure mass, energy, and elementary mole balance. As the experimental data are used to validate the model, the data must satisfy these critical balances. If they do not, the scrubber model will never be able to predict the correct results, as mass and energy balance is fully accounted for in the computational scrubber model, which was described in *Section 7.3: Mass, energy, and mole balances*.

9.3.1 Underlying model

In order to adjust any signal, an underlying physical model must be assumed. In the case of the simple pipe with the two mass flow sensors shown in Figure 9.4, the underlying physical model, which must be obeyed at all times, is simply mass balance. In the case of the experimental setup at the Alfa Laval Test & Training Centre, the underlying physical model is more complex and is described in this subsection.

Ambient air

In order to determine the composition and mass flow of the gas entering the scrubber, the ambient air composition must be determined. The dry air composition is found in literature [Wallace and Hobbs (137)], and the wet air composition is calculated using the partial pressure of H_2O along with the relative humidity according to (4.85) on page 120, where the values used were shown in (9.1). The ambient air composition is shown in (9.1), where it should be noted that N_2 is a combination of all inert gases, which include argon etc.

$$\begin{bmatrix} y^{\mathrm{Air,Dry}}_{\mathrm{g,CO_2}} \\ y^{\mathrm{Air,Dry}}_{\mathrm{g,H_2O}} \\ y^{\mathrm{Air,Dry}}_{\mathrm{g,O_2}} \\ y^{\mathrm{Air,Dry}}_{\mathrm{g,SO_2}} \\ y^{\mathrm{Air,Dry}}_{\mathrm{g,N_2}} \end{bmatrix} = \overbrace{\begin{bmatrix} 380\ \mathrm{ppm} \\ 0\ \% \\ 20.95\ \% \\ 0\ \% \\ 79.01\ \% \end{bmatrix}}^{\text{[Wallace and Hobbs (137)]}} \quad , \quad \begin{bmatrix} y^{\mathrm{Air}}_{\mathrm{g,CO_2}} \\ y^{\mathrm{Air}}_{\mathrm{g,H_2O}} \\ y^{\mathrm{Air}}_{\mathrm{g,O_2}} \\ y^{\mathrm{Air}}_{\mathrm{g,SO_2}} \\ y^{\mathrm{Air}}_{\mathrm{g,N_2}} \end{bmatrix} = \overbrace{\begin{bmatrix} 377\ \mathrm{ppm} \\ 0.812\ \% \\ 20.78\ \% \\ 0\ \% \\ 78.37\ \% \end{bmatrix}}^{\substack{T=5^\circ\mathrm{C} \\ RH=95\ \%}} \tag{9.2}$$

$$\begin{aligned} &\dot{n}_{\mathrm{Fuel}} \cdot \Big(x_{\mathrm{C}}\,\mathrm{C} + x_{\mathrm{H}}\,\mathrm{H} + x_{\mathrm{O}}\,\mathrm{O} + x_{\mathrm{S}}\,\mathrm{S} + x_{\mathrm{N}}\,\mathrm{N}\Big) + \\ &\dot{n}^{\mathrm{Air}}_{\mathrm{g}} \cdot \Big(y^{\mathrm{Air}}_{\mathrm{g,CO_2}}\,\mathrm{CO_2} + y^{\mathrm{Air}}_{\mathrm{g,H_2O}}\,\mathrm{H_2O} + y^{\mathrm{Air}}_{\mathrm{g,O_2}}\,\mathrm{O_2} + y^{\mathrm{Air}}_{\mathrm{g,SO2}}\,\mathrm{SO_2} + y^{\mathrm{Air}}_{\mathrm{g,N_2}}\,\mathrm{N_2}\Big) \\ &\downarrow \\ &\overbrace{\Big(\dot{n}_{\mathrm{Fuel}} \cdot x_{\mathrm{C}} + \dot{n}^{\mathrm{Air}}_{\mathrm{g}} \cdot y^{\mathrm{Air}}_{\mathrm{g,CO_2}}\Big)}^{\dot{n}^{\mathrm{Ex}}_{\mathrm{g,CO_2}}}\,\mathrm{CO_2} + \\ &\Big(\dot{n}_{\mathrm{Fuel}} \cdot \frac{x_{\mathrm{H}}}{2} + \dot{n}^{\mathrm{Air}}_{\mathrm{g}} \cdot y^{\mathrm{Air}}_{\mathrm{g,H_2O}}\Big)\,\mathrm{H_2O} + \\ &\Big(\dot{n}_{\mathrm{Fuel}} \cdot (-x_{\mathrm{C}} - \frac{x_{\mathrm{H}}}{4} + \frac{x_{\mathrm{O}}}{2} - x_{\mathrm{S}}) + \dot{n}^{\mathrm{Air}}_{\mathrm{g}} \cdot y^{\mathrm{Air}}_{\mathrm{g,O_2}}\Big)\,\mathrm{O_2} + \\ &\Big(\dot{n}_{\mathrm{Fuel}} \cdot x_{\mathrm{S}} + \dot{n}^{\mathrm{Air}}_{\mathrm{g}} \cdot y^{\mathrm{Air}}_{\mathrm{g,SO_2}}\Big)\,\mathrm{SO_2} + \\ &\underbrace{\Big(\dot{n}_{\mathrm{Fuel}} \cdot \frac{x_{\mathrm{N}}}{2} + \dot{n}^{\mathrm{Air}}_{\mathrm{g}} \cdot y^{\mathrm{Air}}_{\mathrm{g,N_2}}\Big)}_{\dot{n}^{\mathrm{Ex}}_{\mathrm{g,N_2}}}\,\mathrm{N_2} \end{aligned} \tag{9.3}$$

Combustion process

Having determined the air composition, the exhaust gas from the engine can be calculated, which requires the mass flow and composition of the fuel oil to be known. The combustion process can be expressed according to (9.3) on the prevous page. x_{C}, x_{H} etc. are the mole fractions of carbon, hydrogen etc. in the fuel oil. The exhaust gas composition is defined in (9.4), where $\vec{\dot{n}}_{\mathrm{g}}^{\mathrm{Ex}}$ is composed of the leading coefficient on the product side of (9.3), where $\dot{n}_{\mathrm{g,CO_2}}^{\mathrm{Ex}}$ and $\dot{n}_{\mathrm{g,N_2}}^{\mathrm{Ex}}$ were shown in the equation as examples. The fuel composition vector, $\vec{x}_{\mathrm{Fuel}}$, is shown as well in (9.4).

$$\begin{aligned} \vec{x}_{\mathrm{Fuel}} &= \begin{bmatrix} x_{\mathrm{C}} & x_{\mathrm{H}} & x_{\mathrm{O}} & x_{\mathrm{S}} & x_{\mathrm{N}} \end{bmatrix}^{\mathrm{T}} \\ \vec{\dot{n}}_{\mathrm{g}}^{\mathrm{Ex}} &= \begin{bmatrix} \dot{n}_{\mathrm{g,CO_2}}^{\mathrm{Ex}} & \dot{n}_{\mathrm{g,H_2O}}^{\mathrm{Ex}} & \dot{n}_{\mathrm{g,O_2}}^{\mathrm{Ex}} & \dot{n}_{\mathrm{g,SO_2}}^{\mathrm{Ex}} & \dot{n}_{\mathrm{g,N_2}}^{\mathrm{Ex}} \end{bmatrix}^{\mathrm{T}} \\ \vec{y}_{\mathrm{g}}^{\mathrm{Ex}} &= \frac{\vec{\dot{n}}_{\mathrm{g}}^{\mathrm{Ex}}}{\sum_{\mathrm{i}} \dot{n}_{\mathrm{g,i}}^{\mathrm{Ex}}} \end{aligned} \tag{9.4}$$

Stoichiometric combustion is obtained when no oxygen is present on the product side. The ratio between air and fuel under stoichiometric conditions is calculated using (9.3), which is stated in (9.5).

$$\left(\frac{\dot{n}_{\mathrm{g}}^{\mathrm{Air}}}{\dot{n}_{\mathrm{Fuel}}}\right)_{\mathrm{Stoich}} = \frac{x_{\mathrm{C}} + \frac{x_{\mathrm{H}}}{4} - \frac{x_{\mathrm{O}}}{2} + x_{\mathrm{S}}}{y_{\mathrm{gO_2}}^{\mathrm{Ex}}} \tag{9.5}$$

λ is the *excess air ratio*, which is shown in (9.6) [Turns (132)].

$$\lambda = \frac{\left(\frac{\dot{n}_{\mathrm{g}}^{\mathrm{Air}}}{\dot{n}_{\mathrm{Fuel}}}\right)}{\left(\frac{\dot{n}_{\mathrm{g}}^{\mathrm{Air}}}{\dot{n}_{\mathrm{Fuel}}}\right)_{\mathrm{Stoich}}} = \frac{\left(\dot{n}_{\mathrm{g}}^{\mathrm{Air}}\right)}{\left(\dot{n}_{\mathrm{g}}^{\mathrm{Air}}\right)_{\mathrm{Stoich}}} \tag{9.6}$$

By combining (9.3) to (9.6), an expression for the exhaust gas composition as a function of λ can be obtained. Assuming the compositions of fuel oil, $\vec{x}_{\mathrm{Fuel}}$, and the ambient air, $\vec{y}_{\mathrm{g}}^{\mathrm{Air}}$, to be known along with the fuel flow, $\dot{n}_{\mathrm{Fuel}}$, the exhaust gas flow can be calculated using any of the equations in (9.7).

$$\begin{gathered} \text{Sick 810:} \\ \frac{y_{\mathrm{g,O_2}}^{\mathrm{Ex}}(\lambda)}{1 - y_{\mathrm{g,H_2O}}^{\mathrm{Ex}}(\lambda)} = y_{\mathrm{g,O_2}}^{\mathrm{S810}} \\ \text{Sick 100:} \\ y_{\mathrm{g,CO_2}}^{\mathrm{Ex}}(\lambda) = y_{\mathrm{g,CO_2}}^{\mathrm{S100}} \qquad y_{\mathrm{g,O_2}}^{\mathrm{Ex}}(\lambda) = y_{\mathrm{g,O_2}}^{\mathrm{S100}} \\ y_{\mathrm{g,H_2O}}^{\mathrm{Ex}}(\lambda) = y_{\mathrm{g,H_2O}}^{\mathrm{S100}} \qquad y_{\mathrm{g,SO_2}}^{\mathrm{Ex}}(\lambda) = y_{\mathrm{g,SO_2}}^{\mathrm{S100}} \end{gathered} \tag{9.7}$$

The values in (9.7) on the left-hand sides are calculated values as functions of λ, whereas the values on the right-hand sides are the measured values from the gas analysers. The Sick 810 gas analyser measures the gas composition on a dry basis, so the value of $y_{\mathrm{g,O_2}}$ is normalized by the sum of all mole fractions except $y_{\mathrm{g,H_2O}}$.

Each of the five constraints in (9.7) can be used independently of the others to calculate the gas flow and the exhaust gas composition using (9.2) and (9.3), when the fuel oil mass flow is known. However, the resulting gas flow will differ dependent on which constraints in (9.7) is used due to measurement uncertainties. Therefore, a method of combining all constraints is used to calculate the gas flow in this study.

9.3.2 Least squares adjustment

The underlying physical model for calculating the exhaust gas flow is illustrated in Figure 9.5.

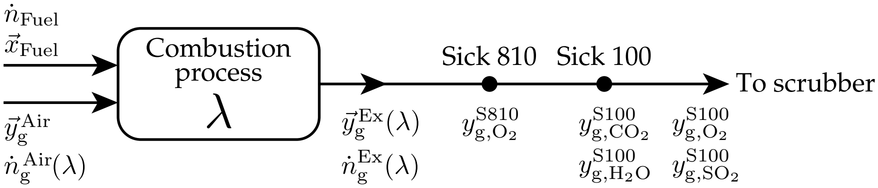

Figure 9.5: An overview of the underlying physical model used for calculating the exhaust gas flow and composition, $\vec{y}_{\mathrm{g}}^{\mathrm{Ex}}$.

As seen in Figure 9.5, fuel and air is mixed during the combustion process, where the resulting gas composition is $\vec{y}_{\mathrm{g}}^{\mathrm{Ex}}$, which is a function of λ. The gas flows obtained using (9.7) differ depending on which measured value is used, so in order to get a more statistically accurate flow, the *Least Squares Adjustment*, LSA, technique is applied [Ghilani (59)]. This technique calculates λ by minimizing the sum of normalized squared errors between the measured and calculated mole fractions in the exhaust gas. This is stated in (9.8).

$$\text{Minimize: } f(\lambda) \tag{9.8}$$

$$f_{\mathrm{i}}(\lambda) = \left(\frac{\frac{y_{\mathrm{g,O_2}}^{\mathrm{Ex}}(\lambda)}{1-y_{\mathrm{g,H_2O}}^{\mathrm{Ex}}(\lambda)} - y_{\mathrm{g,O_2}}^{\mathrm{S810}}}{y_{\mathrm{g,O_2}}^{\mathrm{S810}}} \right)^2 + \left(\frac{y_{\mathrm{g,CO_2}}^{\mathrm{Ex}}(\lambda) - y_{\mathrm{g,CO_2}}^{\mathrm{S100}}}{y_{\mathrm{g,CO_2}}^{\mathrm{S100}}} \right)^2 +$$

$$\left(\frac{y_{\mathrm{g,H_2O}}^{\mathrm{Ex}}(\lambda) - y_{\mathrm{g,H_2O}}^{\mathrm{S100}}}{y_{\mathrm{g,H_2O}}^{\mathrm{S100}}} \right)^2 + \left(\frac{y_{\mathrm{g,O_2}}^{\mathrm{Ex}}(\lambda) - y_{\mathrm{g,O_2}}^{\mathrm{S100}}}{y_{\mathrm{g,O_2}}^{\mathrm{S100}}} \right)^2 + \left(\frac{y_{\mathrm{g,SO_2}}^{\mathrm{Ex}}(\lambda) - y_{\mathrm{g,SO_2}}^{\mathrm{S100}}}{y_{\mathrm{g,SO_2}}^{\mathrm{S100}}} \right)^2$$

Where f_{i} is the objective function for the i^{th} test, so a total of 16 functions are generated from (9.8), as 16 tests were carried out. $f_{\mathrm{i}}(\lambda)$ has five contributions on the right-hand side, which are each of the measured values before the scrubber, which was shown in Figure 9.5.

The problem stated in (9.8) is non-linear, so an iterative least squares algorithm is used to minimize the objective function. The tendencies for $f_{\mathrm{i}}(\lambda)$ are shown in Figure 9.6 for all 16 tests, where the fifth test is highlighted by the thick black line, $f_5(\lambda)$.

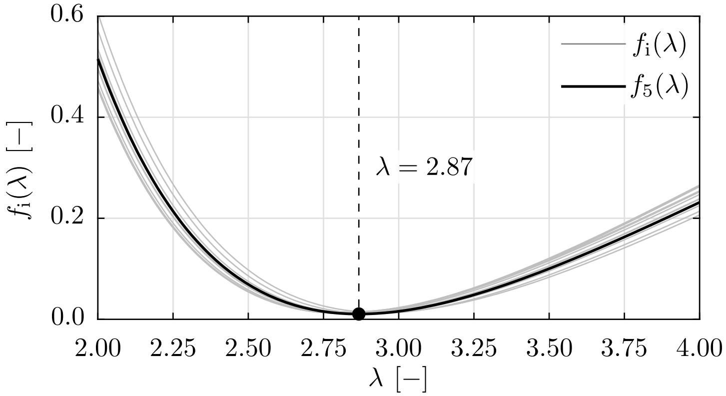

Figure 9.6: The tendency for $f_{\mathrm{i}}(\lambda)$, where the fifth test is highlighted with the black line.

As seen in Figure 9.6, the tendencies for $f_{\mathrm{i}}(\lambda)$ are similar for all tests, which is expected, as the engine will typically operate with constant λ. Minima exist at $\lambda \approx 2.85$, where the minimum for the fifth test was located at $\lambda = 2.87$. This value is higher than expected for a four-stroke diesel engine, which is typically $\lambda \approx 2.2$, but this particular engine was originally adjusted to a tropical climate, and therefore the value of λ is higher than normal. It should be noted that the values of $f_{\mathrm{i}}(\lambda)$ in Figure 9.6 are small but non-zero at the minima. By applying the LSA technique, the statistically most accurate gas flow can be calculated, where all five measured mole fractions from the two gas analysers are taken into account.

9.3.3 Fuel composition

In order to determine the sulfur content in the HFO, multiple samples were sent to different analyses. This was done to compare the result using different techniques for determining the composition. However, the results from the different analyses did not match, and the sulfur content, $w_{\mathrm{S}} = x_{\mathrm{S}} \cdot M(\mathrm{S})$, were reported to be between $2.17\ \%$ and $2.45\ \%$ by mass. As the values differ significantly, an alternative approach was used to get a more accurate estimate for the HFO sulfur content.

The LSA technique, previously described, is used with a constant value for w_S. When doing so, the resulting sum of squares takes a finite value, f_i. This value reflects the overall error between the measurements and the corrected values for the i^th test. By wrapping a loop around the LSA technique, while varying the HFO sulfur content, w_S, the average error can be evaluated as a function of w_S. This is shown in (9.9), where $F(w_\mathrm{S})$ is the average error, when all 16 test are taken into account for a given value of w_S.

$$\begin{gathered}\text{Minimize: } F(w_\mathrm{S}) \\ F(w_\mathrm{S}) = \frac{1}{n_\mathrm{Test}} \sum_{\mathrm{i}}^{n_\mathrm{Test}} \left(\text{Minimize } f_\mathrm{i}(\lambda, w_\mathrm{S}) \text{ by adjuting } \lambda\right)\end{gathered} \tag{9.9}$$

The combined objective function in (9.9), $F(w_\mathrm{S})$, is the average of all 16 values for f_i, which are obtained using (9.8), which is an optimization problem in itself. The combined optimization function allows for calculation of the statistically most accurate value of w_S, where the tendency for $F(w_\mathrm{S})$ is shown in Figure 9.7.

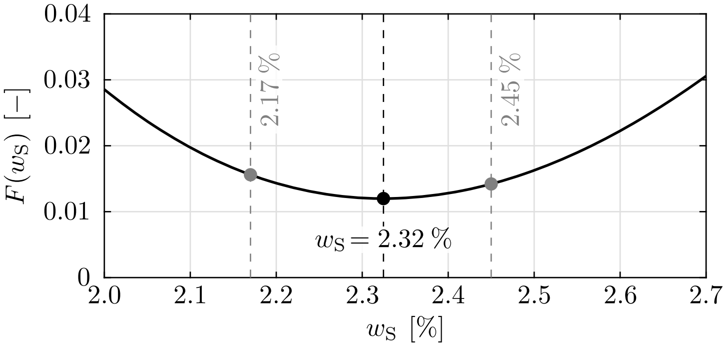

Figure 9.7: The results from tuning the HFO sulfur content to match the gas composition from the experimental data by minimizing $F(w_\mathrm{S})$.

As seen in Figure 9.7, a minimum exists at $w_\mathrm{S} = 2.32$ %, which is in-between the two fuel analyses of 2.17 and 2.45 %. Therefore, the optimized value of 2.32 % is assumed most accurate and is used for further processing. It should be noted that this technique allows w_S to be determined without any prior knowledge of the fuel sulfur content. The resulting fuel composition is shown in Table 9.2 along with the results from the two fuel analyses.

Table 9.2: The two fuel analyses and the optimized fuel composition according to the LSA technique, which was visualized in Figure 9.7. The optimized values for w_C, w_O, and w_N are average values of the two fuel analyses, whereas w_H was adjusted to make the mass fraction sum to unity.

Value	**Analysis 1**	**Analysis 2**	**Optimized**
w_C	$86.90\,\%$	$85.40\,\%$	$86.15\,\%$
w_H	$9.54\,\%$	$10.42\,\%$	$9.97\,\%$
w_O	$1.00\,\%$	$1.29\,\%$	$1.15\,\%$
w_S	$2.17\,\%$	$2.45\,\%$	$2.32\,\%$
w_N	$0.39\,\%$	$0.44\,\%$	$0.41\,\%$
$\sum$	$100\,\%$	$100\,\%$	$100\,\%$

9.3.4 Overview

Having determined the statistically most accurate fuel oil sulfur content of $w_\mathrm{S} = 2.32\ \%$, and having applied the LSA technique to all tests, the gas flow for each test can be calculated. Each of the sensor values are adjusted to satisfy the underlying physical model, where the required changes are shown in Table 9.3.

Table 9.3: The required changes to the filtered signals for all 16 tests, where $w_\mathrm{S} = 2.32\ \%$. The average and the *Root Mean Square*, RMS, errors are shown in the bottom two rows.

Test	$\lambda\,[-]$	Sick 810	Sick 100			
		$y^{\mathrm{S810}}_{\mathrm{g,O_2}}$ [%]	$y^{\mathrm{S100}}_{\mathrm{g,CO_2}}$ [%]	$y^{\mathrm{S100}}_{\mathrm{g,H_2O}}$ [%]	$y^{\mathrm{S100}}_{\mathrm{g,O_2}}$ [%]	$y^{\mathrm{S100}}_{\mathrm{g,SO_2}}$ [%]
1	2.941	–	+3.86	+6.11	+7.99	−4.18
2	2.915	–	+2.96	+5.13	+8.41	−2.51
3	2.884	–	+2.49	+4.55	+8.95	−1.38
4	2.869	–	+2.32	+4.23	+9.21	−0.84
5	2.867	–	+2.03	+3.96	+9.24	−0.35
6	2.864	–	+1.82	+3.73	+9.29	+0.06
7	2.849	–	+1.76	+3.73	+9.56	+0.28
8	2.852	–	+1.60	+3.71	+9.52	+0.42
9	2.818	–	+1.35	+3.22	+10.13	+1.43
10	2.830	–	+1.16	+3.14	+9.91	+1.54
11	2.813	–	+1.29	+2.89	+10.22	+1.80
12	2.814	–	+1.25	+2.81	+10.21	+1.90
13	2.840	+4.60	+2.02	+3.38	+9.72	+2.82
14	2.836	+4.62	+2.09	+3.51	+9.82	+2.71
15	2.834	+4.68	+2.08	+3.59	+9.84	+2.71
16	2.839	+4.82	+2.06	+3.59	+9.75	+2.74
Average	2.854	+4.68	+2.01	+3.83	+9.49	+0.57
RMS	2.854	+4.68	+2.12	+3.92	+9.51	+2.06

Some of the values in Table 9.3 for $y^{\mathrm{S810}}_{\mathrm{g,O_2}}$ are not included, as the sensor failed during these tests. The values of λ in the table, where $f_{\mathrm{i}}(\lambda)$ is minimized, are almost constant. The required changes to satisfy the underlying physical model are shown in the table, where the maximum required change is $10.22\,\%$ (Test number 11 for $y^{\mathrm{S100}}_{\mathrm{g,O_2}}$). Some general tendencies can be seen in the table, where most values are adjusted with positive values. The values of $y^{\mathrm{S100}}_{\mathrm{g,O_2}}$ are adjusted by 9.51 % on average, so this sensor is most likely at fault for the inconsistencies in the data.

9.4 Experimental results

The raw signals were filtered and subsequently adjusted according to the underlying physical model using the LSA technique. It should be noted that the adjustments were only made to the inlet gas flow to the scrubber. The outlet gas concentrations were not modified, and neither were any of the temperature or differential pressure signals. The results from all experiments are shown in Table 9.4 on the next page.

As seen in the table, the engine power is approximately 0.8 MW for the first eight tests, and approximately 1.6 MW for the remaining, which is the design load for the scrubber in the test centre. The mass flow of water into the jet can be seen to be zero for every second case, where the jet nozzles were deactivated as shown in Table 9.1 on page 182.

The outlet temperature can be seen to be generally higher for the high load cases compared to the low load cases, as the mass flow of gas is increased, while the water flow remains constant. The same tendency can be seen for the outlet sulfur equivalent, $S^{\mathrm{Out}}_{\mathrm{Eq}} = y^{\mathrm{S200}}_{\mathrm{g,SO2}}/y^{\mathrm{S200}}_{\mathrm{g,CO2}} \cdot 100/43.3$.

The values for the pressure transmitters are shown in the last column of the table, where the total pressure loss over the scrubber, ΔP, is approximately 250 Pa and 850 Pa for the low and high load cases respectively.

The results in the table will be used as inputs to the model in the next chapter, where the model is tuned to match the experimental results.

Table 9.4: The adjusted results from the experimental tests.

Test [−]	Power [MW]	λ [−]	$\dot{m}_{\mathrm{Fuel}}$ [kg/hr]	$\dot{m}_{\mathrm{l}}^{\mathrm{Abs,In}}$ [kg/s]	$\dot{m}_{\mathrm{l}}^{\mathrm{Jet,In}}$ [kg/s]	$T_{\mathrm{g}}^{\mathrm{In}}$ [°C]	$T_{\mathrm{g}}^{\mathrm{Out}}$ [°C]	$y_{\mathrm{g,CO_2}}^{\mathrm{In}}$ [%]	$y_{\mathrm{g,H_2O}}^{\mathrm{In}}$ [%]	$y_{\mathrm{g,O_2}}^{\mathrm{In}}$ [%]	$y_{\mathrm{g,SO_2}}^{\mathrm{In}}$ [ppm]	$y_{\mathrm{g,SO_2}}^{\mathrm{Out}}$ [ppm]	$S_{\mathrm{Eq}}^{\mathrm{In}}$ [%]	$S_{\mathrm{Eq}}^{\mathrm{Out}}$ [%]	ΔP [Pa]
1	0.809	2.94	195.9	7.55	2.37	255.2	23.1	5.18	4.34	13.47	518.5	106.1	2.31	0.46	141.2
2	0.808	2.92	193.9	7.55	0	261.7	28.3	5.22	4.37	13.40	523.0	155.6	2.31	0.67	102.1
3	0.808	2.88	194.3	7.11	2.36	264.4	25.1	5.28	4.41	13.33	528.5	145.3	2.31	0.62	293.0
4	0.811	2.87	195.2	7.12	0	265.8	27.9	5.30	4.43	13.29	531.2	183.9	2.31	0.79	274.0
5	0.811	2.87	194.9	12.27	2.35	268.0	19.6	5.31	4.43	13.28	531.5	97.4	2.31	0.42	232.5
6	0.813	2.86	193.2	12.30	0	268.7	23.6	5.31	4.43	13.27	532.1	125.8	2.31	0.54	181.6
7	0.805	2.85	194.6	16.12	2.48	269.5	14.5	5.34	4.45	13.24	534.8	70.8	2.31	0.30	303.0
8	0.815	2.85	195.2	16.35	0	270.5	16.4	5.33	4.45	13.24	534.4	87.8	2.31	0.38	273.9
9	1.598	2.82	367.7	7.50	2.35	278.0	31.5	5.40	4.49	13.15	540.6	261.6	2.31	1.11	902.5
10	1.605	2.83	370.1	7.54	0	274.9	35.3	5.37	4.48	13.18	538.5	299.0	2.31	1.27	957.7
11	1.599	2.81	367.6	7.06	2.34	273.7	32.6	5.41	4.50	13.14	541.5	287.7	2.31	1.22	875.5
12	1.590	2.81	366.3	7.10	0	273.0	43.9	5.40	4.50	13.14	541.5	340.6	2.31	1.44	811.9
13	1.591	2.84	366.4	12.19	2.34	272.5	32.4	5.36	4.46	13.21	536.5	222.3	2.31	0.94	761.8
14	1.595	2.84	366.4	12.24	0	272.1	35.2	5.36	4.47	13.20	537.4	247.7	2.31	1.05	696.5
15	1.598	2.83	366.8	15.97	2.46	272.0	24.5	5.37	4.47	13.20	537.6	159.1	2.31	0.67	810.6
16	1.598	2.84	365.2	16.29	0	271.9	25.8	5.36	4.47	13.21	536.7	179.0	2.31	0.76	765.3

10 MODEL TUNING

The scrubber model is comprised of numerous sub-models, where each of these require model parameters, which were found either empirically or theoretically in their respective studies. These parameters affect the results of the model, where the main result is the sulfur equivalent at the outlet of the scrubber. Other output results are of interest as well, which include the outlet temperature of the gas and the overall pressure loss. These three output parameters should match the results from the experimental tests described in *Chapter 9: Experiments*, when simulations are carried out under the same conditions. Therefore, some of the model parameters are tuned, such that the scrubber model will yield realistic results. Each parameter should, ideally, be determined by carrying out controlled experiments, but this is not feasible to do in this study, so an alternative approach is used, where several parameters are tuned simultaneously using a pattern search algorithm. This requires an objective function to be defined, where the errors between the results from the experiments and the simulations can be quantified.

10.1 Objective function

An objective function is defined, which quantifies the error between the experimental results and the model results, such that the model parameters can be tuned. Three values are of interest, which are the temperature at the outlet, $T_{\mathrm{g}}^{\mathrm{Out}}$, the sulfur equivalent at the outlet, $S_{\mathrm{Eq}}^{\mathrm{Out}}$, and the overall pressure loss, ΔP. The quantified error between the measured and simulated values is shown in (10.1), where $f_{\mathrm{i}}(\vec{\beta})$ is the error for the i^{th} test, where a total of 16 tests were carried out as described in *Chapter 9: Experiments*. The model parameters to be tuned are combined in $\vec{\beta}$, and are described in detail in the next section.

$$f_{\mathrm{i}}(\vec{\beta}) = \left(\left(\frac{\widetilde{T}_{\mathrm{g,i}}^{\mathrm{Out}}(\vec{\beta}) - T_{\mathrm{g,i}}^{\mathrm{Out}}}{1\,\mathrm{K}} \right)^{p} \cdot w_{\mathrm{T}} + \left(\frac{\widetilde{S}_{\mathrm{Eq}}^{\mathrm{Out}}(\vec{\beta}) - S_{\mathrm{Eq}}^{\mathrm{Out}}}{0.01\,\%} \right)^{p} \cdot w_{\mathrm{S_{Eq}}} + \left(\frac{\Delta \widetilde{P}_{\mathrm{i}}(\vec{\beta}) - \Delta P_{\mathrm{i}}}{10\,\mathrm{Pa}} \right)^{p} \cdot w_{\Delta \mathrm{P}} \right)^{1/p} \tag{10.1}$$

The values with a tilde accent are from the computational scrubber model, whereas the values without this accent are from the experimental tests. It can be seen that the values from the model are functions of $\vec{\beta}$, such as $\widetilde{T}_{\mathrm{g}}^{\mathrm{Out}}(\vec{\beta})$, which is the outlet gas temperature from the model. The errors between the experimental and model outputs are divided by a constant, which normalizes the error, such that the numerical value of the relative errors all have the same order of magnitude. For instance, the temperature error will be of the order of 10^0 K, whereas the outlet sulfur equivalent is of the order of 10^{-3}. The errors are weighted according to the p-norm, where each error is raised to the power of p, and the sum is raised to the power of $1/p$. By increasing p, the largest error of the three will contribute relatively more to $f_\mathrm{i}(\vec{\beta})$ compared to the others. A value of $p = 3$ was used in this study.

w_T, $w_{\mathrm{S}_\mathrm{Eq}}$, and $w_{\Delta\mathrm{P}}$ are weights, which are used to adjust the relative importance of each variable. It should be noted that each normalization factor and weight pair can be combined to a single scalar, but this is not done in this study. The objective function in (10.1), $f_\mathrm{i}(\vec{\beta})$, applies to the i^th test, so in order to tune the model to match all experimental cases, which spans various scenarios, a global objective function is defined, which is shown in (10.2).

$$\begin{gathered}\text{Minimize: } F(\vec{\beta}) \\ F(\vec{\beta}) = \frac{1}{n_\mathrm{Test}} \sum_{\mathrm{i}}^{n_\mathrm{Test}} f_\mathrm{i}(\vec{\beta})\end{gathered} \tag{10.2}$$

The global objective function is a measure of the fitness across all experimental tests, and this value is to be minimized using a pattern search optimization algorithm.

10.2 Variables

The global objective function stated in (10.2) is a function of $\vec{\beta}$, which is a vector containing the parameters to be tuned. Numerous parameters are used in the scrubber model, but not all affect the results equally. The values chosen for tuning are shown in Table 10.1 on the next page, and are selected such that the output variables can be adjusted.

The six variables of $\vec{\beta}$ in Table 10.1 are tuned using a pattern search algorithm, and this requires limits for each variable along with a step size, which will be described in the next section. Each variable is related to an equation previously described, where the references are shown in the table. The six variables are described below:

- D_{32} and N_RR are related to the sprayer nozzle parameters, where D_{32} is the average droplet size, and N_RR is the spread parameter, where increasing values will result in generally larger droplets.
- $\bar{v}_\mathrm{Inj}$ is the average injection velocity, where the truncated normal distribution was used to calculate the velocities.

Table 10.1: The six variables in $\vec{\beta}$, which are tuned to minimize the global objective function, $F(\vec{\beta})$.

Variable	**Description**	**Equation and page**	**Step**	**Lower limit**	**Upper limit**
D_{32}	Mean injection droplet diameter	Eq. 4.8 Page 67	150 µm	1100 µm	2000 µm
N_{RR}	Rosin-Rammler spread parameter	Eq. 4.8 Page 67	0.1	1.6	2.0
$\bar{v}_{\mathrm{Inj}}$	Mean injection velocity	Eq. 4.5 Page 66	1 m/s	11 m/s	21 m/s
C_{IP}	Instability constant	Eq. 4.66 Page 108	50	1000	2000
ϕ_{h}	Heat transfer coefficient multiplier	Eq. 4.79 Page 118	0.05	0.5	2.0
$\phi_{\mathrm{k,H_2O}}$	Mass transfer coefficient multiplier for H_2O	Eq. 4.84 Page 120	0.05	0.5	2.0

- C_{IP} is the instability constant, which is related to the internal mass and heat transfer coefficients. Decreasing this value results in increased mass and heat transfer coefficients.
- ϕ_{h} is simply a scalar multiplied to (4.79), where the external heat transfer coefficient is calculated. Therefore, increasing this value will increase the heat transfer coefficient.
- $\phi_{\mathrm{k,H_2O}}$ is a scalar multiplied to the mass transfer coefficient for H_2O only. The reason for only applying this to H_2O is that the internal circulation is not taken into account for this species, as the mass fraction of water is practically unity. Therefore, in order to adjust the mass transfer of H_2O, $\phi_{\mathrm{k,H_2O}}$ is introduced.

Having defined the six variables to be tuned in $\vec{\beta}$, the optimization algorithm can be defined.

10.3 Pattern search algorithm

Numerous optimization algorithms exist, where each has its advantages and disadvantages. The global objective function, $F(\vec{\beta})$, is computationally expensive to evaluate, so this must be evaluated a minimum of times, if the computational time is to be kept feasible. As the variable space is very large with six parameters in $\vec{\beta}$, there will probably exist numerous local minima, so a global optimization routine would be beneficial to use, but such algorithms typically require a large number of objective function evaluations. Instead, a modified pattern-search algorithm based upon [Lewis and Torczon (87)] is used.

The pattern search algorithm only allows the elements of $\vec{\beta}$ to be certain values between specified upper and lower limits, thus making it a constrained algorithm. The limits for the different variables were shown in Table 10.1. The local gradient of $F(\vec{\beta})$ is taken into account, which increases the convergence rate. An illustration of the principle of a pattern search algorithm is shown in Figure 10.1.

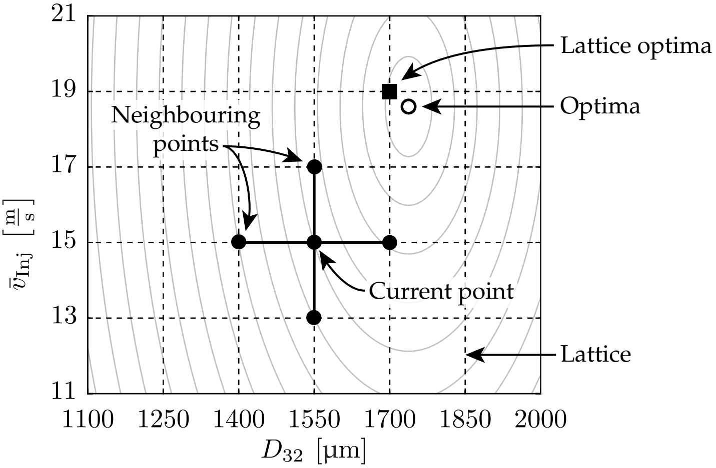

Figure 10.1: An illustration of the advantages and disadvantages of a pattern search algorithm. The grey contour lines indicate any given objective function, where the example in this figure is generated and does not reflect the global objective function, $F(\vec{\beta})$, of the scrubber model.

Figure 10.1 shows the general principle of a pattern search algorithm, where the example is shown with only two free variables, which are D_{32} and $\bar{v}_{\text{Inj}}$, and the objective function is shown as the grey contour lines. Notice that the example is not generated using the scrubber model, but is a constructed example. The free variables are limited to the values on the lattice, so a value of, for instance, $D_{32} = 1325\,\mu\text{m}$ is not valid. The lattice is constructed from the *Step*, *Lower limit*, and *Upper limit* columns of Table 10.1.

The algorithm minimizes the global objective function by evaluating this on the neighbouring points relative to the current point, and if a lower value is found, the current point moves to this. As more and more points are evaluated, the gradient of the global objective function can be approximated, such that the current point can move in the direction, where the objective function is decreasing most rapidly. At some point, the current point will be located on the lattice optima, after which no other point exist, which has a lower objective score. However, the true optima is not reached, as this does not intersect with the lattice in the given example. Some methods refine the lattice, when the neighbouring points all have an objective value greater than that of the current point, such that the true optima can be reached [Lewis and Torczon (87)]. This is however not applied in this study, but rather the method used in this study searches further away to look for other local optima with a lower value of the objective function.

10.3.1 Steps

The patterns search algorithm used in this study can be described in five steps, which are described below:

Step 1: List permutations

The first step is to list all permutations relative to the current point, which is shown in Figure 10.2, where only two variables are present in $\vec{\beta}$: β_1 and β_2.

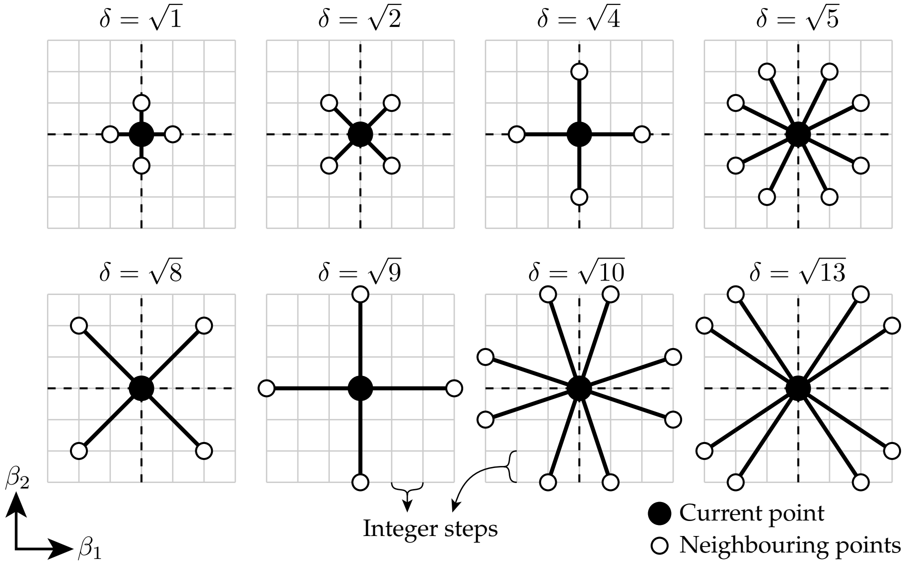

Figure 10.2: An illustration of the permutation process around the current point, which is shown with the solid black dots. The distance to the neighbouring points, δ, are shown for each permutation above each graph, assuming integer steps between the lattice points.

As seen in Figure 10.2, the neighbouring points in the upper left graph are located a distance of $\sqrt{1} = 1$ away from the current point, assuming the lattice to have integer steps. The second graph shows neighbours, which are located a distance of $\sqrt{2}$ away. This process continues, and is directly applicable for multidimensional cases as well, where the number of free variables is greater than two.

Step 2: Calculate gradient

$F(\vec{\beta})$ is computationally expensive to evaluate, so the neighbouring lattice points in the direction of steepest descend should be evaluated first. This is found by calculating the gradient at the current point by using the previously evaluated lattice points, which is illustrated in Figure 10.3.

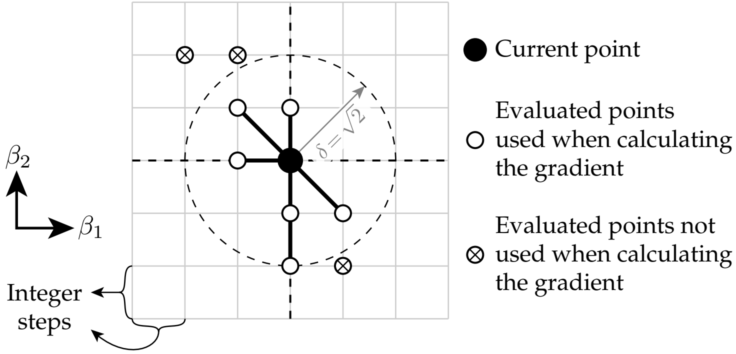

Figure 10.3: An illustration of the points, which are used for approximating the local gradient of $F(\vec{\beta})$. Only the points within a distance of $\sqrt{2}$ are included.

Figure 10.3 shows a lattice with two free variables, β_1 and β_2, where a number of lattice points are shown, on which the objective function, $F(\vec{\beta})$, has been evaluated. The gradient at the current point is approximated by only using the evaluated points, which are located within a distance of $\sqrt{2}$ away from the current point. The gradient is approximated using the method of least squares, which is shown in (10.3) [Versteeg and Malalasekera (135)].

$$
\begin{gathered}
\overbrace{\begin{bmatrix} \Delta\beta_{1,1} & \Delta\beta_{2,1} \\ \Delta\beta_{1,2} & \Delta\beta_{2,2} \\ \vdots & \vdots \\ \Delta\beta_{1,\mathrm{n}} & \Delta\beta_{2,\mathrm{n}} \end{bmatrix}}^{\mathbf{A}} \cdot \overbrace{\begin{bmatrix} \dfrac{\partial F}{\partial \beta_1} \\ \\ \dfrac{\partial F}{\partial \beta_2} \end{bmatrix}}^{\dfrac{\partial F}{\partial \vec{\beta}}} = \overbrace{\begin{bmatrix} F_1 - F_{\mathrm{CP}} \\ F_2 - F_{\mathrm{CP}} \\ \vdots \\ F_{\mathrm{n}} - F_{\mathrm{CP}} \end{bmatrix}}^{\vec{b}} \\
\frac{\partial F}{\partial \vec{\beta}} = \left(\mathbf{A}^{\mathrm{T}} \cdot \mathbf{A}\right)^{-1} \cdot \mathbf{A}^{\mathrm{T}} \cdot \vec{b}
\end{gathered}
\tag{10.3}
$$

Where F_{CP} is the global objective value for the current point. $\Delta\beta_{1,\mathrm{i}}$ is the relative distance in β_1 to the current point for the i^{th} lattice point, and $\Delta\beta_{2,\mathrm{i}}$ is similar but in the direction of β_2. In the example shown in Figure 10.3, $n = 6$ as this is the number of points within a distance of $\sqrt{2}$ relative to the current point, which are shown with the white dots. The linear system of equations shown in (10.3) is typically an overdetermined system, which implies that the fitted plane does not go through all points. The example shown in Figure 10.3 approximates the two gradients, $\partial F/\partial \beta_1$ and $\partial F/\partial \beta_2$, based on six points, so $\mathbf{A}$ has a size of 6×2. By excluding the points with a distance greater than $\sqrt{2}$ relative to the current point, the non-linear tendencies are excluded, so the local gradient is more accurately approximated. An alternative approach could be used, where all evaluated points are included, but are weighted with the inverse distance or a similar metric, which decreases with distance.

Step 3: Predict objective score

Having approximated the local gradient at the current lattice point, the objective function, $F(\vec{\beta})$, can be approximated on the neighbouring points from the first step, $F_{\text{Predict}}(\vec{\beta})$. This is done using (10.4), where $\vec{\beta}_{\text{CP}}$ is the parameter set for the current point.

$$F_{\text{Predict}}(\vec{\beta}) = \left(\frac{\partial F}{\partial \vec{\beta}}\right)^{\text{T}} \cdot \left(\vec{\beta} - \vec{\beta}_{\text{CP}}\right) + F(\vec{\beta}_{\text{CP}}) \tag{10.4}$$

Step 4: Evaluate new point

The neighbouring point with the lowest value of F_{Predict} is evaluated using the new parameter set, $\vec{\beta}$.

Step 5: Update

Having evaluated the neighbouring point with the lowest value of F_{Predict}, the algorithm moves to this point, if the value of the objective function is smaller compared to the current point. The algorithm first investigate all points located a distance of $\sqrt{1}$ away, and if all have greater values of the objective function compared to the current point, the algorithm evaluates the objective function on the lattice points located a distance of $\sqrt{2}$ away. This process continues again and again until a lattice point with a smaller value of the objective function is found. This simple method allows the global minimum to be found instead of a local minimum, as the search distance increases for each iteration instead of getting smaller.

10.3.2 Implementation

Each evaluation of the global objective function, $F(\vec{\beta})$, requires carrying out several CFD simulations coupled with the discrete phase and the wall films. A single simulation takes approximately an hour (see *Section 11.5: Timing*), which will yield an objective score, $f_{\text{i}}(\vec{\beta})$, for the i^{th} test. Each evaluation of the global objective function, $F(\vec{\beta})$, requires 16 simulations. However, in practice, only eight tests were included in the global objective function, so instead of evaluating $f_{\mathrm{i}}(\vec{\beta})$ 16 times, it was only evaluated eight times, which decreased the computational time significantly.

The optimization routine was fully automatized, where a tool was developed in MATLAB. When a simulation was finished, a new simulation was automatically launched, such that the optimization process could run continuously without any manual user interaction. The optimization was carried out on a Linux computer with 40 Intel® Xeon(R) CPU E5-2660 @ 2.60 GHz cores and 128 GB ram. Each simulation was executed in parallel with four cores, which allowed for eight simulations to run at the same time without affecting the performance. An example is shown in Figure 10.4, where two lattice points are evaluated simultaneously, where each MATLAB terminal is running in serial, and each OpenFOAM terminal is running in parallel with four cores.

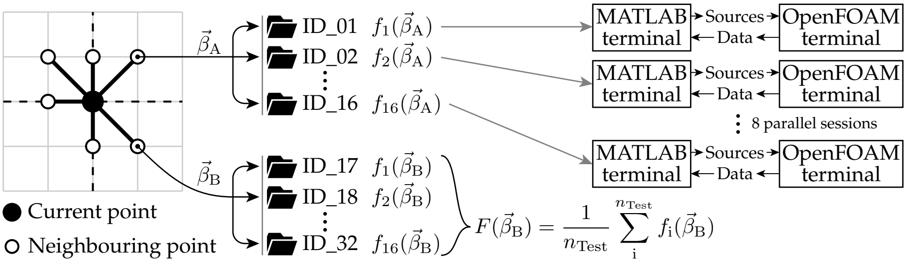

Figure 10.4: An example where two lattice points are evaluated simultaneously. Each lattice point requires evaluating eight different test, where each of these are assigned an objective value, f_{i}. The global objective function, $F(\vec{\beta})$, is the average of these eight objective values.

As seen in Figure 10.4, two lattice points are being evaluated, where the parameter sets are $\vec{\beta}_{\mathrm{A}}$ and $\vec{\beta}_{\mathrm{B}}$. Each lattice point requires 16 simulations to be carried out, where, in practice, only eight different tests were evaluated. The objective function for each of these are evaluated by launching a MATLAB and an OpenFOAM terminal, which exchange source terms and data, which is shown to the right in the figure. When a simulation is finished, the objective function, $f_{\mathrm{i}}(\vec{\beta})$, is evaluated, and when all simulations for a single lattice point are finished, the global objective function is calculated, $F(\vec{\beta})$, where an example was shown for $F(\vec{\beta}_{\mathrm{B}})$ in the bottom of the figure.

10.4 Results

As described in the previous section, only eight tests were included in the global optimization function, $F(\vec{\beta})$. These eight were chosen to be distinct scenarios, which were test number 5-8 and 13-16, where these were shown in Table 9.1 on page 182. The first four of these are with a scrubber load of approximately 50 %, whereas the latter four are with 100 % scrubber load.

The uneven tests, 5, 7 etc., have the jet sprayer nozzle activated, whereas the others do not. Case 7, 8, 15, and 16 also have the top absorber sprayer nozzle activated. The reason for choosing these eight scenarios for tuning is that these reflect typical operating scenarios. The remaining eight tests have a very low liquid mass flow into the scrubber, $\dot{m}_{\mathrm{l}}^{\mathrm{In}}$, so these were excluded during optimization. The optimization itself was carried out over several days, where the optimum parameter set, $\vec{\beta}$, is shown in Table 10.2 along with the initial values used prior to tuning.

Table 10.2: The six variables in $\vec{\beta}$ before and after tuning using the pattern search algorithm. All values are located on the lattice, which was defined using Table 10.1.

Variable	Initial value	Tuned value
D_{32}	$1400\ \mu\mathrm{m}$	$1250\ \mu\mathrm{m}$
N_{RR}	1.8	1.6
$\bar{v}_{\mathrm{Inj}}$	$15\ \mathrm{m/s}$	$17\ \mathrm{m/s}$
C_{IP}	1000	750
ϕ_{h}	1.0	0.4
$\phi_{\mathrm{k,H_2O}}$	1.0	0.55

The tuned injection diameter, D_{32}, can be seen to be $1250\ \mu\mathrm{m}$ and the spread parameter is 1.6, which were $1400\ \mu\mathrm{m}$ and 1.8 prior to tuning. These tuned values will result in smaller droplets, which increases the surface area per unit volume. Furthermore, the injection velocity, $\bar{v}_{\mathrm{Inj}}$, is tuned to be $17\ \mathrm{m/s}$, which is an increase of $2\ \mathrm{m/s}$ compared the to value prior to tuning. This will generally cause more droplets to experience breakup, which again increases the reactive surface area per unit volume. The instability constant, C_{IP}, is decreased during parameter tuning, which increases the overall mass and heat transfer coefficients. However, the values of ϕ_{h} and $\phi_{\mathrm{k,H_2O}}$ decreased during tuning, which decreases the overall heat transfer.

Based on the described observations, the tuned model has, in general, a greater reactive surface area compared to the model prior to tuning. Furthermore, the overall mass transfer coefficients have increased, whereas the heat transfer coefficients have decreased.

Having tuned the parameters to match the experimental data, all 16 tests were evaluated. A comparison between the outlet temperature, the outlet sulfur concentration, and the overall pressure loss between the experiments and the scrubber model is shown in Table 10.3. Notice that the outlet sulfur content is presented in terms of the mole fraction of SO_2 in *parts per million*, $y_{\mathrm{g,SO_2}}^{\mathrm{Out}}$ [ppm]. The relative errors shown in the table are almost identical whether $y_{\mathrm{g,SO_2}}^{\mathrm{Out}}$ or $S_{\mathrm{Eq}}^{\mathrm{Out}}$ is used.

Table 10.3: The results from the experimental tests and the computational model. The results are shown for each of the 16 tests, where the values with a tilde, such as $\widetilde{T}_{\mathrm{g}}^{\mathrm{Out}}$, are from the computational scrubber model, whereas the values without a tilde are from the experimental tests. The differences are shown along with a relative deviations compared to the experimental tests. The highlighted rows are the tests, which were used during parameter tuning. The average and *Root Mean Square*, RMS, errors are shown in the bottom two rows.

Test	Temperature				Sulfur concentration				Pressure loss			
	$T_{\mathrm{g}}^{\mathrm{Out}}$	$\widetilde{T}_{\mathrm{g}}^{\mathrm{Out}}$	$\widetilde{T}_{\mathrm{g}}^{\mathrm{Out}} - T_{\mathrm{g}}^{\mathrm{Out}}$	$\frac{\widetilde{T}_{\mathrm{g}}^{\mathrm{Out}} - T_{\mathrm{g}}^{\mathrm{Out}}}{T_{\mathrm{g}}^{\mathrm{Out}}}$	$y_{\mathrm{g,SO_2}}^{\mathrm{Out}}$	$\widetilde{y}_{\mathrm{g,SO_2}}^{\mathrm{Out}}$	$\widetilde{y}_{\mathrm{g,SO_2}}^{\mathrm{Out}} - y_{\mathrm{g,SO_2}}^{\mathrm{Out}}$	$\frac{\widetilde{y}_{\mathrm{g,SO_2}}^{\mathrm{Out}} - y_{\mathrm{g,SO_2}}^{\mathrm{Out}}}{y_{\mathrm{g,SO_2}}^{\mathrm{Out}}}$	ΔP	$\Delta\widetilde{P}$	$\Delta\widetilde{P} - \Delta P$	$\frac{\Delta\widetilde{P} - \Delta P}{\Delta P}$
[–]	[°C]	[°C]	[K]	[%]	[ppm]	[ppm]	[ppm]	[%]	[Pa]	[Pa]	[Pa]	[%]
1	23.1	26.5	3.4	+14.8	106.1	181.1	74.9	+70.6	141.2	135.6	−5.6	−4.0
2	28.3	32.5	4.1	+14.6	155.6	234.4	78.9	+50.7	102.1	113.6	11.5	+11.3
3	25.1	32.3	7.2	+28.5	145.3	196.0	50.7	+34.9	293.0	206.1	−86.9	−29.7
4	27.9	45.6	17.6	+63.2	183.9	249.1	65.2	+35.4	274.0	188.3	−85.7	−31.3
5	19.6	17.2	−2.4	−12.3	97.4	99.1	1.7	+1.8	232.5	188.6	−43.9	−18.9
6	23.6	18.7	−4.9	−20.8	125.8	124.5	−1.3	−1.1	181.6	169.7	−11.8	−6.5
7	14.5	14.7	0.2	+1.4	70.8	78.8	8.0	+11.4	303.0	233.6	−69.4	−22.9
8	16.4	16.2	−0.2	−1.4	87.8	98.0	10.2	+11.6	273.9	217.4	−56.4	−20.6
9	31.5	43.9	12.5	+39.6	261.6	291.2	29.6	+11.3	902.5	446.1	−456.4	−50.6
10	35.3	62.9	27.6	+78.1	299.0	339.4	40.4	+13.5	957.7	377.5	−580.2	−60.6
11	32.6	44.9	12.3	+37.8	287.7	278.8	−8.9	−3.1	875.5	531.8	−343.7	−39.3
12	43.9	47.1	3.2	+7.2	340.6	324.7	−15.9	−4.7	811.9	480.5	−331.5	−40.8
13	32.4	26.7	−5.6	−17.4	222.3	177.2	−45.0	−20.3	761.8	549.4	−212.4	−27.9
14	35.2	32.1	−3.1	−8.7	247.7	223.3	−24.3	−9.8	696.5	510.4	−186.1	−26.7
15	24.5	23.5	−1.0	−4.0	159.1	137.5	−21.6	−13.6	810.6	594.3	−216.3	−26.7
16	25.8	28.1	2.3	+9.0	179.0	170.8	−8.2	−4.6	765.3	539.8	−225.5	−29.5
Average (All tests)			4.6	14.3			14.6	11.5			−181.3	−26.5
RMS (All tests)			9.8	31.1			39.4	26.6			246.9	31.5
Average (Tuned tests)			−1.8	−6.8			−10.1	−3.1			−127.7	−22.5
RMS (Tuned tests)			3.1	11.5			20.4	11.1			153.1	23.5

10.4.1 Discussion

As seen in the table, the values from the experiments and the simulations are compared, where both the absolute differences and the relative differences are shown. Notice that the relative temperature errors are normalized using the Celsius temperature scale and not the Kelvin scale. The highlighted rows are the eight tests used during parameter tuning, which can be seen to match the experimental tests significantly better compared to the tests, which were not included during parameter tuning. The average and the RMS-errors are shown in the four last rows of Table 10.3, where the white rows labelled *All tests* are calculated using all 16 tests. The shaded rows are indicating the average errors based on the eight shaded rows only: 5-8 and 13-16. The computational scrubber model is not able to match the experimental values accurately for some of the tests, which is addressed in the following subsections.

Outlet temperature

The outlet temperature, $T_{\mathrm{g}}^{\mathrm{Out}}$, can be seen to deviate with $4.6\ \mathrm{K}$ on average for all 16 tests, whereas the RMS-error is $9.8\ \mathrm{K}$. If only the tests with the high water load are included, the average error is $-1.8\ \mathrm{K}$, and the RMS-error is $3.1\ \mathrm{K}$, which translates to $-6.8\ \%$ and $11.5\ \%$ respectively. This indicates that the scrubber model is not accurately capturing the outlet temperature at low water flows, $\dot{m}_{\mathrm{l}}^{\mathrm{In}}$, but is does accurately predict the temperature for high water flows.

Outlet sulfur concentration

The outlet sulfur concentration, $y_{\mathrm{g,SO_2}}^{\mathrm{Out}}$, can be seen to deviate with an error of $14.6\mathrm{ppm}$ and $39.4\mathrm{ppm}$ for the average and RMS-errors respectively. Again, the same tendency applies for the sulfur content as was the case for the outlet temperature, where the high water flow tests match significantly better with the experimental results compared to the low water flow tests. This is apparent in the fourth column for the sulfur concentration, where the relative deviations on average are 11.5 and $-3.1\ \%$ respectively, and the RMS-errors are 26.6 and $11.1\ \%$ respectively.

The reason for these large deviations might be an inaccurately calibrated $\mathrm{SO_2}$ sensor at the outlet, where only a single measurement was available from the Sick 200 gas analyser as seen in Figure 9.2 on page 181.

Pressure loss

The overall pressure loss, ΔP, can be seen to deviate with $-181.3\ \mathrm{Pa}$ on average for all tests, where the general tendency is that the scrubber model predicts a significantly lower pressure loss compared to the experimental tests.

The reason for this is assumed caused by numerous things, where some are listed below:

- **Domain size:** The scrubber is modelled using an axis-symmetric mesh, which only span $\theta_{\mathrm{Mesh}} = 1^\circ$. This size was chosen due to the massive reduction is computation requirements, as described in *Section 8.3: Domain size independence*. The results from the domain size independence study showed that only the pressure loss was significantly affected by θ_{Mesh}, where the domain with $\theta_{\mathrm{Mesh}} = 1^\circ$ showed a relative error of $-15\,\%$ compared to the simulation, where $\theta_{\mathrm{Mesh}} = 180^\circ$.
- **Geometry:** The scrubber installed at the Alfa Laval Test & Training Centre contains various piping, support beams, probes etc., which are not included in the CFD model. These will all contribute to a more disturbed flow, which, in turn, will increase the pressure loss.
- **Discrete phase:** The discrete phase affects the momentum source terms, which are transferred from MATLAB to OpenFOAM. However, the momentum exchange was only modelled for the droplet dynamics, which was described in *Section 4.4: Dynamics*. The momentum source terms associated with collision, breakup, distortion, and impingement were not modelled. These contributions, although assumed small, would also increase the overall pressure loss over the scrubber.
- **Wall film:** The wall film do not affect the continuous phase with any momentum source terms. However, the no-slip condition is applied to all surfaces within the scrubber in the CFD model, but the liquid interaction is not modelled. Also, in case of atomization and separation, the gas flow should be affected with a given momentum source term, but this was not included either.
- **Pressure probe placement:** The differential pressure probe is measuring the static pressure difference between the inlet and the outlet at the inside of the shell. The outlet pressure probe is installed $13.4\ \mathrm{cm}$ above the contraction at the outlet, so the apparent pressure for this probe might be lower compared to the actual averaged pressure. This is illustrated in Figure 10.5 on the next page.

The pressure probe at the top of the scrubber is installed $13.4\ \mathrm{cm}$ above the bend, where the exhaust gas funnel is contracting. The pressure probe itself is mounted to a ring, where four hollow pipes are entering the scrubber, where the openings are flush with the scrubber shell. The static pressure is thus measured inside the ring, where the static pressure should yield the average pressure around the circumference of the shell. Because of the bend, the gas might not stay attached to the shell, so separation can occur. This will interfere with the pressure readings from the probe, so a CFD study is carried out, where this effect can be investigated. The domain shown to the left in Fig-

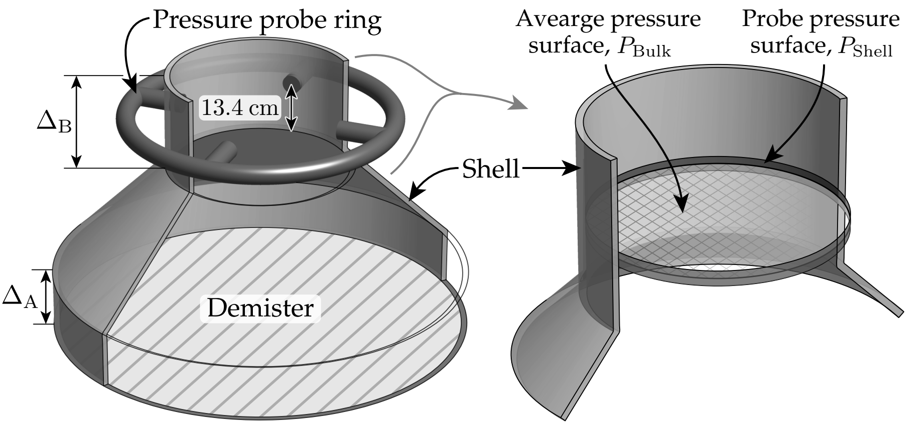

Figure 10.5: The top part of the scrubber above the demister is shown to the left, where the contraction is apparent. The right figure shows a detailed view of the method of evaluating the error between the apparent pressure measured and the bulk pressure of the gas.

ure 10.5 was meshed using a very fine mesh, and a k-ω-SST turbulence model was used to resolve the turbulence. The inlet and outlet sections were sufficiently long, $\Delta_A = \Delta_B = 2$ m, such that the flow was not affected by the inlet and outlet boundaries. The inlet velocity was varied between 1 and 6 m/s, and the area weighted static pressure was evaluated according to (10.5).

$$P_{\text{Avg}} = \frac{\int_A P \, \mathrm{d}A}{\int_A 1 \, \mathrm{d}A} \tag{10.5}$$

Where P_{Avg} is either P_{Bulk} or P_{Shell}, and A is the surface area, on which the integration is carried out according to the two surfaces shown in Figure 10.5. The results from the analysis is shown in Figure 10.6.

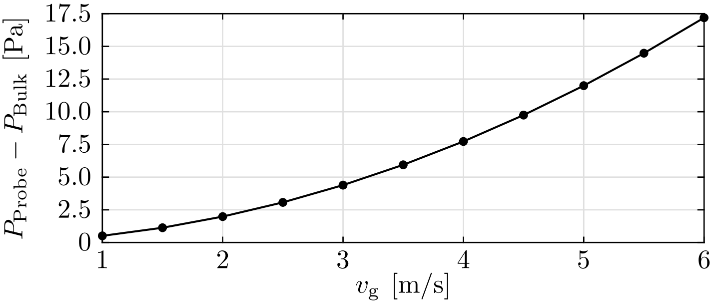

Figure 10.6: The difference between the apparent static pressure measured by the probe and the static pressure of the bulk gas.

As seen in Figure 10.6, the static pressure difference between P_{Probe} and P_{Bulk} is approximately 17 Pa at $v_g = 6$ m/s, where the velocity is measured upstream of the demister. A scrubber typically operates at 4-5 m/s, so the results indicate that the probe is measuring approximately 10 Pa less than the actual static pressure of the bulk.

Numerous sources of uncertainty and errors are present with respect to the overall pressure loss, which might be the cause for the large deviation seen in Table 10.3. If, however, the results are adjusted to take the determinable uncertainties into account, the relative error is reduced. This is done according to (10.6).

$$\begin{aligned} \Delta P' &= \Delta P - (P_{\text{Bulk}}(v_{\text{g}}) - P_{\text{Shell}}(v_{\text{g}})) \\ \Delta \widetilde{P}' &= \frac{\Delta \widetilde{P}}{1 - 15\,\%} \end{aligned} \tag{10.6}$$

Where the values with an apostrophe, $(...)'$, are adjusted to take the determinable uncertainties into account. The first equation in (10.6) states that the pressure loss from the experiments is reduced by the measurement error shown in Figure 10.6. The second equation states that the pressure loss from the scrubber model is adjusted with $15\ \%$, which was the error caused by the domain size being $\theta_{\text{Mesh}} = 1°$ as described in *Section 8.3: Domain size independence*. The results, after having applied (10.6) to the experimental and model results, are shown in Table 10.4.

Table 10.4: The results from the experimental tests and the computational model after the accountable uncertainties are taken into account, which are indicated by the superscripts $(...)'$.

Test [–]	$\Delta P'$ [Pa]	$\Delta \widetilde{P}'$ [Pa]	$\Delta \widetilde{P}' - \Delta P'$ [Pa]	$\frac{\Delta \widetilde{P}' - \Delta P'}{\Delta P'}$ [%]
1	139.3	159.5	20.2	+14.5
2	100.2	133.6	33.4	+33.4
3	291.2	242.4	−48.8	−16.8
4	272.1	221.5	−50.6	−18.6
5	230.8	221.9	−8.9	−3.9
6	179.8	199.7	19.9	+11.1
7	301.4	274.8	−26.6	−8.8
8	272.2	255.8	−16.4	−6.0
9	896.0	524.8	−371.3	−41.4
10	950.8	444.1	−506.7	−53.3
11	869.0	625.6	−243.4	−28.0
12	804.4	565.2	−239.1	−29.7
13	755.2	646.3	−108.9	−14.4
14	689.7	600.4	−89.3	−12.9
15	804.6	699.2	−105.4	−13.1
16	759.2	635.0	−124.2	−16.4
Average (All tests)			−116.6	−12.8
RMS (All tests)			188.0	24.0
Average (Tuned tests)			−57.5	−8.1
RMS (Tuned tests)			77.3	11.5

As seen in Table 10.4, the average relative errors after having taken the accountable uncertainties into account are $-12.8\ \%$ and $-8.1\ \%$ for all tests and the tuned tests respectively, where the RMS-errors are $24.0\ \%$ and $11.5\ \%$ respectively. The remaining errors are assumed to be caused by the other uncertainties previously described, which cannot be quantified without further analyses.

10.4.2 Sensitivity study

Having tuned the model to match the experimental tests, a sensitivity study is carried out to indicate the relative effect on the output variables for each of the model parameters in $\vec{\beta}$. These sensitivities are calculated according to (10.7), where an example is shown for D_{32}. Each parameter is varied with $\pm 2.5\ \%$, which allowed for evaluating the sensitivity of each input variable on the outputs.

$$\begin{aligned}
D_{32}^{\ominus} &= 1250\ \mathrm{\mu m} \\
\beta_{\mathrm{D}_{32}}^{+} &= D_{32}^{\ominus} \cdot (1 + 2.5\ \%) = 1281.25\ \mathrm{\mu m} \\
\beta_{\mathrm{D}_{32}}^{-} &= D_{32}^{\ominus} \cdot (1 - 2.5\ \%) = 1218.75\ \mathrm{\mu m} \\
\frac{\partial\, T}{\partial\left({}^{D_{32}}/_{D_{32}^{\ominus}}\right)} &\approx \frac{\widetilde{T}_{\mathrm{g}}^{\mathrm{Out}}(\vec{\beta}^{+}) - \widetilde{T}_{\mathrm{g}}^{\mathrm{Out}}(\vec{\beta}^{-})}{5\ \%} = +17.2\ \frac{\mathrm{K}}{\%}
\end{aligned} \tag{10.7}$$

The sensitivities are shown in Table 10.5, where the values are reported per percent change according to (10.7). The sensitivity study is carried out for two different cases, where the load is $50\ \%$ and $100\ \%$ of the scrubber design load of $1.6\ \mathrm{MW}$.

Table 10.5: The sensitivity of the output variables relative to the six variables in $\vec{\beta}$. The values are reported as the change per percent change in β_{i} according to (10.7). Two columns are present for each output variable, which correspond to $50\ \%$ and $100\ \%$ scrubber design load. The highlighted cells indicate gradients, which have different signs for the two load cases.

$\frac{\partial -}{\partial({}^{\beta_{\mathrm{i}}}/_{\beta_{\mathrm{i}}^{\ominus}})}$	$\widetilde{T}_{\mathrm{g}}^{\mathrm{Out}}$ [K]		$\widetilde{y}_{\mathrm{g,SO_2}}^{\mathrm{Out}}$ [ppm]		$\Delta\widetilde{P}$ [Pa]	
	$50\ \%$	$100\ \%$	$50\ \%$	$100\ \%$	$50\ \%$	$100\ \%$
D_{32}	$+6.0$	$+17.2$	$+37.3$	$+31.4$	-8.4	-31.5
N_{RR}	$+0.4$	$+0.8$	-20.5	-2.2	$+8.0$	-5.1
$\bar{v}_{\mathrm{Inj}}$	$+10.0$	-9.6	-6.4	-33.3	$+25.1$	$+81.6$
C_{IP}	$+8.9$	$+7.8$	$+75.0$	$+32.8$	-7.9	$+3.0$
ϕ_{h}	-18.0	-32.3	$+32.5$	$+12.5$	-28.9	-80.6
$\phi_{\mathrm{k,H_2O}}$	$+7.2$	-5.7	$+4.2$	-2.9	$+7.9$	$+5.5$

As seen in Table 10.5, the output variables are affected by all input variables in complex manners. For instance, when increasing D_{32}, the surface are per unit volume will decrease, which results in an increase in the outlet temperature and sulfur concentration. The highlighted cells indicate gradients, where the sign is different between the low and high load cases. These illustrate the complex nature of scrubber modelling. For instance, when increasing the injection velocity, $\bar{v}_{\mathrm{Inj}}$, the outlet temperature will increase and decrease for the 50% and $100\ \%$ load cases respectively. One reason why this occurs is that at high load the increase in $\bar{v}_{\mathrm{Inj}}$ will cause more droplets to experience breakup, which increases the surface area and thereby decreases the outlet temperature. At low load, the increase in $\bar{v}_{\mathrm{Inj}}$ will cause the droplets to impinge the wall quicker, which decreases the residence time and the overall reactive surface area. This will cause the temperature to increase at the outlet. The example described is one of the complex phenomena, which are causing the sensitivities in Table 10.5 to be highly non-linear.

10.5 Summary

An objective function was defined to quantify the error between the experiments and the computational scrubber model, which took three model outputs into account: $T_{\mathrm{g}}^{\mathrm{Out}}$, $S_{\mathrm{Eq}}^{\mathrm{Out}}$, and ΔP. A pattern search algorithm was subsequently applied to minimize the global objective function, where eight of the 16 tests were included. Having tuned the model parameters, all 16 tests were simulated with the tuned parameters, where the results were compared in Table 10.3. It was found that the pressure loss over the scrubber was significantly lower in the model compared to the experimental tests, so different uncertainties were investigated. Two of these could be quantified, where the results were corrected to include these determinable uncertainties. A summary of the results presented in this chapter is shown in Table 10.6, where the relative and absolute errors are shown in the upper and lower table respectively.

Table 10.6: A summary of the results from this chapter. The upper and lower table are showing the relative and the absolute errors respectively.

	$\frac{\widetilde{T}_{\mathrm{g}}^{\mathrm{Out}} - T_{\mathrm{g}}^{\mathrm{Out}}}{T_{\mathrm{g}}^{\mathrm{Out}}}$ [%]	$\frac{\widetilde{y}_{\mathrm{g,SO_2}}^{\mathrm{Out}} - y_{\mathrm{g,SO_2}}^{\mathrm{Out}}}{y_{\mathrm{g,SO_2}}^{\mathrm{Out}}}$ [%]	$\frac{\Delta\widetilde{P}' - \Delta P'}{\Delta P'}$ [%]
Average (All tests)	14.3	11.5	-12.8
RMS (All tests)	31.1	26.6	24.0
Average (Tuned tests)	-6.8	-3.1	-8.1
RMS (Tuned tests)	11.5	11.1	11.5

	$\widetilde{T}_{\mathrm{g}}^{\mathrm{Out}} - T_{\mathrm{g}}^{\mathrm{Out}}$ [K]	$\widetilde{y}_{\mathrm{g,SO_2}}^{\mathrm{Out}} - y_{\mathrm{g,SO_2}}^{\mathrm{Out}}$ [ppm]	$\Delta\widetilde{P}' - \Delta P'$ [Pa]
Average (All tests)	4.6	14.6	-116.6
RMS (All tests)	9.8	39.4	188.0
Average (Tuned tests)	-1.8	-10.1	-57.5
RMS (Tuned tests)	3.1	20.4	77.3

PART III

RESULTS

11 | EXAMPLE CASE

Having tuned the scrubber model to the experimental tests, the results form the model can be analysed. The results from a single simulation include details about the discrete phase, the wall films, and the continuous phase. These results are analysed in this chapter for a scrubber scenario, where the load is 75 % of the design load, which is in-between the low and high load cases, which were previously described. An overview of the sections in this chapter is shown in Figure 11.1.

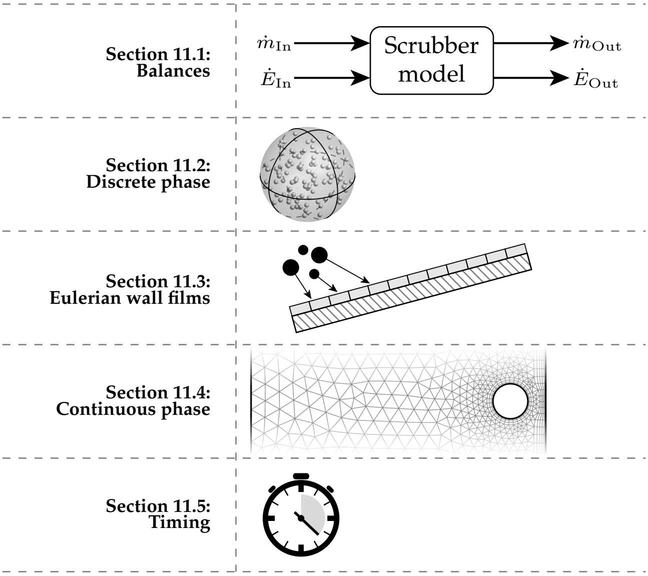

Figure 11.1: An overview of the sections in this chapter.

The simulated case analysed is summarized in Figure 11.2 on the next page, where the different streams going in and out of the scrubber are shown.

A total of $13.88\ \mathrm{kg/s}$ is injected into the scrubber, which is seen for the *Feedwater* stream, where $T = 10°\mathrm{C}$, $\mathrm{pH} = 8.1$, and $A_{\mathrm{T}} = 2.1\ \mathrm{mmol/L}$. The inlet sulfur equivalent is $S_{\mathrm{Eq}} = 2.31\%$, which is reduced to $S_{\mathrm{Eq}} = 0.73\ \%$ at the outlet. Furthermore, the gas temperature decreases from 270 to $28.6°\mathrm{C}$, which is $18.6\ \mathrm{K}$ greater than the water temperature. The relative humidity at the outlet is $84.4\ \%$, so the gas contains large amounts of water vapour and is almost saturated with water.

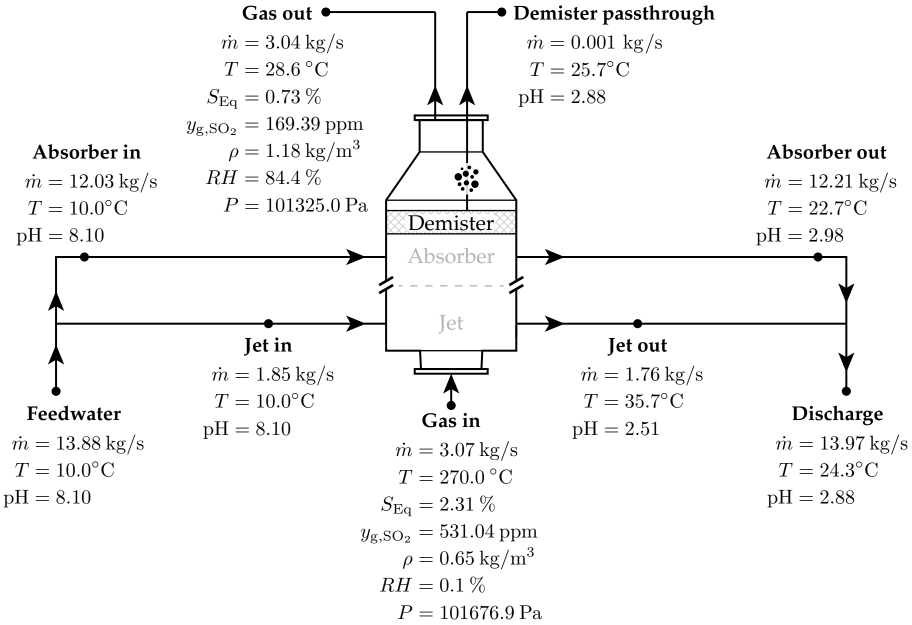

Figure 11.2: An overview of the different gas and water streams going in and out of the scrubber for the case analysed in this chapter.

The water exiting the jet and absorber sections have pH values of 2.51 and 2.98 respectively, which indicates that the jet is more efficient compared to the absorber per unit volume of water, as the pH is lower. The discharge water is the combination of the two outflows where $\mathrm{pH} = 2.88$. A small fraction of the liquid impinging the demister passes through according to *Section 4.8: Demister*, where the temperature is $25.7°\mathrm{C}$ and the pH is 2.88.

11.1 Balances

When the model is initialized, the continuous phase satisfies mass and energy balance. As water is injected into the scrubber through the sprayer nozzles, mass and energy balances are not satisfied, when only the inlet and the outlet are monitored. Instead, the injected water will accumulate towards a finite value, and as the simulation progresses, mass and energy balance will be satisfied again, when the injected water flow equals the outflow of water. These overall balances and accumulations are investigated in this section, where the methods described in *Section 7.3: Mass, energy, and mole balances* are used.

11.1.1 Mass and energy balances

Mass and energy balance during the simulation is shown in the upper graphs of Figure 11.3, whereas the lower graphs are showing the accumulated mass and energy. The x-axes show the discrete phase time.

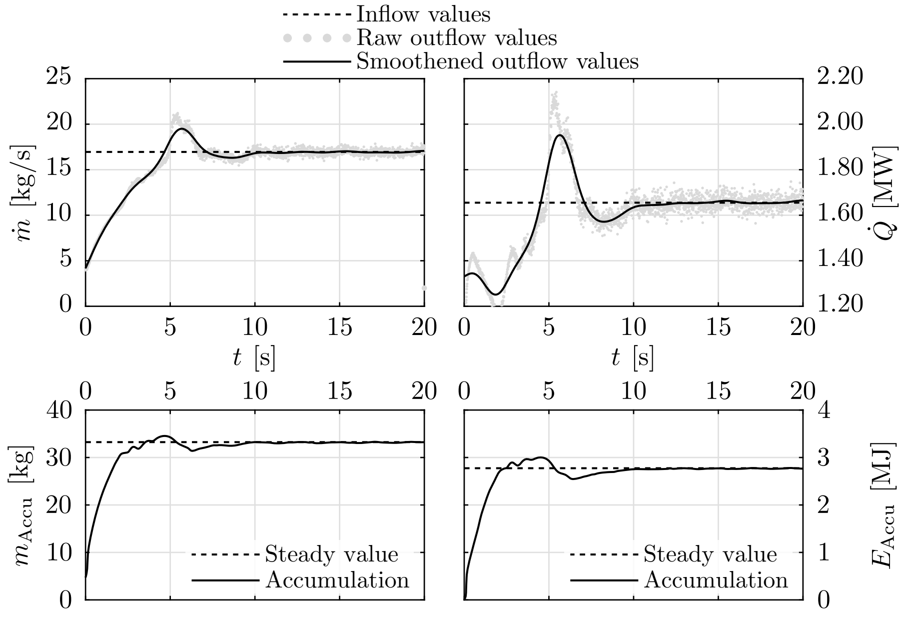

Figure 11.3: Mass and energy balances as the simulation progresses in the upper graphs, and mass and energy accumulation in the lower graphs.

As seen in Figure 11.3, the inlet flow values are constant, which are indicated by the dashed lines, and do not vary as the simulation progresses. As the dispersed liquid phase is modelled using discrete parcels, the number of parcels and their respective masses will not be constant between each time-step. Therefore, the monitored outflow values for each time-step will fluctuate, which are indicated by the grey dots. The solid black lines are smoothed values, which can be seen to be equal to the inflow values after approximately $10\,\mathrm{s}$ in the discrete phase. Both the energy and mass balances can be seen to be non-zero initially, which are caused by the contributions of the continuous phase.

When the inflow and outflow of mass and energy are not equal, accumulation will occur within the scrubber. This is shown in the lower graphs of Figure 11.3, where m_{Accu} and E_{Accu} will tend towards finite values as the simulation progresses. After approximately $10\,\mathrm{s}$, the final values are reached, which are shown by the dashed lines.

11.1.2 Species balances

Elementary species balances must be satisfied, which are calculated using the component matrices, $\mathbf{C}_{\mathrm{l}}$ and $\mathbf{C}_{\mathrm{g}}$, in (3.26) and (6.1) on page 35 and 143 respectively. The relative error is defined according to (11.1), where i indicates the i^{th} species. The values of $\dot{n}^{\mathrm{In}}_{\mathrm{i},\sum}$ and $\dot{n}^{\mathrm{Out}}_{\mathrm{i},\sum}$ were described in *Section 7.3: Mass, energy, and mole balances* on page 159.

$$\epsilon_{\text{Species,i}} = \frac{\dot{n}^{\text{Out}}_{\text{i},\sum} - \dot{n}^{\text{In}}_{\text{i},\sum}}{\dot{n}^{\text{In}}_{\text{i},\sum}} \tag{11.1}$$

The relative error parameter in (11.1), $\epsilon_{\text{Species,i}}$, is evaluated for each species, where the results are shown in Figure 11.4.

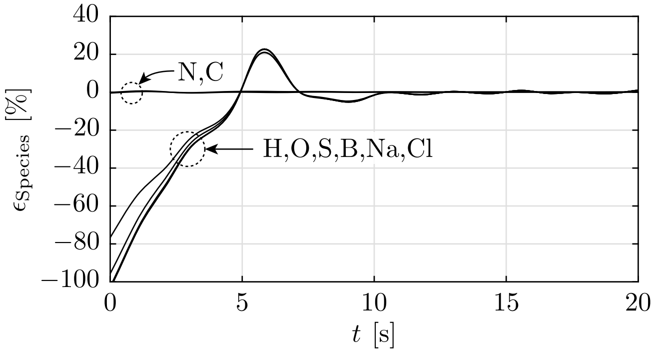

Figure 11.4: Relative species balance as the simulation progresses. $\epsilon_{\text{Species,i}} = 0$ indicates that the mole flow in and out of the scrubber are equal.

As seen in Figure 11.4, nitrogen and carbon are almost constantly zero, as these species are primarily located in the continuous phase. Therefore, the contribution of the liquid water to these species is negligible, and will not affect $\epsilon_{\text{Species,N}}$ and $\epsilon_{\text{Species,C}}$ significantly. The remaining species, H, O, S, B, Na, and Cl, are primarily located in the liquid phase, and will therefore dominate the error parameter. All species can be seen to converge towards $0\,\%$ error after approximately $10\,\text{s}$.

11.2 Discrete phase

The discrete phase is seeded from the sprayer nozzles and several sub-models, which include the wall film atomization model, the separation models, and the demister model. This results in a finite number of parcels, where each of these have 24 degrees of freedom as shown in Table 4.1 on page 123. Some of these properties are investigated in this section.

11.2.1 Distributions

The discrete phase is analysed by plotting the properties of each parcel as functions of the total mass fraction. This is shown in Figure 11.5, where distributions of temperature, diameter, and pH are shown.

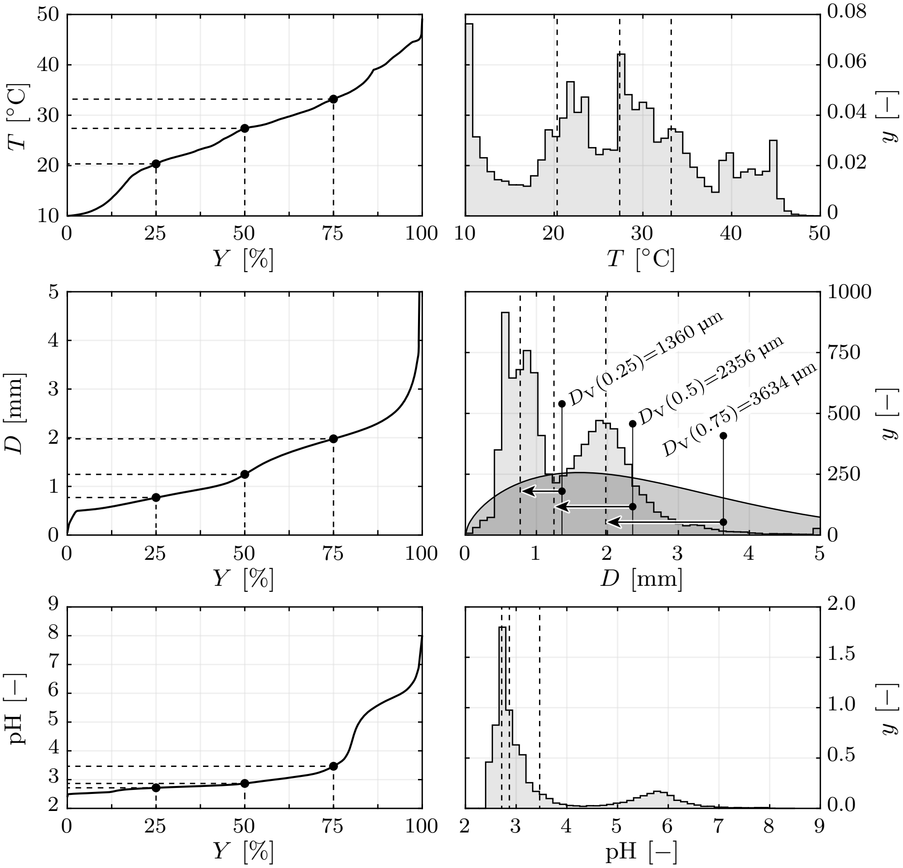

Figure 11.5: The distributions of T, D, and pH for the discrete phase. The left and right figures are showing the cumulative, Y, and probability, y, density functions respectively. The dashed lines are indicating the 25, 50, and 75 % fractiles.

The figures in Figure 11.5 are showing the distributions of three main properties of the discrete phase. The left figures are showing the cumulative distributions, Y, where the 25, 50, and 75 % fractiles are overlaid as the dashed lines. The right figures are showing the probability distributions as histograms, y, where the fractiles from the left figures are shown as well with the dashed lines.

The temperature distribution in the first row shows that most droplet are below approximately $33^{\circ}\mathrm{C}$, which is indicated by the 75 % fractile. However, some droplets/ parcels have a temperature of approximately $45^{\circ}\mathrm{C}$, which were found to be located in the jet section, where the temperature is highest.

The diameter distribution shows that the median diameter is approximately 1200 µm, which is smaller compared to the injected volume mean diameter, which is $D_{\mathrm{V}}(0.5) = 2356$ µm. The analytical distribution is overlaid in the figure, where both $D_{\mathrm{V}}(0.25)$, $D_{\mathrm{V}}(0.5)$, and $D_{\mathrm{V}}(0.75)$ are shown according to (4.6) on page 67. Notice that the injected droplets are seeded according to this distribution, which indicates the relative decrease in droplet sizes due to the various phenomena modelled, such as breakup, atomization, collision etc. The reductions are shown with the horizontal arrows pointing to the left.

The pH distribution shows that most droplets have a pH less than 3.5, which indicates that the scrubber performs well. This is due to the fact that the natural buffer capacity is depleted, which was apparent in Figure 3.8 and 3.9 on page 45, where the alkalinity, A_{T}, was zero at $\mathrm{pH} \approx 4.4$. The droplets, which have not resided long inside the scrubber, have a relatively high pH, which is apparent in the right figure, where a small peak is located at $\mathrm{pH} \approx 5.8$.

The average specific surface area for all droplets/parcels was found to be $5.94\,\mathrm{m}^2/\mathrm{L}$, which is equivalent to a single droplet with a diameter of $1010\,\mu\mathrm{m}$. The specific surface area of the injected droplets is directly available from D_{32}, which defines the diameter, which has the same specific surface area as the injected droplets. The specific surface area for $D_{32} = 1250\,\mu\mathrm{m}$ is $4.8\,\mathrm{m}^2/\mathrm{L}$, which is approximately $20\,\%$ lower compared to $5.94\,\mathrm{m}^2/\mathrm{L}$.

11.2.2 Parcel occurrences

All sub-models for the discrete phase either eliminates, creates, or modifies the parcels in the scrubber model. These tendencies were monitored during simulation, where the results are shown in Table 11.1.

Table 11.1: The results from monitoring the number of seeded or eliminated parcels for each of the sub-models.

Model	n_{Seed} $\left[\frac{\text{parcels}}{\text{time-step}}\right]$	$n_{\mathrm{Eliminate}}$ $\left[\frac{\text{parcels}}{\text{time-step}}\right]$	$\frac{n_{\mathrm{Seed}}}{n_{\mathrm{Eliminate}}}$ $[-]$
Sprayers	416	–	–
Impingement	632	2460	0.26
TAB	354	177	2.00
Collision	998	280	3.56
Evaporation	–	2	–
Demister	19	–	–
Film atomization	324	–	–
Film edges	225	–	–
$\sum$	2968.3	2919.5	1.02

The values in Table 11.1 are proportional to $\widetilde{n}$, which was described in *Section 8.4: Parcel count independence*, which is the average number of parcels per unit volume of water. n_{Seed} is the number of parcels seeded or created within each time-step, whereas $n_{\text{Eliminate}}$ is the number of parcels eliminated each time-step. The last column shows the ratio between the two numbers, $^{n_{\text{Seed}}}/_{n_{\text{Eliminate}}}$.

The first row shows the number of injected parcels each time-step. The two last columns of this row are not applicable, as no parcels are eliminated during the injection process.

2460 parcels impinge with the shell each time-step, which was described in *Section 4.7: Impingement*. Some of these impingements will re-inject droplets into the scrubber again, where approximately 632 parcels are seeded each time-step on average. The ratio between these two numbers is 0.26, which indicates that, on average, 0.26 parcels are seeded for every eliminated parcel. Therefore, the impingement model overall reduces the number of parcels in the computational model.

Approximately 177 parcels experience breakup each time-step, where each event seeds two new parcels, which was described in *Section 4.5: Breakup*. This ratio is a model constant, which can be adjusted to be any whole number, where 2 was chosen for this study.

Approximately 280 parcel collisions occur each time-step, where the outcome can be either *reflexive separation*, *coalescence*, *stretching separation*, or *pass*, which were described in *Section 4.6: Collision*. Each of these outcomes either reduces or increases the overall number of parcels, where a total of 998 parcels were seeded each time-step as seen in Table 11.1, which results in a ratio of 3.56. Therefore, the collision model overall increases the number of parcels in the scrubber model.

2 parcels evaporate each time-step, which means that *all* mass has evaporated and the parcel is eliminated. All parcels experience evaporation, but not in an extent that eliminates the parcel. 19 parcels are injected from the demister each time-step, and the two last rows are related to the film, where approximately 324 parcels are atomized, and 225 are re-injected from the edges.

The sum of the two columns is shown in the last row, where $n_{\text{Seed}} \approx n_{\text{Eliminate}}$ at steady-state. The two summed values are not equal in the table, as some fluctuations will naturally be present. However, the ratio between these two values is 1.02, which will fluctuate slightly around 1.0 during simulation.

11.2.3 Trace components

The trace components, $\dot{\Psi}$, described in *Section 4.12: Trace* were analysed, where the resulting trace fractions are shown in Table 11.2.

Table 11.2: The trace components in each of the liquid stream shown in Figure 11.2.

Stream	$\frac{\dot{\Psi}_{\text{Jet}}}{\sum \vec{\dot{\Psi}}_{\text{Stream}}}$ [%]	$\frac{\dot{\Psi}_{\text{Abs,1}}}{\sum \vec{\dot{\Psi}}_{\text{Stream}}}$ [%]	$\frac{\dot{\Psi}_{\text{Abs,2}}}{\sum \vec{\dot{\Psi}}_{\text{Stream}}}$ [%]	$\frac{\dot{\Psi}_{\text{Abs,3}}}{\sum \vec{\dot{\Psi}}_{\text{Stream}}}$ [%]
Feed-water	13.3	28.9	28.9	28.9
Jet in	100.0	0.0	0.0	0.0
Jet out	90.7	3.1	3.1	3.1
Absorber in	0.0	33.3	33.3	33.3
Absorber out	1.9	32.6	32.1	33.4
Discharge	13.0	28.9	28.5	29.6

As seen in Table 11.2, 13.3 % of the *Feed-water* stream is injected in the jet, whereas the remaining is evenly distributed to the absorber sprayer nozzles. The water injected into the jet naturally has $\dot{\Psi}_{\text{Jet}} / \sum \vec{\dot{\Psi}}_{\text{Jet in}} = 100\,\%$, where the other components are 0. The water injected into the absorber has 33.3 % for each of the three sprayer layers in this section.

The water exiting the jet water trap can be seen to consist of 9.3 % water from the absorber, which indicates that some droplets are passing around the absorber cone and entering the jet section, where it leaves the scrubber through the jet water trap. Similarly, 1.9% of the injected water in the jet exits the scrubber through the absorber water trap, which is seen in the $\dot{\Psi}_{\text{Jet}} / \sum \vec{\dot{\Psi}}_{\text{Absorber out}}$ column for the *Absorber out* stream.

The *Discharge* stream can be seen to be almost identical to the *Feed-water* stream, where only small deviations are seen. These deviations are caused by evaporation and condensation of water, where the trace components are not tracked, as this would require four additional scalars in the continuous phase, which would not provide much more information.

Each parcel has an associated $\vec{\dot{\Psi}}$ vector, so the average properties for the droplets injected from each sprayer nozzle can be investigated. This is shown in Table 11.3, where four properties are shown for each of the sprayer nozzles.

Table 11.3: The accumulated mass and three mass averaged properties for each of the sprayer nozzles.

Sprayer	m_{Accu} [kg]	$T_{\text{l,Avg}}$ [°C]	D_{Avg} [μm]	pH_{Avg} [−]
Jet	1.84	38.1	1695	2.59
Abs 1	3.93	24.7	1482	3.05
Abs 2	3.33	25.2	1270	2.99
Abs 3	3.16	24.1	1362	3.05

As seen in Table 11.3, the accumulated mass of the parcels is larger for the absorber sprayer nozzles compared to the jet, as more water is injected in the absorber section compared to the jet section. The average temperature, $T_{\mathrm{l,Avg}}$ can be seen to be significantly greater in the jet section compared to the absorber section, as the gas temperature is greatest in the jet section. The average droplet diameter, D_{Avg}, is largest in the jet, which is counter intuitive. This is caused by the relatively short residence time for the droplets in the jet, where a large fraction of the water is impinging the shell. The average pH, $\mathrm{pH}_{\mathrm{Avg}}$, can be seen to be lowest in the jet section, where the $\mathrm{SO_2(g)}$ concentration is largest.

11.3 Eulerian wall films

A total of 15 wall films are modelled inside the scrubber. Two large wall films are located in the jet and absorber sections, where some properties of these are shown in Figure 11.6 on the next page.

The jet section spans from zero to approximately $1.5\ \mathrm{m}$, whereas the absorber wall film spans from approximately 1.6 to $6\ \mathrm{m}$. The x-axes show the distance from the bottom of the jet water trap, and is increasing towards the top of the scrubber, so the water is flowing towards the left. A sketch of the scrubber is shown in the top of the figure, where the locations are shown relative to the geometry of the scrubber. It should be noted that the sketch is modified compared to the actual geometry to the scrubber in the Alfa Laval Test & Training Centre.

The first figure shows the mass source term per unit area, $\dot{m}_{\mathrm{F,Source}}/A_{\mathrm{F}}$. The jet section has a single spike, which is located at the tip of the jet cone. The wall film from the top side of the cone separates at the tip and continues onto the wall. The absorber section has a more even source term, which is approximately $2\mathrm{kg}/(\mathrm{s}\cdot\mathrm{m}^2)$, and starts at approximately $4.8\mathrm{m}$. This is the place, where the top sprayer nozzle hits the shell.

The source terms are integrated from the top of each wall film, where the resulting mass flow, $\dot{m}_{\mathrm{F}}$, is seen in the second figure. The absorber mass flow can be seen to increase along the length of the wall film, but at approximately $2.25\ \mathrm{m}$, the mass flow decreases. This is a result of the atomization model, where water is shed from the wall film as droplet, which are injected into the domain again in the form of parcels. A sudden increase can afterwards be seen, which is located at the tip of the absorber cone, where the water from the top side of the absorber cone impinges the shell.

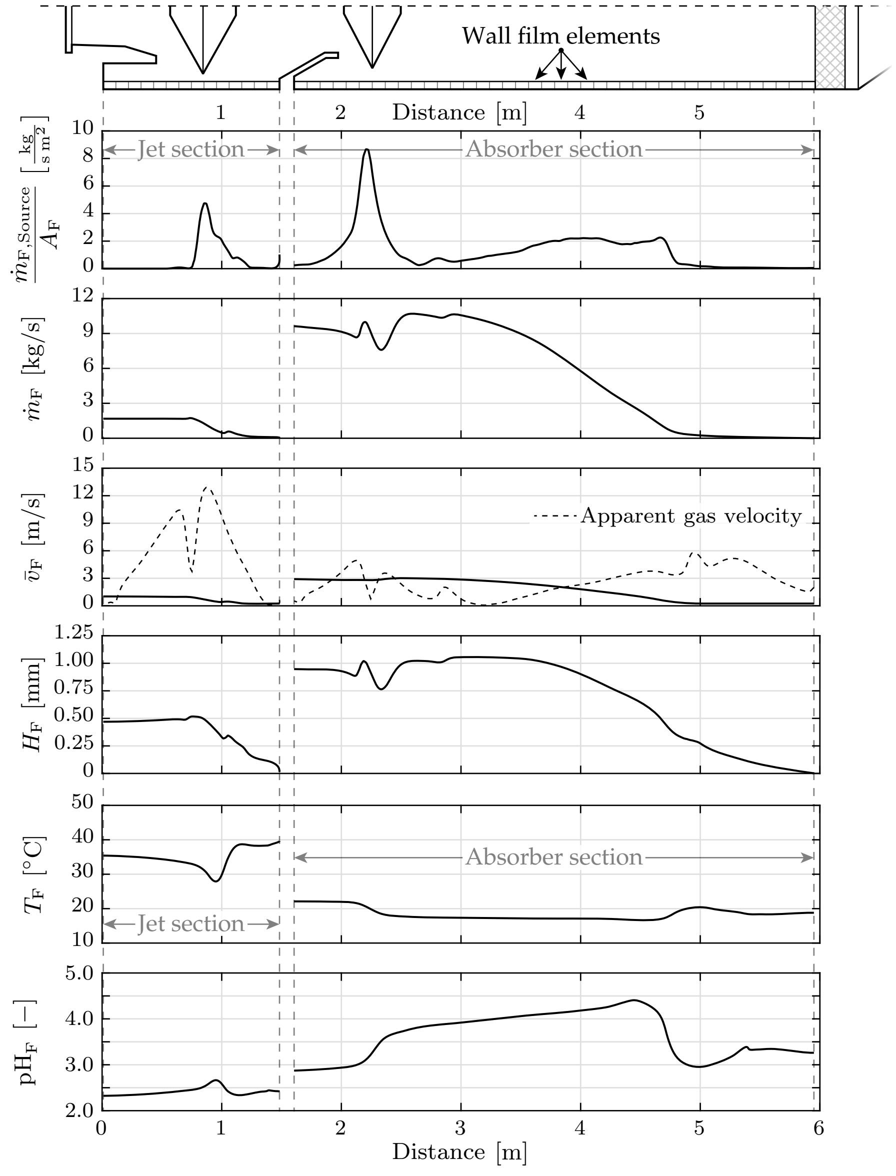

Figure 11.6: The two large wall films present in the jet and absorber sections. The distance is measured from the bottom of the jet water trap. The presented values are from the wall film elements, which are indicated on the outline of the scrubber shown in the top of the figure. Notice that the actual number of wall film elements in the jet and absorber sections are 76 and 218 respectively, so each element has a length of approximately 2 cm.

The third figure shows the velocity of the wall film, $\bar{v}_F$, which can be seen to increase downstream. The apparent gas velocity next to each wall film element is shown as the dashed line. It can be seen that the gas velocity is larger in the jet section compared to the absorber section.

The liquid wall film thickness, H_F, is calculated from $\dot{m}_\mathrm{F}$ and $\bar{v}_\mathrm{F}$, and is shown in the fourth graph. This can be seen to be approximately $1\ \mathrm{mm}$, which is assumed being spread evenly around the circumference of the scrubber. However, as described in *Section 5.4: Atomization*, rivulets are assumed to form along the wall film, so the film might be thicker at some places compared to others.

The temperature of the wall film, T_F, is seen in the fifth graph, where the jet section is significantly hotter compared to the absorber section, where the temperatures are approximately 35 and $20^\circ\mathrm{C}$ respectively.

The last presented property in Figure 11.6 is the pH, which can be seen to be approximately 2.5 and 3.5 in the jet and absorber sections respectively. This indicates that the jet section is efficiently removing sulfur per unit volume, which corresponds to the larger driving force of $\mathrm{SO_2(g)}$ in the jet section.

The wall film was found to account for $5.9\ \%$ of the total mass transfer of $\mathrm{SO_2}$, and $8.5\ \%$ of the total thermal energy transfer. Therefore, the liquid wall films do have a significant contribution to the overall performance of the scrubber.

11.4 Continuous phase

The continuous phase is resolved in OpenFOAM, where each cell has 11 degrees of freedom as described in *Chapter 6: Continuous phase*. Some of these are shown in this section along with some of the source terms calculated in MATLAB and transferred to OpenFOAM via the link files as described in *Section 7.4: Link structure*.

11.4.1 Scalars

Figure 11.7 on the next page shows five scalars from the continuous phase in the top of the figure, where the properties are shown above each sub-plot. Each sub-plot has an associated colour-bar, where the limiting values are chosen such that most values fall within the span. Only half of the scrubber is shown, as axis-symmetry was exploited to reduce computational requirements. It should be noted that the outlines of the scrubber are modified and do not reflect the actual design. However, the overall flow tendencies are captured in the modified scrubber geometry, although some differences are naturally present.

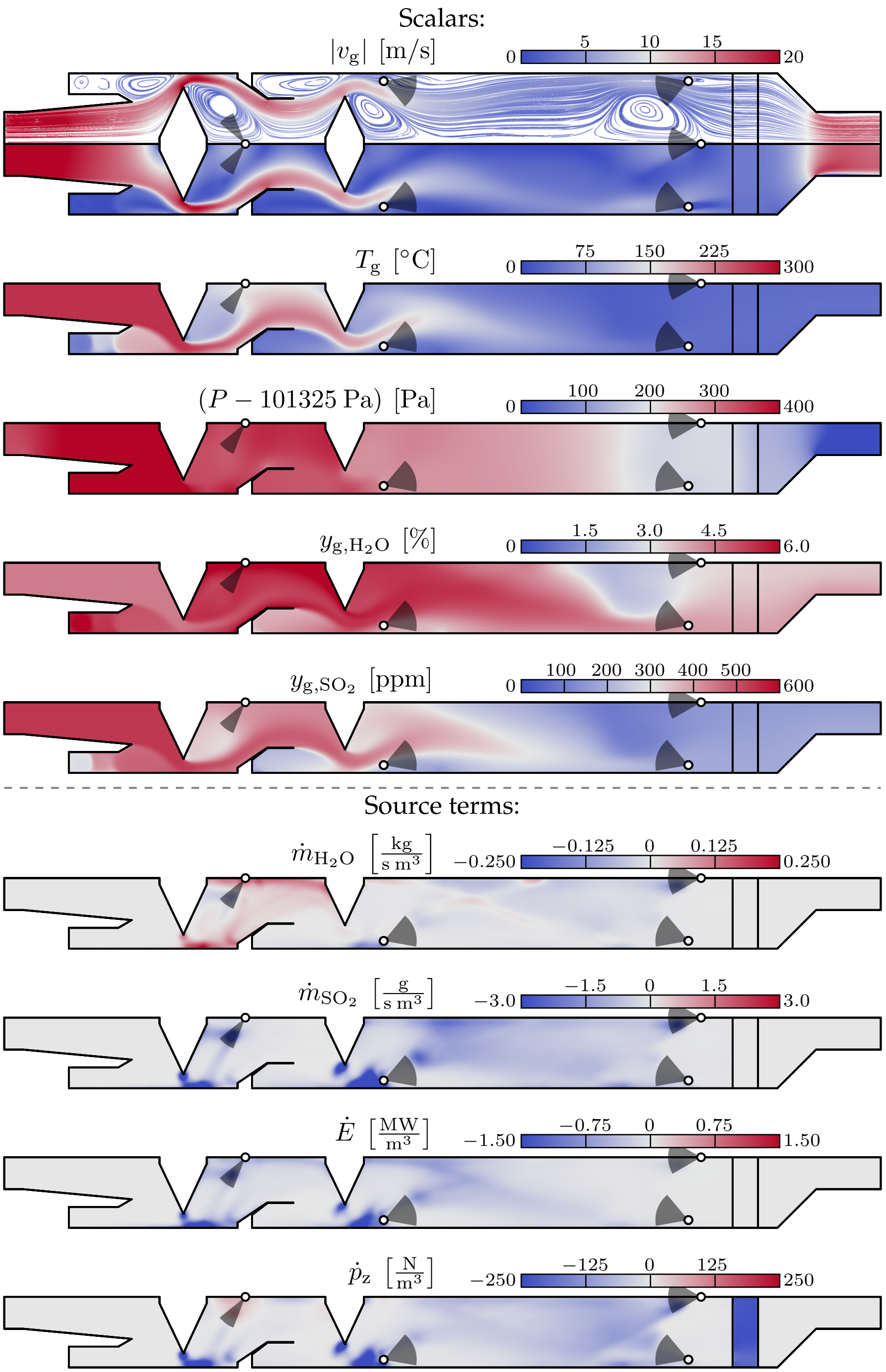

Figure 11.7: Various scalars and source terms in the continuous phase. The top figure shows the streamlines of the flow.

As seen in Figure 11.7, the scalars very along the entirety of the scrubber. The first sub-plot shows the velocity magnitude, $|v_{\mathrm{g}}|$, where the streamlines of the flow is shown as well. It can be seen that numerous recirculation zones are present inside the scrubber. The jet section has a large recirculation zone, which was found to force droplets towards the jet cone. Another large recirculation zone is present at the top of the absorber, which is located below the top sprayer nozzle.

The gas temperature can be seen to rapidly decrease in the jet section, where T_{g} is approximately $100^{\circ}\mathrm{C}$ at the bottom of the absorber section. The temperature in the jet recirculation zone can be seen to be significantly lower compared to the rest of the jet section.

The pressure in the third sub-plot can be seen to be decrease most rapidly in the top of the absorber, where the sprayer nozzles are injecting water in the opposite direction of the gas flow. The pressure over the demister can also be seen to decrease rapidly, where the streamlines in the first sub-plot can be seen to be aligned with the axial direction of the scrubber. This was enforced by increasing the radial resistance according to (4.53) on page 102. The contraction in the top of the scrubber can also be seen to induce a significant pressure loss.

The mole fraction of $\mathrm{H_2O(g)}$ can be seen to be closely linked to the gas temperature, where a local region in the top of the absorber has a significantly low value of $y_{\mathrm{g,H_2O}}$ compared to the rest of the scrubber. This is due to the low temperature in this region, which causes water vapour to condense on the droplets.

The mole fraction of $\mathrm{SO_2(g)}$ can be seen to decrease along the entire length of the scrubber, where, again, a local zone below the top sprayer in the absorber exists, where $y_{\mathrm{g,SO_2}}$ is lowest.

11.4.2 Source terms

The lower part of Figure 11.7 shows four of the eight source terms sent from MATLAB to OpenFOAM. It should be noted that all colour-bars are normalized such that negative values are blue and positive values are red. Furthermore, all source terms are shown per unit volume.

The first sub-plot shows the source term for $\dot{m}_{\mathrm{H_2O}}$, which can be seen to be positive in the jet section, where water evaporates and quenches the gas. The second sub-plot shows $\dot{m}_{\mathrm{SO_2}}$, where the jet section does not remove much $\mathrm{SO_2(g)}$ compared to the absorber section, which was also apparent for $y_{\mathrm{g,SO_2}}$. The primary reason is the lower mass flow of water in the jet section compared to the absorber section.

The energy source term combines both convective heat transfer and the thermal energy associated with evaporation. This can be seen to be negative throughout the scrubber.

$\dot{p}_\mathrm{z}$ shows the momentum source terms in the axial direction of the scrubber. This can be seen to be generally negative, which corresponds to the droplet exerting a force on the continuous phase. Furthermore, the demister can be seen to induce a large pressure loss, which was described in *Section 4.8: Demister*.

11.4.3 Averaged axial values

Six scalars were averaged along the axial direction of the scrubber, which are shown in Figure 11.8 on the next page. The different values in the figures vary along the length of the scrubber, where a modified outline of the scrubber geometry is shown in the top of the figure. The density can be seen to be a function of temperature, where ρ_g is increasing with decreasing T_g. The velocity is naturally a function the cross sectional area and the density, which can be seen to vary with the geometry. A peak is present at $z \approx 5.2\ \mathrm{m}$, which corresponds to the recirculation zone shown in Figure 11.7.

The sulfur concentration, $y_{\mathrm{g,SO_2}}$, can be seen to decrease almost linearly from $z \approx 1\ \mathrm{m}$ to $5\ \mathrm{m}$, which shows that the top most region of the absorber is not contributing the $\mathrm{SO_2(g)}$ absorption. The pressure can be seen in the second to last figure, where both the total, static, and dynamic pressure are shown. The static and total pressure graphs are shown relative to the ambient air pressure of $1\ \mathrm{atm}$. The static pressure before the demister is approximately $150\ \mathrm{Pa}$, where the demister and the contraction account for this loss.

The two turbulence scalars are shown in the last figure, which can be seen to increase in the jet section, where water is injected. Furthermore, an increase is seen at the bottom of the absorber section, where the geometry causes these scalars to increase.

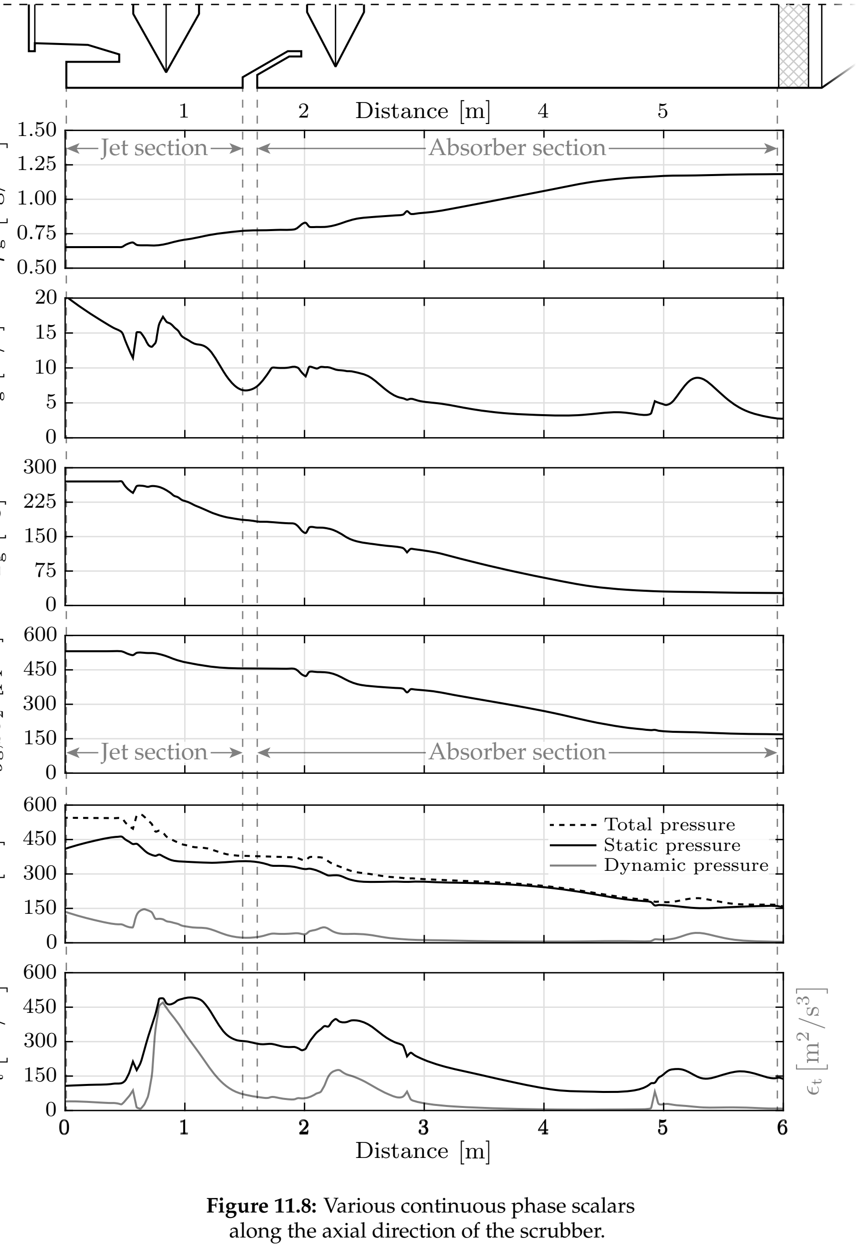

Figure 11.8: Various continuous phase scalars along the axial direction of the scrubber.

11.5 Timing

As all sub-model were implemented manually in either OpenFOAM or MATLAB, some extra insight can be gained by investigating the computational requirements. A single simulation takes approximately an hour, where the distribution between the two software packages is shown in Table 11.4.

Table 11.4: The timing results for the software parts.

Software part	t	$\left(\frac{t}{t_{\text{Total}}}\right)$
MATLAB	$t_{\text{OpenFOAM}} = 24.2\,\text{min}$	$58.3\,\%$
OpenFOAM	$t_{\text{MATLAB}} = 33.8\,\text{min}$	$41.7\,\%$
$\sum$	$t_{\text{Total}} = 58.0\,\text{min}$	$100.0\,\%$

As seen in Table 11.4, MATLAB requires $58.3\ \%$ of the total time, whereas OpenFOAM requires $41.7\,\%$, but this fraction can be adjusted by changing the number of continuous or discrete phase iteration each time a software package is in control, which was described in *Section 7.4: Link structure*. The total time used by MATLAB and OpenFOAM are denoted t_{MATLAB} and t_{OpenFOAM}, and the total time is t_{Total}.

Different parts within the OpenFOAM model were timed as well, where the results are shown in Table 11.5. The columns are indicating the fraction of time spent on each part compared to both t_{OpenFOAM} and t_{Total}.

Table 11.5: The timing results for the OpenFOAM parts.

OpenFOAM part	$\left(\frac{t}{t_{\text{OpenFOAM}}}\right)$	$\left(\frac{t}{t_{\text{Total}}}\right)$
Link	$0.8\,\%$	$0.3\,\%$
Shell heat transfer coefficient	$4.9\,\%$	$2.0\,\%$
Momentum equation	$14.0\,\%$	$5.8\,\%$
Species equations	$14.6\,\%$	$6.1\,\%$
Energy equation	$35.5\,\%$	$14.8\,\%$
Pressure equation	$19.3\,\%$	$8.0\,\%$
Turbulence equations	$11.0\,\%$	$4.6\,\%$
$\sum$	$100.0\,\%$	$41.7\,\%$

As seen in Table 11.5, seven different parts are timed, where most time is spent on solving the continuous phase scalars. Evaluation of the wall heat transfer coefficient according to *Section 5.6: Heat transfer* requires $4.9\,\%$ of the time. The link structure, which combines both reading cell and face data for the whole domain, and reading 12 source term scalars per cell, only requires $0.8\ \%$ of t_{OpenFOAM} and $0.3\ \%$ of t_{Total}.

Different parts in the MATLAB code were analysed as well, where the results are shown in Table 11.6.

Table 11.6: The timing results for the MATLAB parts.

MATLAB part	$\left(\frac{t}{t_{\text{MATLAB}}}\right)$	$\left(\frac{t}{t_{\text{Total}}}\right)$
Link	$1.3\ \%$	$0.8\ \%$
Wall film	$14.7\ \%$	$8.6\ \%$
Discrete phase	$76.8\ \%$	$44.8\ \%$
Various	$7.1\ \%$	$4.1\ \%$
$\sum$	$100.0\ \%$	$58.3\ \%$

Four different parts are shown in the table, where the discrete phase accounts for $76.8\ \%$ of t_{MATLAB}, which is significantly greater compared to the other parts. The wall film requires $14.7\ \%$, and the link part, which includes reading cell and face data for the whole domain, and writing 12 source term scalars per cell, only requires $1.3\ \%$. As the discrete phase requires the majority of the computational time, different parts of this were timed, where the results are shown in Table 11.7.

Table 11.7: The timing results for the discrete phase parts.

Discrete phase part	$\left(\frac{t}{t_{\text{Discrete}}}\right)$	$\left(\frac{t}{t_{\text{Total}}}\right)$
Data projection	$9.4\ \%$	$4.2\ \%$
Equilibrium	$10.7\ \%$	$4.8\ \%$
Impingement	$18.7\ \%$	$8.4\ \%$
Breakup	$8.5\ \%$	$3.8\ \%$
Collision	$10.5\ \%$	$4.7\ \%$
Various	$42.3\ \%$	$19.0\ \%$
$\sum$	$100.0\ \%$	$44.8\ \%$

20 different parts were timed in the discrete phase, but only the major six are shown in Table 11.7, which all requires between 8.5 and $18.7\ \%$ of the time. *Data projection* is the process, where the closest node for each parcel is located, where a *k-d tree* algorithm [Friedman et al. (54)] was used. The scalar values on the nodes are thus the apparent gas properties seen by each parcel. *Equilibrium*

covers the evaluation of the equilibria between most species, where a third-order polynomial was solved for each parcel, which was shown in (3.24) on page 33. *Impingement* requires the most time for the discrete phase, where collision detection with the shell takes the most time. *Breakup* covers the *Taylor Analogy Breakup model* described in *Section 4.5: Breakup*, and *Collision* covers the model described in *Section 4.6: Collision*.

Most parts were optimized for computational speed, although the code can be made faster. Parallelisation of the discrete phase would decrease the computational time drastically, but this was out of the scope for this project. The exchange of data and source terms requires in total only $0.3\,\% + 0.8\,\% = 1.1\,\%$ of the total time, so this is not found to be a limiting factor.

12 PARAMETRIC VARIATIONS

The previous chapter presented results from a single case, where insights from both the continuous phase, the discrete phase, and the wall films were shown. This chapter investigates the overall performance of the scrubber by varying the inlet liquid temperature, $T_{\mathrm{l}}^{\mathrm{In}}$, and the liquid mass flow into the scrubber, $\dot{m}_{\mathrm{l}}^{\mathrm{In}}$. These two parameters are varied independently for three different loads, which are $50\ \%$, $75\ \%$, and $100\ \%$ of the scrubber design load of $1.6\ \mathrm{MW}$. The inlet conditions for all load cases were $T_{\mathrm{g}}^{\mathrm{In}} = 270^{\circ}\mathrm{C}$ and $y_{\mathrm{g,SO_2}}^{\mathrm{In}} = 531\ \mathrm{ppm}$.

Four different parameters are investigated, which are the outlet temperature of the gas, $\widetilde{T}_{\mathrm{g}}^{\mathrm{Out}}$, the overall pressure loss, $\Delta\widetilde{P}$, the outlet sulfur concentration, $\widetilde{y}_{\mathrm{g,SO_2}}^{\mathrm{Out}}$, and the seawater discharge pH, $\mathrm{pH}^{\mathrm{Out}}$. It should be noted that the experimental and model pressure losses are adjusted according to (10.6) on page 206 to take the determinable uncertainties into account.

12.1 Seawater temperature

The first study varies the temperature of the seawater, which is injected into the scrubber in the jet and absorber sections. The temperature is varied from 5 to $35^{\circ}\mathrm{C}$, where the results are shown in Figure 12.1 on the next page.

As seen in Figure 12.1, the four investigated parameters are shown as functions of $T_{\mathrm{l}}^{\mathrm{In}}$. The three curves in each plot are for the different loads of 50, 75, and $100\ \%$, where the legend in the upper left graph applies.

The outlet temperature from the model, $\widetilde{T}_{\mathrm{g}}^{\mathrm{Out}}$, naturally increases with increasing seawater temperature, where the tendencies are linear. The pinch temperature, $T_{\mathrm{g}}^{\mathrm{Out}} - T_{\mathrm{l}}^{\mathrm{In}}$, was found to vary from 13 to $35\ \mathrm{K}$.

The pressure loss is not significantly affected, but it can be seen to increase slightly with $T_{\mathrm{l}}^{\mathrm{In}}$. The reason for this is assumed to be caused by the generally higher gas velocities due to the hotter exhaust gas, which increases the overall pressure loss.

The sulfur concentration at the outlet, $\widetilde{y}_{\mathrm{g,SO_2}}^{\mathrm{Out}}$, can be seen to increase slightly with $T_{\mathrm{l}}^{\mathrm{In}}$, which is caused by the value of $\mathrm{p}K_{\mathrm{SO_3,1}}^{\gamma}$ to increase with temperature, which is apparent from Figure 3.6 on page 30. This causes the equilibrium between $\mathrm{H_2SO_3}$ and $\mathrm{HSO_3^-}$ to tend more towards $\mathrm{H_2SO_3}$, which is the driving force for $\mathrm{SO_2}$ absorption.

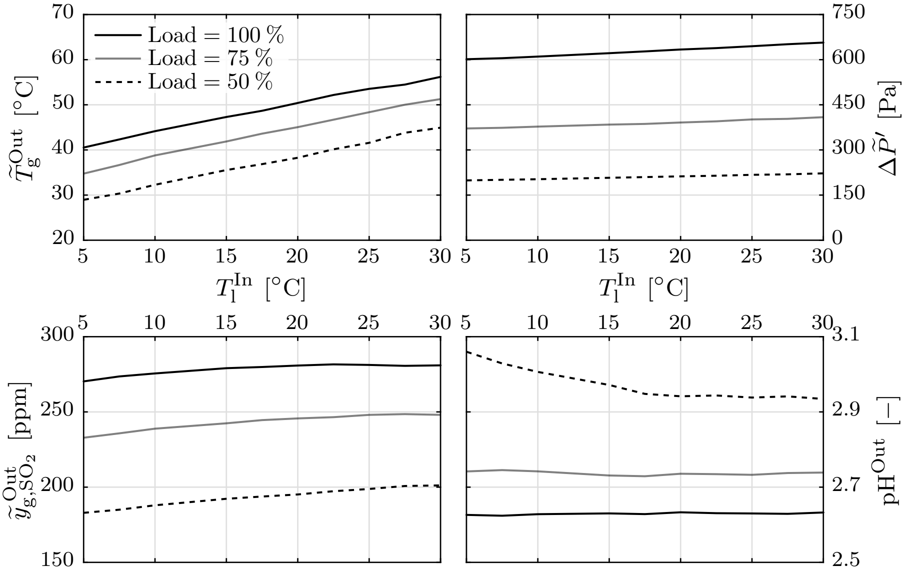

Figure 12.1: The results from varying the seawater temperature from 5° C to 35° C for three different loads.

The pH of the discharge stream can be seen to be affected by the temperature, which is a combination of varying $\mathrm{SO_2}$ absorption and $\mathrm{p}K_{\mathrm{a}}$ dependencies as described in *Chapter 3: Chemistry*.

12.2 Seawater mass flow

The overall seawater mass flow into the scrubber, $\dot{m}_{\mathrm{l}}^{\mathrm{In}}$, was varied from 5 to $20\ \mathrm{kg/s}$, where the results are shown in Figure 12.2 on the next page.

The experimental values are overlaid in Figure 12.2 with the dots. The white dots indicate the experiments with low water flows, whereas the solid dots are for high water flows. The model was tuned to the experiments with the high water flow, as described in *Chapter 10: Model tuning*.

As seen in Figure 12.2, the outlet temperature decreases with increasing $\dot{m}_{\mathrm{l}}^{\mathrm{In}}$ with an exponential decaying tendency. The experimental values are overlaid, where the model can be seen to accurately predict the outlet temperature at high water flows, but overestimates the outlet temperature at low water flows.

The pressure loss can be seen to increase with $\dot{m}_{\mathrm{l}}^{\mathrm{In}}$, as expected. The experimental pressure losses are generally larger compared to the model, which was addressed in *Section 10.4: Results*.

The sulfur concentration at the outlet can be seen to decrease with $\dot{m}_{\mathrm{l}}^{\mathrm{In}}$, where a linear tendency is observed.

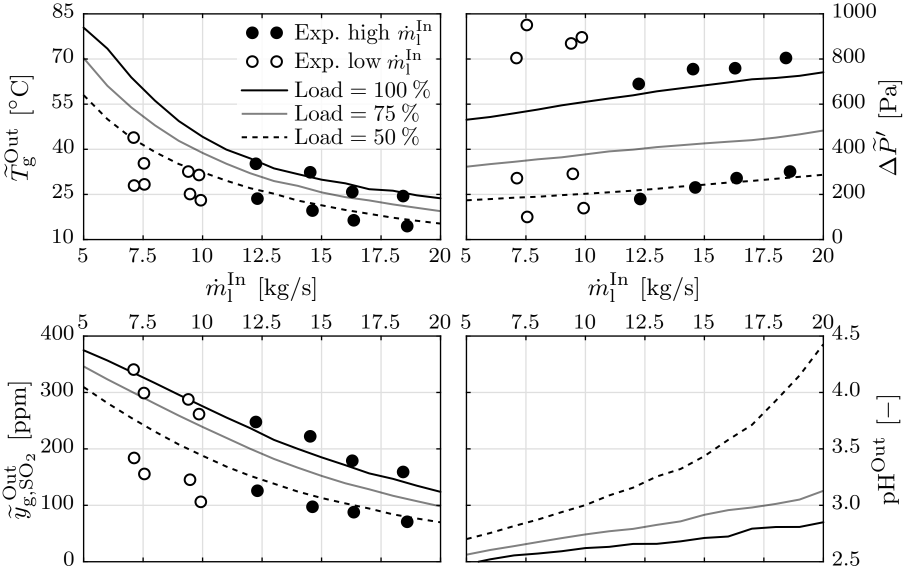

Figure 12.2: The results from varying the seawater mass flow going into the scrubber from 5 to 20 kg/s.

The discharge pH can be seen to increase almost linearly with $\dot{m}_l^{In}$ for the 50 and 75 % load cases, as the overall buffer capacity increases with water flow. However, for the 100 % load case, the value of pH^{Out} increases rapidly, which indicates that the scrubber is not working as efficiently compared to the lower water flows.

The values from Figure 12.2 are normalized with the inlet gas flow, $\dot{m}_g^{In}$, which transforms the x-axis to a water load instead of the absolute water mass flow. This is seen in Figure 12.3 on the next page.

The outlet gas temperature, $\widetilde{T}_g^{Out}$, can be seen to, again, decrease with an exponential decaying tendency. This tendency is also seen for $\widetilde{y}_{g,SO_2}^{Out}$, although the effect is not as apparent.

It should be noted that the inlet conditions to the model, when Figure 12.2 and 12.3 were generated, were not those measured during the experiments. Therefore, the errors between the experiments and the model in the figures are slightly misleading, but it is the tendencies in the graphs, which are of interest.

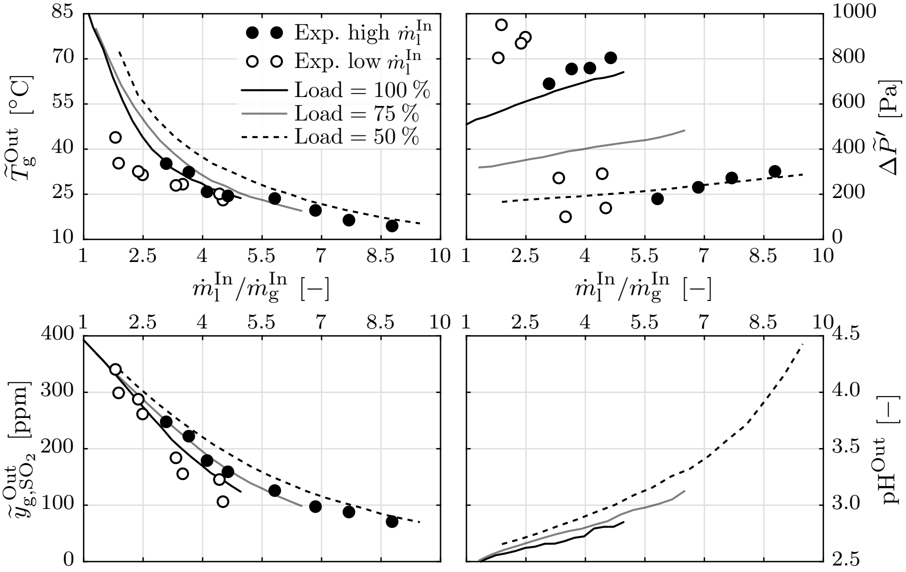

Figure 12.3: The results from varying the seawater mass flow going into the scrubber from 5 to 25 kg/s. The results are normalized with the inlet gas flow, $\dot{m}_{\mathrm{g}}^{\mathrm{In}}$.

13 FUTURE WORK

This study proposed a scrubber model, where three main aspects were included. These are the continuous phase modelling using CFD, discrete phase modelling using a Lagrangian approach, and wall film modelling using an Eulerian approach. These models were defined using numerous sub-models, where most were existing models from previous studies. By combining all the sub-models, an accurate model for wet scrubber modelling was assembled, but some aspects of scrubber modelling were not included, which are addressed in this chapter.

13.1 Continuous phase

The continuous phase was modelled using CFD as described in *Chapter 6: Continuous phase*. The continuous phase was assumed to consist of five species, CO_2, H_2O, O_2, SO_2, and N_2, where the latter was assumed to be inert. The other species interacted with the discrete phase and the wall films, where mass, energy, and momentum were transferred from and to the liquid, and this was implemented as source terms when solving the continuous phase.

13.1.1 Particle removal

An aspect, which was not covered in this study, is particle removal. The fuel oil used by most vessels is HFO, where the exhaust gas contains particulate matter. The larger particles will be removed by the scrubber, where they will stick to the water droplets, but the smaller particles will not be captured, and will thus pass through the scrubber and exit the funnel. These pose both an environmental and a health risk, so removal of these are of great importance. The model proposed in this study could be modified to include particulate matter removal, where the particles could be modelled by introducing multiple continuous phase scalars, where each represent a specific particle size. The interaction with the liquid phase would be modelled in MATLAB, where the source terms for each particle size could be calculated. The implementation would be similar to any chemical species, where the concentration of particles could be tracked and monitored. The absorption rate could subsequently be tuned to match experimental data.

13.1.2 SO_3 modelling

Five species were modelled in the continuous phase, but one component not considered was $SO_3(g)$, which reacts with $H_2O(l)$ to form $H_2SO_4(l)$, where the latter is a strong acid. However, $SO_3(g)$ exists as aerosols in the exhaust gas stream, so the absorption cannot be modelled similar to $SO_2(g)$. Therefore, other correlations or models would have to be included in the model to include the absorption of $SO_3^{2-}(g)$.

13.1.3 Acoustic modelling

Most vessels have a silencer installed, which serve to reduce the noise level from the engine, where especially low frequencies are attenuated. A scrubber attenuates low frequencies as well [Wärtsilä (143)], although not as efficiently as a silencer for the mid-range frequencies at approximately 315 Hz. An aeroacoustic model could potentially be implemented in OpenFOAM, which would allow for evaluating the attenuation curves.

13.2 Discrete phase

13.2.1 Chemistry modelling

The chemistry was resolved in the model, where 18 species were included (17 species and H_E^+). These species apply for open-loop operation, where seawater is used for the scrubbing process. When a vessel enters ECAs near coastlines, where the allowable sulfur equivalent is $0.1\ \%$, closed-loop operation is commonly used, where no discharge is allowed. In this case, fresh-water is used for the scrubbing process instead, where chemicals are added to the water, which allows for SO_x removal. However, the chemistry model proposed in this study is not capable of resolving these species, and this would need to be developed, if closed-loop performance is to be modelled.

13.2.2 Momentum modelling

The momentum coupling between the continuous and the discrete phase is modelled in this study, where only the force associated with particle acceleration is considered. Other momentum sources, such as breakup, droplet oscillations, and collision, are not modelled. A consequence of this is the reduced pressure loss, which was seen in Table 10.3 on page 202, where the modelled pressure loss, $\Delta\widetilde{P}$ was lower compared to the pressure loss measured during the experimental tests, ΔP. By including the momentum sources associated with the mentioned phenomena, the overall pressure loss in the model will increase, which would make the model prediction of the pressure loss more accurate.

13.3 Wall film

13.3.1 3D film modelling

The wall film in this study was modelled assuming axis symmetry. However, as described in *Section 5.4: Atomization*, multiple 3D phenomena govern a wall film, which are not resolved in this study. Therefore, by extending the wall film to include these effects, a more accurate description of the wall film could be modelled, where the rivulet formation due to instabilities could be included.

13.3.2 Momentum modelling

The wall films experience atomization and separation, where the associated momentum sources are not modelled. Furthermore, the atomization model is based on an assumption about wave growth, which would also affect the continuous phase momentum. By modelling the induced forces on the continuous phase, the overall pressure loss in the model would increase, which would make the model match the experimental tests more accurately.

13.4 Temporal modelling

The discrete phase was solved in a temporal manner, where the parcels were advanced in time, and the source terms were averaged over time. However, the continuous phase and the wall films were modelled in a steady-state manner, where the equations were solved by assuming the temporal gradients to be zero. Therefore, the model cannot be used to evaluate temporally varying inlet conditions, but this could be done by modifying the wall film and continuous phase equations to include temporal terms. This would allow for modelling of start-up and shut-down procedures.

13.5 Validation

The scrubber model was verified and tuned by using data obtained from the Alfa Laval Test & Training Centre, where the scrubber is designed for $1.6\ \mathrm{MW}$ engine load with a diameter of $1.092\ \mathrm{m}$. This is a relatively small scrubber, so more experimental data is required to evaluate the accuracy of the model for larger scrubbers. Such data were not available during this study, so the model was only verified for a single scrubber geometry.

The scrubber model was tuned by evaluating three output values, which were the outlet temperature, the outlet sulfur equivalent, and the overall pressure loss. However, it was found difficult to tune some of the model parameters based on the three monitored values. Therefore, smaller and more controllable experiments would be beneficial to carry out, where the sub-models could be tuned separately.

An assumption about rivulet formation was made in *Section 5.4: Atomization*, which stated that a fraction of the wall film mass flow would not experience atomization. This assumption was not validated by any study, so further studies within rivulet formation would be of interest to this study. In particular, a study of the mass flow flowing along the shells would be helpful, as such a parameter could be used to tune both rivulet formation, impingement mass fraction deposition, and the atomization model. A proposed method of measuring the mass flow along the shell is illustrated in Figure 13.1.

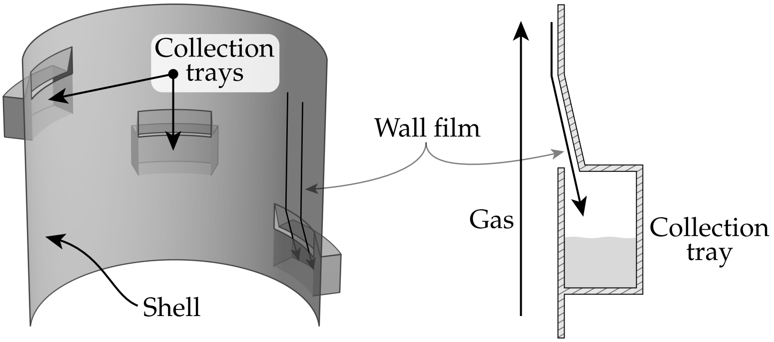

Figure 13.1: An illustration of collection trays, where the wall film mass flows could be measured. The trays should be installed at different locations along the shell, such that the development along the film could be determined.

As seen in Figure 13.1, a simple modification to the scrubber could be done, such that the mass flow along the shell could be measured. The accumulated liquid mass in the trays can be measured after a test, or continuously during the test, where simple drains with mass flow sensors would be required.

14 CONCLUSION

This study focusses on the modelling and analysis of seawater scrubbers for reducing SO_x emissions from marine engines. A scrubber model for SO_x removal was proposed in this study, which combines four main aspects related to scrubber modelling: a chemistry model capable of resolving SO_x absorption in seawater, a discrete phase model for resolving the liquid droplets suspended inside the scrubber, a wall film model for resolving the liquid flowing along the shell of the scrubber, and a CFD model for resolving the continuous gas phase.

The chemistry model included 17 species in the liquid phase, where the relatively slow hydration of $CO_2(l)$ to $H_2CO_3(l)$, the oxidation of sulfur(IV) to sulfur(VI), and eight equilibria were modelled. The method of establishing equilibrium required solving a ninth-order polynomial, which is computationally expensive, so a simplified chemistry model was defined, which only required solving a third-order polynomial. The simplified chemistry model was able to accurately model the absorption of $SO_2(g)$ with an accuracy within $1\ \%$ of the full chemistry model for the pH range between 2 and 8, where scrubbers typically operate.

The liquid phase within a scrubber consists of both suspended droplets and wall films flowing along the surfaces. The suspended droplets were modelled using a Lagrangian approach, where parcels were used to group droplets with similar properties. Numerous sub-models were combined to model the phenomena governing droplets, which included droplet distortion, dynamic drag coefficients, breakup, collision, and wall impingement, where most of these were existing models proposed by other studies. A collision model was proposed in this study, where the outcome of a parcel-parcel collision could be determined using statistical methods. A droplet placed in a gas stream will experience internal circulation, which affects the heat- and mass transfer coefficients. Previous studies have developed analytical solutions to the absorption of species, where this study combined these expressions to take the transient dynamics of circulation into account. This was done by solving the transport equation inside the droplet by assuming an idealized circulating flow. A complete expression for the internal heat- and mass transfer coefficients was developed as a function of the Peclet number and the viscosity ratio. This sub-model is one of the key research achievements in this project.

Liquid wall films flow along the surfaces inside the scrubber, as droplets impinge the walls and deposit fluid. All surfaces within the scrubber were modelled by discretizing the wall films into a number of wall film elements. Multiple sub-models were included to resolve various phenomena related to wall films, which include acceleration, atomization, separation, and mass- and heat transfer. The scrubber shell was modelled as well, where heat transfer with the liquid wall films and the surrounding ambient air was included, while conductive heat transfer in the metal was modelled as well. The wall films inside the scrubber were found to account for approximately $6\ \%$ of the total mass transfer of $SO_2(g)$ and $9\ \%$ of the total thermal energy transfer. Therefore, the liquid wall films were found to have a significant contribution to the overall performance of a scrubber.

The continuous gas phase was modelled with five species: CO_2, H_2O, O_2, SO_2, and N_2. The continuous phase was modelled in OpenFOAM, where the k-ω-SST turbulence model was used to model turbulence. The discrete phase and the wall films were solved in MATLAB and so in order to couple the gas and liquid phases, the two software programs needed to exchange information. It was found that the coupling required approximately $1\ \%$ of the total computational time, which proved that this setup was feasible in practice.

A scrubber designed for $1.6\ \mathrm{MW}$ located at the Alfa Laval Test & Training Centre in Aalborg, Denmark, was used for verifying and tuning the model. 16 different tests were carried out, where the load was changed and different sprayer nozzles were activated. The results from these tests were processed, where a least squares adjustment technique was used to adjust the results according to an underlying physical model. Furthermore, the same technique was used to calculate a statistically accurate sulfur content in the fuel oil used. This showed the importance of post processing experimental results, as the raw signals did not satisfy mass balance due to measurement uncertainties and calibration errors.

The 16 tests were used to tune six model parameters, where a pattern search algorithm was used. An objective function was defined, which quantified the errors between the model and the experimental tests. Each evaluation of the objective function required 16 scrubber simulations, where each simulation required approximately an hour to complete; so in order to decrease computational requirements, only eight of the tests were included during parameter tuning. These eight tests were chosen to be the ones, which reflected the most typical scrubber scenarios. The tuned model was found to be most accurate for the typical scrubber scenarios, which were included during parameter tuning. For these tests, the model was capable of predicting the outlet temperature, sulfur concentration, and overall pressure loss over the scrubber with an average accuracy of $-1.8\ \mathrm{K}$, $-10.1\ \mathrm{ppm}$ (v/v), and $-57.5\ \mathrm{Pa}$ respectively. The *Root Mean Square* errors were $3.1\ \mathrm{K}$, $20.4\ \mathrm{ppm}$ (v/v), and $77.3\ \mathrm{Pa}$, which translates to 11.5, 11.1, and $11.5\ \%$ relative to the experimental tests respectively.

Based on the results it can be concluded that an accurate model capable of simulating wet scrubbers has been developed. The model was tuned and verified based on a single scrubber geometry, where multiple sizes should be included in future studies. Furthermore, some of the sub-models should, ideally, be verified independently, as it was found difficult to tune all six model parameters simultaneously.

This study has contributed with three key scientific achievements. The first is the combination of numerous sub-models to form an accurate scrubber model, where most aspects are resolved. The second is the statistical parcel-parcel collision model, which extends the framework for parcel modelling. The third key scientific achievement is the internal droplet circulation model, which takes the transient tendencies into account when evaluating the heat and mass transfer coefficients.

Back matter

REFERENCES

[1] G. R. Ahmed and M. M. Yovanovich. Approximate analytical solution of forced convection heat transfer from isothermal spheres for all prandtl numbers. *Journal of Heat Transfer*, Vol. 116, Issue 4:838–843, 1994. DOI: 10.1115/1.2911456.

[2] Alfa Laval. Alfa Laval PureSOx. www.alfalaval.com/products/process-solutions/environmental-protection-solutions/wet-exhaust-gas-cleaning-system/puresox, 2018.

[3] Alfa Laval. Alfa Laval PureSOx scrubber technology. www.alfalaval.com/microsites/puresox/technology, 2018.

[4] Alfa Laval. The Alfa Laval Test & Training Centre. www.alfalaval.com/globalassets/images/industries/marine-and-transportation/marine/test-and-training-centre/test-and-training-centre-brochure.pdf, 2018.

[5] ANSYS Inc. Support-request #122549 - Question about critical shear, 2017.

[6] ANSYS Inc. ANSYS Fluent Theory Guide, Release 19.0, 2018.

[7] ANSYS Inc. ANSYS Meshing User's Guide, Release 19.0, 2018.

[8] C. Antoine. Tensions des vapeurs: Nouvelle relation entre les tensions et les températures. *Comptes Rendus*, Vol. 107:681–684, 778–780, 836–837, 1888.

[9] J. Antoine, T. Arts, H. L. Boerrigter, J. M. Buchlin, M. Carbonaro, G. Degrez, R. Dénos, D. Fletcher, D. Olivari, M. L. Riethmuller, and R. A. V. den Braembussche. *Measurement techniques in fluid dynamics – An Introduction*. VKI faculty, 3rd edition, 2009. ISBN: 978-29-3038-996-6.

[10] N. Ashgriz and J. Y. Poo. Coalescence and separation in binary collisions of liquid drops. *Journal of Fluid Mechanics*, Vol. 221:183–204, 1990. DOI: 10.1017/S0022112090003536.

[11] ASTM International. Standard practice for determining data criteria and processing for liquid drop size analysis. *ASTM International, E799 - 03 (2015)*, 2015. DOI: 10.1520/E0799-03R15.

[12] P. Atkins and J. de Paula. *Atkins' Physical Chemistry*. Oxford University Press, 8th edition, 2010. ISBN: 978-01-9954-337-3.

[13] A. G. Bailey, W. Balachandran, and T. J. Williams. The Rosin-Rammler size distribution for liquid droplet ensembles. *Journal of Aerosol Science*, Vol. 14: 39–46, 1983. DOI: 10.1016/0021-8502(83)90083-6.

[14] A. Bandyopadhyay and M. N. Biswas. Modeling of SO2 scrubbing in spray towers. *Science of The Total Environment*, Vol. 383, Issues 1–3:25–40, 2007. DOI: 10.1016/j.scitotenv.2007.04.024.

[15] BETE. BETE spray nozzles. www.bete.com/products/spraynozzles.html, 2018.

[16] E. C. Bingham. The viscosity of binary mixtures. *The Journal of Physical Chemistry*, Vol. 18, No. 2:157–165, 1913. DOI: 10.1021/j150146a005.

[17] R. B. Bird, W. E. Stewart, and E. N. Lightfoot. *Transport Phenomena*. John Wiley & Sons, Inc., 2nd edition, 2006. ISBN: 978-04-7011-539-8.

[18] J. Brandt, J. D. Silver, J. H. Christensen, M. S. Andersen, J. H. Bønløkke, T. Sigsgaard, C. Geels, A. Gross, A. B. Hansen, K. M. Hansen, G. B. Hedegaard, E. Kaas, and L. M. Frohn. Assessment of Health Cost Externalities of Air

Pollution at the National Level using the EVA Model System, 2011, ISSN: 1904-7495. www.ceeh.dk/CEEH_Reports/Report_3/CEEH_Scientific_Report3.pdf, 2011.

[19] A. Bürkholz. *Droplet separation*. VCH Publishers, 1989. ISBN: 978-08-9573-879-0.

[20] K. Brown, W. Kalata, and R. Schick. Optimization of SO2 scrubber using CFD modeling. *Procedia Engineering*, Vol. 83:170–180, 2014. DOI: 10.1016/j.proeng.2014.09.035.

[21] M. Casey and T. Wintergerste. ERCOFTAC - Best Practice Guidelines, 2000.

[22] G. Centeno, G. Sánchez-Reyna, J. Ancheyta, J. A. D. Muñoz, and N. Cardona. Testing various mixing rules for calculation of viscosity of petroleum blends. *Fuel*, Vol. 90, Issue 12:3561–3570, 2011. DOI: 10.1016/j.fuel.2011.02.028.

[23] C. Chicone. *An Invitation to Applied Mathematics: Differential Equations, Modeling, and Computation*. Academic Press, 2016. ISBN: 978-01-2804-153-6.

[24] CIMAC. Guide to Diesel Exhaust Emissions Control Of NOx, SOx, Particulates, Smoke and CO2. www.cimac.com/cms/upload/Publication_Press/Recommendations/Recommendation_28.pdf, 2008.

[25] J. M. Cimbala, Y. A. Cengel, and R. H. Turner. *Fundamentals Of Thermal Fluid Sciences*. McGraw-Hill Education, 5th edition, 2016. ISBN: 978-98-1472-095-3.

[26] CONCAWE. Environmental Impacts of Marine SO2 Emissions. www.concawe.eu/wp-content/uploads/2018/02/Rpt_18-1.pdf, 2018.

[27] R. Cordtz, J. Schramm, and R. Rabe. Investigating SO3 formation from the combustion of heavy fuel oil in a four-stroke medium-speed test engine. *Energy & Fuels*, Vol. 27, No. 10:6279–6286, 2013. DOI: 10.1021/ef4014696.

[28] E. L. Cussler. *Diffusion: Mass Transfer in Fluid Systems*. Cambridge University Press, 3rd edition, 2009. ISBN: 978-05-2187-121-1.

[29] Danish Meteorological Institute. Weather archive. www.dmi.dk/vejr/arkiver/vejrarkiv, 2017.

[30] Danish Ministry of the Environment. Assessment of possible impacts of scrubber water discharges on the marine environment. www2.mst.dk/Udgiv/publications/2012/06/978-87-92903-30-3.pdf, 2012.

[31] H. Darcy. *Les fontaines publiques de la ville de Dijon*. Victor Dalmont, 1856.

[32] M. A. L. de Bertodano, C. Jan, and S. G. Beus. Annular flow entrainment rate experiment in a small vertical pipe. *Nuclear Engineering and Design*, Vol. 178, Issue 1:61–70, 1997. DOI: 10.1016/S0029-5493(97)00175-1.

[33] P. Debye and E. Hückel. Zur Theorie der Elektrolyte. I. Gefrierpunktserniedrigung und verwandte Erscheinungen. *Physikalische Zeitschrift*, Vol. 24, No. 185, 1923.

[34] H. Devoe. *Thermodynamics and Chemistry*. Pearson Education, 2nd edition, 2015. ISBN: 978-01-3096-161-7.

[35] A. G. Dickson. An exact definition of total alkalinity and a procedure for the estimation of alkalinity and total inorganic carbon from titration data. *Deep Sea Research Part A. Oceanographic Research Papers*, Vol. 28, Issue 6:609–623, 1981. DOI: 10.1016/0198-0149(81)90121-7.

[36] A. G. Dickson. Thermodynamics of the dissociation of boric acid in synthetic seawater from 273.15 to 318.15 K. *Deep Sea Research Part A. Oceanographic Research Papers*, Vol. 37, Issue 5:755–766, 1990. DOI:

10.1016/0198-0149(90)90004-F.

[37] A. G. Dickson and C. Goyet. Handbook of Methods for the Analysis of the Various Parameters of the Carbon Dioxide System in Sea Water. www.nodc.noaa.gov/ocads/oceans/DOE_94.pdf, 1994.

[38] A. G. Dickson and J. P. Riley. The estimation of acid dissociation constants in seawater media from potentionmetric titrations with strong base. I. The ionic product of water - Kw. *Marine Chemistry*, Vol. 7, Issue 2:89–99, 1979. DOI: 10.1016/0304-4203(79)90001-X.

[39] DNV-GL. Global Sulphur Cap 2020. www.dnvgl.com/maritime/publications/global-sulphur-cap-2020.html, 2018.

[40] A. Edelman and H. Murakami. Polynomial roots from companion matrix eigenvalues. *Mathematics of Computation*, Vol. 64, Issue 210:763–776, 1995. DOI: 10.2307/2153450.

[41] C. A. Edelmann, P. C. L. Clercq, and B. Noll. Numerical investigation of different modes of internal circulation in spherical drops: Fluid dynamics and mass/heat transfer. *International Journal of Multiphase Flow*, Vol. 95:54–70, 2017. DOI: 10.1016/j.ijmultiphaseflow.2017.05.005.

[42] EGCSA. A practical guide to exhaust gas cleaning systems for the maritime industry. www.egcsa.com/wp-content/uploads/EGCSA-Handbook-2012-A5-size-.pdf, 2012.

[43] A. Einstein. Über die von der molekularkinetischen theorie der wärme geforderte bewegung von in ruhenden flüssigkeiten suspendierten teilchen. *Annalen der Physik*, Vol. 322, No. 8:549–560, 1905. DOI: 10.1002/andp.19053220806.

[44] EKOKEM. Seawater analysis 24-25/10-2016, 2016.

[45] S. R. Emerson and J. I. Hedges. *Chemical Oceanography and the Marine Carbon Cycle*. Cambridge University Press, 2008. ISBN: 978-05-2183-313-4.

[46] EUR-Lex: European Union law. Environmental quality standards applicable to surface water. www.eur-lex.europa.eu/legal-content/EN/TXT/-uri=LEGISSUM:l28180, 2008.

[47] F-Chart. Engineering Equation Solver. www.fchart.com/ees, 2018.

[48] J. H. Ferziger and M. Peric. *Computational Methods for Fluid Dynamics*. Springer-Verlag Berlin Heidelberg, 3rd edition, 2002. ISBN: 978-36-4256-026-2.

[49] A. Fick. Ueber diffusion. *Annalen der Physik*, Vol. 170, Issue 1, 1855. DOI: 10.1002/andp.18551700105.

[50] W. H. Finlay. *The Mechanics of Inhaled Pharmaceutical Aerosols*. Elsevier Academic Press, 2001. ISBN: 978-01-2256-971-5.

[51] D. Flagiello, A. Erto, A. Lancia, and F. D. Natale. Experimental and modelling analysis of seawater scrubbers for sulphur dioxide removal from flue-gas. *Fuel*, Vol. 214:254–263, 2018. DOI: 10.1016/j.fuel.2017.10.098.

[52] M. G. Flanner, C. S. Zender, J. T. Randerson, and P. J. Rasch. Present-day climate forcing and response from black carbon in snow. *Journal of Geophysical Research: Atmospheres*, Vol. 112, Issue D11, 2007. DOI: 10.1029/2006JD008003.

[53] Free Software Foundation, Inc. GNU General Public License. www.gnu.org/copyleft/gpl.html, 2007.

[54] J. H. Friedman, J. L. Bentley, and R. A. Finkel. An algorithm for finding best matches in logarithmic expected time. *ACM Transactions on Mathematical Software*, Vol. 3, Issue 3:209–226, 1977. DOI: 10.1145/355744.355745.

[55] M. A. Friedrich, H. Lan, J. L. Wegener, J. A. Drallmeier, and B. F. Armaly. A separation criterion with experimental validation for shear-driven films in separated flows. *ASME Journal of Fluids Engineering*, Vol. 130, Issue 5, 2008. DOI: 10.1115/1.2907405.

[56] W. L. Friend and A. B. Metzner. Turbulent heat transfer inside tubes and the analogy among heat, mass, and momentum transfer. *AIChE Journal*, Vol. 4, No. 4:393–402, 1958. DOI: 10.1002/aic.690040404.

[57] N. Frossling. Uber die verdunstung fallender tropfen. *Beitr. Geophys. Gerlands*, Vol. 52:170–216, 1938.

[58] C. J. Geankoplis. *Transport Processes and Unit Operations*. Pearson College, 3rd edition, 1993. ISBN: 978-01-3930-439-2.

[59] C. D. Ghilani. *Adjustment Computations: Spatial Data Analysis*. Wiley, 6th edition, 2017. ISBN: 978-11-1938-598-1.

[60] M. M. Gogoi, S. S. Babu, K. K. Moorthy, R. C. Thakur, J. P. Chaubey, and V. S. Nair. Aerosol black carbon over Svalbard regions of Arctic. *Polar Science*, Vol. 10, Issue 1:60–70, 2016. DOI: 10.1016/j.polar.2015.11.001.

[61] R. N. Goldberg and V. B. Parker. Thermodynamics of solution of SO2(g) in water and of aqueous sulfur dioxide solutions. *Journal of Research of the National Bureau of Standards*, Vol. 90, No. 5, 1985.

[62] A. D. Gosman and E. Loannides. Aspects of computer simulation of liquid-fueled combustors. *Journal of Energy*, Vol. 7, No. 6:482–490, 1983. DOI: 10.2514/3.62687.

[63] J. S. Hadamard. Movement permanent lent d'une sphere liquide et visqueuse dans un liquide visqueux. *Comptes Rendus Hebdomadaires des Seances de V Academie des Sciences (París)*, pages 1735–1752, 1911.

[64] L. J. S. Hadlocon, A. B. O. Soboyejo, L. Zhao, and H. Zhu. Statistical modelling of ammonia absorption in an acid spray scrubber. *Biosystems Engineering*, Vol. 132:88–95, 2015. DOI: 10.1016/j.biosystemseng.2015.02.003.

[65] A. Haider and O. Levenspiel. Drag coefficient and terminal velocity of spherical and nonspherical particles. *Powder Technology*, Vol. 58, Issue 1:63–70, 1988. DOI: 10.1016/0032-5910(89)80008-7.

[66] Haldor Topsoe. DNX Catalysts Products. www.topsoe.com/products/catalysts/dnx, 2018.

[67] H. Helmholtz. On discontinuous movements of fluids. *The London, Edinburgh, and Dublin Philosophical Magazine and Journal of Science*, Vol. 36, Issue 244: 337–346, 1868. DOI: 10.1080/14786446808640073.

[68] M. Henschke and A. Pfennig. Mass-transfer enhancement in single-drop extraction experiments. *Fluid Mechanics and Transport Phenomenon*, Vol. 45, No. 10:2079–2086, 1999. DOI: 10.1002/aic.690451006.

[69] M. J. M. Hill. On a spherical vortex. *Philosophical Transactions of the Royal Society of London*, Vol. 185:213–245, 1894. URL: .

[70] IMO. Third IMO Greenhouse Gas Study 2014. www.imo.org/en/OurWork/Environment/PollutionPrevention/

AirPollution/Documents/Third%20Greenhouse%20Gas%20Study/GHG3%20Executive%20Summary%20and%20Report.pdf, 2014.

[71] IMO. Emission control areas. www.imo.org/en/OurWork/Environment/PollutionPrevention/AirPollution/Pages/Emission-Control-Areas-%28ECAs%29-designated-under-regulation-13-of-MARPOL-Annex-VI-%28NOx-emission-control%29.aspx, 2018.

[72] IMO. International convention for the prevention of pollution from ships. www.imo.org/en/about/conventions/listofconventions/pages/international-convention-for-the-prevention-of-pollution-from-ships-(marpol).aspx, 2018.

[73] J. G. M. Kuerten. Point-particle DNS and LES of particle-laden turbulent flow - a state-of-the-art review. *Flow, Turbulence and Combustion*, Vol. 97, No. 3: 689–713, 2016. DOI: 10.1007/s10494-016-9765-y.

[74] J. W. Jawitz. Moments of truncated continuous univariate distributions. *Advances in Water Resources*, Vol. 27, Issue 3:269–281, 2004. DOI: 10.1016/j.advwatres.2003.12.002.

[75] C. L. V. Jayatilleke. The influence of prandtl number and surface roughness on the resistance of the laminar sub-layer to momentum and heat transfer. *Imperial College London*, 1966.

[76] Y. Jia, L. Yin, Y. Xu, Y. Chen, and X. Ding. Simulation of the absorption of SO2 by ammonia in a spray scrubber. *Chemical Engineering and Processing: Process Intensification*, Vol. 116:60–67, 2017. DOI: 10.1016/j.cep.2017.03.001.

[77] L. Jiang, J. Kronbak, and L. P. Christensen. The costs and benefits of sulphur reduction measures: Sulphur scrubbers versus marine gas oil. *Transportation Research Part D: Transport and Environment*, Vol. 28:19–27, 2014. DOI: 10.1016/j.trd.2013.12.005.

[78] K. S. Johnson. Carbon dioxide hydration and dehydration kinetics in seawater. *Limnology and Oceanography*, Vol. 27, Issue 5, 1982. DOI: 10.4319/lo.1982.27.5.0849.

[79] H. F. Johnstone, R. B. Feild, and M. C. Tassler. Gas absorption and aerosol collection in a venturi atomizer. *Industrial & Engineering Chemistry*, Vol. 46, No. 8:1601–1608, 1954. DOI: 10.1021/ie50536a028.

[80] D. M. Kern. The hydration of carbon dioxide. *Journal of Chemical Education*, Vol. 37, No. 1, 1960. DOI: 10.1021/ed037p14.

[81] G. H. Ko and H. S. Ryou. Modeling of droplet collision-induced breakup process. *International Journal of Multiphase Flow*, Vol. 31, Issue 6:723–738, 2005. DOI: 10.1016/j.ijmultiphaseflow.2005.02.004.

[82] I. M. Kolthoff and P. J. Elving. *Treatise on Analytical Chemistry*. Wiley, 2nd edition, 1980. ISBN: 978-04-7105-510-5.

[83] R. Kronig and J. C. Brink. On the theory of extraction from falling droplets. *Applied Scientific Research*, Vol. 2, 1951. DOI: 10.1007/BF00411978.

[84] D. Kuhnke. *Spray/Wall-interaction Modelling by Dimensionless Data Analysis*. Shaker Verlag GmbH, 2004. ISBN: 978-38-3223-539-0.

[85] D. G. Leaist. Diffusion coefficient of aqueous sulfur dioxide at 25 degree C. *Journal of Chemical & Engineering Data*, Vol. 29, No. 3:281–282, 1984. DOI: 10.1021/je00037a015.

[86] G. N. Lewis and M. Randall. The activity coefficient of strong electrolytes. *Journal of the American Chemical Society*, Vol. 43, No. 5:1112–1154, 1921. DOI: 10.1021/ja01438a014.

[87] R. M. Lewis and V. Torczon. Pattern search algorithms for bound constrained minimization. *SIAM Journal on Optimization*, Vol. 9, Issue 4:1082–1099, 1999. DOI: 10.1137/S1052623496300507.

[88] S. Li, C. Li, G. Zeng, S. Li, F. Wang, D. Wang, and P. Lu. Simulation and experimental validation studies on a new type umbrella plate scrubber. *Separation and Purification Technology*, Vol. 62, Issue 2:323–329, 2008. DOI: 10.1016/j.seppur.2008.01.020.

[89] T. J. Lueker, A. G. Dickson, and C. D. Keeling. Ocean pCO2 calculated from dissolved inorganic carbon, alkalinity, and equations for K1 and K2: validation based on laboratory measurements of CO2in gas and seawater at equilibrium. *Marine Chemistry*, Vol. 70, Issues 1–3:105–119, 2000. DOI: 10.1016/S0304-4203(00)00022-0.

[90] MAN Diesel & Turbo. Power Plants Programme 2016/2017. http://powerplants.man.eu/docs/librariesprovider7/stationary-engine-programme/power-plants-programme-2016.pdf-sfvrsn=8, 2017.

[91] MAN Diesel & Turbo. Exhaust Gas Emission Control Today and Tomorrow. https://marine.mandieselturbo.com/docs/librariesprovider6/technical-papers/exhaust-gas-emission-control-today-and-tomorrow.pdf, 2018.

[92] I. Martínez. Mass Diffusivity Data. http://webserver.dmt.upm.es/~isidoro/dat1/Massdiffusivitydata.pdf, 2018.

[93] E. Mayer. Theory of liquid atomization in high velocity gas streams. *Journal of the American Rocket Society*, Vol. 31:1783–1785, 1961.

[94] F. R. Menter. Two-equation eddy-viscosity turbulence models for engineering applications. *AIAA Journal*, Vol. 32, No. 8:1598–1605, 1994. DOI: 10.2514/3.12149.

[95] T. Mi and X. M. Yu. Dust removal and desulphurization in a novel venturi scrubber. *Chemical Engineering and Processing: Process Intensification*, Vol. 62: 159–167, 2012. DOI: 10.1016/j.cep.2012.07.010.

[96] F. J. Millero, R. Feistel, D. G. Wright, and T. J. McDougall. The composition of standard seawater and the definition of the reference-composition salinity scale. *Deep Sea Research Part I: Oceanographic Research Papers*, Vol. 55, Issue 1:50–72, 2008. DOI: 10.1016/j.dsr.2007.10.001.

[97] Munters. Munters DV 270: Droplet Separator. https://www.munters.com/globalassets/inriver/resources/products/mist-eliminators/me_prodsheet_dv-270.pdf, 2018.

[98] A. B. Newman. The drying of porous solid. diffusion and surface emission effects. *Transactions of the American Institute of Chemical Engineers*, Vol. 27: 203–211, 1931.

[99] Nickel Institute. High-Performance Stainless Steels. https://nickelinstitute.org/~/media/Files/TechnicalLiterature/HighPerformanceStainlessSteels_11021_.ashx, 2018.

[100] P. J. O'Rourke. Collective drop effects on vaporizing liquid sprays. *Princeton University*, 1981.

[101] P. J. O'Rourke and A. A. Amsden. The TAB method for numerical calculation of spray droplet breakup. *SAE International*, 1987. DOI: 10.4271/872089.

[102] P. J. O'Rourke and A. A. Amsden. A particle numerical model for wall film dynamics in port-injected engines. *SAE Technical Paper*, 1996. DOI: 10.4271/961961.

[103] J. Ott and J. Boerio-Goates. *Chemical Thermodynamics: Principles and Applications*. Academic Press, 2000. ISBN: 978-00-8050-098-0.

[104] I. Panasiuk and L. Turkina. The evaluation of investments efficiency of SOx scrubber installation. *Transportation Research Part D: Transport and Environment*, Vol. 40:87–96, 2015. DOI: 10.1016/j.trd.2015.08.004.

[105] L. Pauling. *The Nature of the Chemical Bond and the Structure of Molecules and Crystals*. Cornell University Press, 3rd edition, 1960. ISBN: 978-08-0140-333-0.

[106] S. K. Pawar, J. T. Padding, N. G. Deen, J. A. M. Kuipers, A. Jongsma, and F. Innings. Eulerian-lagrangian modelling with stochastic approach for droplet-droplet collisions. *Proceedings of the Ninth International Conference on Computational Fluid Dynamics in the Minerals and Process Industries*, 2012.

[107] B. E. Poling, J. M. Prausnitz, and J. P. O'Connell. *The Properties of Gases and Liquids*. McGraw-Hill Education, 5th edition, 2001. ISBN: 978-00-7011-682-5.

[108] A. Pourmohammadbagher, E. Jamshidi, H. Ale-Ebrahim, B. Dabir, and M. Mehrabani-Zeinabad. Simultaneous removal of gaseous pollutants with a novel swirl wet scrubber. *Chemical Engineering and Processing: Process Intensification*, Vol. 50, No. 8:773–779, 2011. DOI: 10.1016/j.cep.2011.06.001.

[109] D. W.-G. R. E. Zeebe. *CO2 in Seawater: Equilibrium, Kinetics, Isotopes*. Elsevier Science, 2001. ISBN: 978-04-4450-946-8.

[110] W. E. Ranz and W. R. Marshall. Evaporation from drops: Part 1. *Chemical Engineering Progress*, Vol. 48, Issue 3:141–146, 1952.

[111] M. O. Rodrigues. Geometrical laws governing the displacements of a solid system in space, and the variation of the coordinates arising from these displacements considered independently of the causes which can produce them (translated from french). *Journal de mathématiques pures et appliquées*, Vol. 5: 380–440, 1840.

[112] F. Roquet, G. Madec, T. J. McDougall, and P. M. Barker. Accurate polynomial expressions for the density and specific volume of seawater using the TEOS-10 standard. *Ocean Modelling*, Vol. 90:29–43, 2015. DOI: 10.1016/j.ocemod.2015.04.002.

[113] P. Rysselberghe. Further revision of the constants of the Debye-Hückel theory. *Journal of the American Chemical Society*, Vol. 65, Issue 6:1249–1249, 1943. DOI: 10.1021/ja01246a516.

[114] P. Saiyasitpanich, M. Lu, T. C. Keener, F. Liang, and S. J. Khang. The effect of diesel fuel sulfur content on particulate matter emissions for a nonroad diesel generator. *Journal of the Air & Waste Management Association*, Vol. 55:993–1001, 2005.

[115] R. Sander. Compilation of Henry's law constants (version 4.0) for water as solvent. *Atmospheric Chemistry and Physics*, Vol. 15, Issue 8:4399–4981, 2015.

DOI: 10.5194/acp-15-4399-2015.

[116] D. Shindell and G. Faluvegi. Climate response to regional radiative forcing during the twentieth century. *Nature Geoscience*, Vol. 2:294–300, 2009. DOI: 10.1038/ngeo473.

[117] Ship & Bunker. Ship & Bunker - World Bunker Prices. www.shipandbunker.com/prices, 2018.

[118] R. K. Singh, J. E. Galvin, and X. Sun. Three-dimensional simulation of rivulet and film flows over an inclined plate: Effects of solvent properties and contact angle. *Chemical Engineering Science*, Vol. 142:244–257, 2016. DOI: 10.1016/j.ces.2015.11.029.

[119] S. Singh, K. Sørensen, A. S. Simonsen, and T. J. Condra. Implications of fin profiles on overall performance and weight reduction of a fin and tube heat exchanger. *Applied Thermal Engineering*, Vol. 115:962–976, 2017. DOI: 10.1016/j.applthermaleng.2017.01.043.

[120] S. W. Sloan. A FORTRAN program for profile and wavefront reduction. *International Journal for Numerical Methods in Engineering*, Vol. 28, No. 11: 2651–2679, 1989. DOI: 10.1002/nme.1620281111.

[121] S. J. Smith and T. C. Bond. Two hundred fifty years of aerosols and climate: the end of the age of aerosols. *Atmospheric Chemistry and Physics*, Vol. 14:537–549, 2014. DOI: 10.5194/acp-14-537-2014.

[122] M. Sofiev, J. J. Winebrake, L. Johansson, E. W. Carr, M. Prank, J. Soares, J. Vira, R. Kouznetsov, J. Jalkanen, and J. J. Corbett. Cleaner fuels for ships provide public health benefits with climate tradeoffs. *Nature Communications*, Vol. 9, Article number 406, 2018. DOI: 10.1038/s41467-017-02774-9.

[123] G. G. Stokes. On the steady motion of incompressible fluids. *Transactions of the Cambridge Philosophical Society*, Vol. 7, 1848. DOI: 10.1017/CBO9780511702242.002.

[124] W. Sutherland. The viscosity of gases and molecular force. *The London, Edinburgh, and Dublin Philosophical Magazine and Journal of Science*, Vol. 36, No. 223:507–531, 1893. DOI: 10.1080/14786449308620508.

[125] F. X. Tanner. Liquid jet atomization and droplet breakup modeling of non-evaporating diesel fuel sprays. *SAE Technical Paper*, 1997. DOI: 10.4271/970050.

[126] F. X. Tanner and G. Weisser. Simulation of liquid jet atomization for fuel sprays by means of a cascade drop breakup model. *SAE Technical Paper*, 1998. DOI: 10.4271/980808.

[127] G. I. Taylor. The shape and acceleration of a drop in a high speed air stream. *The Scientific Papers of G.I. Taylor*, Vol. 3:457–464, 1963.

[128] G. J. Tee. Surface area of ellipsoid segment. www.math.auckland.ac.nz/Research/Reports/view.php-id=539, 2005.

[129] TEOS-10. Gibbs-SeaWater (GSW) Oceanographic Toolbox Manual - Thermodynamic Equation of Seawater - 2010. www.teos-10.org/pubs/TEOS-10_Manual.pdf, 2010.

[130] The OpenFOAM Foundation. The OpenFOAM Foundation. www.cfd.direct/openfoam/about, 2018.

[131] Trans Oleum. CO2 and sulphur emissions from the shipping industry.

www.transoleum.se/wp-content/uploads/2016/11/
CO2-and-sulphur-emissions-from-the-shipping-industry.pdf, 2016.

[132] S. R. Turns. *An Introduction to Combustion*. McGraw-Hill Education, 3rd edition, 2011. ISBN: 978-00-7338-019-3.

[133] J. H. van't Hoff. *Studies in Chemical Dynamics*. Frederik Muller & Co and Williams & Norgate, 1896.

[134] P. F. Verhulst. Recherches mathématiques sur la loi d'accroissement de la population. *Nouveaux mémoires de l'Académie Royale des Sciences et Belles-Lettres de Bruxelles*, Vol. 18:14–54, 1845. URL: .

[135] H. K. Versteeg and W. Malalasekera. *An Introduction To Computational Fluid Dynamics*. Pearson Education, 2nd edition, 2007. ISBN: 978-01-3127-498-3.

[136] H. Wadell. Volume, shape, and roundness of quartz particles. *The Journal of Geology*, Vol. 43, No. 3:250–280, 1935. URL: .

[137] J. M. Wallace and P. V. Hobbs. *Atmospheric Science: An Introductory Survey*. Elsevier Academic Press, 2nd edition, 2006. ISBN: 978-01-2732-951-2.

[138] R. E. Walpole, R. H. Myers, S. L. Myers, and K. E. Ye. *Probability & Statistics for Engineers & Scientists*. Pearson, 9th edition, 2011. ISBN: 978-03-2162-911-1.

[139] R. F. Weiss. Carbon dioxide in water and seawater: the solubility of a non-ideal gas. *Marine Chemistry*, Vol. 2, Issue 3:203–215, 1974. DOI: 10.1016/0304-4203(74)90015-2.

[140] J. Welty, C. E. Wicks, G. L. Rorrer, and R. E. Wilson. *Fundamentals of Momentum, Heat and Mass Transfer*. Wiley, 5th edition, 2014. ISBN: 978-04-7012-868-8.

[141] WHO. WHO Air quality guidelines for particulate matter, ozone, nitrogen dioxide and sulfur dioxide. http://apps.who.int/iris/bitstream/handle/10665/69477/WHO_SDE_PHE_OEH_06.02_eng.pdf, 2005.

[142] WHO. Ambient Air Pollution - A global assessment of exposure and burden of disease. http://apps.who.int/iris/bitstream/handle/10665/250141/9789241511353-eng.pdf, 2016.

[143] Wärtsilä. Exhaust Gas Scrubber Installed Onboard MT "SUULA". www.annualreport2010.wartsila.com/files/wartsila_2010/Docs/Scrubber_Test_Report_onboard_Suula.pdf, 2018.

[144] J. Zhang and F. J. Millero. The rate of sulfite oxidation in seawater. *Geochimica et Cosmochimica Acta*, Vol. 55, Issue 3:677–685, 1991. DOI: 10.1016/0016-7037(91)90333-Z.

[145] Q. Zhou and S. C. Yao. Group modeling of impacting spray dynamics. *International Journal of Heat and Mass Transfer*, Vol. 35, Issue 1:121–129, 1992. DOI: 10.1016/0017-9310(92)90013-I.

A | CONSTANTS AND CORRELATIONS

This chapter presents all correlations and constants used in the scrubber model, unless they are presented in the main report. The correlations used are both empirical and theoretical, where a dimensionless salinity and temperature are used throughout this chapter, which are shown in (A.1).

$$S' = \frac{S}{{}^{\mathrm{g}}/_{\mathrm{kg}}} \qquad T' = \frac{T}{\mathrm{K}} \qquad T'_{\mathrm{C}} = \frac{T - 273.15\,\mathrm{K}}{\mathrm{K}} \tag{A.1}$$

A.1 pK_a values

The pK_a values are both salinity and temperature dependent. Some pK_a values have been studied thoroughly within the field of chemical oceanography [Emerson and Hedges (45)], where accurate correlations have been developed, which take both temperature and salinity into account. Other pK_a values do not have a direct correlation given, so other theories are used to correlate these pK_a values with temperature and salinity. Table A.1 shows all pK_a values used in this study, where some fields are left blank, and these values are correlated directly in (A.2). The other values are reference values indicated by the superscripts $(...)^{\ominus}$, which are used in combination with other correlations to take temperature and salinity into account.

Table A.1: The pK_a values used in this study. The blank fields are defined in (A.2). The references in the table are: (1) [Dickson and Riley (38)]; (2) [Dickson (36)]; (3) [Lueker et al. (89)]; (4) [Kern (80)]; (5) [Kolthoff and Elving (82)].

Constant	K_a [mol/L]	pK_a	$\Delta H^{\ominus}/R$ [K]	**Ref.**
K_W^{γ}	–	–	–	(1)
K_B^{γ}	–	–	–	(2)
$K_{\mathrm{CO_2}}^{\gamma}$	–	–	–	(3)
$K_{\mathrm{CO_3},1}^{\ominus}$	$2.0 \cdot 10^{-4}$	3.7	921.3	(4)
$K_{\mathrm{CO_3},2}^{\gamma}$	–	–	–	(3)
$K_{\mathrm{SO_3},1}^{\ominus}$	$1.2589 \cdot 10^{-2}$	1.9	−2140.9	(5)
$K_{\mathrm{SO_3},2}^{\ominus}$	$1.0 \cdot 10^{-7}$	7.0	−439.0	(5)
$K_{\mathrm{SO_4},1}^{\ominus}$	$1.0 \cdot 10^{3}$	−3.0	2637.6	(5)
$K_{\mathrm{SO_4},2}^{\ominus}$	$1.2589 \cdot 10^{-2}$	1.9	−2637.6	(5)

The empty fields in Table A.1 are correlated using (A.2), where the references were shown in the above table.

$$
\begin{aligned}
\mathrm{p}K_{\mathrm{W}}^{\gamma}\left(\frac{\mathrm{mol}}{\mathrm{L}}\right)^{-1} &= 148.96502-\frac{13847.26}{T'}-23.6521\cdot\log_{\mathrm{e}}(T')-0.01615\cdot S'+\\
&\quad\Big(118.67/T'-5.977+1.0495\cdot\log_{\mathrm{e}}(T')\Big)\cdot\sqrt{S'}\\
\mathrm{p}K_{\mathrm{B}}^{\gamma}\left(\frac{\mathrm{mol}}{\mathrm{L}}\right)^{-1} &= \Big(-8966.90-2890.52\cdot\sqrt{S'}-77.942\cdot S'+1.728\cdot S'^{3/2}-0.0996\cdot S'^{2}\Big)\cdot\frac{1}{T'}+\\
&\quad 0.053105\cdot\sqrt{S'}\cdot T'-\Big(24.4344+25.085\cdot\sqrt{S'}+0.2474\cdot S'\Big)\cdot\log_{\mathrm{e}}(T')+\\
&\quad 148.0248+137.1942\cdot\sqrt{S'}+1.62142\cdot S'\\
\mathrm{p}K_{\mathrm{CO_2}}^{\gamma}\left(\frac{\mathrm{mol}}{\mathrm{L}}\right)^{-1} &= \frac{3633.86}{T'}-61.2172+9.6777\cdot\log_{\mathrm{e}}(T')-0.011555\cdot S'+0.0001152\cdot S'^{2}\\
\mathrm{p}K_{\mathrm{CO_3,2}}^{\gamma}\left(\frac{\mathrm{mol}}{\mathrm{L}}\right)^{-1} &= \frac{471.78}{T'}+25.9290-3.16967\cdot\log_{\mathrm{e}}(T')-0.01781\cdot S'+0.0001122\cdot S'^{2}
\end{aligned}
\tag{A.2}
$$

Notice that both S' and T' are dimensionless. The $\mathrm{p}K_{\mathrm{a}}$ values, which do not have direct correlations with temperature, are correlated used *van 't Hoff equation* [van't Hoff (133)], which is shown in (A.3).

$$
\begin{gathered}
\frac{\mathrm{d}}{\mathrm{d}T}\log_{\mathrm{e}}(K_{\mathrm{a}})=\frac{\Delta H^{\ominus}}{R\cdot T^{2}}\\
\Downarrow\\
K_{\mathrm{a}}(T)=K_{\mathrm{a}}^{\ominus}\cdot\exp\left(\frac{\Delta H^{\ominus}}{R}\cdot\left(\frac{1}{T^{\ominus}}-\frac{1}{T}\right)\right)
\end{gathered}
\tag{A.3}
$$

Where $\Delta H^{\ominus}$ is the standard enthalpy change for the reaction, and $T^{\ominus}$ is the temperature, at which $K_{\mathrm{a}}^{\ominus}$ was found, and is equal to $25°\mathrm{C} = 298.15\ \mathrm{K}$ for all constants. $\Delta H^{\ominus}$ is calculated using (A.4) [Devoe (34)], where R_{i} and P_{i} are reactants and products respectively.

$$
\begin{gathered}
v_{\mathrm{R_1}}\ R_1+v_{\mathrm{R_2}}\ R_2...+v_{\mathrm{R_n}}\ R_{\mathrm{n}}\quad\longrightarrow\quad v_{\mathrm{P_1}}\ P_1+v_{\mathrm{P_2}}\ P_2...+v_{\mathrm{P_m}}\ P_{\mathrm{m}}\\
\Delta H^{\ominus}=\sum_{\mathrm{i}=1}^{\mathrm{m}}v_{\mathrm{P_i}}\cdot\Delta H_{\mathrm{f}}^{\ominus}(P_{\mathrm{i}})-\sum_{\mathrm{i}=1}^{\mathrm{n}}v_{\mathrm{R_i}}\cdot\Delta H_{\mathrm{f}}^{\ominus}(R_{\mathrm{i}})
\end{gathered}
\tag{A.4}
$$

The values of $\Delta H^{\ominus}$ are shown in Table A.2 for each of the species used in Table A.1.

By applying (A.4) for each of the equilibrium reactions in (3.14) on page 27 with the values in Table A.2, the term $\Delta H^{\ominus}/R$ in Table A.1 can be calculated. It should be noted that after having calculated $K_{\mathrm{a}}(T)$ using (A.3), the values are subsequently correlated with salinity according to (3.17) on page 29, where the ionic activity of each species was calculated as a function of the ionic strength.

Table A.2: The standard enthalpy changes, $\Delta H^\ominus$, required to calculate $\Delta H^\ominus/R$ in Table A.1 for the pK_a values, which do not have direct correlations provided. The references in the table are: (1) [Atkins and de Paula (12)]; (2) [Goldberg and Parker (61)].

Species	$\Delta H_\mathrm{f}^\ominus$ [kJ/mol]	**Ref.**
H^+	0	(1)
H_2CO_3	−699.65	(1)
HCO_3^-	−691.99	(1)
CO_3^{2-}	−677.14	(1)
H_2SO_3	−609.61	(2)
HSO_3^-	−627.41	(2)
SO_3^{2-}	−631.06	(2)
H_2SO_4	−909.27	(1)
HSO_4^-	−887.34	(1)
SO_4^{2-}	−909.27	(1)

A.2 Henry's Law constants

The *Henry's Law constants* are shown in Table A.3, where the temperature dependency is correlated using (A.3) as well, where $T^\ominus = 25°\mathrm{C}$ and $\Delta H^\ominus/R$ is shown in Table A.3.

Table A.3: The *Henry's Law constants* for CO2, O2 and SO2. $K_{\mathrm{H,CO_2}}$ is calculated according to (A.5), where both temperature and salinity is taken into account. The references in the table are: (1) [Weiss (139)]; (2) [Sander (115)].

Constant	K_H $\left[\frac{\mathrm{mol}}{\mathrm{m^3\,Pa}}\right]$	$\Delta H^\ominus/R$ [K]	**Ref.**
$K_{\mathrm{H,CO_2}}$	–	–	(1)
$K^\ominus_{\mathrm{H,O_2}}$	$1.3 \cdot 10^{-5}$	1500	(2)
$K^\ominus_{\mathrm{H,SO_2}}$	$1.3 \cdot 10^{-2}$	2900	(2)

Similar to the pK_a values, salinity affects the values of K_H. No correlation for salinity is used for O_2 and SO_2, but a complete correlation for $K_{\mathrm{H,CO_2}}$ is given in (A.5), where both temperature and salinity is taken into account [Weiss (139)].

$$\begin{aligned}\log_\mathrm{e}\left(K_{\mathrm{H,CO_2}} \cdot \left(\frac{\mathrm{mol}}{\mathrm{L \cdot atm}}\right)^{-1}\right) = \frac{9345.17}{T'} - 60.2409 + 23.3585 \cdot \log_\mathrm{e}\left(\frac{T'}{100}\right) + \\ S' \cdot \left(0.023517 - 0.00023656 \cdot T' + 0.0047036 \cdot \left(\frac{T'}{100}\right)^2\right)\end{aligned} \tag{A.5}$$

A.3 Diffusivity constants

The mass diffusivity for the gas and liquid species are shown in Table A.4.

Table A.4: The mass diffusivity for the reacting species used in this study. The references in the table are: (1) [Martínez (92)]; (2) [Cussler (28)]; (3) [Leaist (85)].

Constant	**Mixture-pair**	$\mathscr{D}_{\mathrm{AB}}\ \left[\frac{\mathrm{cm}^2}{\mathrm{s}}\right]$	T^{Θ} [K]	**Ref.**
$\mathscr{D}^{\Theta}_{\mathrm{g,CO_2}}$	Air-CO_2	14.8	282.0	(1)
$\mathscr{D}^{\Theta}_{\mathrm{g,H_2O}}$	Air-H_2O	28.2	289.1	(1)
$\mathscr{D}^{\Theta}_{\mathrm{g,O_2}}$	Air-O_2	19.0	300.0	(2)
$\mathscr{D}^{\Theta}_{\mathrm{g,SO_2}}$	Air-SO_2	13.0	300.0	(2)
$\mathscr{D}^{\Theta}_{\mathrm{l,CO_2}}$	Water-CO_2	$1.92 \cdot 10^{-5}$	300.0	(2)
$\mathscr{D}^{\Theta}_{\mathrm{l,O_2}}$	Water-O_2	$2.1 \cdot 10^{-5}$	300.0	(2)
$\mathscr{D}^{\Theta}_{\mathrm{l,SO_2}}$	Water-SO_2	$2.0 \cdot 10^{-5}$	300.0	(3)

The diffusivity coefficients in Table A.4 are temperature dependent, where the *Chapman-Enskog theory* [Poling et al. (107)] applies to gases, and the *Stokes-Einstein equation* [Einstein (43)] applies to liquids. These are shown in (A.6).

$$\begin{aligned} &\text{(Chapman-Enskog theory)} \qquad && \mathscr{D}_{\mathrm{g}}(T) = \frac{A_{\mathrm{D}} \cdot \sqrt{\frac{1}{M_{\mathrm{A}}} + \frac{1}{M_{\mathrm{B}}}}}{P \cdot \sigma_{\mathrm{AB}}^2 \cdot \Omega} \cdot T^{(3/2)} \\ &\text{(Stokes-Einstein equation)} \qquad && \frac{\mathscr{D}_{\mathrm{l}}(T_1)}{\mathscr{D}_{\mathrm{l}}(T_2)} = \frac{T_1 \cdot \mu(T_2)}{T_2 \cdot \mu(T_1)} \end{aligned} \tag{A.6}$$

Where A_{D} is an empirical coefficient, σ_{AB} is the average collision diameter between the two species, and Ω is the temperature-dependent collision integral. The correlations in (A.6) require numerous parameters, which are difficult to find. Therefore, simple correlations are instead used in this study by assuming all the constants in (A.6) to be temperature independent. This simplifies (A.6) to the expressions shown in (A.7).

$$\begin{aligned} \mathscr{D}_{\mathrm{g,i}}(T) &= \mathscr{D}^{\Theta}_{\mathrm{g,i}} \cdot \left(\frac{T}{T^{\Theta}}\right)^{(3/2)} \\ \mathscr{D}_{\mathrm{l,i}}(T) &= \mathscr{D}^{\Theta}_{\mathrm{l,i}} \cdot \left(\frac{T}{T^{\Theta}}\right) \end{aligned} \tag{A.7}$$

A.4 Liquid phase properties

The liquid properties are shown in (A.8). The value of c_P is assumed constant, although this varies slightly between 0 and $80°\mathrm{C}$, which is the maximum temperature span for the liquid phase in this study. The dynamic viscosity, $\mu_\mathrm{l}(T)$ is correlated using a common expression [Bird et al. (17)]. The remaining correlations for the surface tension, $\sigma_\mathrm{l}(T)$, the liquid Prandtl number, $Pr_\mathrm{l}(T)$, and the thermal conductivity, $\kappa_\mathrm{l}(T)$, are all fitted to data from *Engineering Equation Solver*, EES [F-Chart (47)].

$$\begin{aligned}
c_\mathrm{P,l} &= 4182\,\frac{\mathrm{J}}{\mathrm{kg\,K}}\\
h_\mathrm{l} &= c_\mathrm{p,l}\cdot T\\
\mu_\mathrm{l}(T) &= (\mathrm{Pa}\cdot\mathrm{s})\cdot 2.41\cdot 10^{-5}\cdot 10^{\left(\dfrac{247.8}{T'-140}\right)}\\
\sigma_\mathrm{l}(T) &= \left(\frac{\mathrm{N}}{\mathrm{m}}\right)\cdot\left(T'^2_\mathrm{C}\cdot -2.66\cdot 10^{-7}+T'_\mathrm{C}\cdot -1.41\cdot 10^{-4}+7.57\cdot 10^{-2}\right)\\
Pr_\mathrm{l}(T) &= 13.51-\left(1-\exp\left(-\frac{T'_\mathrm{C}}{25.83}\right)\right)\cdot 11.81\\
\kappa_\mathrm{l}(T) &= \left(\frac{\mathrm{W}}{\mathrm{m\,K}}\right)\cdot\left(-9.67\cdot 10^{-6}\cdot T'_\mathrm{C}+2.15\cdot 10^{-3}\cdot T'_\mathrm{C}+0.557\right)
\end{aligned}\tag{A.8}$$

A.5 Gas phase properties

The gas phase properties are evaluated using correlations, where the required constants are shown in Table A.5.

Table A.5: The constants required to evaluate the gas phase properties.

Species	c_h1 [−]	c_h2 [−]	c_h3 [−]	$h_\mathrm{fg,i}$ [J/(kg·K)]	$A_\mathrm{s,i}$ $\left[\mathrm{Pa{\cdot}s/K^{0.5}}\right]$	T_s [K]
CO_2	$8.18{\cdot}10^{2}$	$5.26{\cdot}10^{-1}$	$-2.59{\cdot}10^{-4}$	0	$1.69{\cdot}10^{-6}$	285.134
H_2O	$1.86{\cdot}10^{3}$	$1.33{\cdot}10^{-1}$	$2.03{\cdot}10^{-4}$	$2.4415{\cdot}10^{6}$	$2.39{\cdot}10^{-6}$	1021.36
O_2	$9.04{\cdot}10^{2}$	$1.76{\cdot}10^{-1}$	$-4.45{\cdot}10^{-5}$	0	$1.79{\cdot}10^{-6}$	156.052
SO_2	$6.05{\cdot}10^{2}$	$3.31{\cdot}10^{-1}$	$-1.75{\cdot}10^{-4}$	0	$1.67{\cdot}10^{-6}$	373.958
N_2	$1.03{\cdot}10^{3}$	$2.49{\cdot}10^{-2}$	$8.06{\cdot}10^{-5}$	0	$1.41{\cdot}10^{-6}$	107.161

The specific latent heat of evaporation, h_fg, is assumed zero for all species except H_2O, as h_fg for all others species are negligible in both value and mass transfer rates during simulation. The enthalpy of each species, $h_{\mathrm{g,i}}$, is calculated using (A.9), where the average enthalpy for the mixture, $h_{\mathrm{g,Mix}}$, is shown as well.

$$\begin{aligned} h_{\mathrm{g,i}} &= \left(\frac{\mathrm{J}}{\mathrm{kg}\cdot\mathrm{K}}\right)\cdot\left(c_{\mathrm{h1,i}}\cdot T' + c_{\mathrm{h2,i}}\cdot T'^{2} + c_{\mathrm{h3,i}}\cdot T'^{3}\right) + h_{\mathrm{fg,i}} \\ h_{\mathrm{g,Mix}} &= \vec{h}_{\mathrm{g}}\cdot\vec{w}_{\mathrm{g}} \end{aligned} \tag{A.9}$$

The viscosity of the gas phase is calculated using (A.10), where the viscosity for each species is correlated using the *Sutherland viscosity model* [Sutherland (124)]. More than 25 mixing correlations are available [Centeno et al. (22)], where the one used is the *Bingham mixing rule* [Bingham (16)]

$$\begin{aligned} &\text{(Sutherland viscosity model)} \qquad \mu_{\mathrm{g,i}} = \frac{A_{\mathrm{s,i}}\cdot\sqrt{T}}{1+\frac{T_{\mathrm{S}}}{T}} \\ &\text{(Bingham mixing rule)} \qquad \mu_{\mathrm{g,Mix}} = \left(\sum_{\mathrm{i}} \frac{y_{\mathrm{i}}}{\mu_{\mathrm{g,i}}}\right)^{-1} \end{aligned} \tag{A.10}$$

The density is calculated by assuming a perfect gas as described in *Section 6.1: Computational Fluid Dynamics*, where the ideal gas equation is shown in (A.11).

$$\rho_{\mathrm{g}} = \frac{P}{R\cdot T_{\mathrm{g}}}\cdot\underbrace{\left(\vec{M}\cdot\vec{w}_{\mathrm{g}}\right)}_{\text{Average molar mass}} \tag{A.11}$$

B SPHERICITY

The *Taylor Analogy Breakup*, TAB, model and the drag model uses two different definitions of deformation. The breakup model uses a dimensionless deformation parameter [O'Rourke and Amsden (101)], γ, and the drag model uses the sphericity [Haider and Levenspiel (65)], ψ. These relationship between these two parameters is derived in this appendix, where the outcome will be a functional relationship defined as $\psi(\gamma)$. An overview of the parameters is given in Figure B.1.

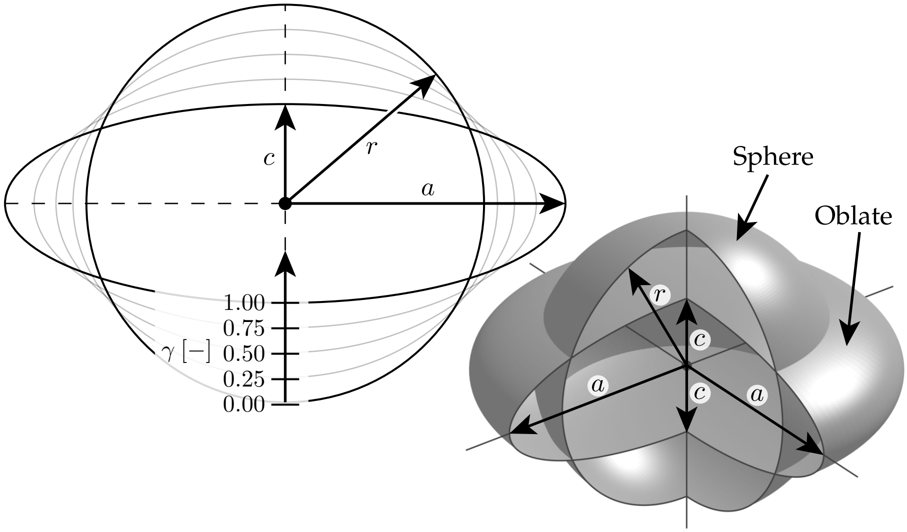

Figure B.1: The notations used in this appendix.

c is the semi-minor axis and a is the semi-major axis. The spheroid, which is the deformed sphere, is called an oblate when $c < a$, and a prolate when $c > a$. A variable used for derivation is introduced, f, which relates c and r as shown in (B.1).

$$\begin{aligned} f &= \left(1 - \frac{\gamma}{2}\right) \\ c &= r \cdot f = r \cdot \left(1 - \frac{\gamma}{2}\right) \end{aligned} \tag{B.1}$$

The geometric properties of both a sphere and an oblate spheroid are defined in (B.2) [Tee (128)].

$$\begin{aligned} V_{\text{Sphere}} &= \frac{4}{3}\,\pi\,r^3 \\ V_{\text{Spheroid}} &= \frac{4}{3}\,\pi\,a^2\,c \\ A_{\text{Sphere}} &= 4\,\pi\,r^2 \\ A_{\text{Spheroid}} &= 2\,\pi\,a^2\left(1+\frac{1-E_{\text{c}}^2}{E_{\text{c}}}\cdot\text{atanh}\left(E_{\text{c}}\right)\right) \quad , \quad c<a \\ E_{\text{c}}^2 &= 1-\frac{c^2}{a^2} \end{aligned} \tag{B.2}$$

Notice that only the surface area of an oblate, $c < a$, is shown, as this is the only relevant shape for this study. E_{c} is the eccentricity. When calculating the sphericity, ψ, the volumes of both the sphere and the spheroid should be kept constant. This constraint implies a new definition of a, which is shown in (B.3).

$$\begin{aligned} V_{\text{Sphere}} &= V_{\text{Spheroid}} \\ {}^4\!/\!_3\,\pi\,r^3 &= {}^4\!/\!_3\,\pi\,a^2\,c \\ &\Downarrow \\ a &= \frac{r}{\sqrt{f}} \end{aligned} \tag{B.3}$$

By substituting c from (B.1) and a from (B.3) into the expression for the eccentricity in (B.2), E_{c} can be expressed in terms of f, which is shown in (B.4).

$$\begin{aligned} E_{\text{c}}^2 = 1-\frac{c^2}{a^2} &= 1-\frac{(r\cdot f)^2}{\left(\frac{r}{\sqrt{f}}\right)^2} = 1-f^3 \\ &\Downarrow \\ E_{\text{c}} &= \sqrt{1-f^3} \end{aligned} \tag{B.4}$$

The sphericity, ψ, is derived as a function of f using (B.1) through (B.4), which is shown in (B.5).

$$\begin{aligned} \psi &= \frac{A_{\text{Sphere}}}{A_{\text{Spheroid}}} \\ &= \frac{4\,\pi\,r^2}{2\,\pi\,\left(\frac{r}{\sqrt{f}}\right)^2\left(1+\frac{1-E_{\text{c}}^2}{E_{\text{c}}}\cdot\text{atanh}\left(E_{\text{c}}\right)\right)} \\ &= \frac{2\cdot f\cdot E_{\text{c}}}{f^3\cdot\text{atanh}\left(E_{\text{c}}\right)+E_{\text{c}}} \\ E_{\text{c}} &= \sqrt{1-f^3} \end{aligned} \tag{B.5}$$

By substituting f with the definition in (B.1), the expression for sphericity as a function of γ can be derived from (B.5), which is shown in (B.6).

$$\begin{aligned}
\psi(\gamma) &= \frac{2 \cdot (1 - \gamma/2) \cdot E_\mathrm{c}}{(1 - \gamma/2)^3 \cdot \operatorname{atanh}(E_\mathrm{c}) + E_\mathrm{c}} \\
&= \left(\log_\mathrm{e}\left(\frac{E_\mathrm{c} + 1}{1 - E_\mathrm{c}} \right) \cdot \frac{(\gamma - 2)^2}{16\, E_\mathrm{c}} - \frac{1}{\gamma - 2} \right)^{-1} \\
E_\mathrm{c} &= \sqrt{1 - \left(1 - \frac{\gamma}{2}\right)^3}
\end{aligned} \tag{B.6}$$

The equatorial velocity, v_Equ, when $\gamma = 1$ is used to determine the normal velocity of the child droplets, when breakup occurs. This velocity is calculated using (B.7).

$$\begin{aligned}
v_\mathrm{Equ} &= \frac{\mathrm{d}a}{\mathrm{d}t} = \frac{\mathrm{d}a}{\mathrm{d}\gamma} \cdot \left(\frac{\mathrm{d}\gamma}{\mathrm{d}t} \right) = \frac{C_\mathrm{b} \cdot r}{2 \cdot (1 - C_\mathrm{b} \cdot \gamma)^{3/2}} \cdot \left(\frac{\mathrm{d}\gamma}{\mathrm{d}t} \right) \\
&\Downarrow (\gamma = 1) \\
v_\mathrm{Equ} &= \frac{C_\mathrm{b} \cdot r}{2 \cdot (1 - C_\mathrm{b})^{3/2}} \cdot \left(\frac{\mathrm{d}\gamma}{\mathrm{d}t} \right)
\end{aligned} \tag{B.7}$$

Reference [O'Rourke and Amsden (101)] calls for a definition for v_Equ, which is proportional to C_b. Therefore, a new dimensionless parameter is introduced, C_v, which scales the equatorial velocity, which is defined in (B.8).

$$\begin{aligned}
C_\mathrm{v} &= \frac{1}{2 \cdot (1 - C_\mathrm{b})^{3/2}} \xrightarrow[C_\mathrm{b}=0.5]{} C_\mathrm{v} = \sqrt{2} \\
v_\mathrm{Equ} &= C_\mathrm{v}\, C_\mathrm{b}\, r \frac{\mathrm{d}\gamma}{\mathrm{d}t}
\end{aligned} \tag{B.8}$$

ISSN (online): 2446-1636
ISBN (online): 978-87-7210-357-0

AALBORG UNIVERSITY PRESS